Alma Mater Studiorum – Università di Bologna

DOTTORATO DI RICERCA IN

CHIMICA

Ciclo XXIX

Settore Concorsuale di afferenza: 03/B1

Settore Scientifico disciplinare: CHIM/03

Performance, Stability and Environmental Impact of Organic Solar Cells: Towards Technology Scale-up

Presentata da: Mario Prosa

Coordinatore Dottorato	**Relatore**
Prof. Aldo Roda	Prof. Margherita Venturi

Correlatori

Dr. Michele Muccini

Dr. Mirko Seri

Esame finale anno 2017

Abstract

The effects of global climate changes are progressively observable on the environment around us. Their direct correlation with the CO_2 emission coming from the fossil fuel combustion and industrial processes elucidates the urgent need of renewable energies. In this context, organic photovoltaics (OPVs) attracts much attention because of the cost-competitiveness and the new device functionalities over existing solar cells. Indeed, the possibility to manipulate the properties of organic materials through chemical modifications and prepare them in the form of inks opens the road to economically sustainable production of flexible, light-weight devices which also meet aesthetical requirements as semi-transparency and color-tunability.

The last decade showed an exponential evolution of OPVs. All over the world, grant-funded programs contributed to the progress of this technology. In particular, the works presented in this thesis contributed to the European project SUNFLOWER (grant number 287594, web site: http://www.sunflower-fp7.eu/site/index.php). Because of the advantages of semiconducting polymers over small molecules, this Ph.D. thesis focuses on solution-processed polymer solar cells (PSCs) where an electron donor polymer is mixed with a fullerene derivative at the solid state leading to the bulk heterojunction active layer, the absorbing and charge producing layer of a PSC. It is noteworthy that, aiming at the industrialization of this technology, the requirements for the large-scale manufacture are considered in the experimental procedures for the device fabrication.

In a preliminary part of this thesis, the development of novel materials, the optimization of the processing conditions and a deeper understanding of the device physics are introduced to clarify the pathways that led to the progressive enhancement of the PSCs efficiency.

However, despite the recent achievements, PSCs still present some issues regarding their stability under operation conditions, which slow down the widespread commercialization of this technology. Indeed, the nature of organic semiconductors makes them potentially susceptible to prolonged illumination and heating. To this end, part of this thesis discusses some specific aspects related to the stability of critical materials/layers of organic solar cells. In particular, the light stability of different active materials and ZnO layers is investigated in order to provide guidelines for the development of

active/functional materials for improved organic solar cells. Moreover, the impact of the processing conditions on the thermal stability of the resulting photovoltaic devices is studied. In detail, through the development of advanced characterization techniques, the choice of the processing solvent for the active layer deposition is demonstrated to be determining for the morphology of the resulting films and their tendency to re-organize under thermal stress.

In this context, the use of an alternative solvent able to reduce the environmental impact of organic solar cells is here presented. In particular, the effect of the replacement of common chlorinated solvents with an environmentally friendlier analogous is investigated both in terms of device efficiency and thermal stability.

Finally, a contribution to the understanding of state-of-the-art tandem architectures is presented as a perspective for the large scale deployment of highly performing solar cells. In the context of the tandem optimization, part of the Ph.D. project was spent at the "Friedrich-Alexander-Universität Erlangen-Nürnberg" (Institute: Materials for Electronics and Energy Technology, i-MEET, Germany) under the supervision of Prof. Christoph J. Brabec, working on a joint project focused on the mechanisms of charges recombination in the interconnecting layer of tandem devices.

The analysis of the crucial aspects of OPVs such as the device performance, stability and environmental impact provides the basis for the development of improved devices heading to the widespread deployment of this technology.

Acknowledgments

Table of Contents

List of Publications

Publications related to the thesis

- *A New Quinoxaline and Isoindigo Based Polymer as Donor Material for Solar Cells: Role of Ecofriendly Processing Solvents on the Device Efficiency and Stability*
  M. Seri, D. Gedefaw, **M. Prosa**, M. Tessarolo, M. Bolognesi, M. Muccini, M. R. Andersson.
  Journal of Polymer Science, Polymer Chemistry, **2017**, *55*, 234.

- *Efficient and Versatile Interconnection Layer by Solvent Treatment of PEDOT:PSS Interlayer for Air-Processed Organic Tandem Solar Cells*
  M. Prosa, M. Tessarolo, M. Bolognesi, T. Cramer, Z. Chen, A. Facchetti, B. Fraboni, M. Seri, G. Ruani, M. Muccini.
  Advanced Materials Interfaces, **2016**, *3*, 1600770.

- *"Enhanced Ultraviolet Stability of Air-Processed Polymer Solar Cells by Al-doping of the ZnO Interlayer"*
  M. Prosa, M. Tessarolo, M. Bolognesi, O. Margeat, D. Gedefaw, M. Gaceur, C. Videlot-Ackermann, M. R. Andersson, M. Muccini, M. Seri, J. Ackermann.
  ACS Applied Materials & Interfaces, **2016**, *8*, 1635.

- *Impact of environmentally friendly processing on polymer solar cells: Performance, thermal stability and morphological study by imaging techniques*
  M. Bolognesi, **M. Prosa**, M. Tessarolo, G. Donati, S. Toffanin, M. Muccini, M. Seri.
  Solar Energy Materials & Solar Cells, **2016**, *155*, 436.

- *Induced photodegradation of quinoxaline based copolymers for photovoltaic applications"*
  D. Gedefaw, M. Tessarolo, **M. Prosa**, M. Bolognesi, P. Henriksson, W. Zhuang, M. Seri, M. Muccini, M. R. Andersson.
  Solar Energy Materials & Solar Cells, **2016**, *144*, 150.

- *Synthesis and characterization of benzodithiophene and benzotriazole-based polymers for photovoltaic applications*
  D. Gedefaw, M. Tessarolo, M. Bolognesi, **M. Prosa**, R. Kroon, W. Zhuang, P. Henriksson, K. Bini, E. Wang, M. Muccini, M. Seri, M. R. Andersson.
  Beilstein Journal of Organic Chemistry, **2016**, *12*, 1629.

- *Tuning the Electron-Acceptor Properties of [60]Fullerene by Tailored Functionalization for Application in Bulk Heterojunction Solar Cells*
  M. Cristofani, E. Menna, M. Seri, M. Muccini, **M. Prosa**, S. Antonello, M. Mba, L. Franco, M. Maggini.
  Asian Journal of Organic Chemistry, **2016**, *5*, 676.

Other Publications

- *High-performance ternary organic solar cells with thick active layer exceeding 11% efficiency*
  N. Gasparini, L. Lucera, M. Salvador, **M. Prosa**, G. D. Spyropoulos, P. Kubis, H. Egelhaaf, C. J. Brabec, T. Ameri.
  Energy & Environmental Science, **2017**, DOI: 10.1039/C6EE03599J.

- *Indacenodithienothiophene (IDTT)-Based Ternary Organic Solar Cells*
  N. Gasparini, A. García-Rodríguez, **M. Prosa**, Ş. Bayseç, A. Palma-Cando, A. Katsouras, A. Avgeropoulos, G. Pagona, V. G. Gregoriou, C. L. Chochos, S. Allard, U. Scherf, C. J. Brabec, T. Ameri.
  Frontiers in Energy Research, **2017**, doi: 10.3389/fenrg.2016.00040.

- *Recent Development of Quinoxaline Based Polymers/Small Molecules for Organic Photovoltaics*
  D. Gedefaw, **M. Prosa**, M. Bolognesi, M. Seri, M. R. Andersson.
  Submitted for publication.

- *A self-assembled lysinated perylene diimide film as multifunctional material and neural interface*
  S. Bonetti, **M. Prosa**, A. Pistone, L. Favaretto, A. Sagnella, I. Grisin, M. Zambianchi, S. Karges, A. Lorenzoni, T. Posati, R. Zamboni, N. Camaioni, F. Mercuri, M. Muccini, M. Melucci, V. Benfenati.
  Journal of Materials Chemistry B, **2016**, *4*, 2921.

- *Predicting thermal stability of organic solar cells through an easy and fast capacitance measurement*
  M. Tessarolo, A. Guerrero, D. Gedefaw, M. Bolognesi, **M. Prosa**, X. Xu, M. Mansour, E. Wang, M. Seri, M. R. Andersson, M. Muccini, G. Garcia-Belmonte.
  Solar Energy Materials & Solar Cells, **2015**, *141*, 240.

- *Integration of a silk fibroin based film as a luminescent down-shifting layer in ITO-free organic solar cells*
  M. Prosa, A. Sagnella, T. Posati, M. Tessarolo, M. Bolognesi, S. Cavallini, S. Toffanin, V. Benfenati, M.Seri, G. Ruani, M. Muccini, R. Zamboni.
  RSC Advances, **2014**, *4*, 44815.

Proceeding article

- *Predicting thermal stability of organic solar cells through real-time capacitive techniques (Presentation Recording)*
  M. Tessarolo, A. Guerrero, M. Seri, **M. Prosa**, M. Bolognesi, G. Garcia-Belmonte.
  Proc. SPIE 9567, Organic Photovoltaics XVI, 956715 (October 5, **2015**); doi:10.1117/12.2186998;

x

List of Abbreviations

A	Electron acceptor
AFM	Atomic force microscopy
AM	Air mass
a-Si	Amorphous Silicon
ATR-FTIR	Attenuate Total Reflection - Fourier Transform Infrared Spectroscopy
AZO	Aluminum-doped ZnO
BHJ	Bulk heterojunction
CB	Chlorobenzene
CFL	Compact fluorescence light
CIGS	Copper-Indium-Gallium-Diselenide
CIS	Copper-Indium-Selenide
CN	1-chloronaphtalene
CPV	Concentrating photovoltaic
c-SI	Crystalline Silicon
CT	Charge transfer
D	Electron donor
DFT	Density functional theory
DIO	1,8-diiodooctane
DSSC	Dye-sensitized solar cell
Eg	Energy band-gap
EL	Electroluminescence
EPA	Environmental protection agency
EPBT	Energy payback time
EPR	Electron paramagnetic resonance
EQE	External quantum efficiency
ETL	Electron transporting layer
FC	Free charges
FF	Fill factor
FRET	Förster resonant energy transfer
G	Global
HOMO	Highest occupied molecular orbital
HTL	Hole transporting layer
IARC	International agency for research on cancer
ICBA	indene-C60 bisadduct
ICL	Interconnecting layer
IPA	Isopropanol
IPCC	Intergovernmental Panel on Climate Change
IQE	Internal quantum efficiency
IR	Infrared
ISOS	International Summit on OPV Stability
ITO	Indium Tin Oxide
Jdark	Current density under dark conditions
Jillum	Current density under standard illumination
Jph	Photo-generated current density

Jsc	Short-circuit current density
KPFM	Scanning Kelvin Probe Force Microscopy
LBIC	Laser beam induced current
LCA	Life cycle assessment
LCOE	Levelized cost of energy
LED	Light emitting diode
LSCM	Laser scanning confocal microscopy
LSPM	Laser scanning photocurrent microscopy
LSVM	Laser scanning photovoltage microscopy
LUMO	Lowest unoccupied molecular orbital
MB	Methyl-substituted benzene
mc-Si	Multi Crystalline Silicon
MDMO-PPV	poly[2-methoxy-5-(3',7'-dimethyloctyloxy)-1,4-phenylenevinylene]
MEH-PPV	poly[2-methoxy-5-(2-ethylhexyloxy)-1,4-phenylenevinylene]
M_N	Number average molar mass
M_W	Mass average molar mass
OD	Optical density
o-DCB	Orthodichlorobenzene
ODT	1,8-octanedithiol
OLED	Organic light-emitting diode
OPV	Organic photovoltaic
OSC	Organic solar cell
PCE	Power Conversion Efficiency
PDI	Poly dispersive index
PEIE	polyethylenimine ethoxylated
PET	poly(ethylene terephthalate)
PffBT4T-C9C13	poly[(5,6-difluoro-2,1,3-benzothiadiazol-4,7-diyl)-alt-(3,3'''- di(2-nonyltridecyl)-2,2';5',2";5",2'''-quaterthiophen-5,5'''-diyl)]
PFN	poly[(9,9-bis(3'-(N,N-dimethylamino)propyl)-2,7-fluorene)-alt-2,7-(9,9-dioctylfluorene)]
PL	Photoluminescence
PMDPP3T	poly[[2,5-bis(2-hexyl-decyl-2,3,5,6-tetrahydro-3,6-dioxopyrrolo[3,4c]pyrrole-1,4-diyl]-alt-[3?,3?-dimethyl-2,2?:5?,2?-terthiophene]-5,5?-diyl]
PPV	poly(phenylenevinylene)
PSC	Polymer solar cell
PTB7-Th	Poly[4,8-bis(5-(2-ethylhexyl)thiophen-2-yl)benzo[1,2-b;4,5-b']dithiophene-2,6-diyl-alt-(4-(2-ethylhexyl)-3-fluorothieno[3,4-b]thiophene-)-2-carboxylate-2-6-diyl)]
PV	Photovoltaic
Q or Qx	quinoxaline
R2R	Roll-to-roll
RMS	Root mean square
Rp or Rsh	Parallel or shunt resistance
rpm	Rounds per minute

Rs	Series resistance
S$_{(0, 1, 2, ...)}$	Singlet electronic state
sc-Si	Single crystalline Silicon
SJ	Single-junction
SWV	Square wave voltammetry
T$_{(0, 1, 2, ...)}$	Triplet electronic state
TCB	Trichlorobenzene
Tg	Glass transition temperature
TREPR	Time resolved electron paramagnetic resonance
Tz	Benzotriazole
UV	Ultraviolet
V$_0$	Compensation voltage
vis	Visible
Voc	Open circuit voltage
WF	Work function
µ-Si	Micromorph Silicon
π-π*	pi-pi* electronic transition

Chapter 1

Organic photovoltaics: critical review and aim of the work

1.1   General overview on renewable energies

The effects of global climate change are progressively observable on the environment. The world mean temperature continuously rises up causing glaciers melting and raising the sea level, heavy precipitations become more frequent and hurricanes stronger. These are just some evidences around us of the effects of climate warming. Nevertheless, the Intergovernmental Panel on Climate Change (IPCC) forecasts a temperature rise of 1 to 5 degrees Celsius over the next century stating that "…the net damage costs of climate change are likely to be significant and to increase over time." which clearly indicates the importance of the problem.[1]

Recent studies identified a near-linear relationship between the global mean temperature and the CO_2 concentration in the atmosphere.[2] CO_2 is indeed a greenhouse gas which means that, by absorbing sunlight and reemitting it in the form of thermal energy, heats the Earth providing mankind of a comfortable climate. However, by continuously adding extra greenhouse gases to the atmosphere, the planet's temperature is raising with wide-ranging impacts.

This direct connection with the global temperature elucidates the significant impact of CO_2 emissions from fossil fuel combustion and industrial processes on the global warming thus highlighting the necessity to control the CO_2 concentration in the atmosphere. In this context, to limit the harmful consequences, the emissions should be reduced up to ensure a global mean temperature of maximum 1.5 - 2°C above pre-industrial levels. Nonetheless, despite the Kyoto Protocol, the last decades were characterized by a positive growth rate of CO_2 emission (Figure 1.1). The strong increase in economic activity of emerging countries, indeed, led to a local redistribution of the CO_2 emissions, with the negative growth contribution from Europe more than offset by a largely positive contribution from China and India, for instance.[3]

Moreover, as the global energy consumption is predicted to rise up to 30 TW in 2050 (17 TW in 2010), the employment of the continuously depleting fossil fuel, *i.e.* in the form of coal, oil and gas, needs to be drastically reduced towards the deployment of new alternative low-carbon energy resources.[4][5]
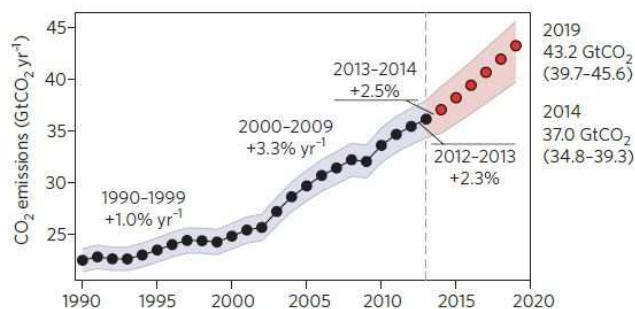
Figure 1.1. Global CO_2 emission over 1990-2013 period (black dots) and estimates to 2019 (red dots). Reprinted by permission from Macmillan Publishers Ltd: Nature Geoscience [3], copyright 2014.

In this view, renewable energy sources show an enormous potential, which could meet many times the global energy demand, with limited impact on the human health and on the environment. They are indeed a class of sources derived from nature and can be furthermore considered inexhaustible for a relatively long time scale. Among them, wind power, solar energy, hydropower, biomass and geothermal energy are the most deployed. Nonetheless, they currently supply only 11% of world's total energy demand while fossil fuel dominates with more than 80%. Within renewable sources, the greatest contribution comes from hydroelectric sources followed by wind power, while new sources as solar and geothermal energy currently represent only a limited part of the employed renewables, each contributing for only 2% (Figure 1.2).[6]
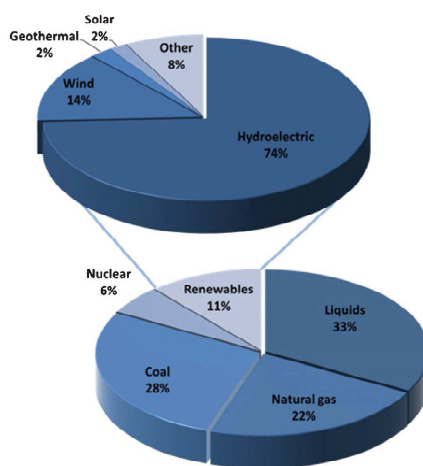
Figure 1.2. Global energy consumption in 2013.[6]

With 0.5 TW, hydropower is the most widespread renewable energy covering around three-quarters of the deployed sources. However, this technology is not expected to emerge since most of the locations have already been explored leaving little room for new installations. Similarly, wind energy had important growth in the recent years, however the technical exploitable energy is limited and cannot satisfy the global energy demand. Concerning geothermal energy, the deep drilling of the planet crust represents an important limitation for the deployment of this source.

In this view, solar energy is a valid and promising alternative among renewables. Sun is indeed a star, which continuously pours a huge amount of electromagnetic radiations on the Earth surface and one hour of illumination has the potential to power the entire planet for one year. As shown in Figure 1.3, few small areas covered with solar panels would be enough to satisfy the current global energy consumption. Moreover, considering a 2% of surface crust with solar panels and accounting that not all the incident light can be collected and converted into electricity, around 67 TW of energy is estimated to be obtained, which represents more than 2 times the global energy consumption predicted for 2050 (30 TW).[6]
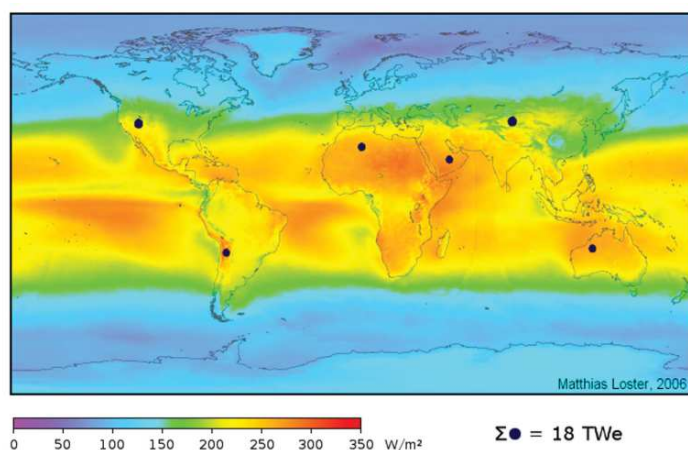
Figure 1.3. Average of the solar irradiance on the earth surface. Black dots represent the areas covered with solar panels required to satisfy the actual global energy demand.[7]

Solar energy is a natural source available all over the world, in this view, photovoltaics (PVs) can be considered as a "democratic" technology. Contrarily to the global economic scene, it is accessible to all single individuals and Africa, with its different programs for the development of photovoltaics, represents a remarkable example. Among all the programs, the Kingdom of Morocco solar plan is considered one of the largest projects on solar energy with around 9 billion dollars involved.[8]

Besides all the advantages as renewable energy, photovoltaic technology has furthermore no fuel need and relatively low maintenance costs. Nevertheless, new challenges are expected from a massive diffusion. Indeed, smart conversion systems should be suitably developed to power high energy-demanding structures such as industries and skyscrapers. Storage components need to be integrated in the photovoltaic systems in order to provide the required amount of energy over the right time. In this context, materials abundance, sustainability and scalability are parameters to be considered in designing innovative solutions.[9]

Over the years, many different materials were employed and developed for photovoltaic applications with the result of a wide range of technologies present nowadays on the market. They are usually classified in three generations depending on the materials used in the device and their commercial maturity.

The first generation comprises commercially available systems and is typically associated to silicon founded technology. Silicon is one of the most abundant materials in the earth's crust and is suitable for photovoltaic applications because of its semiconducting properties and the advantageous bandgap of 1.1eV. The derived technology employs wafers of silicon in crystalline (c-Si), single crystalline (sc-Si) or multi-crystalline (mc-Si) state with the first two typically consisting of rigid structures, while the latter is often mechanically flexible. The use of abundant and non-toxic elements, in conjunction with the remarkable energy conversion efficiency and lifetime of the devices, demonstrate why silicon solar panels are dominating the market. Despite that, the production and installation is typically expensive and even if the costs continuously decreased over the years,[10] the commercialization of silicon panels requires an economic investment by the consumer.

The second generation of photovoltaics accounts for technologies in early market deployment. It consists of thin-films of semiconductor deposited on a support and includes amorphous (a-Si) and micromorph (μc-Si) silicon, Cadmium Telluride (CdTe), Copper-Indium-Selenide (CIS) and Copper-Indium-Gallium-Diselenide (CIGS). If compared to the first generation, the use of thin films is an advantage both in terms of required material and because widens the deposition methods towards large area coating, which reduces the production costs and opens to the possibility of integration into building components. However, this generation suffers for issues of durability (a-Si), materials availability (In, Ga) and toxicity (Cd).[11]

The third generation of solar cells consists of new technologies and concepts at the pre-commercial stage, which still require some research and development. Compared to the previous photovoltaic generations, innovative device applications, good performance under non-standard illumination and temperature are introduced. Moreover, lower requirements in terms of quality and quantity of raw materials are present in the third photovoltaic generation, which however is still affected by limited device efficiency and durability. This generation includes concentrator photovoltaics (CPVs), dye-sensitized solar cells (DSSCs), organic solar cells (OSCs) and the emerging class of perovskite solar cells.

CPVs typically exploits systems of lens to focus and increase the intensity of solar light reaching the device. This type of technology is usually applied on systems characterized by multiple semiconducting layers stacked in a single device (multi-junction architecture) in order to absorb as much solar photons as possible. The structure is very efficient but also highly complex. As a result, it is expensive if compared to conventional photovoltaics and the use of concentrated light notably increases the temperature, thus requiring an additional cooling system. Not less important, it is mainly applicable in regions with clear skies as CPV needs direct sunlight to fully exploit its potential.

DSSCs are considered hybrid solar cells since they couple organic absorbing dyes with an inorganic scaffold. As working mechanism, they mime the natural photosynthesis. In particular, the solar light is absorbed by an organic dye typically based on a Rutenium complex and free charges are generated at the interface between the organic molecule and the inorganic counterpart (typically porous TiO_2). The use of a multi-component device confers the possibility to exploit the full potential of this type of solar cells by optimizing the single parts. Despite that, the power conversion efficiency (PCE) of DSSCs, after reaching values around 11% in 1997, did not improved so much (Figure 1.4). The limitations of this type of devices arise from the typically narrow absorption of organic molecules and from the need of a liquid electrolyte to restore the initial neutrality of the dye, which can freeze at operating temperatures. The physical detainment of the liquid during device operation introduces limitations in terms of flexible applications and issues related to the device durability. Despite solid electrolytes were recently developed, their efficiency is still limited.

The evolution of the hybrid PV technology is represented by the use of perovskite, a crystal which refers to ABX_3 structure where A is the organic cation, B is the metal cation and X is the halide anion. The most used crystals are methylammonium lead halides,

$CH_3NH_3Pb(I,Cl,Br)_3$. This technology is at the forefront of recent research on photovoltaics since in only five years the power conversion efficiency of this type of devices has risen from about 3% to more than 21% (certified).[12][13] Compared to DSSCs, the benefits of perovskite cells arise from the use of a simplified device structure which avoids the need of an electrolyte. Moreover, this class of materials presents physical properties comparable to inorganic materials and the advantages of organic compounds such as wet deposition and large area coverage at relatively low-cost. This undoubtedly confers enormous potential to perovskite solar cells to succeed. However, since perovskite rapidly degrades under operating temperatures, some concerns are still devoted to the device stability and furthermore to the strong environmental impact due the presence of toxic elements such as lead (Pb).

Diversely, organic photovoltaics (OPVs) is a technology based on a thin film of π-conjugated organic small molecules or polymers with a thickness ranging from tens to hundreds of nanometers. The advantage to use organic materials offers the opportunity to have flexible, semitransparent and lightweight modules with very low economic impact restrained from the possibility to employ relatively simple manufacture processes for large scale production. The power conversion efficiency of organic solar cells reached values approaching 13% for lab-scale devices (active area: < 1 cm^2)[14] and 9.5% (certified) for mini-modules (active area: ≈ 25 cm^2).[15] However, the commercialization of this technology is still slowed by stability issues, in particular under harsh operating conditions, related to thermal- and light-induced changes of the organic compounds.
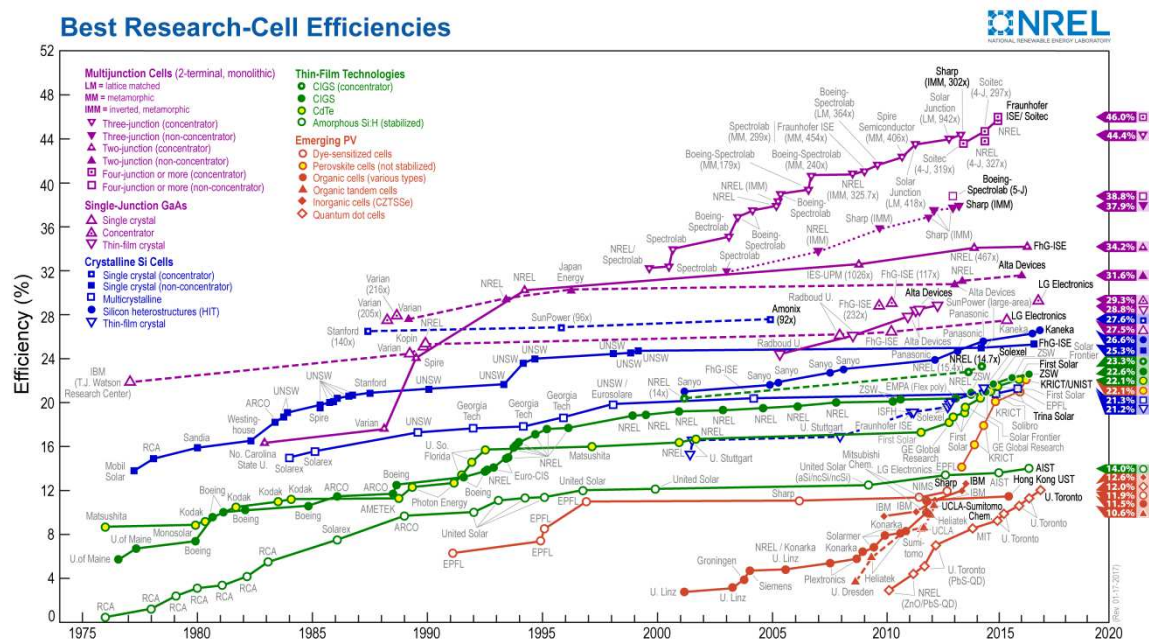
Figure 1.4. Chart of the best power conversion efficiencies for different photovoltaic technologies over the time published by the National Renewable Energy Laboratory (NREL).[16]

An overview on the trend of the power conversion efficiencies of the different photovoltaic technologies is reported in Figure 1.4. As shown, the record among all the photovoltaic technologies was obtained using inorganic materials. However, to economically evaluate and compare different photovoltaic technologies, besides their power conversion efficiency, other two indicators should be considered: *i*) the Levelized Cost of Energy (LCOE) and *ii*) the Energy Payback Time (EPBT).[4][6]

The LCOE valuates the cost-effectiveness of the technology as the ratio between all the costs involved in the life-cycle of the system (construction, operation, maintenance and decommission) and the total energy produced, including efficiency and lifetime. Organic solar cells, despite their still limited power conversion efficiency, present many benefits compared to other technologies. Indeed, the lightweight and flexibility of the devices drastically reduce the distribution costs as transport and installation, and their processability in streamlines also contributes to lower the production costs making them competitive with traditional fossil fuel sources.

The EPBT is a parameter which accounts for the energy involved in the production and decommission of the system and considers the time required by the technology to produce the same amount of energy. Similarly to LCOE analysis, forecasts estimate an EPBT in the order of days for organic photovoltaics[17] while in the order of years for the currently mature technologies, showing again the great competitiveness of organic solar cells.

In summary, to be competitive and lower the electricity cost, a photovoltaic technology should be characterized by a high efficiency, a good reliability and durability, low costs of the materials and economic production (Figure 1.5). Organic photovoltaics represents in this context a promising technology.
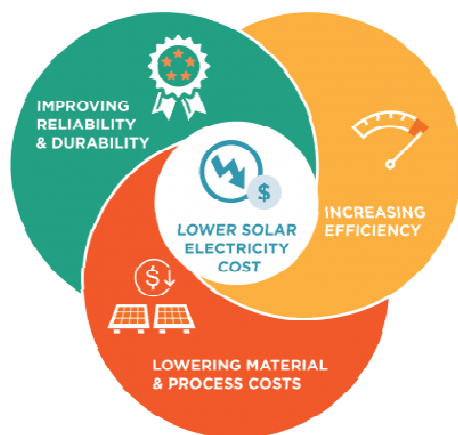
Figure 1.5. Requirements for photovoltaic technologies to reduce the cost of electricity.[18]

1.2   **Organic photovoltaics: concepts and evolution**

As a prospective solar technology, OPVs is one of the most promising alternatives in the emerging scenario because of the unique device functionalities over the other technologies. As source of the advantages, the possibility to synthesize and manipulate the semiconductors offers the outstanding potential to deliberately tune the device properties. Organic photovoltaics is indeed based on π-conjugated small molecules or polymers which can be unlimitedly modified by chemical synthesis.

An overview of the opportunities that OPVs could offer, motivates the large investments on this technology over the recent years.

- Scalability at low cost: the possibility for organic semiconductors to be prepared as inks opens the road towards the use of fast-printing techniques for the massive production of solar modules. The highly automated and roll-to-roll (R2R)

processing confers the further advantage of an economically-sustainable production of organic solar cells with low material consumption (Figure 1.6a).

- Good form-factor: the fabrication of solar cells from solutions allows for module designing and the use of flexible and light-weight supports. This opens towards solar panels, which roll up or can be adapted on curved surfaces, that is innovative for the overall photovoltaic market. These functionalities represent a distinction feature for organic solar cells as they can potentially be installed on existing surfaces, integrated in architectural structures or, for instance, applied on moving objects (*e.g.* on cars, trains, etc. to prevent discharging of batteries). Moreover, as the properties of organic materials can be tuned on purpose, devices can also meet aesthetic requirements as semi-transparency and color tunability for application in items of daily use (Figure 1.6).

- Harvesting factor: organic modules offer an effective PV response at relatively high temperatures and also at low light illumination. Organic materials indeed exhibit increased charge mobility by increasing the temperature. Moreover, they offer the attractive capability to efficiently respond at the low light intensities (or diffused light) and, almost indifferently, to different sunlight angles of incidence. Diversely from the other photovoltaic technologies, this represents a remarkable benefit for the outdoor application of organic solar modules since they provide an almost constant power over the entire daily cycle. The effective response at low light intensities, in conjunction with the possibility to have semi-transparent and colored devices, represent remarkable characteristics of organic modules for indoor applications. In this context, the organic solar modules can be used as window coverings, *e.g.* curtains or colored window films, which are innovative applications of the photovoltaic technology.

Furthermore, the characteristic narrowed absorption of organic compounds can be exploited for additional applications of organic solar cells such as the indoor light recycling. The concept is to use indoor lighting from light emitting diodes (LEDs) or compact fluorescence lights (CFLs) to power solar modules, which are applied on indoor items.[19] As a result, part of the energy used for indoor lighting is recycled through the use of solar cells.

- <u>Low environmental impact potential</u>: the use of organic materials results in solar modules which are fully free of rare Earth elements, precious metals and toxic substances and hence potentially excellent in terms of environmental sustainability.
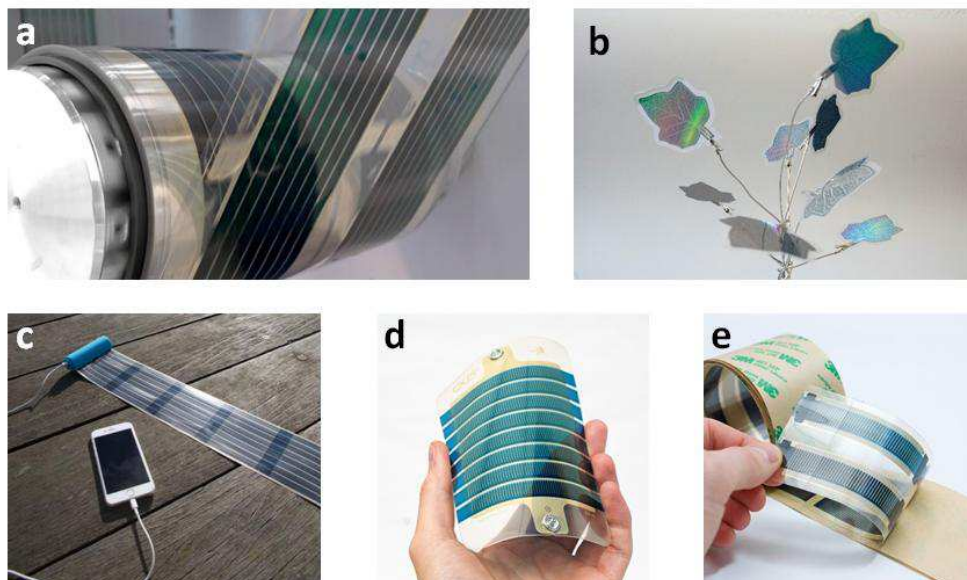
Figure 1.6. Organic solar modules fabrication through printing technique (a) and application as solar tree (b),[20] phone charger (c), mini-module (d) and solar tape (e).[21]

Despite the attracting characteristics, organic photovoltaics should not be conceived as a replacement of the existing technologies. Rather, it represents a clear example on how different solar technologies can be complementary in terms of applications. For instance, one of the major drawbacks of organic solar modules is their poor device efficiency which is, on the other hand, among the main advantages of silicon photovoltaics. On the contrary, properties such as lightness and semi-transparency are typical of organic modules while lacking in the silicon technology. In the short term, the expectation to have organic modules with performance similar to those of the inorganic ones is indeed erroneous. Similarly, silicon modules are not expected to show semi-transparency. The photovoltaic energy production can be indeed exploited in different but synergic ways. For instance, the long durability and high efficiency of the rigid silicon modules are suitable for massive outdoor use such as roof-application. On the contrary, the color-tunability, flexibility and light weight of OPV modules are more suitable for specific applications such as their integration in pre-existing passive systems, indoor

environments, portable electronics and various objects where the OPV peculiarities are essential.[22]

1.2.1 Evolution and working principles

Different from other photovoltaic technologies, organic solar cells exploit the semiconducting properties of organic molecules or polymers to convert light into electricity. In an organic semiconductor, a series of superposed p_z orbitals from sp or sp^2 hybridized carbon atoms creates the so called π-conjugation where a cloud of spatially delocalized electrons above and below the molecular plan confers semiconducting properties to the molecular structure (Figure 1.7a). The extended π-conjugation results in new molecular orbitals (Figure 1.7b) with the energy difference (band gap, E_g) between the highest occupied molecular orbital (HOMO) and the lowest unoccupied molecular orbital (LUMO) matching the solar radiation energies (1.5 – 3 eV).

Upon photo-excitation, the organic semiconductor passes from a ground relaxed state to an excited state in which tightly bound electron-hole pairs, called excitons, are formed. Diversely from inorganic semiconductors, the dielectric constant of organic materials is typically low ($\varepsilon_r \approx 2 - 4$) and Frenkel excitons are created. This type of excitons presents electrostatic binding energies in the order of 0.3 – 1 eV, much higher than the kinetic energy at room temperature (≈ 0.026 eV). As a consequence, they cannot spontaneously dissociate into free charges as in inorganic materials and the presence of a driving force that overcomes the Coulombic binding energy is necessary.
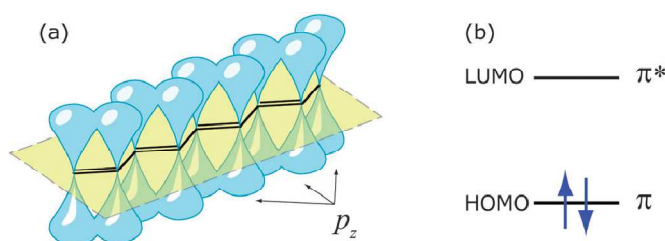
Figure 1.7. Example of conjugated molecule with overlapping P_z orbitals (a) and the relative frontier orbitals (b). Reproduced from Ref. [23] with permission of The Royal Society of Chemistry.

At the early stage, organic solar cells were composed by a single organic layer sandwiched between two electrodes with different work functions (WFs). In this system, the organic layer establishes an ohmic contact with one electrode and a Schottky junction with the other, typically the cathode (Figure 1.8a). At this interface, a band bending of the

organic frontier orbitals induces the formation of a depletion region where excitons can dissociate into free charges. Because of the spatially narrowed depletion region, most of the excitons are formed outside it and decay back to the ground state instead of dissociating. Moreover, considering the typically limited charge mobility of organic materials and since opposite free charges travel across the same phase, the probability of bimolecular recombinations is very high.

The combination of all these factors explains the low photovoltaic performance observed in single layer organic solar cells that did not exceed 0.1% of power conversion efficiency.[24]

To overcome the limitations of the single layer structure, Tang *et al.* developed a bilayer architecture where an hole transporting (p-type) and an electron transporting (n-type) layers are in contact through a planar junction (heterojunction) and the entire stack is comprised between two different electrodes (Figure 1.8b).[25] Using materials with different electron affinity, their interface acts similar to a p-n junction thus excitons formed in the proximity of the other material, diffuse to the interface between the two materials forming charge transfer excitons (CT state or CT excitons). Lying across two different phases, the reduced Coulomb binding energy allows CT excitons to split into free charges. The presence of an electric field drives the free electrons and holes through the relative phase and towards the respective electrodes where can be collected. Bimolecular recombination losses are highly reduced since opposite charges travel in separated phases. However, the short lifetime of the excitons ($\leq$ 1 ns) limits their diffusion length to short distances, between 5 and 14 nm.[26] To dissociate as many excitons as possible, the layers should be thin enough to ensure that all the excitons can reach the interface with the other material. This represents an important limitation since the reduction of the thickness affects the optical absorption of the layer and hence the amount of formed excitons.
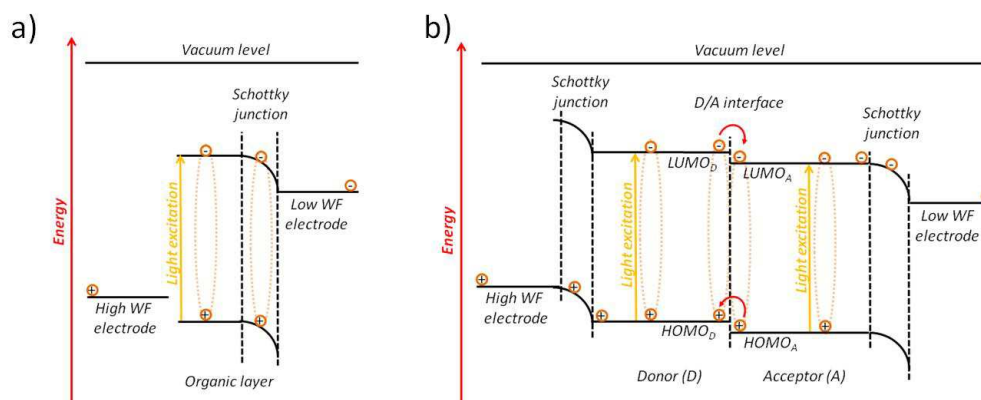
Figure 1.8. Energy level diagram for single layer (a) and planar bi-layer (b) organic solar cells.[27]

The major breakthrough for organic photovoltaics was established independently by Yu *et al.*[28] and Halls *et al.*[29] in 1995, when the concept of bulk heterojunction (BHJ) was developed. In BHJ devices, a large contact exists between the p-type and n-type materials. The two materials are indeed mixed to form an interpenetrating network. In sight of this, the domain size is optimized in the order of the excitons diffusion length in order to dissociate all the excitons formed upon photo-excitation. The mixture of the two materials should however ensure bicontinuous paths for free charges to reach the respective electrodes.

In this type of structure, the p-type material is usually a small molecule or polymer with an absorption spectrum as wide as possible in order to absorb the whole solar light. The efficient photo-induced electron transfer from a conjugated polymer to fullerene (C_{60}) observed by Morita *et al.*[30] and Sariciftci *et al.*[31] started the era of using fullerene derivatives as n-type materials. Indeed, the great electron delocalization properties of fullerenes, which results in a suitable electron affinity, the great electron mobility and the possibility to obtain fullerene derivatives soluble in organic solvents ([6,6]-Phenyl $C_{61/71}$ butyric acid methyl ester (PCBM)), makes PCBM one of the most suitable n-type materials for BHJ devices. In sight of this, BHJs are typically composed by an organic semiconducting small molecule or polymer mixed with PCBM to form films with thicknesses ranging from tens to hundreds of nanometers (Figure 1.9).[32]
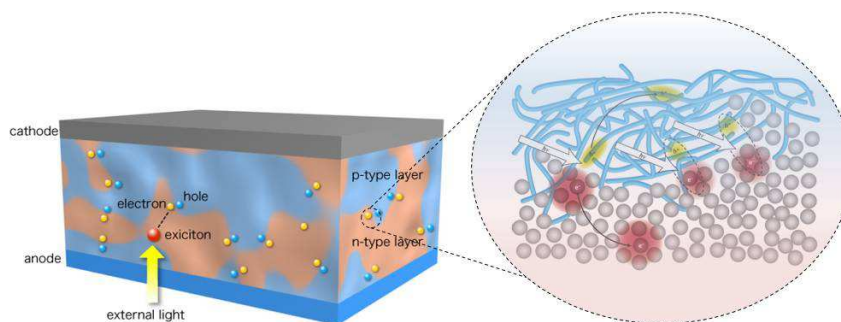
Figure 1.9. Representation of an organic BHJ solar cell with polymer as p-type while fullerene derivative as n-type material. Adapted by permission from Macmillan Publishers Lts: Nature Materials [33], copyright 2014.

Working principles

The working principles of BHJ solar cells are schematically represented in Figure 1.10. A detailed description of the main steps is reported hereafter.
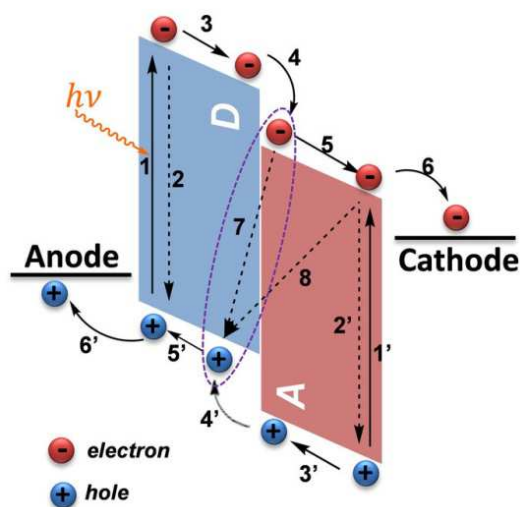
Figure 1.10. Representation of the possible processes involved in an organic solar cell. Reproduced from [34].

<u>Light irradiation.</u> The first process occurring in a solar cell is the light irradiation of the device where solar photons reach the BHJ active layer. However, before reaching the active compounds, the sunlight passes through other fundamental layers of the photovoltaic device where reflection, absorption and transmission of the solar photons can occur. For an efficient device operation, all the layers should indeed ensure high transparency in order to effectively transmit the sunlight directly to the organic

semiconductor. The substrate is the first part of the solar cell reached by solar photons where a rigid glass or a flexible plastic [poly(ethylene terephthalate), PET] are usually employed. These materials are typically characterized by an absorption in the UV region which limits the photons supply of the active layer. While an additional cause of photon losses arises from a partial reflection of the sunlight from the support.

Over the substrate, a conductive material is required as electrode. Intense research has been devoted to the development of transparent, conductive and possibly flexible materials. Metals are the best choice in terms of conductivity, however they are characterized by null band gap and therefore this class of materials is poorly transparent even as thin films. So far, inorganic mixed oxides as Indium Tin Oxide (ITO) or polymeric materials as poly(ethylenedioxy thiophene)poly(styrenesulfonate) (PEDOT:PSS) offer the best trade-off between conductivity and optical transparency.

Once reached the active layer, the first requirement for an efficient collection of the sunlight consists in an optimum overlap between the BHJ absorption spectrum and the spectral solar emission. This process is possible if the solar radiation has equal or greater energy than the semiconductor band gap. In this case, the intensity of absorption at each wavelength is determined by the Lambert-Beer law, where the absorbance linearly depends on the product of the optical density of the film (correlated to the molar extinction coefficient, the mass density of the layer and the orientation of absorbing molecules) and on the film thickness (further details can be found in Chapter 2). Since part of the photons are typically not absorbed and can pass through the active layer, an important role is played by the back electrode, which can act as a mirror by reflecting the residual photons back to the active layer where they can be absorbed afterwards.

Exciton formation. The process of photon absorption consists of the excitation of the semiconductor from its ground electronic state (S_0) to excited electronic states with the same spin (singlet states, *e.g.* S_1, S_2, etc.) (Figure 1.10 – process 1). The excited system first relaxes to the relative ground vibrational state *via* thermal relaxation, then it decays to lowest excited electronic state S_1 (Kasha rule).

From S_1, the system can deactivate again to the ground state S_0 (Figure 1.10 – process 2), radiatively (fluorescence) or thermally (internal conversion), or to electronic states with a different spin, *e.g.* triplet states (T) (intersystem crossing, vibrational conversion). However, if the excitation is maintained, a single molecule interacts with neighbors inducing a reorganization of the intermolecular distances with a consequent partial

polarization of the system. This collective response corresponds to the previously mentioned Frenkel exciton.

Exciton migration. Once Frenkel type excitons are formed, they migrate across the material. This process is considered a diffusive migration of excitons *via* energy transfer processes occurring between an excited molecule and a molecule in the ground state (Figure 1.10 – process 3).[23] It consists in the reorganization of electronic configurations without involving any electron transfer or radiative processes. The Coulombic or Förster resonant energy transfer (FRET) is one type of energy transfer based on a dipole-dipole interaction between molecules separated by a distance of 1-5 nm. This mechanism strongly depends on the distance (to the power of 6) and requires the overlap between the emission spectrum of the excited specie and the absorption spectrum of the specie in the ground state. A second mechanism for the exciton migration, called Dexter energy transfer, can occur. This requires a strong orbital overlap between the two species and a distance of about 1 nm. However, FRET usually outperforms the efficiency of Dexter energy transfer and is indeed considered the main mechanism of excitons diffusion in organic solar cells.

As mentioned, Frenkel excitons are typically characterized by short lifetime and limited diffusion length thus a prolonged diffusion could lead to deactivation to the ground state (Figure 1.10 – process 2). Diversely, if excitons during the diffusion meet another material with a sufficient electron affinity so as to overcome their binding energy, electron transfer processes can occur (Figure 1.10 – process 4).

Exciton separation. In a simplified view, excitons which reach the interface with an electron acceptor material are described to undergo to an electron transfer mechanism, which results in the formation of free holes and electrons. However, the process of formation of free charges is strongly dependent on a multitude of competing mechanisms. Indeed, once an exciton reaches the interface and splits in electron and hole, the electron transferred to the acceptor material still experiences a Coulomb interaction with the hole even if the two charges are localized in different phases. This interaction, previously described as CT state, does not allow opposite charges to escape one from the other and recombinations eventually occur (geminate recombination, Figure 1.10 – process 7). Intrinsic properties of the donor material, such as the dipole moments of the ground and excited states, play a relevant role on the exciton dissociation.[35] If these conditions are

optimized and the internal electric field is great enough, the CT pair dissociates in free electrons and holes.

From excitons to free charges. The process of free charges formation *via* interfacial CT is strongly dependent on the vibrational states of the CT state and on the excess of photon energy associated to the excited donor molecule. Indeed, a direct pathway from the excited state (S_1) to separate charges (FC) exists *via* high vibrational states of the CT (hot CT state) (Figure 1.11, process 2).[36] Diversely, the vibrationally excited CT state can relax to its ground state where, if sufficiently delocalized, can dissociate into free charges. Which of the two mechanisms is prevalent is still under debate and the nano-morphology distribution of the BHJ molecules plays a relevant role in this context.

Once free charges are formed, they can recombine back to form CT excitons (Figure 1.11, process 3). Since holes and electrons are spin-uncorrelated, they can either lead to the formation of singlet (^{1}CT) or triplet (^{3}CT) charge transfer excitons in ratio 1 to 3 according to the spin statistics. ^{1}CTs can recombine to the ground state in radiative (luminescence) or vibrational way (thermally). On the contrary, ^{3}CTs can decay to the triplet state of the excited molecule (T_1) (Figure 1.11, process 4) or re-ionize back to free charges. However, depending on the organization of molecules at the solid state, the re-ionization back to free charges occurs faster leaving only the deactivation of ^{1}CTs as possible loss mechanism.[37]
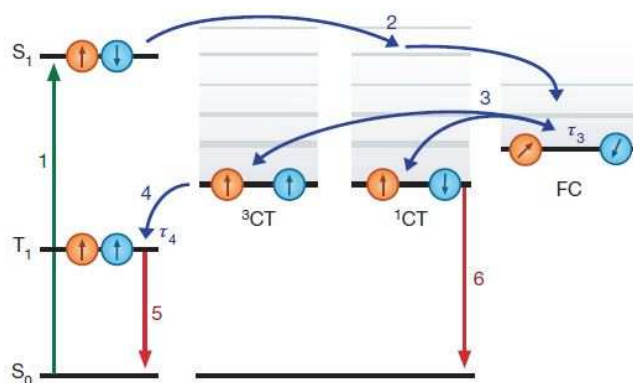
Figure 1.11. Processes of CT and free charges formation with the possible recombination processes. Reprinted by permission from Macmillan Publishers Ltd: Nature [37], copyright 2013.

Charge transport. If free charges do not recombine back in a CT state (Figure 1.10 – process 8), pushed by the internal electric field, they diffuse across the respective material to reach the electrode (Figure 1.10 – process 5). Holes move toward the anode through the p-type material and electrons to the cathode through the n-type material. The process

of charge transport is governed by the degree of order of the molecular species. Due to different relative orientations between molecules or polymeric chains, a characteristic spread in the energy of the levels does not allow the formation of energy bands as in inorganic materials. Hence, the charge transport mechanism is an intermediate between band-like transport, typical of inorganic materials, and hopping between local states. As a result, the charge mobility of organic semiconductors is generally in the order of 10^{-3} $cm^2/V \cdot s$.

A crucial role in the charge transport is played by the nanoscale morphology. The molecular packing (intermolecular distances), the dimensions of the p-type and n-type domains, the length and continuity of the domain paths are indeed determining factors in the conductivity of the photoactive film. In this sight, a suitable solid state ordering is required to minimize the probability of non-geminate recombination of free charges (bimolecular recombination) and ensure the maximum charges diffusion to their respective electrodes.

Charge collection. The last step of the photovoltaic process consists in the charge collection at the electrodes (Figure 1.10 – process 6). The main requirements are *i*) the choice of materials with suitable conductivity as electrodes and *ii*) the need of ohmic contacts at the active layer/electrode interfaces. The choice of materials for the front electrode was previously discussed. As back reflecting electrode, thin films (≈ 100 nm) of evaporated metals are usually employed for lab scale devices while, in the view of large scale fabrication, a bi-layer system based on PEDOT:PSS/silver grid is now one of the best choices since it is printable and suitable for flexible systems. Concerning the ohmicity of the contact, an energy alignment should be established between the LUMO of the n-type material and the cathode, and the HOMO of the p-type material and the anode. However, at the metal/semiconductor interface, the electrode Fermi level usually pins to the HOMO/LUMO level of the semiconductor with negligible influence on the device performance. Nonetheless, the use of interlayers with suitable energy levels was adopted to improve the ohmic contact thus avoiding charge accumulation and, furthermore, improving the charge selectivity through the suppression of bimolecular recombinations at low electric field.

Interfacial layer. Despite the internal electric field directs the flow of charges anisotropically towards the correspondent electrode, field independent diffusion processes can occur and free charges in proximity of the opposite electrode can recombine at the

interface resulting in performance losses for the device. As a result, additional layers between the BHJ blend and the electrodes, called interfacial, blocking or buffer layers are typically introduced. The role of the buffer layers is to facilitate the charge extraction of majority charge carriers at the respective electrodes thus avoiding charge accumulation and suppressing the extraction of minorities. In this sight, the additional layers typically reduce the BHJ surface roughness to improve the interfacial quality with the electrodes, selectively transport one type of charge carriers and are characterized by energy levels suitably aligned to the HOMO of the electron donor material (HOMO$_D$) and the anode Fermi level, or to the LUMO of the electron acceptor material (LUMO$_A$) and the cathode Fermi level.

Over the years, several interfacial materials were suitably designed and developed in order to maximize the solar cell performance. Among the hole transporting layers (HTLs), PEDOT:PSS and MoO$_x$ are the most used. PEDOT:PSS consists of a water dispersion of PEDOT and PSS chains and because of the limited thickness necessary to ensure optimal operation ($\approx$ 30 nm) offers the advantage of an effective solution-processed HTL, which does not affect the device light harvesting. On the contrary, despite the remarkable advantages in terms of transparency and operation, MoO$_x$ is typically deposited by thermal evaporation and hence is not fully compatible to wet large-scale manufacture processes. Nonetheless, MoO$_x$ in the form of nanoparticles was recently developed allowing the solution processing of MoO$_x$ layers.[38]

Concerning materials used as electron transporting layers (ETLs), a plethora of low-work function materials was effectively demonstrated, from metals, to metal oxides, inorganic salts or polymer electrolytes. Among them, the most common employed are Calcium, ZnO,[39] TiO$_x$,[40] LiF, poly[(9,9-bis(3'-(N,N-dimethylamino)propyl)-2,7-fluorene)-alt-2,7-(9,9-dioctylfluorene)] (PFN),[41] polyethylenimine (PEI) and polyethylenimine ethoxylated (PEIE).[42] While ZnO, TiO$_x$, PFN, PEI and PEIE are processable from solution, LiF and Calcium are deposited by thermal evaporation as thin films.

Besides the aforementioned advantages from the use of buffer layers, further benefits were demonstrated in the case in which the buffer layers act as optical spacer. Here, the light distribution inside the solar cell stack is modified resulting in an improved active layer absorption and hence enhanced solar cell performance.

1.2.2   State of the art and limitations

Organic photovoltaics can be considered one of the most promising renewable energies in the emerging scenario. Foldability, wearability, color tunability, light weight are some of the attracting device features, which prompted the study and development of this technology with an exponential evolution over the last years.

Particular efforts were devoted to the development of novel materials, the understanding of the device physics, the manipulation of film morphology and the meticulous optimization of single parts of the device.

High performing organic semiconductors as photoactive materials were progressively developed and their solid state self-organization was optimized either by the introduction of solvent additive in the initial solution or through post-processing methods as solvent or thermal annealing on the resulting films. Interfaces were improved by the introduction of surface modifiers or multifunctional interlayers acting, for instance, as optical spacer to enhance the light distribution inside the device. The introduction of innovative semi-transparent and flexible electrodes compatible with large area production progressively led to semitransparent organic solar cells fabricated on plastic foils. All these advances converged in a series of more general development in terms of device structure and architecture. To better exploit the incident solar photons, indeed, new concepts for the active layer were introduced and significant efficiencies were obtained from devices based on ternary BHJ blends, through the combination of a donor, a sensitizer and an acceptor material. More significantly, multi-junction architectures, where two or more interconnected sub-cells with complementary absorption regions are stacked in a single device, were developed to enhance the light-to-current efficiency and the record efficiency of 12.7% was established using 2 series-connected sub-cells.

All these progresses led to an extensive growth of the technology with the achievement of devices power conversion efficiencies beyond the marketing threshold of 10%.[43]

In this view, the first companies on organic photovoltaics were born. One of the pioneering was Konarka Technologies, founded in 2001 in Massachusetts as a spin-off. However, perhaps because of the "immature" organic technology, the company bankrupted in 2012. Still, the list of organic photovoltaic companies is not wide. However, the significant advancement of the technology allowed companies as Heliatek, Belectric (OPVIUS) and InfinityPV to place on the market the first gadgets and systems fully powered by organic solar cells.

Despite the relevant breakthrough in terms of device efficiency, state-of-the art organic solar cells still present some issues of stability. The nature of organic semiconductors makes them susceptible to prolonged illumination, heating or even only ambient conditions. Lifetime, light and thermal stability are basic requirements for marketing organic solar cells, nevertheless the literature is not exhaustive in this view and devices are not suitably stable under operation conditions. Many external agents result to be harmful for organic solar cells and cause the reduction of the cell performances. Among them, diffusion of water and oxygen into the device promotes chemical degradation of the active materials, interfaces and contacts, which drastically limit the cell lifetime. Over the years, encapsulating systems were properly developed and resulted effective to slow down or even neglect the ingress of external agents, which would degrade the device. However, light and heat represent two causes of device degradation which, diversely from water and oxygen, cannot be eliminated using physical barriers. They might induce chemical reactions, degradation at the interfaces and morphological changes which drastically reduce the device performance over time. Through material design, modification of the device configuration and interface engineering, the device lifetime was extended from months to years.[44]

Furthermore, important challenges in terms of large area manufacturing and environmental compatibility are still ongoing. Several works still focus on devices fabricated with laboratory scale processing techniques. Not less important are the issues arising from the use of environmentally hazardous solvents to process the active materials, which represent a big concern for a technology conceptually friendly to nature. This critical overview aims to provide a general analysis of the state-of-the-art of organic photovoltaics as well as the issues, which still need to be addressed for a large diffusion and commercialization of this technology.[32][15]

1.2.3 Aim of the thesis

The general outline of this thesis can be represented by the three fundamental aspects which reflect the key requirements for the commercialization of OPV devices: *i*) efficiency, *ii*) stability and *iii*) low environmental impact (Figure 1.12).
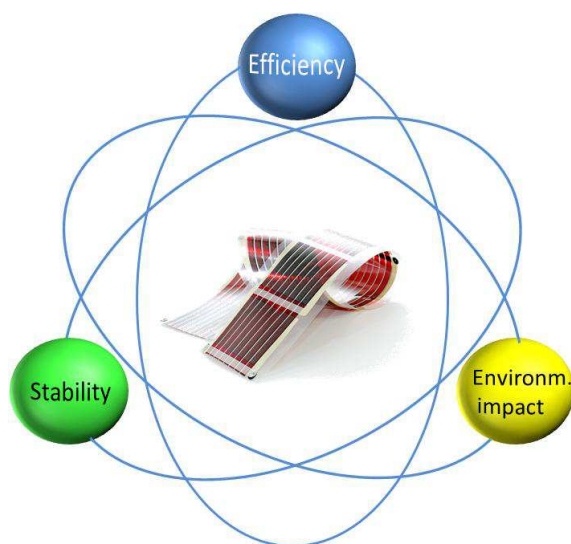
Figure 1.12. Representative outline of the thesis.

In this thesis, all the organic solar cells consist in BHJ devices using polymers as electron donor materials and fullerene derivatives as electron acceptors. Despite part of the current research is devoted to small molecules solar cells, the use of polymers represents a valid strategy to exploit most of the properties of organic materials. Polymers can be indeed easily dissolved in a solvent to make inks suitable for large scale manufacturing. In this sight, an experimental section is devoted to the presentation of the deposition techniques, the device fabrication and the characterization methods used in this thesis. Then, an introductive chapter focuses on the chemistry of materials typically employed in polymer solar cells (PSCs). The historical evolution of the materials, the synthetic procedures and the structure - properties relationship are deeply analyzed to understand the innovations and concepts, which led to the state-of-the-art organic semiconducting materials.

This thesis can be framed in the context of the industrialization and commercialization of the organic photovoltaic technology. Indeed, particular attention is paid to the analysis of some critical issues as the stability of devices.

A first part concerns the stability towards thermal stress. International protocols are followed and investigations on both single materials or complete devices are carried out.

The effect of the nanostructure of the active layer as a function of the processing solvent is studied and an innovative characterization technique is developed to selectively distinguish among different degradation mechanisms in complete devices. In addition, a study on a particularly light-sensitive interlayer and a comparative analysis on the effect of the light on different active layers are discussed.

A second section focuses on the development of state-of-the-art device architectures, *i.e.* multi-junction, to reach great light-to-current efficiencies. Despite literature presents many studies showing highly performing multi-junction devices, the intermediate contact, which represents the junction between different sub-cells, is still one of the main causes of loss for this kind of devices. Still, a general understanding of the loss mechanisms lacks. In this sight, by coupling charge extracting and injecting techniques and a selection of several different materials, a general comprehension of the possible loss mechanisms is provided. Then, the optimization of an organic double-junction solar cell to meet the industrial requirements is presented.

Finally, an important part of the thesis is dedicated to the replacement of common hazardous solvents, typically used to process the active materials, with solvents characterized by low environmental impact. In detail, the effect of a "green" solvent on the device efficiency and stability is presented.

The experimental works presented in this thesis are the result of scientific collaborations with national and international research groups. An important contribution arises from the collaboration within the consortium of the European project SUNFLOWER (grant number 287594, web site: http://www.sunflower-fp7.eu/site/index.php).

Regarding the experimental part, this PhD project focused on the fabrication and characterization of single-junction and double-junction organic solar cells and the relative device sub-structures. In detail, the I – V and EQE measurements, the absorption and emission spectroscopy, the AFM investigations, the confocal microscopy analyses and the stability tests were carried out at the "Istituto per lo Studio dei Materiali Nanostrutturati (ISMN) – Consiglio Nazionale delle Ricerche (CNR)" of Bologna (Italy).

Part of this Ph.D project was spent at the "Friedrich-Alexander-Universität Erlangen-Nürnberg" (Institute: Materials for Electronics and Energy Technology, i-MEET, Germany), under the supervision of Prof. Christoph J. Brabec, where the optoelectronic devices were fabricated and characterized through I – V measurements at different light

illuminations, EQE measurements at different applied biases, absorption/emission spectroscopy and electroluminescence analyses.

All the other experimental procedures and analyses of this thesis, such as the synthesis of the polymers, their chemical and electrochemical characterization, etc., were carried out by external collaborators.

It is worthy of note that, although this thesis focuses on devices processed on small scale, all the concepts, approaches, deposition techniques, and materials were developed heading to industrial applications. The critical approaches and the promising results evidence the possibility to improve organic photovoltaics and aim at contributing to solve some crucial issues in view of an upcoming spread of this technology.

Chapter 2

Experimental section: materials and methods

This chapter describes all the materials, experimental procedures, characterization techniques and details relative to the investigations reported and discussed throughout this thesis.

2.1 Materials

All semiconducting polymers and fullerene derivatives used in this thesis, respectively as electron donor and acceptor materials of BHJ blends, are listed in Table 2.1. The reported materials were used as received without any further purification. The chemical structures of the donor polymers are showed in Figure 2.1 (the chemical structure of HBG-1, which is property of the Merck, is not provided) while those of the fullerene acceptors are reported in Figure 2.2.

Table 2.1. List of the active materials used in the BHJ solar cells of this thesis.

BHJ component	Abbreviation	Provider	Mn [kDa]	Mw [kDa]	Purity [%]
Electron donor polymer	PTzBDT-1	-	20.2	88.9	-
	PTzBDT-2	-	41.7	105.5	-
	HBG-1	Merck	-	-	-
	PFQBDT-OR	-	32	82	-
	PFQBDT-TROR	-	24	54	-
	PFQBDT-TR	-	37	133	-
	PFQTT	-	19	53	-
	PFQ2T-BDT	-	27.7	66.0	-
	PMDPP3T	-	-	-	-
	rr-P3HT	Rieke Metals	-	50-70	-
	PCDTBT	1-Material	-	5.27	-
	pDPP5T-2	BASF	-	47	-
	PBDTQx-ii	-	21.4	82.9	-
	PTB7	1-Material	-	-	-
Electron acceptor	1	-	-	-	-
	2	-	-	-	-
	3	-	-	-	-
	4	-	-	-	-
	5	-	-	-	-
	6	-	-	-	-
	PC$_{61}$BM	Solenne BV	-	-	> 99
	PC$_{71}$BM	Solenne BV	-	-	90-95%
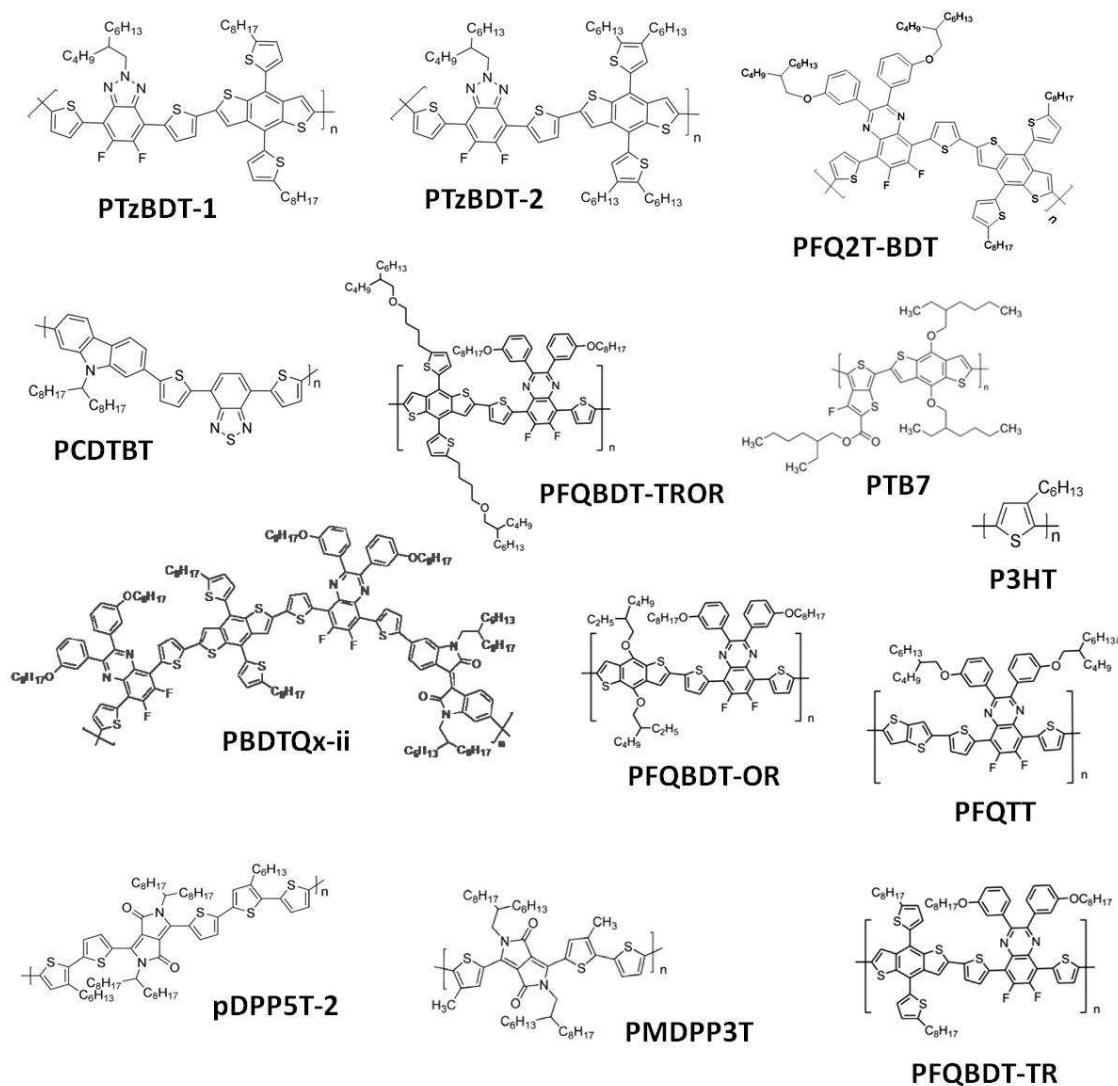
Figure 2.1. Electron donor polymers used in the BHJ solar cells of this thesis.
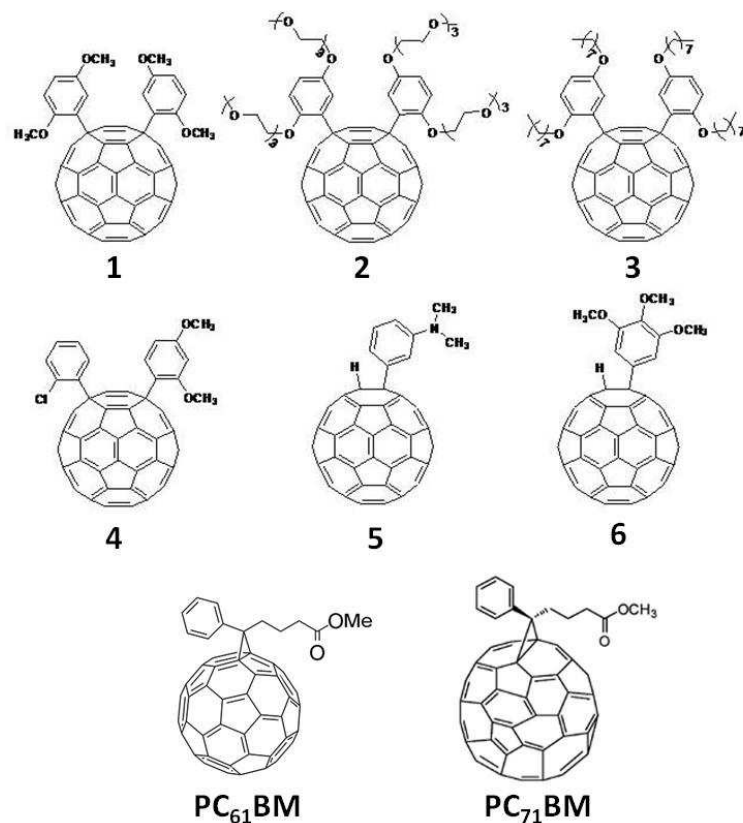
Figure 2.2. Electron acceptor materials used in the BHJ solar cells of this thesis.

The materials used as HTL or ETL are listed in Table 2.2, while some of their molecular structures are showed in Figure 2.3.

Table 2.2. List of the charge selective materials used as HTL or ETL in BHJ solar cells.

Charge selectivity	Material	Provider	Product number/ Abbreviation	Solvent
HTL	PEDOT:PSS	Heraeus	AI4083	Water
	PEDOT:PSS*	Heraeus	HIL3.3N	Water
	MoO$_x$	-	-	-
ETL	LiF	-	-	-
	ZnO NPs	Genes'Ink	-	Isopropanol
	ZnO NPs	Nanograde	-	Isopropanol
	ZnO NPs	-	-	Isopropanol
	AZO NPs	-	AZO$_x$	Isopropanol
	PEI	-	-	2-methoxyethanol

*PSS-free
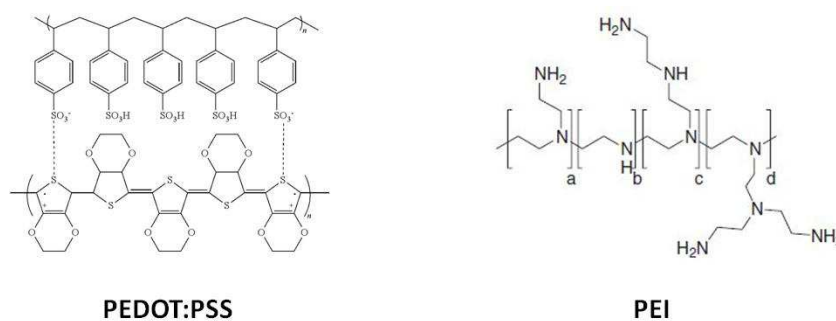
Figure 2.3. Molecular structure of PEDOT:PSS and PEI, respectively used as HTL and ETL of BHJ solar cells.

All the solvents used in this thesis were purchased from Sigma Aldrich and used without further purification.

2.2   Device fabrication

All the BHJ solar cells were fabricated on a transparent glass substrate covered by a ≈ 150 nm thick ITO film (sheet resistance ≈ 10 Ω/square). The ITO layer presented a specific lateral pattern and a surface roughness lower than 1 nm to allow the subsequent deposition of smooth thin layers on it.

Before the deposition of all the required layers, the glass/ITO supports were sequentially cleaned in acetone and isopropanol for 15 minutes. Then, the glasses were blow-dried with argon gas and an oxygen plasma treatment was used for 10 minutes to improve the surface wettability and remove any trace of organic contaminants.

Single junction

For the fabrication of BHJ solar cells with single-junction architecture and standard geometry, a thin layer of PEDOT:PSS (40 nm) was deposited in ambient conditions over the ITO substrate and then thermally annealed at 150°C for 15 minutes (in air) to optimize the morphology and eliminate eventual water traces. In the case of inverted geometry, a similarly thick layer of ETL (ZnO, AZO_x, PEI or ZnO/PEI) was deposited in ambient conditions and then thermally annealed at 80°C for 5 minutes (in air). For the deposition of the active blend, a mixture of electron donor polymer and fullerene

derivative was previously dissolved in the optimal organic solvent whereas the D:A ratio, solution concentration and eventual solvent additives were chosen to ensure an optimal solar cell operation. Depending on the device geometry, the active solution was deposited either on the HTL (standard) or ETL (inverted) and post-processing methods were eventually applied to further improve the solid state morphology, *e.g.* thermal annealing. To complete the solar cell fabrication, a thin layer of LiF (0.6 nm, standard geometry) or MoO_3 (10 nm, inverted geometry) was thermally evaporated under high vacuum ($\approx 10^{-6}$ Torr) followed by the deposition of 100 nm of Aluminum or Silver (respectively for standard and inverted geometry) as top metal electrode. Alternatively, MoO_3 was replaced by a solution-processed PEDOT:PSS (AI4083) layer, which was deposited from solution by adding 1% v/v of the nonionic wetting agent fluorosurfactant Zonyl FS-300 (m-PEDOT:PSS) to ensure an optimal deposition over the active layer.

Tandem sub-structures

All the tandem sub-structures were fabricated with an inverted geometry while, depending on the position of the interconnecting layer (ICL), two different configurations were eventually adopted. Indeed, the ICL was placed between the ITO electrode and the active layer or, alternatively, over the active layer before the evaporation of the metal electrode.

In the first case, a 40 nm thick layer of PEDOT:PSS (AI4083 or HIL3.3N) was deposited over a pre-cleaned ITO and then thermally annealed for 5 minutes at 120°C. Successively, a thin layer of ZnO (≈ 40nm), PEI (≈ 5 nm) or ZnO/PEI was deposited over PEDOT:PSS and then annealed at 80°C for 5 minutes. The BHJ solution was deposited over the resulting glass/ITO/PEDOT:PSS/(ZnO, PEI or ZnO/PEI) stack and a bi-layer of MoO_x/Ag was thermally evaporated over the active film as previously described.

In the second configuration, the ICL was deposited over the glass/ITO/ZnO/active layer stack. In detail, a 100 nm thick layer of m-PEDOT:PSS was deposited over the active layer and, eventually, a surface washing using pure isopropanol was performed before a thermal annealing at 80°C for 20 minutes in air. The formation of a layer of m-PEDOT:PSS was followed by the deposition of ZnO nanoparticles to form a layer with a thickness of 40 nm, which was thermally annealed at 80°C for 5 minutes in air. The sub-structure was completed by the thermal evaporation of Ag as previously described. To note, apart from the top electrode, all the layers were deposited in ambient conditions.

Tandem fabrication

All the tandem solar cells in this thesis presented an inverted geometry. A layer of ZnO and the BHJ layer were sequentially deposited over a pre-cleaned glass/ITO substrate as previously described. Two different methods of deposition were adopted for the ICL preparation. In the first case, as previously described, a layer of m-PEDOT:PSS (AI4083) was deposited over the active film, then an IPA-treatment and a thermal annealing were performed before the deposition of ZnO.

Alternatively, a 10 nm thick layer of MoO_x was thermally evaporated over the active layer and then the pristine solution of PEDOT:PSS (AI4083 or HIL3.3N) was deposited on it, followed by a thermal annealing at 120°C for 5 minutes. Then, a layer of ZnO or PEI was formed on the top of the PEDOT:PSS as previously described.

After the ICL deposition, a second active layer was deposited over the ITO/ZnO/active layer/ICL stack followed by eventual post-processing treatments. The tandem cell was then completed by the thermal evaporation a bi-layer of MoO_x and Ag (10 nm/100 nm), as previously described.

The active area of the solar cells for all the architectures used in this thesis was determined by the dimension of the top electrode, which was defined through the use of masks of 6 mm^2 or 10.4 mm^2 (rectangular shape) for the thermal evaporation.

2.3   Deposition techniques

Organic solar cells offer the great advantage to be fabricated from solution. Over the years, a plethora of deposition techniques was adopted for the fabrication of solution-processed organic solar cells, from methods suitable for laboratory scale such as spin coating, to techniques conceived for massive production such as inkjet printing, roll-to-roll coating, etc., passing through the use of intermediate techniques such as doctor blading and slot die coating.[45] In this context, OPVs is still an evolving technology and hence a continuous research of new performing, safe and stable materials is ongoing. As a result, the use of large scale manufacture techniques is unnecessary to investigate new materials or alternative device architectures. Hence, in this thesis, two different

techniques, spin coating and doctor blading, were adopted. While spin coating deposition was used to fulfill some specific requirements or for the investigation of new materials, doctor blading was adopted as scalable method to more easily transfer the generated know-how towards large scale production of solar modules.

The spin coating consists in the deposition of a small amount of solution on a small sized and (preferably) rigid substrate, which is fixed at the center of a holder (Figure 2.4a). The holder rotates immediately after casting the solution, which is quickly spread over the entire substrate. The use of a volatile solvent in conjunction with the centripetal acceleration allows the evaporation of the solvent and the formation of a thin solid film. The nature of the solvent, the concentration of the solution, the wettability of the substrate and the processing parameters such as acceleration, speed of rotation and duration are fundamental for the resulting morphology and thickness of the solid film. Typically, the substrate size is lower than 25 cm^2 and hence is suitable for laboratory scale analysis on small devices. In this thesis, the spin coating deposition was mainly employed in inert atmosphere to avoid the exposure of sensible materials to air conditions.

Diversely from spin coating, doctor blading represents a fully scalable, robust and reproducible technique for the preparation of multi-layered devices both on small and relatively large scale. It requires the use of small volume of solution and allows the deposition over substrates with dimensions from few square centimeters to A4 sheet size with a great control of the film thickness and homogeneity. It consists of a heatable plate, which is the support for the substrate, and a mechanically moving blade (Figure 2.4b). A dose of solution (μL) is dropped between the stationary blade and the substrate to create a meniscus. Then, the blade moves over the entire substrate to spread the solution and form a wet film. Depending on the hot plate temperature, nature, amount and temperature of the solution, the wettability of the substrate, the distance between the blade and the substrate and the blading speed, a fine control of the film morphology and thickness is obtained.

In this thesis, except the electrodes, all the layers comprised in the solar cells were processed from solutions.
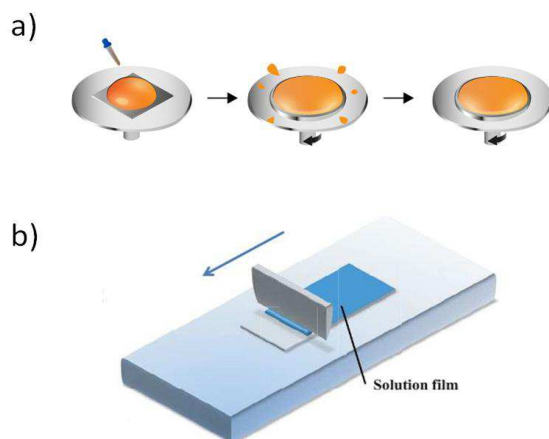
Figure 2.4. Representation of the two techniques used in this thesis to form thin films from solution: spin coating (a)[46] and doctor blading (b), reproduced with permission from Ref. [47].

A list of the processing parameters for the active layers used in the organic solar cells of this thesis is reported in Table 2.3.

Table 2.3. Processing parameters and deposition techniques to process the active blends used in this thesis.

Active layer	Solvent	D:A ratio [wt/wt]	Solar cell architecture	Deposition technique
PTzBDT-1:PC$_{61}$BM	TCB or o-DCB	1:2	Standard	Spin coating
PTzBDT-2:PC$_{61}$BM	o-DCB	1:1	Standard	Spin coating
P3HT:PC$_{61}$BM	o-DCB:CB (1:1 v/v)	1:1	Standard	Spin coating
P3HT:2	o-DCB:CB (1:1 v/v)	1:1	Standard	Spin coating
P3HT:3	o-DCB:CB (1:1 v/v)	1:1	Standard	Spin coating
HBG-1:PC$_{61}$BM	o-DCB or o-xylene	1:2	Inverted	Doctor blading
PFQBDT-OR:PC$_{61}$BM	o-DCB	1:1	Standard	Doctor blading
PFQBDT-TROR:PC$_{61}$BM	o-DCB	1:1	Standard	Doctor blading
PFQBDT-TR:PC$_{61}$BM	o-DCB	1:1	Standard	Doctor blading
PFQTT:PC$_{61}$BM	o-DCB	1:1	Standard	Doctor blading
PFQ2T-BDT:PC$_{61}$BM	o-DCB	1:1	Inverted	Spin coating
PMDPP3T:PC$_{71}$BM	CHCl$_3$:o-DCB (9:1 v/v)	1:2	Inverted	Doctor blading
PCDTBT:PC$_{61}$BM	o-DCB	1:4	Inverted	Spin coating
pDPP5T-2:PC$_{71}$BM	CHCl$_3$:o-DCB (9:1 v/v)	1:2	Inverted	Doctor blading
PBDTQx-ii:PC$_{61}$BM	o-DCB or o-xylene	1:2	Inverted	Doctor blading
PTB7:PC$_{71}$BM	CB	1:1.5	Inverted	Spin coating

2.4   Methods of characterization

Current – voltage characteristics

The most important characteristics of an organic solar cell can be obtained by measuring its response in terms of current density (J) as a function of an externally applied bias (V). This measurement is usually carried out at room temperature since the properties of organic materials strongly depend on the temperature, while the cell response is typically analyzed both in dark conditions and under standard illumination. The standard illumination consists in the reproduction of the solar light at the temperate areas of the world, where most of the people live. At these latitudes, the solar light hits the world surface at an angle of $\approx 48°$, referring to the zenith. Moreover, the sunlight is attenuated via absorption and scattering processes while travelling through the atmosphere and hence the solar spectrum is partially modified. Considering all these processes, a specific spectrum of the sunlight valid at the temperate latitudes on the Earth's crust is established and used as international standard to characterize the J – V response of solar cells under illumination. Accounting for the air mass (AM) attenuation, the light incident angle α (1/cos α = 1.5) and considering both the direct and diffused photons (global, G) the standard solar spectrum with is coded as AM1.5G and has an approximate intensity of 100 mW/cm^2.

An example of J – V measurement is shown in Figure 2.5 where the most relevant parameters to characterize a solar cell are indicated.
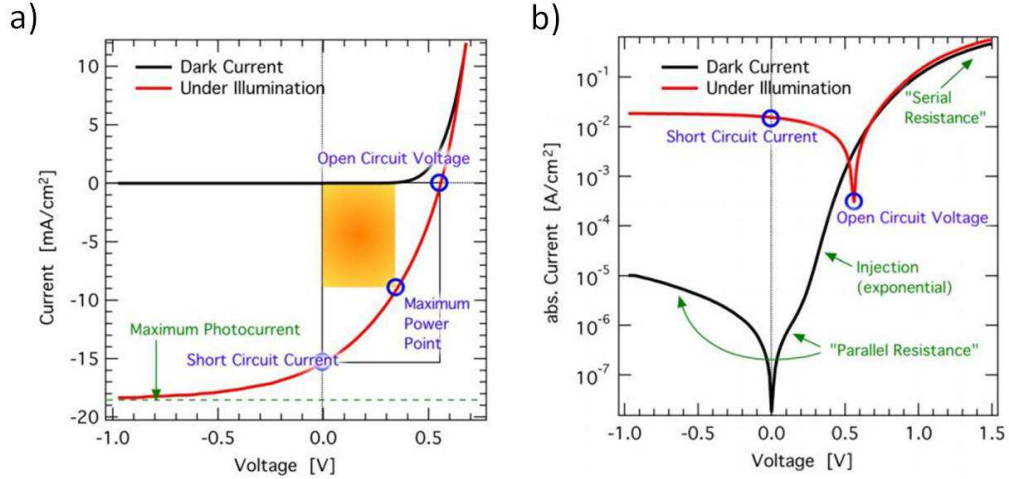
Figure 2.5. J – V characteristics in linear – linear (a) and semi-logarithmic (b) plot of an organic solar cell under standard AM1.5G illumination (red) and under dark conditions (black). Reproduced with permission from [48].

The most important parameter of a solar cell is the power conversion efficiency, which is the represented by the power exploited by the cell (P_{OUT}), under standard illumination, compared to the power of illumination ($P_{ILL} = 100$ mW/cm^2), and is calculated as:

$$PCE = \frac{P_{OUT}}{P_{ILL}} = \frac{J_{sc} \cdot V_{oc} \cdot FF}{P_{ILL}} \qquad 2.1$$

where Jsc is the device current density under short circuit conditions, Voc is the voltage of open circuit and FF is the abbreviation for fill factor. The FF consists in the ratio between the product Jsc x Voc, which represents the maximum power exploitable by the solar cell, and the maximum power exploited by the cell (Maximum Power Point, Figure 2.5a). This ratio provides an indication of the losses, which reduce the full potential of the solar cell. Indeed, if equal to the unity, no electrical losses occur during operation.

In order to model the operation of organic solar cells, the Shockley diode equation derived for inorganic cells can be approximately used. In this model, the solar cell is conceived as a conjunction of a generator of photocurrent and a diode, where the net current density under illumination is given by:

$$J = J_0 \left[exp\left(\frac{qV}{nkT}\right) - 1 \right] - J_{ph} \qquad 2.2$$

where J_0 is the saturation current density, q the elementary charge, kT the thermal energy and Jph the photo-generated current density. This accounts for both the rectifying behavior of a diode and the charge generation under illumination. By solving the equation at J = 0 and assuming that Jsc = Jph at any voltage, the extrapolated voltage corresponds to the device Voc:

$$Voc = \frac{nkT}{q} \ln\left(\frac{J_{sc}}{J_0} + 1\right)$$

2.3

In order to consider the case of a real device operation, the equation should be further extended to two resistors. Indeed, the series resistance (Rs), arising from contact and BHJ resistances, and the parallel resistance (Rp), due to charge recombinations in the bulk and at the contacts, need to be included. The extended equation is:

$$J = J_0 \left[exp\left(\frac{q(V-JR_S)}{nkT}\right) - 1\right] - \frac{V - JR_S}{R_p} - J_{ph}$$

2.4

Despite this equation is a good approximation adapted from inorganic cells models, it is not fully valid for organic devices because of their field dependent resistances.[49]

Dependence of the OPV parameters on the illumination intensity

Advanced numerical methods were developed over the years in order to accurately describe the J – V behavior of organic solar cells. In this sight, an equation which includes drift and diffusion of charges, bimolecular recombinations and the effect of field and temperature dependent generation of free charges in organic solar cell was developed by Koster *et al.*.[50] This equation is approximately described under open circuit condition as:

$$Voc = \frac{E_{DA}}{q} - \frac{kT}{q} \ln\left(\frac{(1-P)\gamma N_C^2}{PG_R}\right)$$

2.5

where E_{DA} is the difference between the HOMO level of the electron donor and the LUMO level of the electron acceptor component, P the dissociation probability of excitons, G_R the generation rate of excitons, N_C is the effective density of states in the

conduction band while γ is the Langevin recombination constant for bimolecular recombination of free charge carriers. This represents a very good approximation of the equation derived by Koster *et al.* where the Langevin recombination rate (R) is re-written as equal to γnp, with n and p representing the concentration of electrons and holes under illumination.

This model differs from Equation 2.3 because a field dependence of the photo-generated current is included and both drift and diffusion are indeed accounted. Interestingly, from Equation 2.5, since P and γ do not depend on the light intensity and G_R is directly proportional to the light intensity, the Voc versus the natural logarithm of the light intensity scales as kT/q.[49] Considering the competition within an organic solar cell between trap-assisted and bimolecular recombinations, an enhanced dependence of the Voc on the light intensity over 1 kT/q is representative of trap limited recombinations in the device.[51] Therefore this represents a method which allows to investigate the presence of traps in BHJ solar cells.

While, the behavior of Jsc upon light intensity was reported as a power law dependence:

$$J_{SC} \propto I^{\alpha} \qquad\qquad 2.6$$

where I is the light intensity and α a coefficient typically ranging from 0.85 to 1 for BHJ solar cells. The deviation of α from 1 was demonstrated to arise from losses of charge carriers due to bimolecular recombinations.[52][49][53][54]

In this thesis, the J-V characteristics were recorder inside the glove-box (inert atmosphere) by using an Abet Technologies Sun 2000 Solar Simulator and a Keithley 236 source-measure unit. The light intensity was determined by a calibrated silicon cell fitted with a KG5 color glass filter to bring the spectral mismatch to unity. Calibrated masks were used during measurement to avoid parasitic currents. Alternatively, an Oriel Sol 1A from Newport was used as AM1.5G illumination system while a BoTest was used as source measurement unit. To modulate the light intensity, calibrated optical filters were placed over the sample to reduce the intensity of incident photons.

External quantum efficiency measurements

The external quantum efficiency (EQE) is the ratio between the number of charges generated by a solar cell and the number of photons, with a given wavelength, reaching

the device. This measurement is indeed similarly named as Incident-Photon-to-Current Efficiency (IPCE) and it accounts for the optical properties of the solar cell, *i.e.* the amount of incident photons which are absorbed by the device, and all the processes involved in the conversion of absorbed photons into collected free charge carriers (internal quantum efficiency, IQE) as described by:

$$EQE\,(\lambda) = \frac{n_n\,(\lambda)}{n_{ph}(\lambda)} = \left|\,\eta_{ABS}\cdot\eta_{IQE}\,\right|_\lambda =$$

$$= \left|\,\eta_{Abs}\cdot\eta_{Diff}\cdot\eta_{Diss}\cdot\eta_{Tran}\cdot\eta_{Coll}\,\right|_\lambda \qquad 2.7$$

where n_n and n_{ph} are respectively the number of charges extracted from the device and the incident photons per time, η_{Abs} represents the efficiency of the processes of light absorption and η_{IQE} comprises the efficiencies of all the processes of excitons diffusion (η_{Diff}), excitons dissociation (η_{Diss}), charge transport across the device (η_{Tran}) and charge collection at the electrodes (η_{Coll}).

The instrumental part consists of a xenon lamp which, through a diffraction grating, emits monochromatic radiations towards the solar cell. A lock-in amplifier and a chopper are commonly used to amplify the current signal from the device and discriminate the contribution arising from external light. An appropriate software records the electrical response of the device at each wavelength and, to universally quantify the percentage of charges generated, a calibrated photodiode is used as reference. In order to ensure the total collection of photo-generated charges, EQE measurements are typically performed under short circuit conditions and, the integration of the spectral responsivity of collected charges indeed matches the Jsc of the device under standard illumination.

As above mentioned, the use of a lock-in amplifier neglects additional current contributions arising from external light sources different from the xenon lamp. However, following this approach, eventual currents arising from an external electric field or from intrinsic charge carriers would be similarly canceled and hence some contributions would not be properly considered in the EQE measurement of a solar cell. However, since the EQE is measured under short circuit conditions, eventual additional contributions are zero as confirmed by the absence of current generated or injected in a solar cell under dark illumination at 0 V (Figure 2.5). On the contrary, the measurement of EQE spectra at biases different than zero would account only for the photo-generated charges without

considering the effect of charges injected from the electrodes or from intrinsic charge carriers. This results in a specific method to exclusively evaluate the processes of charges photo-generation, which was effectively adopted to distinguish eventual losses in the solar operation in Chapter 5.

In this thesis, the EQE measurements were performed in ambient conditions on encapsulated devices by using an home-built setup. A monochromatic light was obtained with a xenon arc lamp from Lot-Oriel (300 W) coupled with a Spectra-Pro monochromator. A lock-in digital amplifier SR 830 measured the voltage drop arising from the device photocurrent passing through a calibrated resistance of 50 Ω. The signal was exclusively collected from the current at 300 Hz, which was the frequency at which the light was chopped before reaching the solar cell. Alternatively, an automatic QE-R instrument from Enlitech was used in air to measure the EQE response of solar cells under an externally applied bias.

Photophysical characterization methods

Absorption spectroscopy

The investigation of the photophysical properties is a key requirement for an accurate analysis of BHJ solar cells. The photovoltaic conversion indeed consists in the sunlight absorption and conversion into charges and hence the optical processes are at the basis of the solar cell operation. The process of absorption, as described in Chapter 1, strongly depends on the photophysical properties of the BHJ materials. It indeed includes the excitation of the active components from their ground state to excited electronic states by following the Lambert-Beer law:

$$I_T(\lambda) = I_0(\lambda) \cdot 10^{-OD\,(\lambda)} \qquad\qquad 2.8$$

where I_T is the intensity of the light transmitted by the sample, I_0 is the intensity of the incident light and OD is the abbreviation for *optical density*, also named *absorbance*, which depends on the thickness (d) and absorptivity (ε) of the sample as follows:

$$OD\,(\lambda) = \varepsilon\,(\lambda) \cdot d \qquad\qquad 2.9$$

Apart from the thickness, the intensity of the light absorbed by the active components of a solar cell is strongly dependent on the intrinsic characteristics of the materials, from their nature and from their morphological organization at the solid state, as discussed in Chapter 3.

In this thesis, the absorption spectra were measured by using a Jasco V-550 spectrophotometer.

Photoluminescence

The photoluminescence (PL) is the light emitted, in any form, from an excited material. It indeed comprises both fluorescence or phosphorescence deactivation pathways of excited states generated from the light irradiation of absorbing sample. In the case of BHJ films, the semiconducting polymer typically deactivates through radiative processes also accompanied by a non-radiative component. However, in presence of a fullerene acceptor, the excited states of the polymer are quenched via electron transfer to the fullerene derivative and hence the radiative decay is typically neglected. The quenching of luminescence from a BHJ blend is indeed a method to analyze the processes of excitons dissociation in organic solar cells. Despite that, a residual decay of excitons to the ground state through photoluminescence is still present and hence a limited amount of photons emitted from the donor polymer can be detected. This can provide information on the donor/acceptor interfaces and on the degree of aggregation of the polymer in the BHJ.

In this thesis, PL spectra were measured by illuminating the devices with a 445 nm Argon laser. The PL emission was dispersed by a 600 lines mm^{-1} grating monochromator (HRS-2) and detected by an Indium Gallium Arsenide (InGaAs, ADC 403L) or a Silicon detector through lock-in technique. The spectra were corrected for the sensitivity of the detector.

Electroluminescence

Diversely from the absorption and photoluminescence, the electroluminescence (EL) in organic solar cells does not arise from the excitation of the BHJ blend after light irradiation. Electroluminescence is a form of light emission which generates from the injection of charges from the electrodes in complete devices. Hence, to inject charges into

the BHJ layer, the solar cell is biased at voltages higher than the device Voc, *i.e.* the cell operates in the light-emitting-diode regime. Following the J – V plot of a solar cell, a forward bias applied to the device allows the injection of charges from the electrodes to the BHJ, where the acceptor component transports electrons whereas the donor polymer transports holes across the active film. Once opposite charges meet at the donor/acceptor interfaces, CT excitons are formed and their deactivation produces the emission of photons with an energy approximately corresponding to the $HOMO_D$-$LUMO_A$ energy difference.[55] The dependence of the solar cell Voc on the $HOMO_D$-$LUMO_A$ difference highlights also the direct correlation between the CT state emission and the device Voc[56][57][58] as recently demonstrated by Baran *et al.*[59] who reported an elegant method which predicts the optimized conditions for the best polymer-fullerene combination by avoiding the fabrication of complete solar cells.

Photoluminescence and electroluminescence are also used as complementary methods to investigate the solid state morphology of the solar cell BHJ, the degree of polymeric interchain order, the effectiveness of the donor-acceptor interfaces, etc..[60]

In this thesis, the electroluminescence measurements were performed with the same instrument used to collect the device photoluminescence. Diversely, the cell was kept in dark conditions and a forward bias was applied through a Keithley 2400 source measurement unit.

Atomic Force Microscopy

The atomic force microscopy (AFM) is a technique for the surface characterization. The instrument consists of a cantilever with a sharp tip, which is influenced by Van del Waals forces in proximity of the sample surface, thus causing the deflection of the cantilever. The investigation, depending on the tip-surface interactions, could be realized in *i) contact mode*, which monitors the short-range repulsive forces, *ii) non-contact mode*, which analyzes the longer range attractive forces, or *iii) tapping mode*, where the cantilever vibrates. While scanning, the force between the tip and the sample is measured through the detection of the cantilever deflection. A topographic image of the sample is obtained by plotting the detection of the cantilever versus its position on the sample. This results in qualitative images however, quantitative measurements are possible through the analysis of parameters such as the root mean square (RMS) of the surface, which is defined as:

$$RMS = \sum_{i=1}^{N} \left[\frac{(z_i - \bar{z})^2}{N} \right]^{1/2} \qquad\qquad 2.10$$

where z_i is the height at each data point of the surface profile, $\bar{z}$ is the average height of the surface profile and N is the number of data points.

AFM allows the three dimensional analysis of sub-nanometric structures without requiring any special treatment of the sample. However, the high accuracy of the measurement turns out to be a limit because the maximum surface height detectable is in the order of 10 micrometers and the maximum scanning area is about 150x150 micrometers.

In this thesis, AFM images were taken with a Solver Pro (NT-934 MDT) scanning probe microscope in tapping mode.

Confocal microscopy

Confocal microscopy is a non-invasive technique of imaging, which confers a better lateral resolution and contrast than the classic optical microscopy. Indeed, a confocal microscope is endowed of a more complex system of lens and spatial filters, which allow to control the depth of field, eliminate out-of-focus details and measure fluorescence from optical sections of the sample. In a conventional confocal microscope, a xenon lamp shines light which is reflected by a dichroic mirror towards an objective lens, which focuses the ray on the sample. The photo-excitation of the sample results in a radiative decay where the emitted photons pass through the same optical system and, transmitted by the dichroic mirror, reach a photomultiplier detector. The system has the advantage to move the focused spot of exciting light in the x and y positions over the sample and hence allows for photoluminescence imaging of a specific area of the sample. The possibility to use laser sources instead of a xenon lamp offers the advantage of a monochromatic light while the lateral resolution of the confocal image is limited by the wavelength of the laser.

In this thesis, a laser scanning confocal microscope (LSCM) was used to detect the photoluminescence arising from the residual exciton recombinations inside the BHJ layer. Two different lasers were used to excite the sample either at 405 nm or 488 nm, which reach the BHJ active layer through the transparent bottom electrode of the device

(glass/ITO). The laser was focused on the sample through a 60x numerical aperture (NA) 0.70 air objective while the photoluminescence images were collected exclusively from the red channel of the detector, which corresponded to the range of wavelengths 565 – 683 nm. Besides that, the spectral photoluminescence of the sample was also measured through the use of an optical fiber to collect the emitted photons from a selected area of the sample to a multichannel analyzer (Hamamatsu).

Moreover, the confocal microscope was also upgraded to measure local currents generated by the photo-excitation of complete solar cells. In this view, the device under short circuit conditions was electrically connected via external contacts to a lock-in amplifier. The connection of a pulsed laser source (405 nm pulsed at 5kHz) and the lock-in amplifier allowed to collect images of local photocurrent over a selected area of the sample. This technique, named laser scanning photocurrent microscopy (LSPM), results similar to the laser beam induced current (LBIC) method, but is able to provide an improved lateral resolution thanks to the use of a confocal system. The combination of the LSCM and LSPM gave the possibility to simultaneously analyze the morphology and quality of both the active layer and electrodes of an organic solar cell over the same area and at sub-micron resolution. This gave the advantage to correlate the photophysical/morphological properties of the BHJ with the OPV response of the entire solar cell without damaging the device as discussed in Chapter 4.

Alternative characterization techniques

Additional characterization methods were used in this thesis to further improve the understanding of the investigations. The experimental details are here reported.

Attenuate Total Reflection - Fourier Transform Infrared Spectroscopy (ATR-FTIR) spectra were measured with a Bruker Vertex 70 interferometer using a DLaTGS detector, a KBr beam splitter and a Platinum-ATR accessory with a diamond crystal. The recorded spectral region was 370–7500 cm^{-1} with a scan velocity of 10 kHz and spectral resolution of 4 cm^{-1}.

Scanning Kelvin Probe Force Microscopy (KFPM) measurements were performed with a Park NX10 system operated in non-contact mode using Point Probe Plus (PPP)-Non Contact High Resonance Frequency - Reflex Coating (NCHR) or PPP-Non Contact/Soft

Tapping Mode (NCST)Au probes (nanosensors). In KPFM mode an AC signal of 1 V was applied to the tip at 17 kHz. Measurements were performed under controlled ambient conditions. Tip wear effects were excluded due to strict noncontact operation minimizing mechanical shear forces between sample and tip.

The thickness of the thin films were measured by using a profilometer KLA-Tencor P-6.

2.5   Degradation tests

Thermal stress tests

Thermal stability tests were carried out in dark and inert atmosphere (inside the glove-box) on unencapsulated devices, placing the cells on a hot plate at 65°C or 85°C for a certain time period. As discussed in Chapter 4, standard protocols such as the ISOS-D-2 were followed. After a defined time, the sample was removed from the hot-plate for non-invasive analysis performed in inert environment, such as J – V measurements, and then placed again over the hot-plate to continue the thermal stress. To note, the solar cell properties were measured after the cooling of the device (room temperature). Concerning the confocal microscopy investigations, the measurements were performed after the degradation period on encapsulated aged cells.

Light stress tests

Unencapsulated solar cells were subjected to light stress tests by keeping the device in inert environment (inside the glove-box) under AM1.5G illumination for a defined time interval. The test was temporarily interrupted to monitor the properties of the solar cell during ageing. It is noteworthy that these analysis were performed always in glove-box after the cooling of the device (room temperature).
In order to account for the light heating effects caused by the prolonged illumination, identical reference devices were covered with a black tape and kept exposed to light heating for the same test period.

Concerning tests performed on pristine polymeric films, solution processed films were exposed to AM1.5G illumination under ambient conditions without any encapsulation, in accordance with analogous studies reported in literature (see Chapter 4 for further details).

Chapter 3

Materials for organic photovoltaics

3.1 General overview

The solar radiation consists in a set of photons with an energy distribution of 50% in the infrared (IR), 40% in the visible (vis) and 10% in the ultraviolet (UV) region, partially attenuated as it travels through the atmosphere. To efficiently harvest solar energy, the absorption of organic solar cells should overlap with the solar spectrum. This means that the absorbing material should be characterized by a suitable energy gap. For instance, a band gap of 1.1 eV can absorb approximately 77% of the solar energy while a band gap exceeding 2 eV only about 30%. Therefore, the first criteria in designing new organic semiconductors for photovoltaic applications is the obtainment of a suitable band gap to harvest most of solar photons at different energies. The optical properties of the active layer are indeed directly correlated to the amount of charges produced in the device, which means that the current density exploited at short circuit conditions (Jsc) strictly depends on the absorbed photons. To utilize as much solar energy, the combination of an electron donor and acceptor materials in a BHJ device should preferentially have a narrow band gap in order to absorb also the low energetic photons (infrared radiation), which represent half of the solar energy. Besides the Jsc, another fundamental parameter for the efficiency of OSCs is the open circuit voltage (Voc), which consists in the maximum bias exploitable by the device. Voc was demonstrated to depend on the offset between the HOMO level of the electron donor (polymer) ($HOMO_D$) and the LUMO level of the electron acceptor material ($LUMO_A$) (Figure 3.1). This means that a first way to simultaneously improve both Jsc and Voc, is: *i)* the design of donor polymers with low band gap and deep HOMO energy levels, and *ii)* the selection of a suitable acceptor material with a relatively high LUMO energy level. Importantly, for an efficient exciton splitting, an offset of 0.3 eV (ΔE_{LUMO}, Figure 3.1) between the LUMO of the donor ($LUMO_D$) and the LUMO of the acceptor ($LUMO_A$) should be ensured to overcome the exciton binding energy. This value is a general consideration for the materials employed at the present since theoretical models demonstrate that the use of materials with raised

dielectric constant (ε) allows for a smaller ΔE_{LUMO} offset approaching values around 0.15 eV.[61][62]

In summary, to improve the device efficiency, the optical band gap and the $HOMO_D$ level need to be simultaneously reduced as far as ensuring the minimum driving force for exciton splitting. Scharber *et al.* estimated that, using a fullerene derivative as acceptor of the BHJ, a polymer band gap in the range 1.35-1.65 eV represents good compromise to simultaneously maximize the Jsc and Voc of the solar cell.[63] Nonetheless, the properties of the acceptor counterpart can be similarly tuned. While the $LUMO_A$ level can be opportunely raised to improve the V_{oc} of the solar cell, the band gap can be reduced to contribute to the photon harvesting, even though a sufficient ΔE_{HOMO} (Figure 3.1) with the donor should be guaranteed to allow the hole transfer from the acceptor to the donor phase.
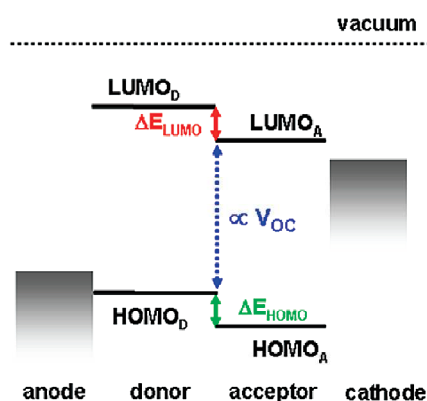
Figure 3.1. Diagram of the correlation between the energy levels and the Voc of organic solar cells. Adapted with permission from Ref. [64]. Copyright 2010 American Chemical Society.

Despite a suitable energy alignment of the BHJ components is fundamental, many other parameters are equally important for the device operation. Typically, organic materials are characterized by poor charge mobility. To ensure an efficient charge transport and to avoid bimolecular recombination in the active layer, a high carrier mobility needs to be ensured. To this end, the solid state morphology of the BHJ plays a crucial role since the mechanism of conduction occurs through the hopping of charges from localized states. As a consequence, the enhancement of the solid state packing would benefit the hopping mechanism thus ensuring a better device operation. The strong dependence between the electrical properties and the film morphology of a BHJ film, underlines the key role of the

processing conditions for the achievement of efficient blends. As little variations of the processing parameters are demonstrated to relevantly change the device characteristics in terms of both optical and electrical properties, the choice of *i)* materials with suitable chemical-physical properties as well as *ii)* a proper donor-acceptor ratio, *iii)* solution concentration and *iv)* nature of the dissolving solvent, represent fundamental requirements for the device optimization. In addition, post processing methods can be usefully adopted for additional modifications after the active film is deposited.

Hereafter, an analysis of the optoelectronic properties of the electron donor and acceptor materials is given. Then, some conventional methods to optimize their self-organization in BHJ are reported and briefly discussed.

3.2 Electron donor materials

The design, synthesis and development of organic electron donating polymers are topics of extended research efforts over the years. Many different requirements need to be simultaneously fulfilled by the polymers for their application in organic solar cells. Indeed, despite the energetic constrains for device application, *i.e.* suitable HOMO and LUMO levels, the materials should simultaneously provide a good environmental stability, a high absorption coefficient, a proper solubility in organic solvents, a high mobility at the solid state, great resistance to thermal and light stress and good film-forming properties.

In this sight, organic compounds offer the great advantage to be chemically modified thus allowing a fine tuning of the resulting properties. Hence, a fundamental understanding of the molecular design as well as the strategic synthetic routes are of extreme importance to generate advanced donor materials for efficient OSCs.

3.2.1 General overview

3.2.1.1 Synthesis

The synthesis of semiconducting polymers is based on the coupling of aromatic units (monomers) to form conjugated chains. The formation of a bond between two aromatic

rings involves the reaction between two carbon atoms with sp^2 or sp hybridization, which is usually obtained through transition-metal catalyzed cross-coupling reactions. The most common cross-coupling reactions were developed by Stille, Suzuki-Miyaura and Sonogashira and differ for the organometallic nucleophiles employed, which are respectively stannyl, boron or copper based aromatic systems.[65] The catalyst of the reaction is usually a transition metal based on complexes of palladium or nickel. In these reactions (Figure 3.2), the catalyst first reacts with an electrophile aromatic specie (Ar) through an oxidative addition process and then includes, in its coordination sphere, the nucleophile (Ar') through a transmetalation process. The reaction ends with the reductive elimination of the catalyst which favors the carbon-carbon bond formation between the two aromatic species, Ar-Ar'.
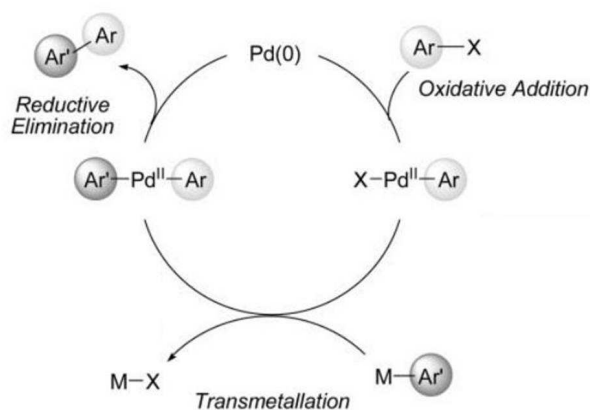
Figure 3.2. General scheme of a Palladium catalyzed cross-coupling reaction. Adapted from Ref. [66] with permission of The Royal Society of Chemistry.

New methods for the synthesis of conjugated polymers were recently developed in order to reduce the number of synthetic steps and avoid the use of toxic chemicals typically involved in the transition-metal catalyzed cross-coupling reactions. One of the emerging synthetic procedures is the direct arylation where the unstable organometallic components are replaced by more stable and cheaper alternatives.[66] Despite this method results facile and attractive for the reduced environmental impact, it still suffers from side reactions, which affect the structural purity of the resulting polymer.

3.2.1.2 Strategies for the energy gap modulation

The energy gap and the relative position of the HOMO and LUMO energy levels are some of the most important characteristics for the optoelectronic properties of the resulting conjugated polymers. Since almost 50% of the total solar energy consists of low energetic infrared photons, for an efficient harvesting, the polymer band gap should be suitably narrowed. Several factors contribute to tune the energetic characteristics of the polymer including the resonant stabilization energy of aromatic rings, the bond-length alternation, the structure planarity and the effect of eventual substituents (Figure 3.3).[26][67][68][69]
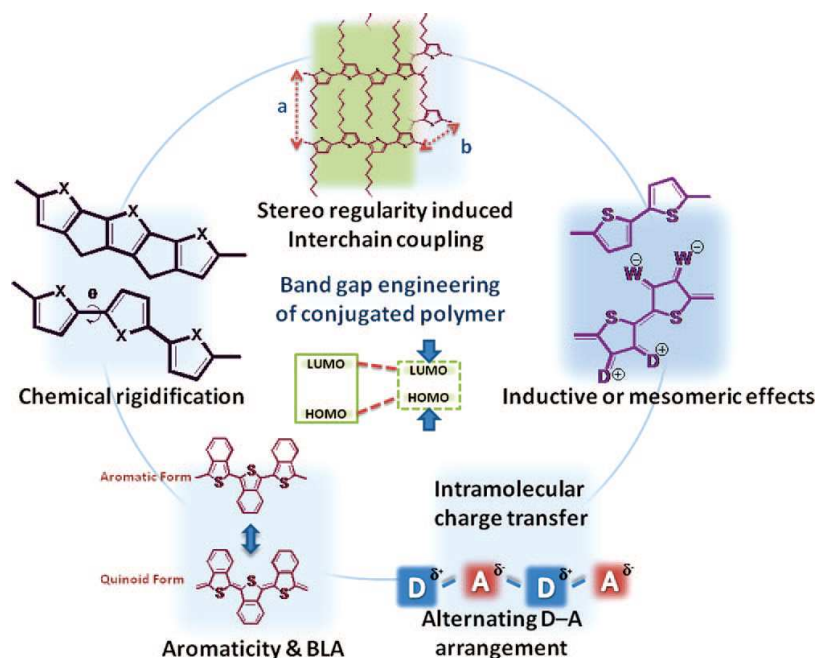
Figure 3.3. Possible strategies to reduce the energy gap of a conjugated polymer. Reprinted with permission from Ref. [26]. Copyright 2009 American Chemical Society.

The main strategies to lower the polymer energy gap are hereafter summarized.

Extension of the π-electron delocalization along the polymer structure. This can be obtained by inserting more conjugated monomers in the polymer backbone. However, the effect on the energy gap was demonstrated to become negligible beyond 7-10 conjugated units.

Rigidification of the polymer backbone. Similarly to the elongation of the polymer backbone, this method extends the π-conjugation length through the planarization of the structure by limiting the torsion angles. This can be obtained by chemically bonding

adjacent aromatic rings with a bridging atom and by avoiding the use of pendant groups, which determine steric hindrance with subsequent structure distortion. To note, the reduction of side groups or more in general the rigidification of the structure can limit the solubility of the polymer, still highlighting the need of a delicate modulation/control of all the parameters.

Inter-molecular interactions. In this case, the polymer should present an organization at solid state where the chains tightly arrange in ordered π-stacks. This packing is favored for chemical structures having an intrinsic order. For instance, polymers characterized by identical repeating pendant groups (regioregular, RR) typically show strong inter-chain interactions with a reduced energy gap arising from an energetic stabilization of the system.

Introduction of substituents. Another strategy to narrow the polymer band-gap consists in the incorporation of specific substituents able to modulate the energy position either of the HOMO or the LUMO levels. Typically, the HOMO level is raised by inserting electron-donating groups while the LUMO is lowered in presence of electron-withdrawing groups.

Stabilization of the quinoidal resonance form. This method relates to the balance between the two resonant structures of conjugated polymers, the aromatic and the quinoidal form. Diversely from the more stable aromatic form, the quinoidal gives a partial double bond character to single bonds which, reducing their bond length and enhancing the planarization of the whole system, determine the reduction of the polymer band gap. The stabilization of the quinoidal structure is favored if an additional and different aromatic ring is fused to the backbone monomer.

Donor-acceptor approach. An alternative strategy to effectively reduce the band gap of a π-conjugated polymer consists in the alternation of electron-rich and electron-deficient building blocks. Here, the molecular orbitals of the adjacent electron rich and poor moieties, also called donor (D) and acceptor (A), interact after polymerization leading to new molecular orbitals with lower energy gap (Figure 3.4). This class of polymers often shows a partial quinoidal effect in the resonant structure D^+-A^-, which further modifies the energy levels and hence the band gap of the corresponding material.
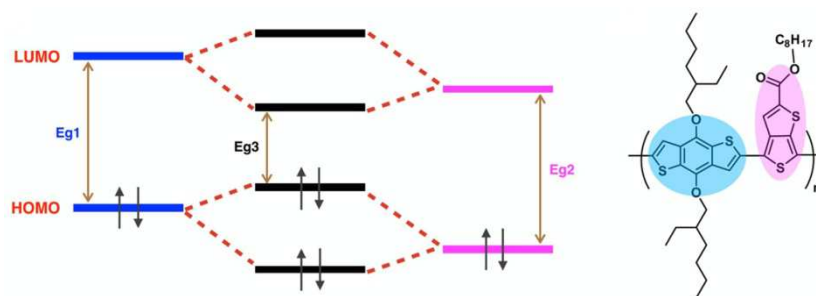
Figure 3.4. Mechanism of the donor-acceptor approach to reduce the polymer bandgap. Adapted with permission from Ref. [69]. Copyright 2015 American Chemical Society.

Introduction of π-bridges in push-pull polymers. As previously mentioned, the planarity of the backbone is one of the possible routes to modulate the energy gap and the solid state packing of the polymer. Often, aliphatic chains or aromatic rings are chemically bound to the polymer backbone to make the material soluble in common organic solvents or to extend the π-conjugation over other directions. However, the presence of steric hindering substituents bounded to adjacent D-A units can considerably influence the spatial conformation of the polymer backbone which, to minimize the overall energy of the system, twists determining a partial interruption of the π-delocalization with a subsequent effect on the energy levels. Since the presence of substituents is of necessary importance, aromatic rings or conjugated units are typically introduced, as π-spacers, between the two adjacent donor and acceptor moieties (π-brigdes) in order to spatially stave them off preserving the planar conformation of the polymer, which is a key factor for the resulting inter-molecular interactions and charge transport properties. In this way, the push-pull character of the polymer is not influenced by the presence of the substituents. Moreover, the π-electron delocalization is further extended thus contributing to the additional reduction of the polymer band gap.

Note that the reduction of the band gap allows for a more efficient device operation, however not less important is the environmental stability of the polymer, which strictly depends on the position of its HOMO level. As a result, a fine modulation of the polymer HOMO-LUMO energy levels is necessary to ensure both great operation and stability of the corresponding BHJ blends.

3.2.1.3 Additional requirements for OPV applications

All the reported methods are powerful design strategies to reduce the polymer band-gap through chemical synthesis. However, in view of their application in BHJ solar cells, some other constrains, which require a further tuning of the polymer structure, are present.

For instance, a good solubility in organic solvents is the first requirement to fulfill. Indeed, to obtain enough absorbing films, a suitable concentration of the pristine solution needs to be guaranteed. The molecular structure is therefore modified by the introduction of aliphatic pendant groups, which should enhance the solubility of the polymer without affecting the energetic properties.

A second fundamental requirement is a suitably high mobility to ensure the efficient charge transport at the solid state. Hence, the solid state organization of the polymer and the film formation ability are likewise important for the device operation. Some general rules can be considered during the polymer design, however predictions on the self-assembly of the molecules are challenging. In this context, the number, position and nature of the substituents on the polymer backbone are important since they influence the solubility, as previously mentioned, but also the solid state organization/packing.

Besides that, two other important parameters, which influence the device performance, are the molecular weight and the poly dispersive index (PDI) of the polymer. Indeed, since the polymerization process is not fully controllable, the final polymer is characterized by a number of chains with different length and hence molar mass. For this reason two different parameters define the mass of the final product, the number average molar mass (M_N) and the mass average molar mass (M_W). M_N refers to the ratio between the total weight of the material and the number of polymer chains and hence is the average weight of an individual chain. On the contrary, M_W depends more on the contribution from longer chains than short chains. The ratio between M_W and M_N of a polymer is called PDI and is indeed a parameter which evaluates how spread is the molecular weight distribution. Spread distributions consist of a set of chains with a length consistently different from the average. This affects the molecular packing, causing reduced interchain interactions, and the presence of energy defects in the structure, which affect the charge mobility. As a consequence, low PDIs are preferred for a greater device operation.

Concerning the average molecular mass, higher values were demonstrated to favor the interchain interactions leading to an increase of the extinction molar coefficient as well as a broadening in the absorption spectrum towards lower energies.[70] As a result, higher values often lead to greater device performance. However, since higher molecular weights lead to stronger chain-chain rather than solvent-chain interactions, the solubility of the polymer is therefore reduced and hence a fine balance between the solubility and the solid state organization should be found to exploit the potential of a polymeric structure.[71]

Besides the role of the substituents on the polymer backbone, the molecular weight and poly dispersivity index, additional parameters such as the solvent, concentration and processing conditions of the active blend have a strong influence on the film formation. General rules for these parameters cannot be furnished since they strongly depend on the nature of the polymer. However, their influence on the device efficiency is discussed in the Paragraph 3.4.

3.2.1.4 Evolution of the polymeric structures

At the dawn of the organic photovoltaic technology, researchers focused on polymers consisting of a single repeating unit (homo-polymers) and devoted much efforts in the optimization of the energy levels through the continuous development of new efficient structural units composing the polymer backbone. The first polymer introduced in BHJ solar cells was based on poly(phenylenevinylene) (PPV) derivatives as poly[2-methoxy-5-(2-ethylhexyloxy)-1,4-phenylenevinylene] (MEH-PPV) and poly[2-methoxy-5-(3',7'-dimethyloctyloxy)-1,4-phenylenevinylene] (MDMO-PPV). The first studies on these polymers reported power conversion efficiencies (PCEs) in BHJ devices approaching 3%. The limited performance arose from the relatively high band gap of the polymer (≈ 2.2 eV) which, blended with the poor optical absorbing $PC_{61}BM$, limited the light harvesting of the active blend. More attention was devoted to regioregular poly(3-hexylthiophene) (rr-P3HT), based on a repeating substituted thiophene unit, which initially showed a PCE of 3% in BHJ solar cells. The attracting properties lying in the band gap of ≈ 1.9 eV and a relatively high cristallinity at the solid state encouraged the intensification of the research on this polymer leading to impressive improvements in terms of device performance with record PCEs over 7%.[72][73]

Despite P3HT played a significant role in the development of organic solar cells, the major contribution for this technology concerns the successful introduction of alternating copolymers in which two moieties with different electron affinity (donor-acceptor design) are chemically bounded to form a composed monomer, which is successively polymerized.

Over the last decade, many donor and acceptor moieties were developed and systematically combined to finely tune the polymer properties.[74] Among electron rich systems, fluorene, cyclopentadithiophene (CPDT), oligothiophene, benzodithiophene (BDT) and indacenodithiophene (IDT) are the most employed units while benzothiadiazole (BT), diketopyrrolopyrrole (DPP) , thienothiophene (TT), quinoxaline (Q) and isoindigo (IID) represent effective electron deficient counterparts (Figure 3.5).[44]
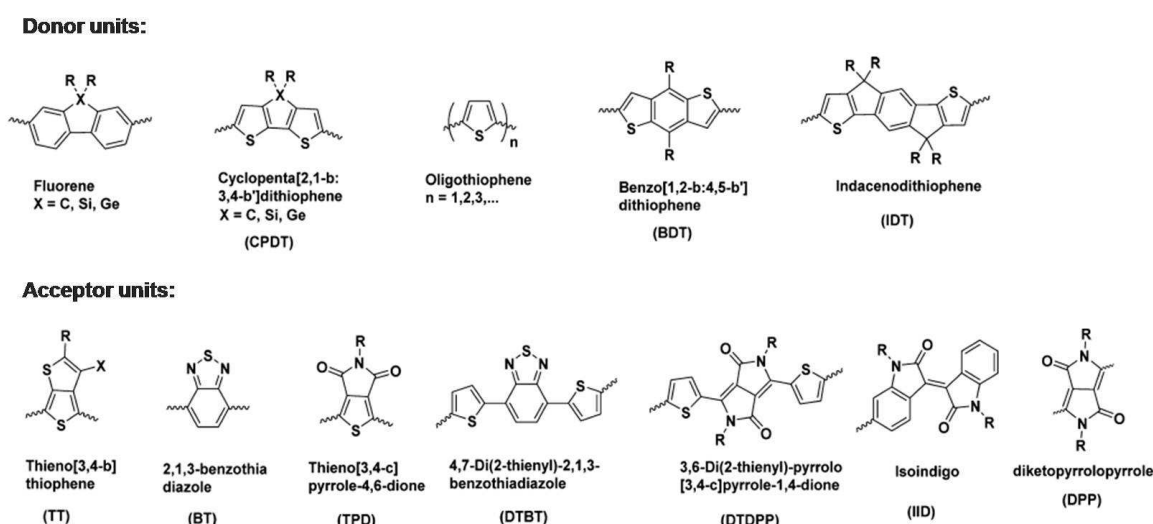
Figure 3.5. Chemical structures of some donor and acceptor moieties for application in D-A polymers. Reprinted with permission from Ref. [68]. Copyright 2015 American Chemical Society.

The combination of CPDT and BT units led to one of the first copolymers with a reduced band gap of ≈ 1.4 eV. The exploitation of a larger part of the solar spectrum gave BHJ devices with high Jsc (> 10 mA/cm^2) and device efficiencies approaching 6%.[75] The performance were further improved by introducing an electron donating oxygen substituent in the CPDT unit and two electron withdrawing fluorine atoms in the BT moiety, which led to solar cell PCEs approaching 8%.[76]

The impressive results obtained using the D-A approach pushed the investigation of new combinations of donor and acceptor moieties, which resulted in the development of high performing categories such as the BDT-Q polymers which achieved PCEs up to 8.6%,[77] the BDT-TT family (*e.g.* PTB7 or PTB7-Th) which surpassed the milestone PCE of

10%[78][79][80] and the thiophene-BT based polymers which established the remarkable PCE of 11.7% in single-junction BHJ device (PffBT4T-C_9C_{13}).[81] The great improvements of the device performance over the years arise from a continuous investigation of the structural, energetic, electrochemical as well as morphological properties of the semiconducting polymers, which allowed the development of increasingly efficient materials.

In this context, our research group contributed with studies on the structure – properties relationship for many different D-A polymers.[82][83][84] In particular, an additional contribution comes from this PhD program, where the effect of the substituting chains of the polymer backbone on the device performance was investigated.

3.2.2 Synthesis and characterization of benzodithiophene and benzotriazole-based polymers for photovoltaic applications

Over the past decade many novel polymers have been developed to improve the solar cell performance. Most of the research focused on the design and synthesis of low band gap materials to improve the exploitation of sunlight by organic solar cells. However, an ideal donor should simultaneously ensure great absorbing properties as well as a suitable position of the energy levels to favor high Voc in the device. In this context, low band gap materials bring excellent light absorbing properties to the solar cell but their high lying HOMO often represents a limit for the Voc. A fine balance is represented by the class of medium band gap polymers which are able to produce great Voc ensuring good sunlight absorption. By using the donor-acceptor approach, medium band gap polymers can be synthesized by coupling electron rich and electron deficient moieties presenting weak push or pull characteristics. One of the most popular electron donating unit is BDT which shows desired properties as structural rigidity, planarity, extended π conjugation length and favor the interchain π-π stacking. Moreover, alkyl or aryl groups can easily be introduced to BDT basic units as side groups to finely tune the properties of the resulting polymers, not only in terms of solubility but also contributing, for example, to extend the π-conjugation from the backbone to the lateral substituent (2D π-conjugated systems), thus leading to a bandgap reduction and higher charge carrier mobilities.[85] On the other

hand, a weak electron acceptor moiety is represented by benzotriazole (Tz),[85][86][87] a structure similar to BT (Figure 3.5) where the sulfur atom is replaced by a nitrogen. This substitution gives less accepting character to the unit if compared to BT since the lone pair on the nitrogen atom is more easily donated into the triazole ring thus making the ring more electron rich. Moreover, Tz is easily synthesizable and provides the advantage of incorporating solubilizing alkyl chains on the acceptor unit rather than on the rest of the polymer backbone thanks to the possibility to functionalize the reactive nitrogen atom. This reduces possible steric repulsions between adjacent moieties thus allowing a more planar conformation of the polymer structure. As discussed in the previous section, the energetic, optical and transport properties of a polymer are strongly dependent on the presence of side chains. Despite they are fundamental for the miscibility of the donor and acceptor material of the BHJ and for making the polymer soluble in organic solvents, their nature, position and number have a strong effect on the spatial distribution of the polymer structure and on the device properties as a result. In sight of this, copolymers based on benzo[1,2-*b*:4,5-*b'*]dithiophene (BDT) and 5,6-difluoro-2*H*-benzo[*d*][1,2,3]triazole (Tz) separated by a thiophene ring as π spacer were differently substituted on the BDT unit with either 2-octylthienyl (PTzBDT-1) or 2,3-dihexylthienyl (PTzBDT-2) (Figure 3.6).[88] The effect of the different alkylthiophene side chains on the resulting polymers was analyzed both on film of pristine polymer and in organic BHJ solar cells. As shown in Figure 3.6, PTzBDT-1 and PTzBDT-2 polymers were synthesized through Stille cross coupling reaction between BDT (monomer 1 or 2) and Tz (monomer 3) units opportunely functionalized. The reactions gave the desired polymers in excellent yield and their number average molecular weights M_N, determined using size exclusion chromatography, resulted 20.2 kDa and 41.7 kDa for PTzBDT-1 and PTzBDT-2, respectively. The slightly lower M_N for PTzBDT-1 arose from a reduced solubility of the polymer because of the lower content of alkyl side chains compared to PTzBDT-2. As a consequence, chlorobenzene was used as extracting solvent after the synthesis of PTzBDT-1 diversely from PTzBDT-2 which was extracted with chloroform thanks to its better solubility. The two polymers dissolved in their respective solvents were characterized and compared using UV-visible absorption spectroscopy both in dilute solution and solid films (Table 3.1 and Figure 3.7).
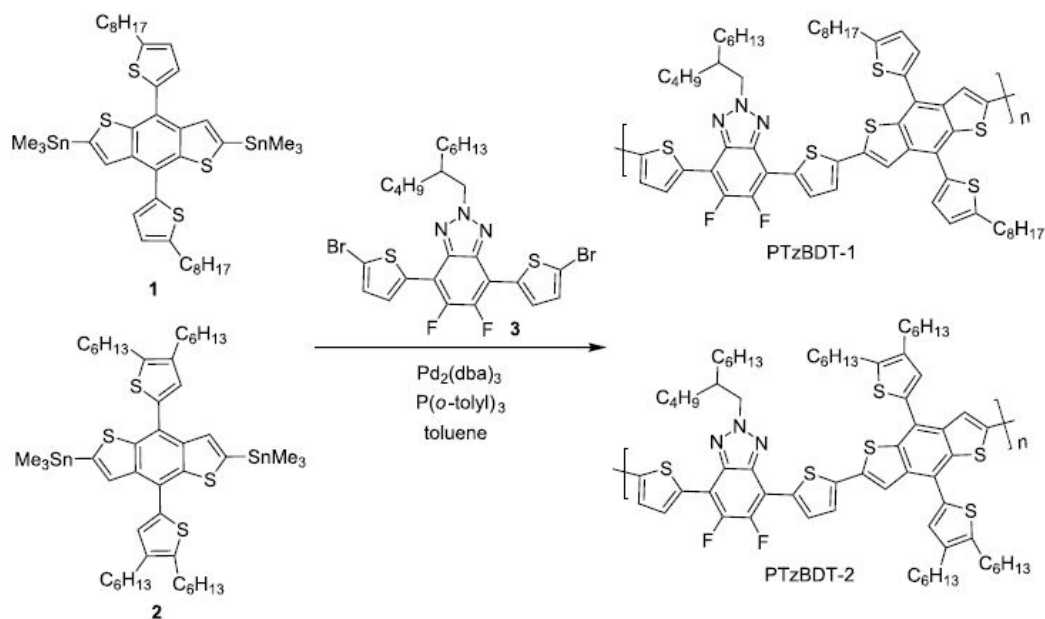
Figure 3.6. Synthesis of PTzBDT-1 and PTzBDT-2 polymers through Stille cross coupling reaction.
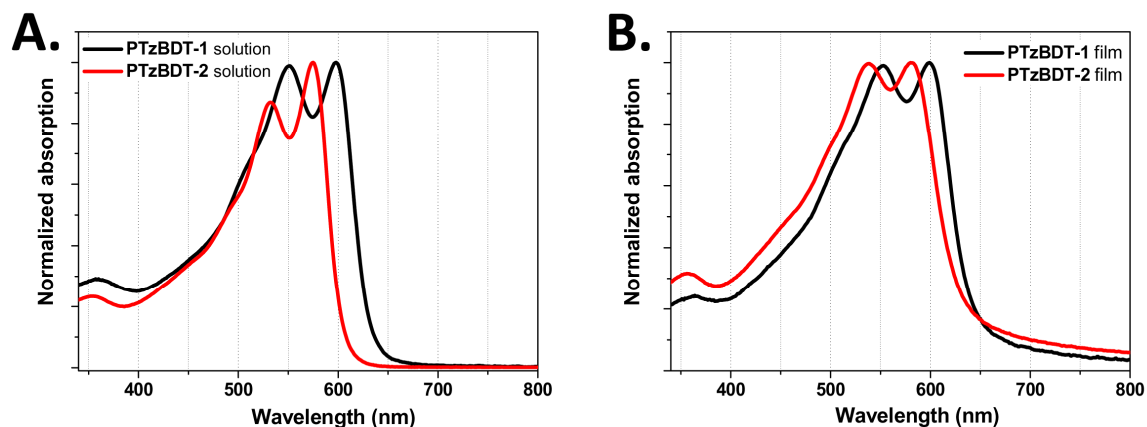
Figure 3.7. UV-visible absorption spectra of PTzBDT-1 (black) and PTzBDT-2 (red) polymers in dilute solution (A) and thin film (B). Chlorobenzene and chloroform were used to dissolve and process PTzBDT-1 and PTzBDT-2, respectively.

For both polymers, a modest absorption peak was present at around 360 nm and is ascribed to thiophene side groups bound to the BDT unit while an evident double peaked band between 500 and 650 nm is due to charge transfer processes between the BDT and Tz moieties and to inter-molecular interactions between the polymer chains. The two polymers presented similar absorption features despite a different energy positions of the peaks. In particular, the absorption spectrum in solution (Figure 3.7a) of PTzBDT-1 was 20 nm red-shifted compared to that of PTzBDT-2 as revealed by the band at lower energies, in detail characterized by two peaks at 550 and 598 nm for PTzBDT-1 and 530

59

and 574 nm for PTzBDT-2. In addition, PTzBDT-1 presented a broader absorption than PTzBDT-2 with an energy offset (λ_{ONSET}) at 633 and 605 nm for PTzBDT-1 and PTzBDT-2, respectively. Despite the two polymers have similar chemical structures their different optical properties confirms the crucial role of the alkyl aril side chains bound to the BDT unit on the polymer properties. The presence of two n-hexyl chains on the thiophene side groups in the PTzBDT-2 likely causes steric hindrance between the BDT and Tz units leading to a partial structural twisting responsible for the observed blue-shifted absorption than PTzBDT-1. This effect was less evident at the solid state where the two polymers showed only a modest difference in their energy offset (Figure 3.7b and Table 3.1). This means that, despite the twisted structural conformation of PTzBDT-2 in dilute solution, strong inter-chain interactions led to a well π-packed organization at the solid state for PTzBDT-2, as revealed by the significant red-shift in the absorbance passing from dilute solution to thin film ($\Delta\lambda_{ONSET} = 31$ nm). On the contrary, the presence of a single n-octyl side chain bound to each thiophene side group in PTzBDT-1 is not sterically hindering and promotes a more planar conformation of the structure even in dilute solution. This favors a partial pre-aggregation of the polymer in solution despite the high dilution and, as a result, the absorption of the relative thin film was not significantly red-shifted than that in solution ($\Delta\lambda_{ONSET} = 13$ nm).

Table 3.1: Summary of the optical and electrochemical properties of PTzBDT-1 and PTzBDT-2.

Polymer	M_N [kDa] (a)	PDI	Solution			Thin-film			E_{HOMO} [eV]	E_{LUMO} [eV]
			λ_{max} [nm]	λ_{onset} [nm]	E_{gap}^{opt} (b) [eV]	λ_{max} [nm]	λ_{onset} [nm]	E_{gap}^{opt} (b) [eV]		
PTzBDT-1	20.2	4.40	550, 598	633	1.96	553, 598	646	1.92	- 5.94	- 3.25
PTzBDT-2	41.7	2.53	530, 574	605	2.05	536, 580	636	1.95	- 5.86	- 3.21

a) Determined by GPC relative to polystyrene standards using 1,2,4-trichlorobenzene as eluent. b) $E_{gap}^{opt} = 1240/\lambda_{onset}$.

The energy levels of the two polymers were measured through Square Wave Voltammetry (SWV) using the electrochemical oxidation and reduction peak values, respectively for the HOMO and LUMO levels, while the ferrocene/ferrocenium (Fc/Fc$^+$) was used as reference system in the relation $E_{HOMO/LUMO} = - (E_{OX/RED} + 5.13)$ to calculate the correct values. PTzBDT-1 reported HOMO and LUMO levels located at -5.94 and -

3.25 eV, respectively. Similarly, PTzBDT-2 showed the two frontier orbitals at -5.86 and -3.21 eV , respectively for HOMO and LUMO (Table 3.1).

Note that the number of alkyl chains linked to the aromatic side groups of the polymers are not expected to significantly affect the π-electron density distribution and thus the energetic properties of the two polymers, however the subsequent different organization at the solid state might be the main factor responsible for the observed variation of the HOMO and LUMO energy levels, which is in perfect agreement with the different optical properties. Interestingly, the deep HOMO energies of both polymers would result in devices with a high Voc, according to the difference $LUMO_A$-$HOMO_D$. Good air-stability is also expected from these polymers as suggested by their relatively deep HOMO level.

On the other hand, the relatively high lying LUMO level for both polymers is likely ascribed to the weak electron deficient nature of the Tz moiety. It should be noted that there is a certain discrepancy between the energy gap derived from electrochemical and optical measurements. This incongruence can be ascribed to the difference in the two characterization methods. Indeed, in optical measurements, the excitation of the polymers lead to opposite charges still electrostatically bound (excitons) while, during the electrochemical measurements, the polymer is in a ionized state.[89] In addition, the quality and the solid state organization of the polymeric film are known to influence the absorption characteristics. Differently from the absorption measurements, in the electrochemical analysis the film is prepared over the electrode surface. As a consequence, the self-organization and hence the properties of the film can be likely influenced as well as a possible energy barrier at the electrode surface/film interface can be present in the electrochemical analysis.

In order to understand the impact of the different alkyl side chains on the photovoltaic performance of the two polymers, PTzBDT-1 and PTzBDT-2 were used in BHJ solar cells as electron donor materials using $PC_{61}BM$ as acceptor counterpart. For the relative solar cells a standard configuration consisting in glass/ITO/PEDOT:PSS/PTzBDT-1: or PTzBDT-2:PC_{61}BM/LiF/Al was adopted and, in order to exploit the optimal photovoltaic response, the two active layers based on 1:2 (wt/wt) PTzBDT-1:PC_{61}BM and 1:1 (wt/wt) PTzBDT-2:PC_{61}BM, were deposited by spin coating from 1,2,4-trichlorobenzene (TCB) and 1,2-dichlorobenzene (o-DCB) solutions, respectively. The different optimal processing conditions were the result of a different character of the two polymers in terms of solubility and film forming (Table 3.2 and 3.3). The photovoltaic parameters of the relative solar cells are shown in Figure 3.8. As reported, PTzBDT-1 based devices

showed relatively low performance with a Voc = 0.67 V, Jsc = 7.6 mA/cm^2 and FF = 64% resulting in a PCE of 3.3% (Table 3.2). On the contrary, PTzBDT-2 based cells exhibited a PCE of 4.7% resulting from a Voc = 0.86 V, Jsc = 8.6 mA/cm^2 and FF = 64%. Jsc and Voc were the main parameters responsible for the different photovoltaic responses of PTzBDT-1 and PTzBDT-2 based cells, while the identical FF (64%) indicated suitable charge transport characteristics of the two active layers.
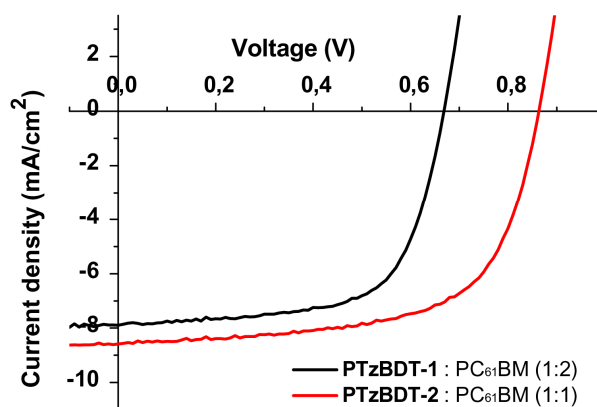
Figure 3.8. Average J - V plot of BHJ solar cells based on PTzBDT-1:PC$_{61}$BM (black) or PTzBDT-2:PC$_{61}$BM (red) active layer. In bracket, the donor:acceptor ratio in wt/wt is reported for each BHJ film.

Table 3.2: Photovoltaic characteristics of optimized PTzBDT-1:PC$_{61}$BM and PTzBDT-2:PC$_{61}$BM based devices. The reported results are averaged over at least 4 devices.

D:A ratio [wt/wt]	Solvent	Thickness [nm]	Annealing [°C]	J$_{SC}$ [mA/cm^2]	V$_{OC}$ [V]	FF [%]	PCE [%]
PTzBDT-1:PC$_{61}$BM [1:2]	TCB	100	110 [a]	7.6	0.67	64	3.3
PTzBDT-2:PC$_{61}$BM [1:1]	o-DCB	90	--	8.6	0.86	64	4.7

[a] annealing time: 10 min.

Table 3.3: PV characteristics of optimized PTzBDT-1:PC$_{61}$BM and PTzBDT-2:PC$_{61}$BM BHJ devices using different donor:acceptor ratios and processing conditions.

Active blend	D:A ratio [wt/wt]	Solvent (a)	Annealing [°C]	J_{SC} [mA/cm^2]	V_{OC} [V]	FF [%]	PCE [%]
PTzBDT-1: PC$_{61}$BM	1 : 1	TCB	-	8.0	0.63	42	2.1
	1 : 1	TCB	110 (b)	7.4	0.66	62	3.0
PTzBDT-2: PC$_{61}$BM	1 : 1	o-DCB	110 (b)	8.3	0.84	60	4.2
	1 : 2	o-DCB	-	6.6	0.87	65	3.7
	1 : 2	o-DCB	110 (b)	4.7	0.85	60	2.4

a) additional solvents have been also tested for each polymer, however the resulting films were not homogeneous and showed a poor morphology. For this reason BHJ Devices were not fabricated; b) annealing time: 10 min.

Passing from PTzBDT-1 to PTzBDT-2, an increase in the Voc of 0.19 V was observed despite the lower lying HOMO level of PTzBDT-1 polymer. This difference was likely ascribed to the different alkyl side chains bound to the thiophene substituent. In particular, the influence of the n-octyl side chains on the solubility and film forming properties of the polymer was likely the cause of a particular molecular aggregation and phase separation in the BHJ film which slightly modified the interfacial energy between the components, strongly related to the device Voc.[83] The improved Jsc ($\approx$ 15%) for PTzBDT-2 based cells can be ascribed to the different optical properties of the two active films (Figure 3.9a). Therefore, despite the similar shape of their absorption spectra, the polymer content in the PTzBDT-2:PC$_{61}$BM was two times higher than that of the PTzBDT-1:PC$_{61}$BM film since they presented the same thickness and concentration of the initial solution. This results in a higher amount of solar photons which can be harvested by the PTzBDT-2 based devices and, as a consequence, possibly converted in excitons and free charges.

Interestingly, the absorption spectra of the two active layers presented similar features observed for pristine materials (Figure 3.7b). In addition, the relative absorption maxima for PTzBDT-2:PC$_{61}$BM film were accordingly blue-shifted if compared to those of PTzBDT-1:PC$_{61}$BM film, whereby confirming that the twisted structural conformation of PTzBDT-2:PC$_{61}$BM at the solid state was maintained even in mixture with PC$_{61}$BM.
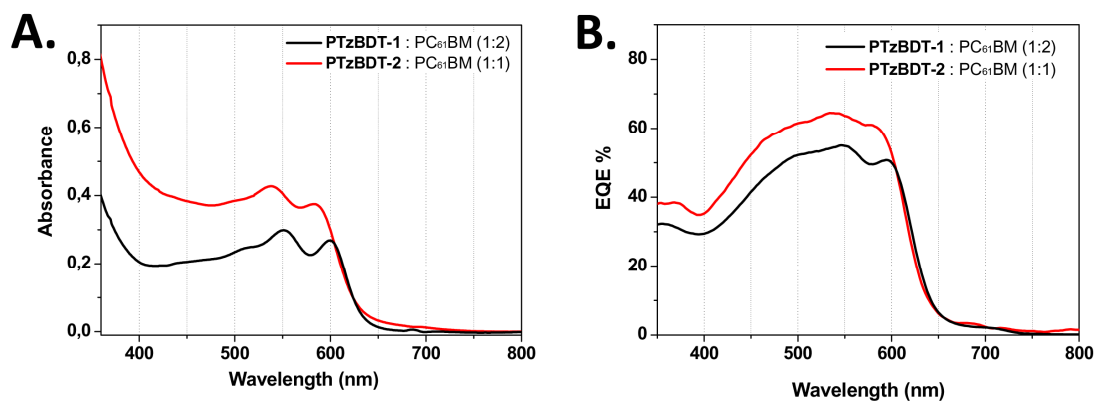
Figure 3.9. UV-visible absorption (A) and external quantum efficiency (EQE) (B) spectra of PTzBDT-1 (black) and PTzBDT-2 (red) based solar cells.

These results suggest that the presence of different alkyl side chains plays an important role for the photovoltaic response of a polymer. Indeed, the slightly different solubility and film forming properties of PTzBDT-2 in comparison to PTzBDT-1, not only allowed for a higher polymer content in the active blend which was responsible for more light absorption, but also seemed to be relevant for the kinetics of film forming which presented a strong impact on the phase segregation and morphological organization of the active blend reflected in the higher photovoltaic response.

The greater performance of PTzBDT-2:PC$_{61}$BM devices was previously ascribed to more efficient processes of excitons formation and splitting while the similar FF of the PTzBDT-1:PC$_{61}$BM and PTzBDT-2:PC$_{61}$BM solar cells suggested similar charge transport properties. As a confirmation of this hypothesis, EQE spectra were measured for both the optimized solar cells. As shown in Figure 3.9b, besides the typical double peaked band between 500 and 600 nm, the EQE spectra were consistent with the absorption spectra of the corresponding active films also in terms of relative intensity. In particular, the EQE response of PTzBDT-1:PC$_{61}$BM based devices reached maximum values around 55% (at 546 nm) while PTzBDT-2:PC$_{61}$BM cells around 64% (at 536 nm) with the integrated currents calculated from the EQE plots which resulted, within the experimental error (10%), perfectly in agreement with the Jsc from the J-V plot. This indicates that similar processes of charge collection occur at each wavelength albeit a different amount of charges are produced by the two different devices.

To further investigate the solid state phases distribution, AFM images were taken on the final devices (Figure 3.10). Their surfaces resulted slightly different in terms of roughness and domain distribution, with the PTzBDT-1:PC$_{61}$BM-based film characterized by a relatively featureless and rougher (RMS ≈ 1.5 nm) surface (Figure 3.10a) different from

that of PTzBDT-2:PC$_{61}$BM-based film (Figure 3.10b) which resulted more structured and smoother (RMS ≈ 0.5 nm) thus indicating a higher donor-acceptor intermixing and finely ordered domains in agreement with the improved photovoltaic performance. However, the better self-organization of the PTzBDT-2:PC$_{61}$BM based blend is in contrast with the intrinsic structural features of the polymer where the double side chains are likely responsible for the partial structural twisting of the polymer backbone. The enhanced solubility however promotes the quality of the resulting thin films demonstrating that the nature and number of side chains play a crucial role to reach the best compromise between solubility and molecular packing at the solid state for this class of polymers, key factor for the photovoltaic response in BHJ solar cells.
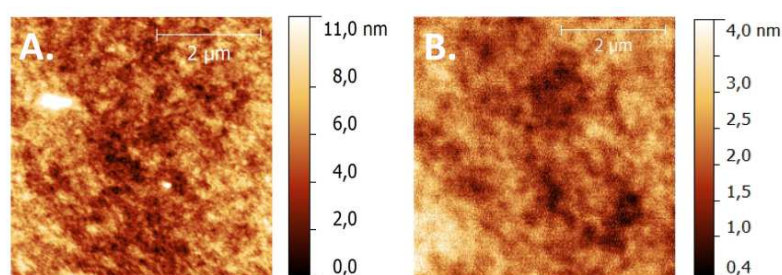
Figure 3.10. AFM images (5 µm x 5 µm) of optimized BHJ blends based on PTzBDT-1:PC$_{61}$BM (A) and PTzBDT-2:PC$_{61}$BM (B).

3.3 Electron acceptor materials

The turning point for the OPV technology was the development of the BHJ concept. The main limitation of the organic materials in terms of excitons dissociation was overcame *via* their combination with materials showing enough electron affinity to allow a photo-induced charge transfer process. As a result, a plethora of conjugated polymers as electron donors was synthesized and developed for BHJ application. While less efforts were devoted to the acceptor counterparts thanks to the discovery of fullerene derivatives which, besides a relatively complex chemistry, immediately showed advantageous properties and dominated the OPV research for decades. The recent achievement of device efficiencies over the commercialization milestone due to the development of well performing donor polymers pushed the intensification of the research on new (non-fullerene) acceptor materials (small molecules and polymers) in order to overcome some

limitations of the fullerene based acceptors towards lower expensive, more stable and potentially more efficient solar cells.

3.3.1   General overview

So far, the most employed accepting component in organic BHJ solar cells is buckmisterfullerene and its derivatives. The discovery of fullerenes occurred in the 1985 when, purely accidental, a cluster of carbon atoms was detected by evaporating graphite in dense helium flow under laser irradiation. The optimization of the process led to a specie consisting of 60 atoms of carbon arranged in a spherical structure with a diameter of $\approx$ 0.7 nm. The sphere was demonstrated to be composed by sp^2 hybridized carbon atoms, which confer aromatic character to the structure thanks to a sea of π electrons flowing in the inner and outer surface. At the very beginning, fullerene was believed a highly stable structure, inert and difficult to be functionalized. However, the sp^2 orbitals, which are forced to be curved, generate angle tensions which confer a certain grade of reactivity to the structure making fullerenes possibly functionalized to obtain soluble and processable materials. Thanks to the peculiar molecular structure, fullerene can generate stable anions with the ability to take up to 6 electrons in reversible way. In addition, charge transfer processes take place with efficiencies close to unit and, furthermore, the spherical shape facilitates the migration of charges through the fullerene layer. These properties reflect the huge potential of fullerene species and explain the reason of its success as acceptor component in organic solar cells.[90]

The era of fullerene for photovoltaic devices began with the discovery of the photoinduced electron transfer from MEH-PPV. Then, a series of fullerene derivatives soluble in organic solvents were designed and synthesized to suitably meet the energy requirements for BHJ applications. The successful debut in BHJ solar cells occurred with the development of methano fullerenes, in particular with the introduction of a phenyl butyric methyl ester functionality through a cyclopropane methano bridge. The introduction of the functional group to the carbon cage, not only made the carbon cage soluble in organic solvents, but even resulted effective to break the electron conjugation and rise the LUMO level, desirable to increase the device Voc. The result was the phenyl-C61-butyric acid methyl ester ($PC_{61}BM$) compound (Figure 3.11), soluble in organic solvents, with HOMO and LUMO levels lying around -6 and -4 eV, showing electron

mobility in the order of 10^{-3} cm^2/V·s and endowed with the ability to aggregate in both pure and mixed domains of appropriate length in BHJs.
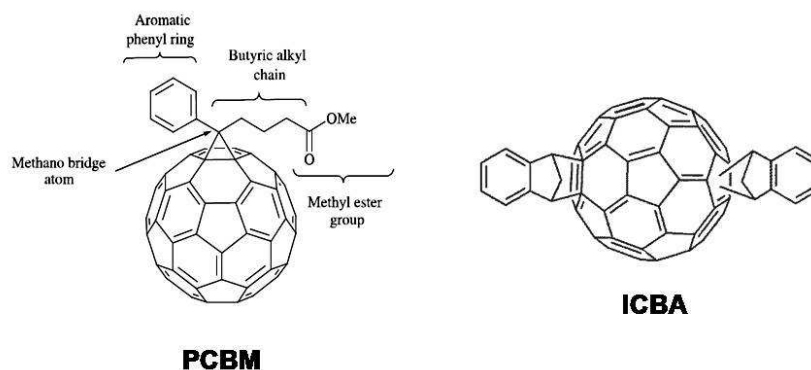
Figure 3.11. Molecular structure of fullerene derivatives.

PC$_{61}$BM is currently a reference as electron acceptor material for BHJ solar cells. Nevertheless, it has some drawbacks. For instance, it is characterized by a weak absorbance in the visible region, which limits the full potential of the device since does not contribute to the light harvesting. Fullerenes with higher molecular weight were demonstrated to have a significantly larger absorption and, in this view, a PCBM with a cage of 70 carbon atoms (PC$_{71}$BM) was developed and readily led to higher efficient solar cells. Indeed, despite its absorption is typically not very strong, it extends up to 750 nm. The use of fullerenes with higher molecular weight than PC$_{71}$BM did not contribute to further improvements to the device performance. For this reason, to expand the optical properties until the infrared region, the energy levels of PCBM need to be modified. In this perspective, new fullerene derivatives were developed. Particular interest was addressed to PCBM adducts as indene-C$_{60}$ bisadduct (ICBA, Figure 3.11), which revealed a LUMO level as high as -3.74 eV, resulting in photovoltaic devices with higher Voc.[91]

Besides the advent of ICBA, the typically difficult extension of the fullerene conjugation hinders a finely tuning of the frontiers energy levels.[92] Moreover, the synthetic procedures of fullerene derivatives result generally expensive (especially for PC$_{71}$BM) and, furthermore, their easy aggregation to form aggregates under heating typically affects the device stability.

For these reasons, much research efforts were devoted to the development of new electron acceptor materials and recently non-fullerene compounds have been effectively introduced. These new acceptors consist in small molecules[93] or polymers[94] (Figure 3.12), which offer the great advantage to be easily prepared. Moreover, their properties

can be tuned through fine structural modifications giving the opportunity to suitably modify both their electrical and optical characteristics, thus allowing for a possible contribution to the light harvesting and the photocurrent generation of relative solar cells.[95] Moreover, the possibility to tune the energy level positioning led to devices showing Voc > 1V and allowed the achievement of remarkable PCEs approaching 10%.[96] These results are particularly interesting if considering that the replacement of fullerene derivatives potentially reduces the formation of aggregates in the active layer during operating conditions and, accordingly, might enhance the lifetime of organic solar cells.

However, despite the attractive features of this class of materials, some issues need to be addressed. Non-fullerene acceptors are indeed characterized by a poor ability to form ordered domains in the BHJ active layer which represents an important limitation in terms of charge transport properties. As a result, a fine and meticulous morphological optimization is often required for an efficient operation of the BHJ blend.
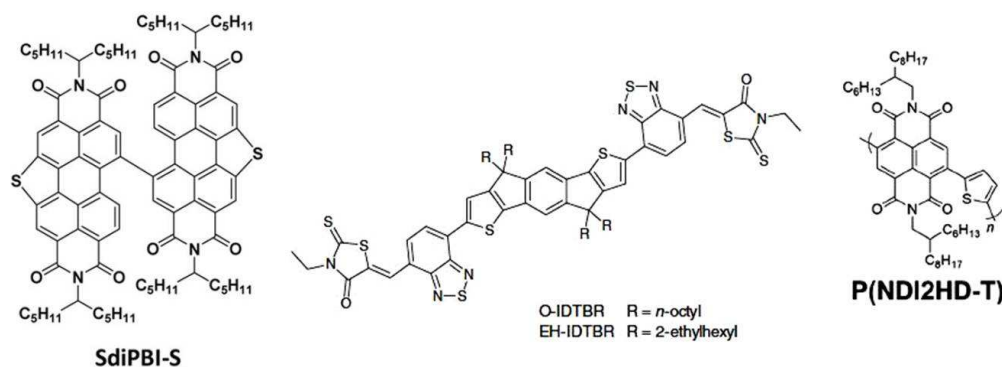
Figure 3.12. Molecular structure of some representative non fullerene acceptors.[97]

Despite the promising results of non-fullerene acceptors, PCBM still represents an effective and consolidated reference system for BHJ solar cells, which can offer room for further improvements. In this contest, a contribution to the search of methods to tune the energy levels of PCBM and to evaluate their effect on the OPV properties of corresponding devices is hereafter presented.

3.3.2 Tuning the electron-acceptor properties of [60]fullerene by tailored functionalization for application in bulk heterojunction solar cells

Researchers tried for long time to find a valid fullerene-based compound which would additionally benefit the device performance by delivering a high Voc. In sight of this, the introduction of different functionalizing groups on the carbon cage was attempted with the aim of raising the LUMO energy level. This was addressed by the development of polyadducts such as ICBA. However this approach is often detrimental for the electron mobility because of the increased molecular bulkiness. A second method could be the introduction of electron withdrawing or donating substituents on the fullerene cage. In this case, a fine balance in the number and dimension of the functional groups is required to optimize the device performance. Alternatively, aryl groups directly bound on the fullerene cage were demonstrated to induce an orbital shift with an effective change in the Voc of the relative solar cell.[98] Furthermore, the presence of electron-donating substituents as methoxy groups in ortho position of the aryl showed an influence on the fullerene orbitals by means of a through-space interaction.[99]

In this view, a series of 1,2-hydrofullerenes and 1,4-diaryl fullerenes were investigated (Figure 3.13).
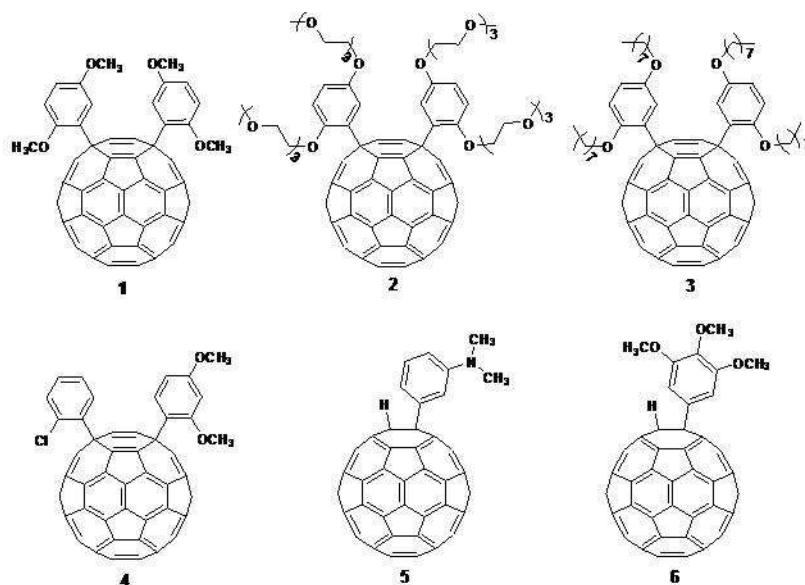
Figure 3.13. Molecular structure of the investigated 1,2-hydrofullerenes (5 and 6) and 1,4-diaryl fullerenes (1-4).

As shown in Figure 3.13, the structures 1-4 refer to 1,4-diaryl fullerenes with a cage of 60 carbon atoms. In particular, the compound 1 was substituted with two di-methoxy phenyl groups; the compounds 2 and 3 were similar to structure 1 but, to increase the solubility of the fullerene compound, the functionalizations on the aryl substituents were different; while, the compound 4 presented one di-methoxy phenyl substituent and one chlorophenyl group with the electron-withdrawing chlorine atom instead of the electron-donating methoxy groups which characterized the compounds 1-3. Structures 5 and 6 refer to 1,2-hydro fullerenes where the carbon spheres were functionalized with a single aromatic ring and an hydrogen atom which breaks the electron conjugation of the carbon cage. While the compound 5 presented, as substituting aromatic ring, a di-methyl amine phenyl group, the compound 6 was functionalized with a tri-methoxy phenyl group.

Electrochemical analyses (cyclic voltammetry) were carried on all the compounds to investigate their redox behavior and estimate the resulting energy levels. Indeed, the different nature, position and number of groups bound to the fullerene sphere were supposed to differently influence the energetic characteristics of the compounds. As reference system, $PC_{61}BM$ was used for all the measurements.

Table 3.4. LUMO energy values of fullerene derivatives in ACN/o-DCB 1:4 with Bu4NPF6 (0.1 M) or theoretically calculated.

Compound	E_{LUMO} (exp.) [eV]	E_{LUMO} (calc.) [eV]
PC$_{61}$BM	-4.20	-3.53
1	-4.15	-3.24
2	-4.13	-3.33
3	-4.11	-3.22
4	-4.17	-3.39
5	-4.18	-3.45
6	-4.19	-3.50

For all the derivatives, the LUMO energies resulted less negative than those of PC$_{61}$BM which indicate higher levels (Table 3.4). Despite a comparison is difficult for the different experimental conditions, the shift in the LUMO energies appears more pronounced in the 1,4- than 1,2- functionalizations. In addition, the results confirm that the methoxy group in ortho position of the phenyl substitution effectively influences the energy levels. The deviations in the correlation between theoretical and experimental values may result from specific solvent effects in some of the fullerene derivatives.

The behavior of these electron acceptors at the solid state and also in BHJ films using P3HT as electron donor was investigated using light induced electron paramagnetic resonance (LEPR) spectroscopy, time resolved EPR (TREPR) and Density Functional Theory (DFT) calculations. LEPR measurements showed the efficient photogeneration of radical anions from all the blends indicating that all the derivatives can be used in BHJ solar cells. The TREPR detection of short-lived photogenerated polaron pairs in P3HT:1,4-fullerene derivatives suggested a decreased binding energy of the initially generated charges favorable for a more rapid charge dissociation. For a more detailed analysis and discussion on the mentioned results please refer to ref. [100].

The promising characteristics of the fullerene derivatives allowed the investigation of their potential as acceptor materials in BHJ solar cells. P3HT was used as benchmark donor polymer in single junction standard architecture as described in Chapter 2. Because of the limited solubility of the compounds 1, 4, 5 and 6 [< 15 mg/mL^{-1} in o-DCB/chlorobenzene (CB) v/v = 1:1] it was not possible to prepare homogenous films with these derivatives. For this reason, only the photovoltaic performance of compounds 2 and 3 were tested. For comparison, BHJ solar cells based on P3HT:PC$_{61}$BM were used as reference system. Devices with the new compounds were fabricated following the

processing conditions used for the benchmark P3HT:PC$_{61}$BM blend (except the thickness and the total concentration of the initial BHJ solution) which were likely not the optimal processing parameters if considering the different properties of each fullerene. However, the optimization of the photovoltaic performance was beyond the aim of this work thus leaving room for improvements.

The devices based on the compound 3 showed a modest FF of 42% likely ascribed to a morphology which needs to be improved in terms of self-organization and phase segregation of the donor and acceptor materials in order to limit the bimolecular recombinations and maximize the charge transport properties of the BHJ (Figure 3.14 and Table 3.5). To minimize the deleterious effect of the sub-optimal morphology, relatively thin active layers were used ($\approx$ 170 nm instead of $\approx$ 300 nm of the reference P3HT:PC$_{61}$BM active layer) and, as a consequence, the devices showed a reduced Jsc of 5.6 mA/cm^2 ascribed to the limited harvesting capability of the active film. Interestingly, despite an average PCE of only 1.5%, the devices employing the compound 3 showed an improved Voc of 0.63V which resulted 70 mV higher than that of the reference system (0.56 V). This is consistent with the higher LUMO level of the fullerene derivative as compared to that of PCBM and pushes for further optimization and investigation of this class of acceptor materials.

In contrast, the use of compound 2, containing a triethylene glycol chain instead of an alkyl group, did not give any photovoltaic response. This is likely ascribed to the presence of long chains with hydrophilic character on the fullerene derivative which leads to poor nanoscale distribution of the active materials at the solid state. This correlates with some reports which highlight the role that the substitutions on the fullerene cage have on the physical parameters, precipitation kinetics, miscibility with the donor polymer and nanomorphology of the active blend.[101]
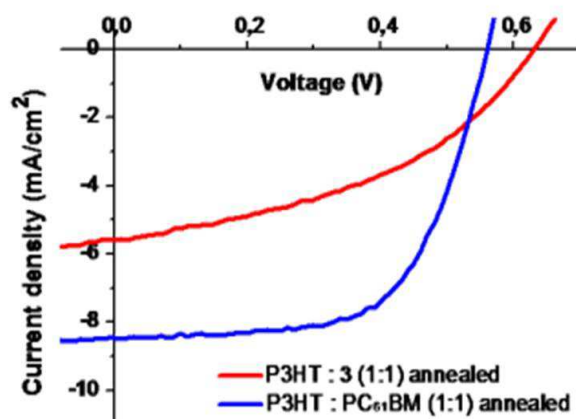
Figure 3.14. J - V plot, under standard illumination, of P3HT:3 and P3HT:PC$_{61}$BM BHJ solar cells.

Table 3.5. OPV characteristics, under standard illumination, of P3HT-based BHJ solar cells.

D:A ratio [wt/wt][a]	J$_{SC}$ [mA/cm^2]	V$_{OC}$ [V]	FF [%]	PCE [%]
P3HT : **2** (1:1) [b]	No photovoltaic response			
P3HT : **3** (1:1) [c]	5.6	0.63	42	1.5
P3HT : PC$_{61}$BM (1:1) [d]	8.5	0.56	63	3.0

[a] Annealed at 110°C for 10 minutes; [b] ~170 nm; [c] ~170 nm; [d] ~300 nm.

The absorption characteristics of P3HT:2 and P3HT:3 BHJs were investigated and compared to the P3HT:PC$_{61}$BM reference. As shown in Figure 3.15, the absorption profiles were similar for all the blends with the typical double peaked absorption band between 500 and 600 nm which is ascribed to π-π* transitions and a shoulder at around 600 nm arising from the inter-chain interactions. Despite there were not evident differences between the three systems, it is worthy to note that a lower absorbance at around 400 nm characterized the BHJs based on the new fullerene derivatives as compared to P3HT:PC$_{61}$BM. As this absorption feature is typically due to the absorption of PC$_{61}$BM, a reduced light harvesting in that region influenced the new fullerene compounds. This is likely one of the causes the reduced charge photogeneration in P3HT:3 based solar cells. However, the very low FF indicates that the main loss mechanisms arose from a sub-optimal morphology induced in the BHJ by the compound 3.
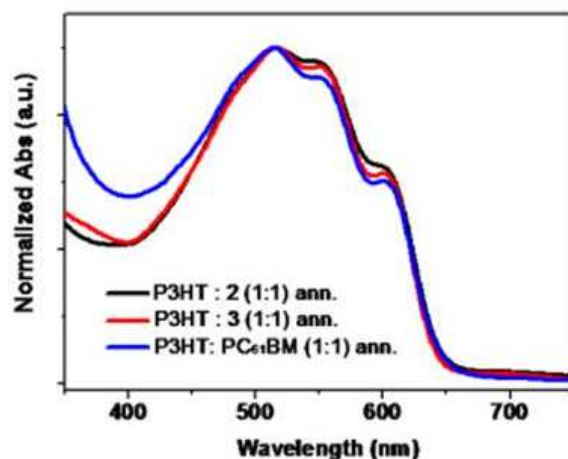
Figure 3.15. Absorption spectra of P3HT:2 (black line), P3HT:3 (red line) and P3HT:PC$_{61}$BM (blue line) BHJ films.

The surface morphology of the different active blends were investigated by AFM measurements. As shown in Figure 3.16c, the structured surface of the P3HT:3 film characterized by defined domains (RMS ≈ 16.5 nm) well correlates with the photovoltaic response of the relative device as similar features were present in the reference P3HT:PC$_{61}$BM surface (RMS ≈ 16.7 nm) (Figure 3.16a). This suggests a relatively good phase separation of the BHJ components with the formation of bicontinuous and organized percolation paths. According to the lack of photovoltaic response of the P3HT:2 solar cells, the relative topographic image (Figure 3.16b) showed a smooth and almost featureless surface with large and poorly defined domains (RMS ≈ 14.1 nm) which explain the inefficient BHJ morphology.
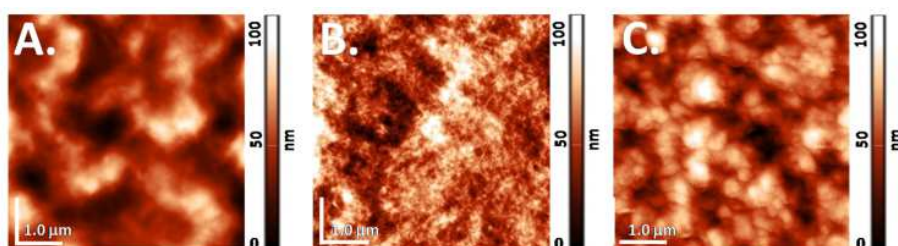
Figure 3.16. AFM images (5 µm x 5 µm) of BHJ film based on P3HT:PC$_{61}$BM (A), P3HT:2 (B) and P3HT:3 mixture (C).

The results clearly indicated that the lateral solubilizing chains on the fullerene are probably the main contributors to the morphology of the blends and play an important role, along with the electronic effects, to define the overall efficiencies of the BHJ solar cells. Accounting for the optimization process to be done, the interesting improvements in

the device V_{OC}, with respect to $PC_{61}BM$, using the fullerene derivative 3 represents a promising result towards the achievement of more performing organic solar cells.

3.4 Morphology control of the bulk heterojunction

Besides the chemical nature and the energy level positioning of the donor and acceptor materials, their distribution and organization at the solid state is of relevant importance for the performance of organic solar cells because of the intrinsic limitations in terms of excitons lifetime and charge transport. In this context, the BHJ concept aims to maximize the yield of exciton splitting through a fine intermixing of the donor and acceptor materials. However, a BHJ blend can be characterized by a multitude of possible combinations of pure or mixed domains of the electron donor and acceptor compounds with crystalline or amorphous phases (Figure 3.17). By analyzing the representative scenario reported in Figure 3.17, the possibility to have pure PCBM in contact with crystals of polymer (domain type 1) is minimal if considering well performing solar cells. In addition, since pure amorphous polymer phases at the interface with small molecules are thermodynamically not allowed, the domain types 2 and 3 are scarcely possible. As a result, the dominating phases in BHJ active layers are mixed domains with some amount of aggregates and crystals of polymer or PCBM (Figure 3.17, 4-6).[102]
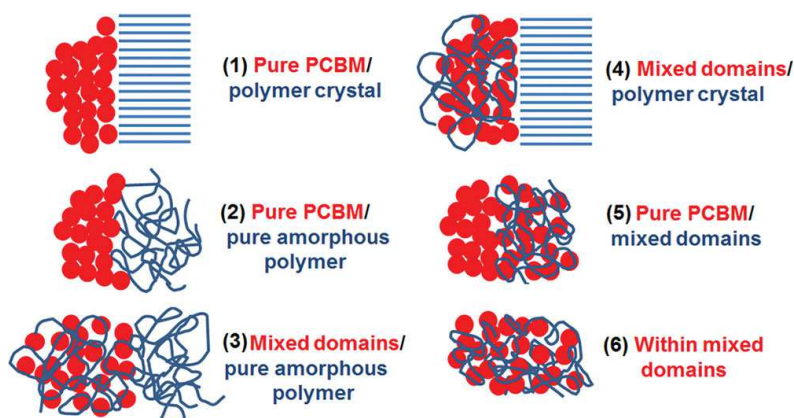
Figure 3.17. Possible domains and interfaces between polymer and PCBM in a BHJ blend. Reproduced with permission from Ref. [102].

Despite the BHJ concept appears characterized only by three possible types of domains/interfaces, variations in the film compositions of 10-20% are demonstrated to

affect charge mobilities by orders of magnitude and, as a consequence, favor bimolecular recombinations.[103] In addition, despite phases of electron donor polymer directly mixed with the electron acceptor are known to potentially suppress charge recombinations, an excess of mixed phases can reduce bicontinuous pathways likewise increasing bimolecular losses; on the opposite, crystalline phases are preferred to reduce the optical band gap for a better light harvesting as well as to improve the charge transport properties. These represent just few examples to demonstrate the key role of the BHJ composition/organization on the device operation. In sight of this, a fine control of the materials intermixing at the nanoscopic scale results necessary, and hence effective methods to manipulate the materials intermixing are of fundamental importance. Hereafter, some of the most relevant methods/strategies are discussed.

Role of the processing solvent

Typically, the electron donor and acceptor materials are dissolved in the same solution and then deposited to form the BHJ active layer. As the dissolution process is controlled by the interactions between the materials and the solvent, a solvent with suitable polarity is necessary. However, the solubility of each compound in the solvent is not only important for the initial solution but results also determinant for the BHJ formation. Indeed during the film formation, as the solvent evaporates, the materials start to precipitate and aggregate as a function of their solubility. In particular, the material with lower solubility starts to aggregate when the other is still dissolved, thus favoring the formation of separate domains. In sight of this, the dissolving solvent should provide similar solubility for both the components to ensure a suitable degree of phase separation. Nonetheless, the process of film forming is also dependent on the evaporation time of the solvent. A slow evaporation rate, typically favored by the use of high boiling solvents, prolongs the solid state formation. As a result, the materials remain longer in solution so to promote the maximization of the interactions and, in accordance, the reduction of the potential energy of the system. This could allow the π-π stacking of polymeric chains as well as the formation of bicontinuous phases.

On the contrary, the BHJ morphology can be kinetically frozen by accelerating the solvent evaporation. This limits the interaction time among and within the materials thus leading to a system with higher potential energy. As a result, the phase separation is typically limited with a consequent increase of the donor/acceptor interfaces.

This means that, on the basis of the chemical physical properties of the dissolving solvent, a fine balance between the kinetics and thermodynamics aspects involved during the drying process (film forming) can be achieved for a BHJ blend.

Use of processing solvent additives

A recent approach to further modulate the BHJ morphology consists in the use of solvent additives into the initial active solution. As previously discussed, the solvent used to dissolve the donor and acceptor materials typically possesses good solubility for both compounds. However, during film forming, the aggregation tendency of the two organic materials can differ determining a sub-optimal phase separation. The introduction of a solvent additive was demonstrated to optimize the thin-film quality. Note that the use of an additive is not generally effective for the performance of the resulting solar cells as it strongly depends on the nature of the BHJ components. Typically, the solvent additive possesses: *i)* a higher boiling point than the host solvent used for the solution and *ii)* a preferential solubility to one of the BHJ components (generally for the fullerene derivatives).[104] In sight of this, during solvent evaporation, the PCBM stays longer in solution because of the lower surface tension of the additive, which allows the polymer compound to crystallize. As a result, the BHJ is composed by a higher degree of phase separation, which favors the optical and charge transport properties of the active layer.[105] In other studies, where the two components of the BHJ showed a poor degree of phase intercalation, the use of solvent additives was demonstrated to increase the solubility of PCBM resulting in a better miscibility with the donor polymer. As a result, the formation of smaller D:A domains resulted in better performing solar cells due to the increased interfaces for the splitting of the excitons.[106] Among all the additives investigated for BHJ solar cell application, 1,8-diiodooctane (DIO), 1,8-octanedithiol (ODT) and 1-chloronaphtalene (CN) are the most employed.

Donor:Acceptor blend ratio

A fundamental parameter for the solar cell operation is the ratio (weight/weight) between the donor and acceptor materials. This indeed influences the size and distribution of the domains at the solid state thus affecting the operation of the BHJ. The optimal blend ratio is difficult to predict as several parameters such as the nature and molecular weight of the

polymer, the size of the fullerene acceptor as well as their aggregation tendency play a simultaneous role.

Concentration of the initial solution

The initial concentration of the BHJ solution is an important parameter for the active layer morphology since the kinetics of film forming depends on the interactions between the solvent and the compounds. Typically during the active layer processing, in relatively concentrated solutions, the solvent remains trapped inside the polymeric chains causing a slow drying of the deposited film. On the contrary, diluted solutions allow a faster evaporation of the solvent determining a rapid freezing of the BHJ morphology.[107] These should be considered as general considerations since the processing technique and parameters have a strong impact on the kinetics of film drying as well.

Recently, an additional impact of the initial solution concentration on the final BHJ morphology was reported. The aggregated state of the initial solution was demonstrated to partially entangle the polymeric chains and preserve a certain degree of organization after the film formation. This results from the lower degrees of freedom of the components that, with a reduced possibility of diffusion during drying, lead to more ordered BHJs.[108] In sight of this, a concentrated initial solution is preferred to increase the chains interaction. Then, without perturbing the solution, further solvent can be added to reach the optimal concentration for the film processing.

Role of the deposition techniques

A determining factor for the BHJ morphology is represented by the processing conditions of the BHJ solution. Several techniques and methods can be adopted to form a solid film and all of them require a meticulous optimization to obtain an efficient active layer. Among the most employed deposition techniques, the spin coating allows the formation of thin films by spreading, through centripetal acceleration, a relatively small amount of the initial solution over a small-sized substrate. The morphology of the final layer depends on the characteristics of the solution and on the spinning conditions such as the speed (rounds per minute, rpm), acceleration (rpm/s) and time. An alternative processing method, conceptually similar to roll-to-roll while developed for laboratory scale depositions, is the doctor blading. Here, the deposition process consists in the formation

of a meniscus of the initial BHJ solution between a moving blade and the substrate. As the blade passes over the entire substrate, the solvent evaporates forming the active layer. The film forming characteristics depend on the *i)* blade speed, *ii)* elongation of the meniscus, *iii)* amount and characteristics of the BHJ solution and *iv)* temperature of the hot plate over which the substrate is placed. Despite the multitude of parameters which simultaneously influence the film thickness and morphology, this technique results efficient in terms of film quality and hence device efficiency.

Further details on these deposition techniques are reported in Chapter 2.

Post-processing treatments

As the BHJ film is formed, the morphology and domain composition can be still tuned through post-processing methods.[109] Among them, the most employed consist of thermal treatment or solvent annealing over the solid layer. In particular, as part of the processing solvent remains inside the BHJ film after the deposition, by heating the sample, the small amount of solvent starts to evaporate allowing a partial re-organization of the materials at the solid state towards the maximization of the interactions. This typically results in the formation of partially crystalline domains especially in film previously amorphous. In this way, the optical properties as well as the charge transport are often improved through a better polymer packing, responsible for enhanced device performance. An alternative method is the use of solvent vapors over the BHJ film. This slows the drying process thus promoting the formation of continuous and homogeneous domains.

Several other post-processing methods have been developed over the years such as the solvent treatment of the BHJ surface. However, all the processes aim to obtain a suitable ordering of the donor and acceptor phases through a post modification of the kinetics and thermodynamics of film formation.

Chapter 4

Stability investigations on complete devices

4.1   General review of the principal degradation agents

The last decade showed the exponential evolution of organic photovoltaics. Through the development of novel materials, the optimization of the processing methods and a deeper understanding of the device physics, continuous improvements in terms of performance were achieved. Despite the efficiencies of organic solar cells went beyond the marketing threshold of 10%, relatively poor attention was devoted to the device reliability over time, which is of fundamental importance for the technological deployment. Economic assessments demonstrated that a module with a 7% PCE is competitive if a lifetime of 5 years is attained.[43] However, organic materials are by nature susceptible to ambient factors. As a consequence, many agents can induce physical chemical modifications in the device during operating conditions whereby causing detrimental effects on the device performance. In this context, the limiting factors for the solar cell lifetime are manifold, both intrinsic and external.[110]

As **intrinsic limitation**, the BHJ morphology is itself a representative example. Indeed, the morphology which ensures optimal device operation is generally not at thermodynamic equilibrium. The best compromise of the phases distribution in terms of charge transport, optical and electronic properties is typically not correspondent to the minimum potential energy of the system. As a result, the BHJ nano-domains can rearrange over time towards more stable but less efficient morphologies, which influence the device stability. Careful investigations on the evolution of the BHJ morphology allowed the understanding of some general causes of meta-stability. For instance, the use of high boiling solvent additives, if still present as residual traces in the active layer after device fabrication, might confers some degrees of freedom to the polymeric chains, which could partially reorganize over time. Similar processes occur in BHJs where the donor polymer has a glass transition temperature (Tg) below the operating temperature. The thermally-induced physical mobility of the polymeric chains can lead to modifications of

the domains composition during device operation thus limiting the performance of the corresponding devices.

These specific cases represent just few examples of degradation pathways, however manifold are the intrinsic mechanisms of degradation which can occur within the active layer. A general concept to stabilize the active blend is to reduce diffusion processes of the BHJ components *via* the physical stabilization of the morphology. This can be obtained for instance by: *i*) avoiding the presence of residual solvents after device processing, *ii*) increasing entanglements between polymer chains or *iii*) using cross linkable materials.

Except the BHJ, internal degradation can also occur from the diffusion of atoms or ions from the adjacent buffer layers or electrodes to the active layer. As the diffused species typically act as recombination centers for charge carriers, the functionality of the resulting solar cells is therefore affected. For instance, the use of water-processed layers as PEDOT:PSS can leave some residual traces of water in the layer, which can diffuse in the device or, at the same time, as a consequence of the acidic character of the PSS, can promote the diffusion of Indium atoms from the ITO electrode. This phenomena become negligible if a thermal annealing treatment is performed after PEDOT:PSS deposition. This highlights the importance of: *i*) the nature of the selected materials and *ii*) the optimization of the material processing in order to limit the migration of species into the active layer, thus preserving the initial device performance.

The investigation on the causes of the BHJ morphology dynamism and the diffusion mechanisms greatly contributed to limit the intrinsic degradation processes, enhancing the device lifetime.

Nonetheless, some **external factors** are also detrimental for the solar cell operation (Figure 4.1). Ambient agents as <u>oxygen</u> and <u>moisture</u> are the most common. The diffusion of oxygen or humidity at the electrode/active layer or electrode/buffer layer interfaces can oxidize the low work function electrode with the subsequent formation of an oxide layer, which represents an electrical barrier inside the device. Oxygen can also give rise to photo-oxidation processes of the active materials, which likely induce a modification of their optoelectronic properties or even allow the formation of new species, which act as recombination centers for charges. Similarly, the diffusion of humidity into the device can cause physical and chemical defects, thus reducing the photovoltaic performances of the solar cell.

To preserve the initial device operation, the use of an inverted device configuration where the low work function electrode is not exposed to external environment is a fruitful strategy to avoid oxidation processes. However, to limit the harmful effects caused by the external diffusion of oxygen and water, the most successful method is the encapsulation of the device. The solar cell is indeed laminated between two rigid (glass) or flexible (plastic) barriers sealed by specific epoxy resins. As a result, by a proper packing, the diffusion of external agents is demonstrated to be physically blocked thereby preserving the device performance over time.

Despite the great improvements by using encapsulating systems, BHJ devices are still susceptible to additional external factors including prolonged illumination and the subsequent solar heating. Light can cause polymer degradation such as chain scission, ring opening, cross links formation or, more generally, the modification/reduction of the π-delocalization along the polymer backbone.[111] In addition, light can be eventually harmful also for additional layers present in the BHJ device.[112]

On the contrary, heating is mainly a trigger for diffusive processes as migration of species from electrodes/interlayers or the morphological re-arrangement of the BHJ with the subsequent reduction of the device performance.

Diversely from other external agents, degradation mechanisms due to light exposure and heating cannot be eliminated as they represent the operational conditions for a photovoltaic device. Furthermore, as they are usually interlinked it is difficult to discern among them. In sight of this, the degradation pathway was rationalized in three general categories.[113] The first typically occurs in the initial 200 hours and mainly arises from light induced traps, which exponentially reduce the performance of about 20%. The second category accounts for a linear degradation over time and is the less known. While, the third mechanism comprises a thermal induced burn-in, which is characterized by an initial efficiency drop that stabilizes over time.

However, deeper analyses are necessary in order to predict and eventually improve the light and thermal stability of organic solar cells.

Despite the multitude of degradation factors (intrinsic and external), flexible devices can be also subjected to a mechanical stress as they can be repeatedly stretched, bent or twisted.[114] Here, efficiency losses mainly occur through the formation of cracks/fractures in some layers of the device or from decohesion/delamination between adjacent layers which cause the formation of defects at the interfaces. Moreover, the occurrence of similar processes in the encapsulation system facilitates the ingress of harmful agents

(*e.g.* oxygen and water) inside the solar cell. By enhancing the polymer entanglements, optimizing of the layer/layer adhesion and using of polymeric electrodes, great improvements can be obtained in terms of mechanical stability of flexible solar cells.

Figure 4.1. Representation of the main external harmful agents for organic solar cells.[114]

Since in a complete device a multitude of degradation processes simultaneously occur (Figure 4.1), to proper evaluate the effects arising from individual agents, the scientific community developed testing protocols where the device stability is classified on the basis of the degradation conditions applied.[115] The aim is to avoid inconsistency in the stability tests reported in literature thus allowing for a rational comparison among the different materials, device configurations and architectures employed. A summarizing overview of the different types of testing protocols proposed during the International Summit on OPV Stability (ISOS) is given in Figure 4.2.

As the unsolved issues mainly concern the degradation of organic solar cells arising from thermal stress and the prolonged illumination, a more detailed analysis is given hereafter through the discussion of scientific results.

Three levels

Basic (Level 1)	"Hand held" measurements using the simplest equipment and few conditions
Intermediate (Level 2)	Fixed conditions and protocols suited for most labs
Advanced (Level 3)	Standardized tests applied in certified labs. Extended range of parameters to monitor, etc.

Test type	Dark			Outdoor		
Test ID	ISOS-D-1 Shelf	ISOS-D-2 High temp. storage	ISOS-D-3 Damp heat	ISOS-O-1 Outdoor	ISOS-O-2 Outdoor	ISOS-O-3 Outdoor
Light source	None	None	None	Sunlight	Sunlight	Sunlight
Temp.[a]	Ambient	65/85 °C	65/85 °C	Ambient	Ambient	Ambient
Relative humidity (R.H.)[a]	Ambient	Ambient (low)	85%	Ambient	Ambient	Ambient
Environment[a]	Ambient	Oven	Env. chamber	Outdoor	Outdoor	Outdoor
Characterization light source	Solar simulator or sunlight	Solar simulator	Solar simulator	Solar simulator	Sunlight	Sunlight and solar simulator
Load[b]	Open circuit	Open circuit	Open circuit	MPP or open circuit	MPP or open circuit	MPP

Test type	Laboratory weathering testing			Thermal cycling		
Test ID	ISOS-L-1 Laboratory weathering	ISOS-L-2 Laboratory weathering	ISOS-L-3 Laboratory weathering	ISOS-T-1 Thermal cycling	ISOS-T-2 Thermal cycling	ISOS-T-3 Thermal cycling
Light source	Simulator	Simulator	Simulator	None	None	None
Temp.[a]	Ambient	65/85 °C	65/85 °C	Between room temp. and 65/85 °C	Between room temp. and 65/85 °C	−40 to +85 °C
Relative humidity (R.H.)[a]	Ambient	Ambient	Near 50%	Ambient	Ambient	Near 55%
Environment/setup	Light only	Light & Temp.	Light, Temp. and R.H.	Hot plate/oven	Oven/env. chamb.	Env. chamb.
Characterization light source	Solar simulator	Solar simulator	Solar simulator	Solar simulator or sunlight	Solar simulator	Solar simulator
Load[b]	MPP or open circuit	MPP or open circuit	MPP	Open circuit	Open circuit	Open circuit

Test type	Solar-thermal-humidity Cycling		
Test ID	ISOS-LT-1 solar-thermal cycling	ISOS-LT-2 solar-thermal-humidity cycling	ISOS-LT-3 solar-thermal-humidity-freeze cycling
Light source	Simulator	Simulator	Simulator
Temp.	Linear or step ramping between room temp. and 65 °C	Linear ramping between 5 and 65 °C	Linear ramping between −25 and 65 °C
Relative humidity (R.H.)	Monitored, uncontrolled	Monitored, controlled at 50% beyond 40 °C	Monitored, controlled at 50% beyond 40 °C
Environment/setup	Weathering chamber	Env. chamb. with sun simulation	Env. chamb. with sun simulation and freezing
Characterization light source	Solar simulator	Solar simulator	Solar simulator
Load[b]	MPP or open circuit	MPP or open circuit	MPP or open circuit

[a] The ambient conditions are defined as 23 °C/50%RH in general, and 27 °C/65%RH accepted in tropical countries according to ISO 291(2008): Plastics—Standard atmospheres for conditioning and testing.
[b] Open circuit refers to a simply disconnected device or device connected to a sourcemeter set to 0 current.

Figure 4.2. Overview of the different testing protocols proposed in ISOS. Reprinted from Ref. [115], Copyright 2011, with permission from Elsevier.

4.2 Thermal degradation

4.2.1 General overview

During outdoor applications, organic solar cells are subjected to thermal heating due to the intense illumination which results in temperatures estimated in the range of 65 - 85 °C. Despite the relatively high temperatures, organic materials are not expected to degrade as their degradation usually occurs at higher temperatures. However, a reduction of the device efficiency can arise from physical degradations of the BHJ.

As above mentioned, within the active layer the effects of physical modifications due to thermal heating are manifold: *i)* re-organization of the BHJ morphology, *ii)* formation of

aggregated domains of the fullerene derivatives or crystallization of the polymer, *iii)* segregation of the polymeric phase towards one electrode, *iv)* doping of the BHJ with diffusing species/ions from adjacent layers. In this context, the pathway of degradation depends on the interplay of thermodynamic[116] and kinetic factors.[117] While the thermodynamic derives from the nature of the materials, the kinetic depends on their distribution. According to that, both the components and the morphology of the BHJ are of extreme importance since determine the initial energy of the system and the activation energy barrier for physical modifications of the active layer.

Typically, if the Tg of the BHJ materials is below the operating temperature, some degrees of freedom are provided to the system, which can reorganize to some extent by following the thermodynamic pathway. This means that the phases re-distribute with a subsequent change in the polymer/fullerene interfaces and domains composition, which typically affect the photovoltaic efficiency. In sight of this, materials with high Tg are preferred for their use in the active layer of PSCs, even though the thermal behavior of an optimized BHJ blend is often more complex than that indicated from a sensitive parameter such as the measured Tg of a single/blended material.[118]

Concerning the kinetic processes in view of a thermally stable BHJ morphology, the activation energy needs to be higher than the thermal energy supplied to the system. This can be obtained by increasing the height of the energy barrier. In this approach, the degrees of freedom of the BHJ components can be limited by introducing physical constrains such as chemical cross-linking within the BHJ nano-domains, light induced PCBM oligomerization, the addition of fullerene dimmers, etc.. Other physical constrains include the chemical-physical interactions at the interfaces between the BHJ components and adjacent layers. For instance, the use of different substrates was demonstrated to strongly influence the thermal stability of the active layer because of the limited diffusion and aggregation of the fullerene derivatives and the reduction of the amount of nucleation centers.[119]

A kinetic alternative to the reported approaches is the obtainment of a BHJ morphology characterized by low potential energy and high photovoltaic efficiency at the same time. This is quite challenging because the minimization of the energy between the two BHJ components at the solid state (absolute minimum energy, point A in Figure 4.3) is detrimental in terms of photovoltaic performances as the two materials usually tend to form pure and separate phases, which result in poor device efficiency. Indeed, the most performing BHJ morphology typically differs from the most stable. However, by

exploring the potential energy surface of the BHJ, there is the possibility to find a local energy minimum which is sufficiently efficient in terms of light-to-charges conversion and that is surrounded by energy barriers high enough that the system results energetically trapped (Figure 4.3 – point C). This means that part of the maximum exploitable PCE (Figure 4.3 – point B) is sacrificed towards a better thermal stability.

In this sight, a meticulous tuning of the BHJ morphology is necessary to find an optimal initial position of the system over the whole potential energy surface. In this view, both the BHJ solution and the processing conditions are of extreme importance as they determine the resulting BHJ morphology. In the following section, a study on the BHJ tuning in view of thermal stable PSCs is provided.
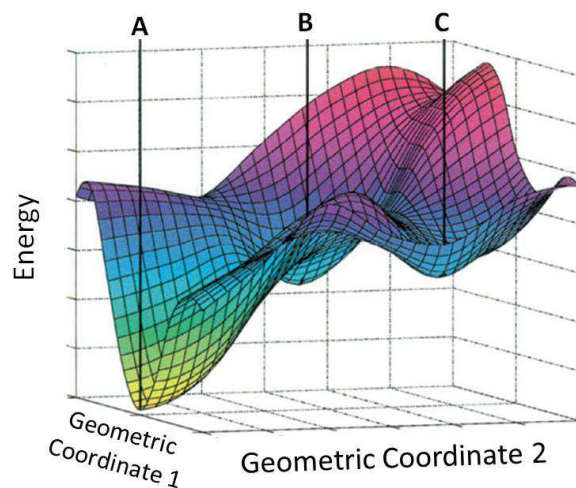
Figure 4.3. Schematic potential energy surface (PES) with two relative (B and C) and an absolute (A) minimum points. To note, this PES is only representative and does not depict a real BHJ PES.

4.2.2   Role of the processing solvent

Part of this paragraph is adapted from:

M. Bolognesi, M. Prosa, M. Tessarolo, G. Donati, S. Toffanin, M. Muccini, M. Seri, *Sol. Energy Mater. Sol. Cells* **2016**, *155*, 436, with permission from Elsevier.

Over the years, the best performing PSCs were obtained through a meticulous optimization of the BHJ materials intermixing *via* a fine modulation of the initial BHJ solution properties and the processing conditions. In this context, the choice of the solvent used to dissolve the active materials is of particular importance as it strongly determines the final nanoscale distribution.[120] The effect of the solvent on the device performance is

typically investigated for outcoming polymers in view of exploiting the maximum potential of the BHJ and, as a result, relevant breakthroughs in terms of device efficiency were obtained over the years. However, additional effects or benefits of this approach were scarcely investigated. For instance, poor attention was devoted to the effect of processing solvent on the thermal stability of PSCs.

In this sight, a mixture of a benchmark donor polymer (coded as HBG-1) and $PC_{61}BM$ was dissolved and processed from o-DCB or o-xylene with the aim to investigate not only the impact on the initial efficiency but also on the thermal stability of the resulting BHJ devices.[121]
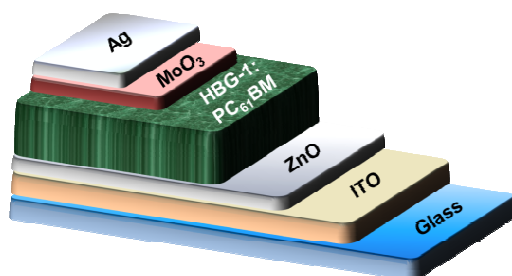
Figure 4.4. Schematic representation of the HBG-1:PC_{61}BM-based device.

As depicted in Figure 4.4, an inverted device configuration glass/ITO/ZnO/active layer/MoO_3/Ag was employed. The reproducible and scalable doctor blading deposition was used for the deposition of all the layers except the top contacts (MoO_3/Ag). The selection of the best processing conditions for HBG-1:PC_{61}BM was carried out using the following dissolving solvents: *i*) o-DCB, *ii*) o-DCB + 2.5% (v/v) of DIO, *iii*) o-xylene and *iv*) o-xylene +2.5% (v/v) of DIO. The relative devices were individually optimized in order to compare the best performing solar cells.

Table 4.1. Photovoltaic performance of optimized HBG-1:PC_{61}BM based solar cells processed from different solvents. The reported data are averaged over 5 different cells.

Donor:acceptor ratio [wt/wt]	Processing Solvent	DIO [v/v]	Thickness [nm]	V_{OC} [V]	J_{SC} [mA/cm^2]	FF [%]	PCE [%]
HBG-1:PC_{61}BM [1:2]	o-DCB	--	290	0.79	10.9	71	6.1
		2.5 %	290	0.72	10.1	59	4.3
	o-xylene	--	260	0.79	5.5	51	2.2
		2.5 %	260	0.78	11.7	68	6.2
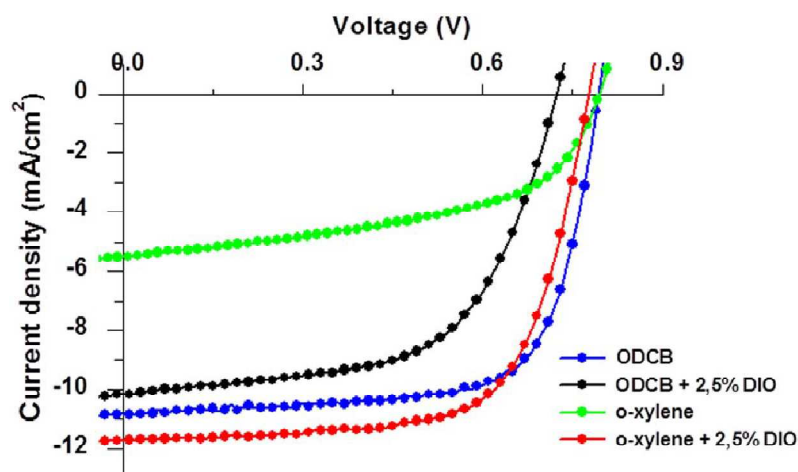
Figure 4.5. J - V plots measured under standard illumination, of HBG-1:PC$_{61}$BM based solar cells processed from o-DCB (blue), o-DCB + 2.5% DIO (black), o-xylene (green) or o-xylene + 2.5% DIO (red).

As summarized in Table 4.1 and Figure 4.5, the different solvents employed for the active layer deposition strongly influenced the photovoltaic response of the resulting devices. In particular, solar cells processed from o-DCB showed a remarkable PCE of 6.1% with Voc of 0.79V, Jsc of 10.9 mA/cm^2 and FF of 71%. The good Jsc and FF indicate a good self-organization and phase segregation of the BHJ components at the nanoscopic level which likely promote a good charge generation yield and charge transport within the active layer. In agreement to that, AFM topography revealed a regular surface characterized by fine and continuous nanostructures (Figure 4.6a) with a relatively low roughness (RMS = 1.8 nm).
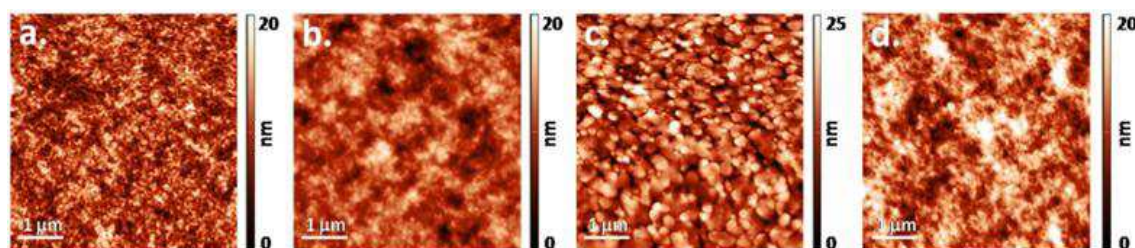
Figure 4.6. AFM images (size: 5 µm x 5 µm) of HBG-1:PC$_{61}$BM based solar cells processed from: a) o-DCB (RMS = 1.8 nm), b) o-DCB + 2.5% DIO (RMS = 2.8 nm), c) o-xylene (RMS = 5.1 nm) and d) o-xylene + 2.5% DIO (RMS = 2.9 nm).

The introduction of DIO to the o-DCB solvent resulted detrimental for the performance of the corresponding BHJ devices. Indeed, a reduction of the PCE from 6.1% to 4.3% was observed. This was mainly due to a drop of Voc from 0.79V to 0.72V and a consistent reduction of the FF from 71% to 59%. The self-organization of the BHJ blend was likely limited by the presence of DIO which induced the generation of relatively large and

poorly defined domains as suggested by the corresponding AFM image (Figure 4.6b). This well correlates with the reduction in the solar cell Voc and FF, both related to the phase-segregation of the active layer.

The electrical response of analogous BHJ cells processed from pure o-xylene showed a PCE of 2.2% with a Voc of 0.79 V, Jsc of 5.5 mA/cm^2 and FF of 51% (Table 4.1). These results could be related to the formation of a sub-optimal thin-film morphology as a possible consequence of the poorer solubility for fullerene derivatives, combined to the faster evaporation rate of o-xylene compared to o-DCB, which can determine a drastic phase segregation of the donor and acceptor materials in the cast film. This consideration is clearly supported by the corresponding AFM image (Figure 4.6c), which revealed the formation of regular unconnected grains, accompanied by a higher surface roughness. This kind of morphology is expected to result in inefficient exciton separation and lacks of the bicontinuous interpenetrating pathways necessary for the charge transport, in agreement with the relatively low Jsc and FF.

The introduction of DIO to the o-xylene based solution greatly enhanced the performance and the nanoscale morphology of the resulting HBG-1:PC$_{61}$BM film. The presence of the small amount of solvent additive likely enhanced the solubilization of the fullerene molecules and prolonged the drying time of the film, thus promoting an appropriate self-organization of the BHJ components. Figure 4.6d confirms the formation of fine nanustructures characterized by an optimal donor:acceptor intermizing and continuous domains, in agreement with the more than doubled photocurrent and PCE (6.2%) compared to cells processed from pure o-xylene.

Besides the evaluation of the initial photovoltaic response, the diversely processed solar cells were subjected to prolonged heat stress to investigate eventual effects of the processing solvent on the thermal stability of the resulting devices. As the cells differed only for the solvent used to process the active blend, eventual differences in the degradation could be ascribed exclusively to the processing solvent. The thermal stability was investigated only for the best performing devices, *i.e.* the solar cells processed from o-DCB (named device 1) and o-xylene + 2.5 (v/v) of DIO (named device 4). However, to understand the differences in terms of resistance to thermal stress, it is fundamental to first analyze the shelf life of the solar cells, in order to exclude eventual additional degradation pathways. In this sight, identical reference devices were left at room temperature (25°C) for 150 hours in inert atmosphere (glove-box).

As shown in Table 4.2, both the differently processed solar cells showed a similar drop in PCE of 5% which evidenced an optimal shelf-life of the devices. In sight of these results, eventual differences of the photovoltaic parameters after the thermal test can be ascribed exclusively to degradation processes induced by the heat stress.

Table 4.2. Photovoltaic responses of solar cells processed from o-DCB or o-xylene + 2.5% (v/v) of DIO, freshly prepared or stored for 150 hours at room temperature in inert atmosphere.

D:A ratio [wt/wt]	Proces. Solvent	Ageing T [°C]	Ageing time [hours]	J_{SC} [mA cm^{-2}]	V_{OC} [V]	FF [%]	PCE [%]
HBG-1: PC$_{61}$BM (1:2)	o-DCB	-	-	10.9	0.79	71	6.1
		25	150	10.8 (-1%)[a]	-0.78 (-1%)[a]	69 (-3%)[a]	5.8 (-5%)[a]
	o-xylene + DIO	-	-	11.7	0.78	68	6.2
		25	150	11.5 (-2%)[a]	-0.77 (-1%)[a]	67 (-1%)[a]	5.9 (-5%)[a]

[a] in brackets the loss percentages of the photovoltaic parameters relative to the corresponding parameters at time 0.

According to the ISOS-D-2 standard testing protocol (Figure 4.2), the solar cells were kept for 150 hours at 85°C in inert atmosphere (glove-box). Although the initial efficiency of devices 1 and 4 was comparable, they exhibited a different thermal stability (Table 4.3 and Figure 4.7). In particular, while device 1 showed a reduction in PCE of 49%, the PCE of device 4 dropped of only 19%. The reduced photovoltaic efficiency for device 1 included a drop in all the main parameters, FF (-28%), Jsc (-12%) and Voc (-19%). As evidenced by the shape of the J - V curves of device 1 (Figure 4.7), it is evident that the drop of FF and Voc after thermal ageing was mainly due to a consistent variation of the internal resistances within the active layer, which can be related to an increase of charge recombination processes resulting from a probable demixing of the BHJ components. On the contrary, device 4 showed only a limited drop in the photovoltaic efficiency after the thermal stress. All the photovoltaic parameters were slightly affected, however limited below 9% of difference than the initial values. This clearly demonstrates the improved resistance of device 4 to prolonged heating compared to device 1. As above mentioned, the two types of solar cells differed only for the processing solvent to deposit the active layer. Hence, despite the similar initial photovoltaic responses, the BHJ components likely presented different self-organization as cast, which suggests that the

potential energy surface was characterized by two points similarly efficient in terms of light-to-charge conversion but surrounded by different energy barriers.

Table 4.3. Photovoltaic responses of devices 1 and 4, freshly prepared (data from Table 4.1) and aged for 150 hours at 85°C in inert atmosphere. The reported data are averaged over 5 different cells.

OSCs (Processing solvent)	Aging conditions	V_{OC} [V]	J_{SC} [mA/cm^2]	FF [%]	PCE [%]
Device 1 (from o-DCB)	fresh	0.79	10.9	71	6.1
	aged	0.64 (-19%)[a]	9.6 (-12%)[a]	51 (-28%)[a]	3.1 (-49%)[a]
Device 4 (from o-xylene + DIO)	fresh	0.78	11.7	68	6.2
	aged	0.73 (-6%)[a]	10.9 (-7%)[a]	62 (-9%)[a]	5.0 (-19%)[a]

[a] in brackets the loss percentages of the photovoltaic parameters relative to the corresponding parameters at time 0 (fresh device).
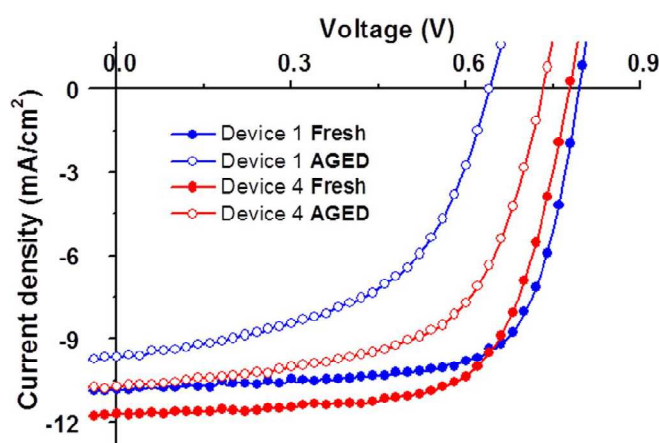
Figure 4.7. J-V plots of device 1 (blue) and device 4 (red), respectively processed from o-DCB and o-xylene + DIO, fresh (filled circles) and after ISOS-D-2 thermal stress (empty circles).

For a deeper investigation of the variations on the thermal stability of the described devices induced by the different processing solvents, the local micro and sub-micro morphology was investigated on fresh and aged solar cells through laser scanning confocal microscopy (LSCM) and laser scanning photocurrent microscopy (LSPM).

LSCM provides images of photoluminescence (PL) of the active blend. Despite most of the photoexcited states of the BHJ components are quenched due to electron transfer and charge generation processes typical of BHJ solar cells, some residual PL arising from unquenched photoexcited states of the donor or acceptor domains is still possible to collect. The lateral resolution of the images of photoluminescence is in the order of hundreds of nanometers (sub-micron) as it is strongly dependent on the laser wavelength

(488 nm). Detailed analysis on the physical nature of emitting species can be obtained through emission spectra at local point of the BHJ to distinguish between polymer- or fullerene-rich domains.

LSPM similarly exploits the advantages of a confocal microscope allowing to record images of local photocurrent. Indeed, it is an analogous of the laser-beam induced current (LBIC)[122] with the advantage of a higher resolution. While LSCM allows to visualize selectively the morphology of the active layer as the PL comes from the BHJ components, LSPM can be considered complementary to LSCM because includes the electrical contribution from all the layers of the solar cell. As a result, a map of the short circuit photocurrent is obtained and, if compared to the image of LSCM on the same area, the local photovoltaic response can be correlated to local features of the active layer or the contacts of the device. Further details are provided in Chapter 2.

As shown in Figure 4.8, the LSCM images of fresh device 1 (Figure 4.8a) and device 4 (Figure 4.8c), in the area outside the top metal electrode, exhibited almost featureless morphology at the instrumental resolution which indicates similar and optimal self-organization in accordance with the AFM images (Figures 4.6a and 4.6d, respectively) and the photovoltaic response reported above (Table 4.1). After the thermal stress, the morphology of the BHJ films in the area outside the top electrode drastically changed for both devices (Figures 4.8b and 4.8d) with the formation of large rod-like aggregates in the order of several micrometers even confirmed by AFM images on aged devices (Figures 4.8b2 and 4.8d2).

Figure 4.8. Left: Representation of the area of the device investigated. Right: LSCM images (size: 50 µm x 50 µm) in the area outside the top electrode of fresh device 1 (a), aged device 1 (b), fresh device 4 (c) and aged device 4 (d); AFM images (size: 20 µm x 20 µm) of aged device 1 (b2) and device 4 (d2) in the area outside the top electrode.

The LSCM images of aged devices 1 and 4 showed a homogeneous background, reflecting the initial blend morphology with well intermixed BHJ components, and the presence of bright aggregates with rod-like shape, which indicate a suppression of the charge separation in that region. In sight of this, PL spectra localized on the bright (spectrum A, black line) and background (spectrum B, orange line) regions of Figure 4.8b were registered (Figure 4.9a). As shown, the two spectra were characterized by similar spectral shape and differed only in terms of intensity. This means that they arose from the same emissive specie, which corresponds to the HBG-1 polymer as confirmed by the same spectral emission of the pristine HBG-1 (Figure 4.9a, red line). Moreover, PCBM emission cannot be detected as this specie scarcely absorbs at the employed excitation wavelength and because of the very low emission quantum yield. As a result, brighter regions are ascribed to polymer enriched domains while the darker background arises from a finely intermixing between the BHJ components. This reveals a consistent de-mixing of the donor and acceptor phases of the BHJs.
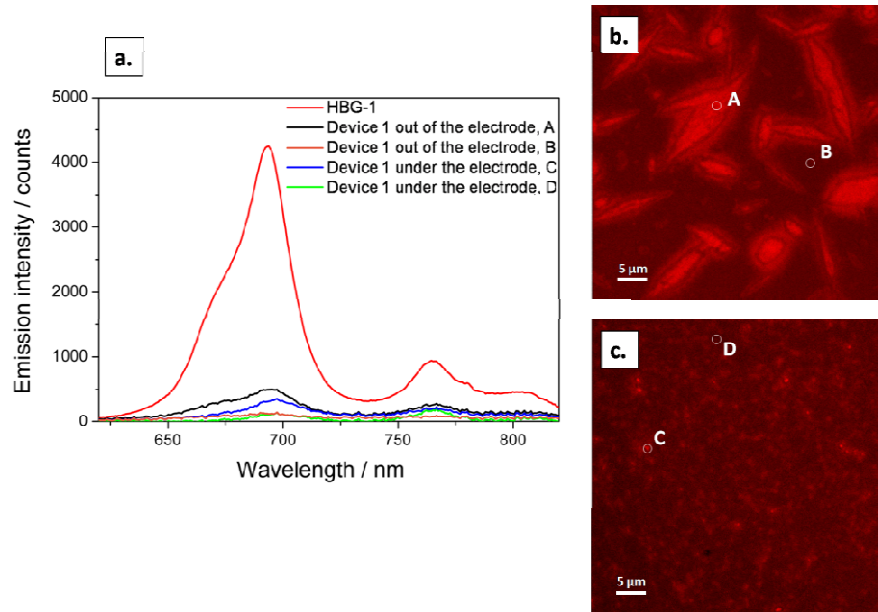
Figure 4.9. Localized emission spectra (a) measured on the bright and dark spots both outside (b) and under the top electrode (c). Regions A and C refer to brighter spots while regions B and D to darker spots of device 1. The emission spectrum of a film of pristine HBG-1 is reported as red line.

Despite aged device 4 showed similar micro-sized and rod-like features (Figures 4.8d and 4.8d2), the amount of aggregates appeared reduced if compared to aged device 1. It may be surprising that such drastic morphological changes occurring with thermal ageing do not correspond to drastically reduced OPV performances of the solar cells (Table 4.3). However, it is worthy to note that the presence of chemical-physical interactions at the BHJ/contact interface could stabilize the morphology of the active layer and influence the re-organization during aging through the "confinement effect". To clarify the real correlation between the micrometric morphological features with the drop of the photovoltaic response of the aged devices, LSCM images were similarly measured under the top electrode, which is the area leading to the photovoltaic response of the devices. Fresh device 1 (Figure 4.10a) and device 4 (Figure 4.10c) showed featureless LSCM maps according to the images taken outside the top electrode (Figures 4.8a and 4.8c). However, images of aged device 1 (Figure 4.10b) and device 4 (Figure 4.10d) under the top electrode resulted consistently different from the LSCM maps outside the top electrode (Figures 4.8b and 4.8d). The BHJ morphology of aged device 1 showed an inhomogeneous distribution of micro and sub-micro-sized bright aggregates which likely indicate a partial de-mixing process of the polymer and fullerene phases during thermal degradation. This is confirmed by the localized emission spectra (Figure 4.9a) measured

on bright (Figure 4.9c, point C) and dark (Figure 4.9c, point D) spots and is in agreement with the significant reduction of the device FF and Voc (Table 4.3).

Figure 4.10. Left: Representation of the area of the device investigated. Right: LSCM images (size: 50 µm x 50 µm) in the area under the top electrode of fresh device 1 (a), aged device 1 (b), fresh device 4 (c) and aged device 4 (d).

Concerning aged device 4, LSCM images under the top electrode (Figure 4.10d) resulted almost featureless with a morphology similar to the image measured on the fresh solar cell (Figure 4.10c). This fully correlates with the modest variation of the photovoltaic response of the device after thermal aging. Since a small reduction in the OPV parameters after the heat stress was observed (Table 4.3), a partial re-organization of the BHJ or eventual degradation at the interlayers or contacts is supposed to occur at the scale lower than the instrumental resolution.

It is worth mentioning the marked difference between the images, of both aged device 1 and 4, in the areas outside (Figures 4.8b and 4.8d) and under (Figures 4.10b and 4.10d) the top metal electrode. This evidences the fundamental role of the top electrode in stabilizing the BHJ sub-micro morphology. This phenomenon is due to the interactions at the BHJ/metal oxide/metal interfaces, which appear to be stronger than the de-mixing tendency of the BHJ components thus hindering the formation of the rod-like aggregates, which would be otherwise favored.

In order to shade light on the effect of the processing solvent on the stability of BHJ solar cells, LSPM maps of both freshly prepared and aged devices were measured as complementary characterization method to LSCM. As described above, LSPM allows to

directly correlate the local morphology of the active layer with the corresponding local photocurrent response of the device since LSPM includes the contribution in terms of photocurrent from all the layers. When compared to LSCM maps, it is possible to distinguish whether eventual features induced by the thermal stress arise from BHJ aggregation or from contacts degradation.

It should be noted that Laser Scanning photoVoltage Microscopy (LSVM) would have been more suitable for the analysis of the morphological changes in the devices after thermal stress. Indeed, the photovoltaic parameter which changed most during degradation was Voc (Table 4.3). However, LSPM and LSVM on the same area reported similar images while higher resolution was obtained in short circuit rather than in open circuit conditions, therefore LSPM was preferred.

According to the LSCM analysis under the top electrode (Figures 4.10a and 4.10c), the LSPM images of fresh device 1 and device 4 (Figures 4.11a and 4.11c, respectively) revealed a finely structured sub-micro morphology. In the case of device 1, the morphology evolved towards a much coarser one with phase segregated domains after thermal aging (Figures 4.11a and 4.11b) in accordance with what observed in the LSCM images recorded under the electrode (Figures 4.10a and 4.10b). On the contrary, device 4 preserved a finely structured morphology of the BHJ blend even after the thermal stress (Figure 4.11c and 4.11d), which well correlated with the LSCM analysis (Figure 4.10c and 4.10d).
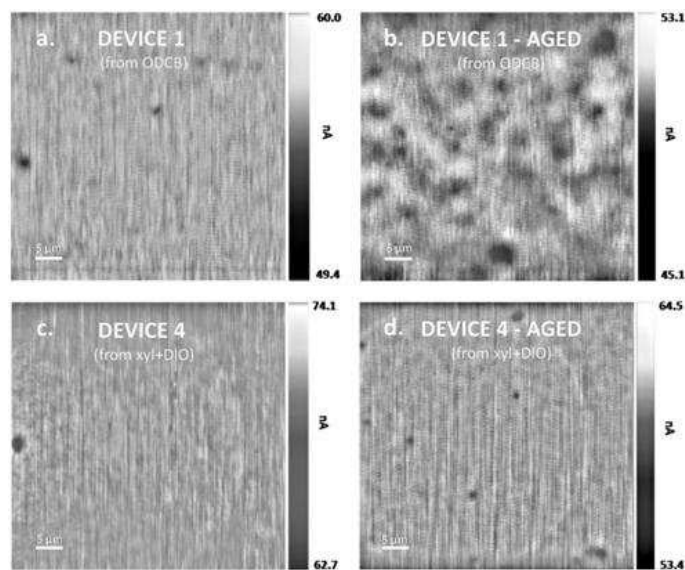
Figure 4.11. LSPM images (size: 50 µm x 50 µm) of fresh (a) and aged (c) device 1, fresh (b) and aged (d) device 4.

In view of understanding the role of the BHJ processing solvent on the thermal degradation of the corresponding devices, the comparison of LSCM and LSPM images (measured on the same area) in aged cells allows to distinguish between the thermally-induced features ascribed to the BHJ layer and those of buffer layer/electrodes. As previously discussed, the LSCM image of aged device 1 (Figure 4.10b) showed partially de-mixed phases with an inhomogeneous distribution of micrometric and sub-micrometric brighter aggregates corresponding to polymer rich domains of the BHJ layer. Figure 4.12a shows the same image where blue circles indicate those aggregates. The correspondent circles in the LSPM image (Figure 4.12b) comprise dark areas characterized by lower photocurrent. This confirms that the phase segregation process of the BHJ blend occurring with the thermal ageing is responsible for the observed lowered photovoltaic performance of the device as a consequence of polymer aggregates which limit the charge formation process in that region. In addition to the BHJ blend reorganization, the thermal stress partially affected the buffer layer/electrodes as revealed by the presence of micro-sized spots with low photocurrent, evidenced by the red arrows in Figure 4.12b, which do not have correspondent features in the LSCM image (Figure 4.12a). A similar degradation ascribed to the contacts was reported in the case of device 4 where little spots, highlighted by the red arrows, were present only in LSPM images (Figure 4.12d) thus confirming the effect of prolonged thermal stress on the device contacts. On the contrary, the BHJ appeared featureless both in LSCM and LSPM maps (Figures 4.12c and 4.12d) in accordance to the modest reduction of the photovoltaic performance of device 4 after thermal aging (Table 4.3). Only one micro-sized spot is showed inside the blue circle (Figure 4.12c and 4.12d), which reveals a defect likely occurring during the BHJ film processing.
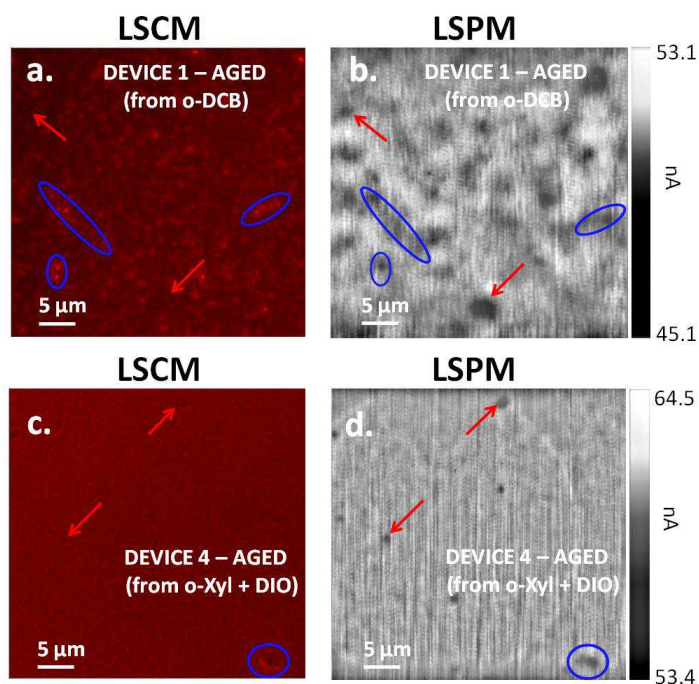
Figure 4.12. LSCM and LSPM images of aged device 1 (a and b, respectively) and device 4 (c and d, respectively). The red arrows indicate contact defects while blue circles highlight defects in the BHJ layer. This image is only a reproduction of Figures 4.10b, 4.10d, 4.11b and 4.11d.

These techniques demonstrate the possibility to directly correlate the photovoltaic performance with the local morphological changes in organic solar cells. Importantly, they allow to visualize the evolution of the morphology with thermal stress thus evidencing the effect of the processing solvent on the morphology of the BHJ. It is worth to note that, because of the complementarities between LSCM and LSPM, it is possible to discern the effects of thermal stress on the morphology of the BHJ and on the eventual degradation of the contacts, effect that is not correlated to the processing solvent of the active layer. Furthermore, a great advantage of laser scanning microscopy over other characterization techniques consists in the possibility to study working devices and investigate crucial areas unlike accessible (*e.g.* under the top electrode).

In conclusion, concerning the BHJ processing, the o-xylene was here demonstrated an effective solvent to obtain a thermally stable morphology of the active layer without sacrificing the photovoltaic performance of the corresponding BHJ solar cells.

In general, the use of solvents with different chemical-physical properties than the common chlorinated ones can represent a powerful method to further explore the potential energy surface of the BHJ towards stable and highly performing PSCs.

4.3 Light degradation

4.3.1 General overview

Despite the presence of light is a key factor for the operation of organic solar cells, it represents one of the main triggers for device degradation. Indeed, organic compounds are susceptible to prolonged illumination, which can result in chemical and physical degradation of the active layer, buffer layers or interfaces. In sight of this, the active layer represents the part of the solar cell most susceptible to photo-degradation processes.

In this context, the presence of oxygen plays a crucial role in the photo-stability of the device as a plethora of oxygen dependent photo-reactions can take place. Nonetheless, degradation processes might occur even in total absence of oxygen through photolysis processes, which involve chemical structure modifications.

Concerning the **donor polymer**, the molecular structure can be subjected to rearrangements, chain scissions, cross-linking or photo-oxidation reactions, which determine the reduction of the device performance.[123][124] In detail, the modification of the chemical structure through scission of the polymer chains affects the light-absorption of the material as, by interrupting the π-conjugation, the energy gap is raised while the extinction coefficient is lowered.[70] As a consequence, a smaller amount of excitons is generated in the active layer. In addition, the presence of new species leads to the formation of sub band-gap levels which can generate trap-state recombinations in the active layer or energetic disorder with influences on the charge mobility and built-in potential. Furthermore, the modification of the energy levels influences the energetic alignment among the different materials with possible limitations in terms of device operation.[114] These processes of degradation are strongly dependent on the polymer structure. As reported by Manceau *et al.*, the differences in the chemical structure and, more precisely, in the backbone side chains causes, for instance, lower photo-stability of MDMO-PPV if compared to P3HT.[125]

It is worthy to note that the photo-degradation processes occurring in inert environment are notably slow as evidenced by the 10000 hours of illumination furnished to P3HT to observe a reduction of 20% of the absorbance. On the contrary, the presence of oxygen during illumination has a detrimental effect as it accelerates and introduces additional degradation processes. The stability of P3HT is considerably reduced and the oxidation of

the side-chains starts a radical reaction which induces the photobleaching of the polymer. Figure 4.13a reports the degradation mechanism of P3HT where the abstraction of the allylic hydrogen is followed by a photo-oxidation reaction of the side-chain. This stepwise radical processes end up in compounds with a higher oxidation state. The occurrence of radical reactions is strongly dependent on the stabilization of the radical specie and, depending on the nature of the polymer, other photo-degradation mechanisms can become predominant. In this context, reactions proceeding via sensitized pathways through the highly reactive singlet oxygen similarly represent major mechanisms of light-induced degradation. Here, the photo-excited polymer leads to the formation of superoxide radical anions ($O_2^{\bullet-}$) or singlet oxygen ($^1O_2$), which cause oxidation processes. Which of the two pathways of reaction is predominant is difficult to predict. It depends on the degradation conditions, the characteristics of the polymer and its physical state. For instance, the degradation mechanism of P3HT in solution involves singlet oxygen while thin films of P3HT are subjected to chain radical oxidation processes.

In this context, the presence of **fullerene** is relevant as it can sensitize the production of reactive oxygen species thus contributing to the oxidation processes (Figure 4.13b). Despite several stability studies focused on films of pristine polymer, it is worthy to note that the contribution from the aggregation state and the presence of the electron acceptor material in the BHJ is not negligible. According to the degradation mechanism of polymer via oxygen reactive species, photo-excited fullerenes are similarly able to transfer energy or electrons to molecular oxygen to form reactive species.[126] This increases the probability of formation of harmful compounds, which elucidate the reason of the still limited stability of BHJ solar cells.
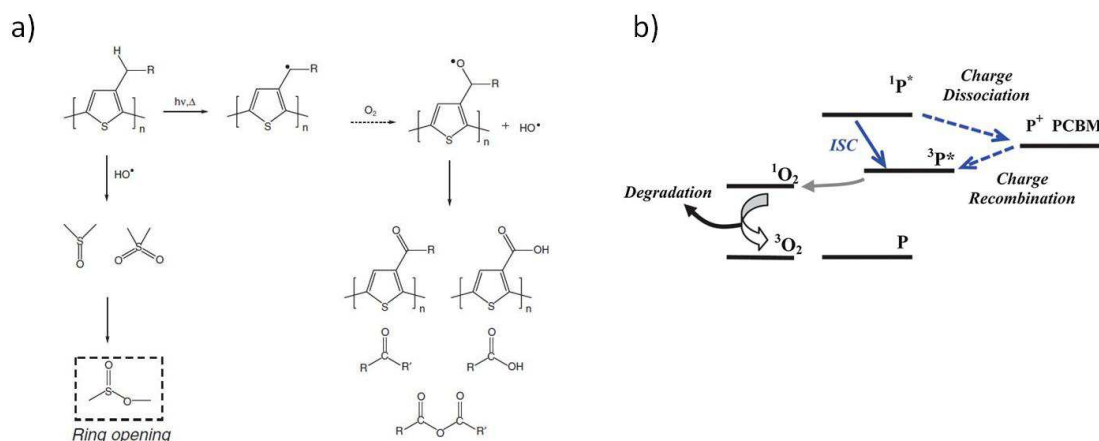
Figure 4.13. a) Radical photo-oxidation mechanism of P3HT;[127] reprinted from Ref. [128] with permission from Elsevier; b) Singlet oxygen formation mechanism in film of pristine polymer (blue solid arrows) and in BHJ (blue dashed arrows). Adapted from Ref. [129] with permission of The Royal Society of Chemistry.

Furthermore, fullerene derivatives can be object of photo-dimerization processes, which are reported to be the responsible for the "burn in" loss of device efficiency in the first part of the degradation pathway. Despite the mechanism of dimers formation is not clarified yet, Heumueller *et at.*[130] demonstrated the dependence of the Jsc drop during light illumination to the formation of fullerene dimers. In this context, the BHJ morphology is crucial as it determines the proximity of fullerene species and hence their probability to react. Nevertheless, the presence of fullerene in the BHJ revealed also some beneficial effects to the device stability. Inside the BHJ, fullerene acts as: *i)* light screener towards polymer thus reducing the amount of incoming UV photons; *ii)* radical scavenger, which suppresses the harmful radical species; *iii)* beneficial agent to limit the formation of fullerene aggregates upon heating as the presence of dimers revealed to prevent their formation.

The dual role of fullerene in stabilizing/destabilizing the BHJ and the variety of possible degradation mechanisms highlight the complexity of this type of studies and confirms the importance of the nature and morphology of the BHJ active layer.

In this context, the presence of some residual **solvent additive** in the active layer represents another possible source of degradation. Solvent additives are typically used to improve the BHJ morphology and hence the device performance. As previously discussed, they are characterized by a relatively high boiling point which prolong the drying time primarily of the fullerene derivative. However, this might leave some residual solvent additive in the active film which, due to the presence of the top electrode, remains trapped inside the device. Despite the detrimental effect in terms of device lifetime

previously mentioned, the presence of residual additive might have detrimental impact also in terms of light stability. Indeed, the use of additives such as DIO, which is characterized by the presence of the light-labile halogen-carbon bond,[131] leads to the formation of radical species which can react with the polymer and the fullerene thus affecting the device operation.[132] The presence of DIO was demonstrated to be removed by thermal or vacuum treatments of the active film before the deposition of a capping layer.[133] However, the effect of DIO on polymers, which are intrinsically not very stable like the class of the PTB7 derivatives, was found to be particularly detrimental as it contributes to the degradation of the active film even without a top layer.[134]

This demonstrates that the chemical structure of the polymer has a relevant role in determining the stability of the BHJ under prolonged irradiation. In sight of this, some general design rules were developed in order to avoid the use of light-sensitive chemical groups. While aromatic polycyclic groups are suggested for the backbone because of their good photostability, the use of *i*) exocyclic double bonds in the main backbone, *ii*) functional groups containing quaternary sites, *iii*) cleavable bonds such as C-N or C-O, should be avoided because destabilize the active layer. Concerning the side-chains, CO_2R, OR and H are progressively considered more light-stable.[135]

Despite the relevant role of the nature, morphology and composition of the BHJ on the stability of solar cells under prolonged light stress, other parts of the device need to be carefully considered in this context. The investigation of the active layer/electrode interface revealed the important effect of the **interlayers** on the device stability. In detail, Williams *et al.*[136] showed that the direct contact of the electrode with the active layer results in a pronounced degradation of the relative device when compared to similar cells endowed with electrode interlayers. This highlights the role of buffer layers in the device stability and evidences the complexity of the degradation processes occurring in organic solar cells.

During the PhD project, a contribution to the comprehension of the light stability of push-pull polymers and ZnO derivatives used in PSCs was provided and hereafter discussed.

4.3.2 Light stability of photoactive materials

The chemical and physical stability of the BHJ active layer is one of the most critical aspects. Despite the advantages in the use of polymers are manifold, one of the major issues associated with their application concerns their vulnerability under operation conditions.

In this context, several studies focused the attention on the stability of various donor polymers under prolonged illumination. In most of them, the UV-visible photo-bleaching is monitored, under ambient conditions, as a function of the degradation time. However, the degradation processes which change the polymer properties are significantly fastened in air. Moreover, further light-induced processes occur in presence of oxygen.[125] As previously described, the polymer stability and the rate of degradation are strongly dependent on the structural properties of the material. For instance, the number, size and nature of the polymer side chains, which are fundamental to tune properties such as solubility, processability, energy levels, structural conformation and physical-chemical interactions, have crucial role for the polymer photo-stability. To generate knowledge and guidelines in view of designing stable chemical structures, the effect of side chain manipulation on the prolonged illumination stability of the relative polymers was investigated and then correlated with the photovoltaic performance and lifetime of the corresponding BHJ solar cells. In detail, during the PhD program, a specific study on a series of polymers based on a quinoxaline (FQ) acceptor unit combined with differently substituted benzodithiophene (BDT) or an unsubstituted thieno[3,2-b]thiophene (TT) (Figure 4.14) was carried out.[137] The polymers were compared in terms of optical, electrochemical and photovoltaic properties in order to investigate the impact of the structural modifications on the photo-stability of the resulting pristine or blended films.
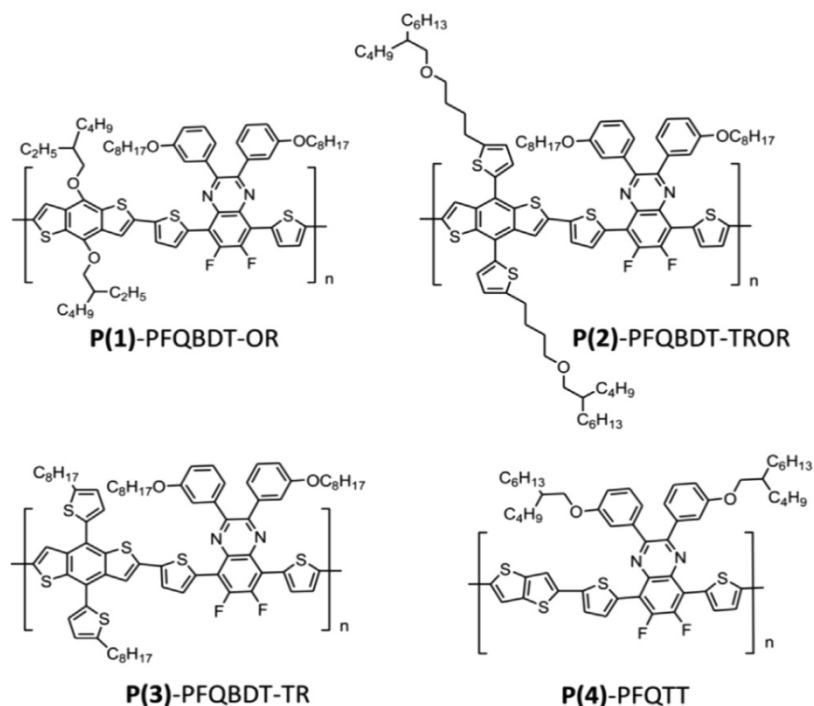
Figure 4.14. Chemical structures of P(1), P(2), P(3) and P(4).

The first polymer PFQBDT-OR (named P(1)) was based on the BDT unit functionalized with electron-donating alkoxy groups (2-ethylexyloxy) which were replaced in PFQBDT-TROR (named P(2)) with alkyl-oxy-alkyl substituted thiophene (2-butyloctyloxybutyl-thiophene) side chains (2D conjugated polymer). PFQBDT-TR was characterized by a linear octyl-substituted thiophenes (named P(3)) while in the last polymer (PFQTT, named P(4)) the BDT unit was replaced by an alternative unsubstituted thieno[3,2-b]thiophene (TT) co-monomer. The synthesis of P(3) is described in a previous work[83], while the synthetic routes and detail on the characteristics of P(1), P(2) and P(4) are reported in the reference [137].

The purified polymers exhibited comparable molar masses (Table 4.4) and good solubility in the organic solvents typically used for device fabrication (> 15 mg/mL in o-DCB) due to the presence of suitable side chains linked to the polymer backbone. To note, in P(4) the phenyl rings linked to the quinoxaline moiety were on purpose functionalized with branched alkoxy side chains, instead of linear octyloxy chains, to compensate the reduction in solubility induced by the use of unsubstituted TT group.

Figure 4.15 shows the optical absorption spectra of the pristine polymers P(1)-P(4) in dilute chloroform solution (Figure 4.15a) and thin films (Figure 4.15b). They all exhibited a higher energy absorption band between 380 and 480 nm, assigned to localized π-π* transitions, and a lower energy band between 500 and 700 nm (up to ≈ 750 nm for P(4))

arising from the inter-molecular interactions between the polymer chains and from intra-molecular charge-transfer-like interactions between the electron rich (BDT or TT) and the electron poor (FQ) moieties.[138] While for P(4) the vibrational structure of the low energy band was well resolved showing two peaks at ≈ 630 nm and ≈ 670 nm respectively, for the other polymers the two peaks were not discernible. The different position of the absorption bands for all the polymers, both in solution and at the solid state, arose from the different chemical structures of the polymers. For instance, the replacement of the alkoxy chains of the BDT unit (P(1)) with thiophene-based side groups (P(2) and P(3)) extends the π-conjugation resulting in a red-shifted absorption profile. As expected, the increase of the donor-acceptor behavior of the polymer through the use of the electron richer TT unit (P(4)) instead of BDT (P(1)-P(3)) led to a further red-shift (≈50 nm) of the absorption spectrum.

By comparing the solution and solid state spectra for each polymer, the similar features and the 10-20 nm of red-shift in the onset of the thin film spectra suggested a partial aggregation of the polymer chains at the solid state. The onset values of the thin film absorptions were used to estimate the optical band gap of the polymers (Table 4.4).

The blue-shift of the maximum of absorption for P(1)-P(3) when passing from solution to solid state (Table 4.4) arose from the inversion of the relative intensities of the two vibrational transitions of the low energy band. While in solution the most intense peak of the vibrational structure was the lower energy one, at the solid state the most intense was that at higher energy (Figure 4.15).

Table 4.4. Molecular weights, optical and electrochemical properties of polymers P(1)-P(4).

Polymer	M_n^a [kDa]	M_w^a [kDa]	Solution		Thin-film		E_{gap}^b [eV]	E_{HOMO} [eV]	E_{LUMO} [eV]
			λ_{MAX} [nm]	λ_{ONSET} [nm]	λ_{MAX} [nm]	λ_{ONSET} [nm]			
P(1)	32	82	602	693	595	702	1.77	-5.74	-3.50
P(2)	24	54	622	705	607	720	1.72	-5.84	-3.56
P(3)	37	133	614	710	610	726	1.71	-5.89	-3.61
P(4)	19	53	629, 669	740	629, 676	750	1.65	-5.64	-3.45

a) in brackets the loss percentages of the photovoltaic parameters relative to the corresponding parameters at time 0 (fresh device); b) Optical $E_{gap} = 1240/\lambda_{ONSET}$.
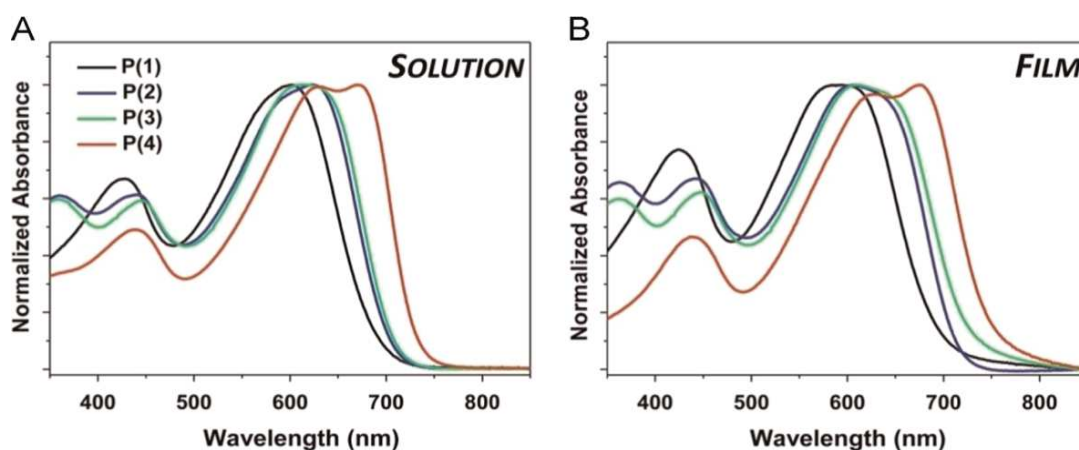
Figure 4.15. Normalized UV-vis absorption spectra of pristine polymers in dilute chloroform solution (a) and thin films (b) deposited on glass from chloroform solution (thickness ≈ 80 nm).

As shown in Table 4.4, P(2) and P(3) were characterized by similar HOMO and LUMO energies (estimated by SWV)[137] while the analogous P(1) presented a slightly higher HOMO which arose from the more electron donating effect of the alkoxy chain bond to the BDT unit. Similarly, the electron rich TT of the P(4) raised both the HOMO and the LUMO compared to the other polymers and resulted in a smaller energy gap. This is in agreement with other studies as the reduction of the band gap is a consequence of the increased push-pull character of the chemical structure.[139] Interestingly, all the P(1)-P(4) polymers showed relatively deep HOMO levels which favor high values of device Voc according to the energy difference $LUMO_A – HOMO_D$ and are in the ideal range to ensure a good air-stability.[140]

To note, the electrochemical band gaps resulted larger than the corresponding optical gaps. This arises from the differences in the measurements.[89] Indeed, after light absorption, excitons are formed in conjugated polymers. On the contrary, ionized states are created during electrochemical measurements. Moreover, this latter measurement is subjected to interface barrier at the polymeric film/electrode which might influence the measurement. Finally, the nanomorphology and the resulting energetic distribution of the states is strongly dependent on the processing conditions and hence a film prepared over the electrode or over a flat substrate could significantly differ.

The photochemical stability of P(1)-P(4) polymers was investigated by depositing films of neat polymer on glass substrates and then keeping them under standard light illumination in air.

Figure 4.16 shows the evolution of the UV-vis absorption profiles of P(1)-P(4) as a function of the irradiation time. The general tendency was similar for all polymers, with

the magnitude of the peaks decreasing over time (photo-bleaching). Despite the different rate of the photo-bleaching as a function of the polymer structure, it was evident that, concerning the low energy band transition, the absorption of the low-energy peak decreased, for all the polymeric films, faster than the higher energy one during illumination. This resulted in a change of the absorption profiles which was ascribed to a reduction of the π-conjugation length as a result of saturation/opening of the π-conjugated units or chain scission reactions caused by photo-induced oxidation of the polymers. To evaluate the photodegradation of P(1)-P(4), the evolution of the absorption profiles was monitored for 72 hours by focusing on the reduction over time of the peak at higher energy of the low-energy absorption band (Figure 4.16).
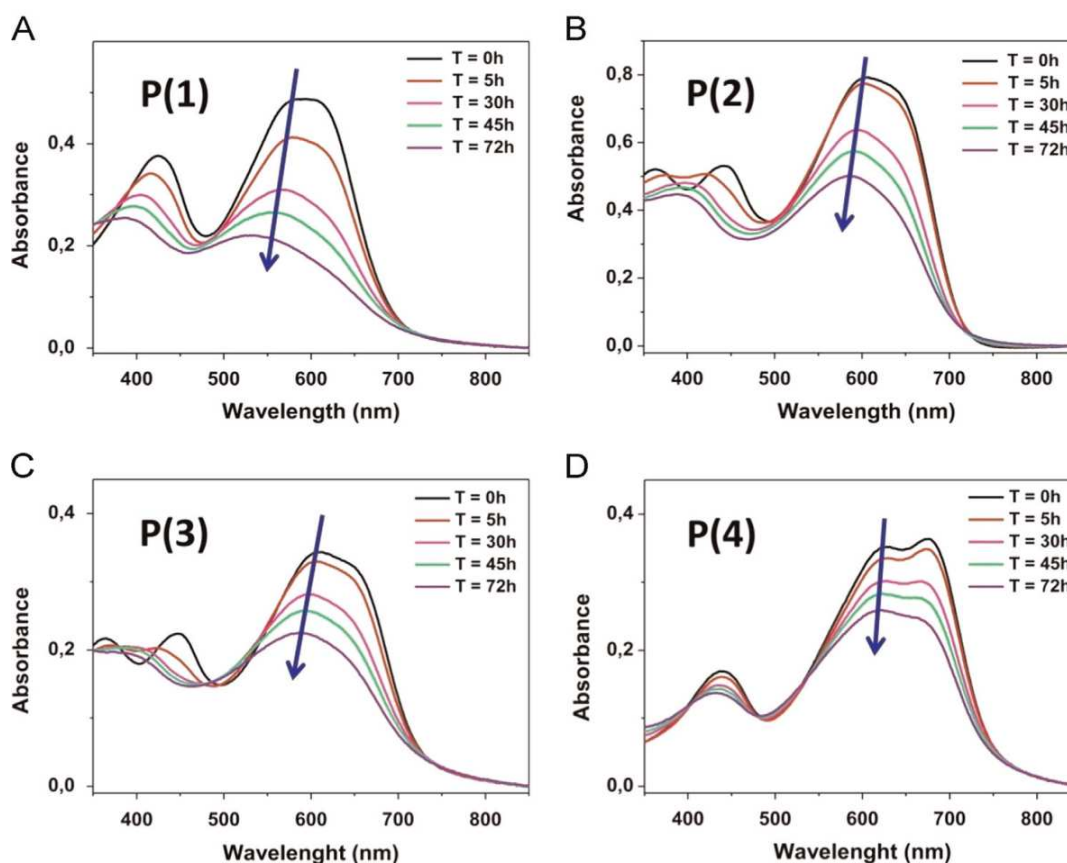
Figure 4.16. UV-vis absorption spectra of P(1)-P(4) neat polymeric films (from chloroform, thickness ≈ 80 nm) measured over time (up to 72 hours) during 1 Sun light illumination in air. The blue arrows indicate the absorption peak taken as reference for the absorption decay of each polymeric film.

The remaining absorption peak intensity (Rm_{ABS}) as a function of the ageing time was used to quantify the photodegradation of the polymeric films. Rm_{ABS} was calculated using the equation:

$$Rm_{ABS} (\%) = \frac{A_{max}(t)}{A_{max}(t_0)} \times 100 \qquad\qquad 4.1$$

where $A_{MAX}(t)$ is the residual absorbance after a specific time t (5, 30, 45 and 72 hours) extrapolated from the UV-vis spectra in Figure 4.16, while $A_{MAX}(t_0)$ is the initial absorbance of the freshly processed film.

Figure 4.17 reports the trend of Rm_{ABS} for all the neat polymer films over irradiation time.

While P(2), P(3) and P(4) showed similar degradation rate resulting in a final value of absorbance close to 60% of the initial intensity, P(1) presented a faster photo-bleaching since after 5 hours of illumination a drop of about 15% of the initial intensity was reported. Then, the trend was similar to the others and finally reaching a value of 45% of the initial intensity. This indicated the poor photo-stability of P(1) in these conditions if compared to P(2), P(3) and P(4) which resulted in higher final Rm_{ABS} values after 72 hours, respectively 63%, 65% and 73%.
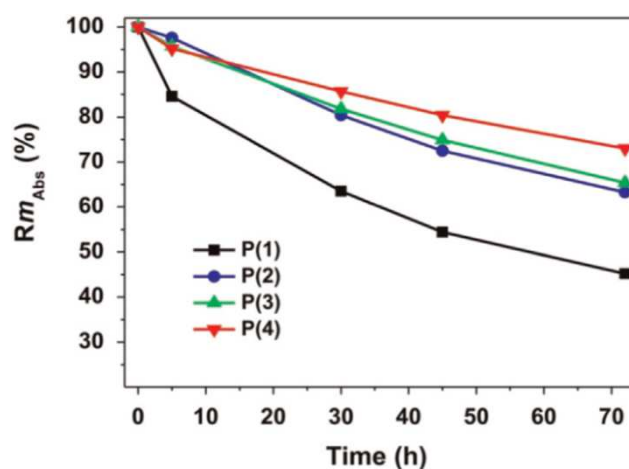
Figure 4.17. Evolution over illumination time of the residual higher energy peak intensity (Rm_{ABS}) of the lower transition band extracted from the UV-vis absorption profiles of P(1)-P(4) neat polymer films.

As previously mentioned, the polymer structure and in particular the nature, number and length of the side chains bond to the polymer backbone strongly influence the photo-chemical stability of the resulting films. By analyzing the chemical structures, P(1) contains alkoxy side chains where the oxygen atoms are linked to the BDT monomer which are easily cleavable under illumination thus starting the polymer degradation. Indeed, the resonance stabilizing effect of the oxygen atom is known to weaken the energy of the C-H bond of the adjacent CH_2 group (α position) thus favoring the

hydrogen abstraction by a free radical leading first to side chain oxidation and then to the subsequent stepwise oxidations as similarly above described for other polymers (Figure 4.13a). For P(2) and P(3), the replacement of the oxygen atoms with aromatic units (thiophene) significantly improved the resulting photo-chemical stability. Interestingly, the nature of the residual alkyl-oxy-alkyl or alkyl (for P(2) and P(3), respectively) portion of the side-chain bond to the thiophene ring revealed a negligible impact on the degradation rate of the corresponding neat film. P(4) where the BDT was replaced with an un-substituted TT unit showed the best stability to prolonged illumination in the series. These results are in agreement with other reports thus highlighting that the absence of substitutions on the polymer backbone enhances the light-stability of the structure.

It is noteworthy that the photo-chemical stability of polymer films is generally not only related to the intrinsic properties of the different structural motifs and energy levels but also to the self-organization and of the polymer chains at the solid state as, for instance, the polymer packing, the void fraction, etc. Indeed, this would result in a different rate of oxygen diffusion inside the layer thus inducing eventual differences in terms of the light-degradation rate. Besides that, the obtained results offer useful indications and guidelines to further clarify the structure-photostability relationship for this class of polymer in agreement with other reports.[135]

The reported polymers were used in combination with $PC_{61}BM$ as active layers for PSCs with the conventional structure: glass/ITO/PEDOT:PSS/active layer/LiF/Al. All the BHJ layers were processed by blade-coating in air from o-DCB solutions without any further post-processing treatment. The corresponding OPV results measured under standard illumination are summarized in Table 4.5 and the J - V plots are shown in Figure 4.18.

Table 4.5. Photovoltaic results of freshly prepared BHJ solar cells based on P(1)-P(4):$PC_{61}BM$ films as active layer. The data are averaged over 5 cells.

Polymer:$PC_{61}BM$ [a]	Thickness [nm]	V_{OC} [V]	J_{SC} [mA/cm^2]	FF [%]	PCE [%]
P(1)	90	0.77	7.7	68	4.1
P(2)	115	0.85	7.6	58	3.8
P(3)	105	0.81	10.2	63	5.2
P(4)	110	0.65	9.2	64	3.8

[a] As cast BHJ films with polymer:$PC_{61}BM$ ratio 1:1 (wt/wt).
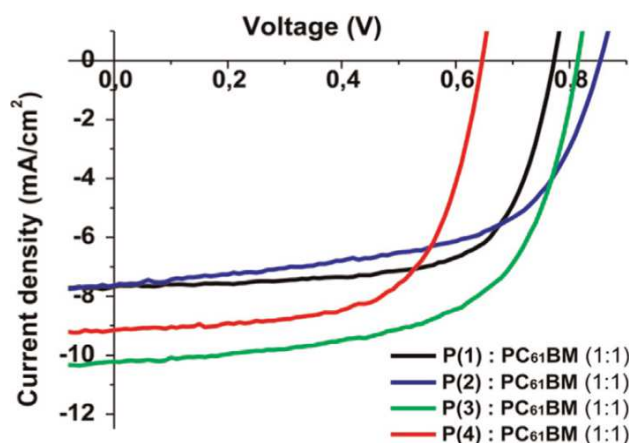
Figure 4.18. J - V plots, under 1 Sun illumination, of optimized BHJ solar cells based on P(1)-P(4):PC$_{61}$BM active layers.

The different solar cells showed remarkable photovoltaic responses for all the polymers. The best result was obtained using P(3):PC$_{61}$BM as active blend which reached a PCE of 5.2% with Jsc = 10.2 mA/cm^2 Voc = 0.81 V and FF = 63%, in agreement with a previously published work.[83] Concerning P(1)-based solar cells, the PCE of 4.1% resulted consistent with the values reported for similar systems.[141] Slight discrepancies arose from little differences in the chemical structure or in the values of molecular weight and PDI of the polymer.

All P(1)-P(4):PC$_{61}$BM solar cells were characterized by Voc values in great correlation with the differences in the HOMO levels of the donor polymers as PC$_{61}$BM is the acceptor for all the BHJs. In detail, the low-lying HOMO (≈ -5.8 eV) of the BDT-endowed polymers resulted in higher Voc (≈ 0.8 V) if compared to the Voc of P(4)-based device (0.65 V), where the PFQTT polymer is characterized by a relatively higher HOMO level (-5.64 eV).

The FF seems to follow a trend with a certain dependence on the complexity of the polymer chemical structures. Indeed, FF of 68%, 63% and 58% were respectively reported for P(1), P(3) and P(2)-based solar cells where the polymers are characterized by the BDT unity substituted with: *i)* alkoxy, *ii)* alkyl-thienyl and *iii)* a longer akyl-oxy-alkyl-thienyl side chain, respectively. On the contrary, the different chemical structure of P(4) where un-substituted TT replaces the BDT unit, cannot be correlated with the other structures. The FF of 64% suggests a proper phase segregation and inter-chain interactions likely promoted by the planar TT moiety.

The Jsc generated by P(1)-P(3):PC$_{61}$BM based cells varies between ≈ 7.6 mA/cm^2, for P(1) and P(2), and 10.2 mA/cm^2, for P(3). Since the three polymers presented similar UV-

vis absorption profiles in the same spectral range (Figure 4.16 and Table 4.4), the variations in Jsc are likely due to different morphological organization of the corresponding BHJs. For instance, the absorption intensity of P(2) doubled that of P(1) (Figure 4.16a and 4.16b) despite their resulting device Jsc were very similar. This is ascribed to a reduced amount of split excitons, which can be associated to a different organization of the respective BHJs at the solid-state likely due to differences in the molecular weight of the respective polymers. Similar considerations involve P(4)-based solar cells that, despite the red-shifted absorption spectrum of P(4) compared to that of the other polymers (Table 4.4), showed a comparable Jsc of 9.2 mA/cm^2.

Beside the evaluation of the initial photovoltaic performance, the photo-stability of the resulting P(1)-P(4)-based solar cells was investigated in order to identify eventual correlations of the intrinsic properties of the polymers with the stability of complex systems (BHJ devices) where several factors simultaneously play a role. A meaningful comparison is ensured by the use of an identical device structure for all the different polymers. To simulate the degradation processes occurring in operating devices, the freshly prepared solar cells were illuminated under inert atmosphere (analogously to an encapsulated system). As during prolonged illumination the devices are typically subjected to light-induced heating, an additional set of identical devices was fabricated as control and, entirely masked using black tape, was exposed to the heat stress from irradiation (Figure 4.19a).
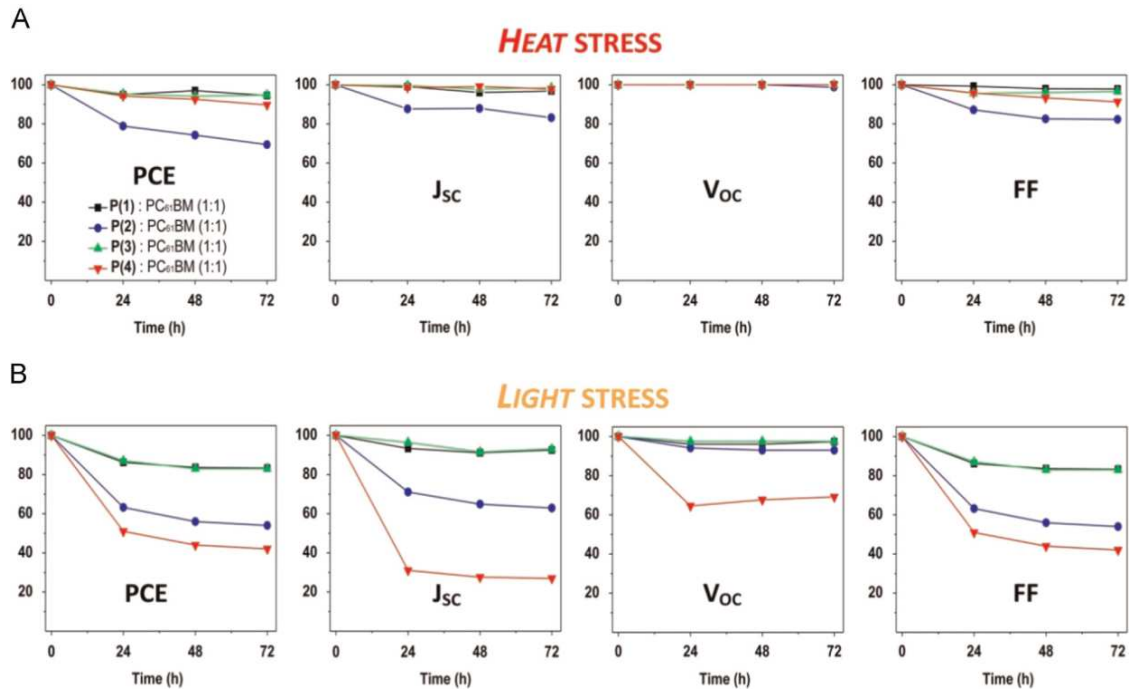
Figure 4.19. Evolution of the normalized OPV parameters from P(1)-P(4):PCBM based solar cells over illumination time. a) Heat stress refers to fully covered devices under illumination heating (≈ 50°C); b) devices under prolonged illumination (both heat and light stress).

The control devices exposed to heat stress exhibited similar and satisfying thermal resistance, which resulted in photovoltaic efficiencies close to ≈ 90% of their initial values after the thermal test. However, an exception concerns the solar cells based on P(2), whose efficiencies dropped of about 30% after 72 hours of aging. This was likely due to thermally induced morphological modifications of the BHJ as suggested by the reduction in Jsc and FF over time. Indeed, the presence of relatively long and branched side chains causes steric hindrance in solid films, which might increase the interchain distances and in turn generate some void fractions at the solid state. This might facilitates, under thermal stress, the diffusion of PCBM molecules, which would promote the formation of aggregates/clusters in the BHJ blend and hence limit the OPV performance. These results suggest that, except the case of P(2), eventual reductions of device efficiency during light soaking can be mainly ascribed to light-induced degradation since the contribution of the thermal stress is comparable and not substantial for the other cells. As shown in Figure 4.19b, the degree of device photo-degradation is remarkably different among the polymers. The decrease of the PCE was generally caused by a decrease in FF and Jsc, whereas the Voc was more or less stable during the 72 hours of measurement, except the case of P(4) based cells. Note that, the Voc loss during photoinduced degradation has been recently demonstrated to become relevant in amorphous materials

as a result of a redistribution of the charges in a broader density of states.[142] The amorphous character of the P(4) based blend might be related to the relatively low molecular weight of the polymer (M_N = 19 kDa and PDI = 2.8).

Besides the comparison of the individual light-resistances within P(1)-P(4)-based solar cells, it is similarly important to analyze the differences of stability trend passing from the application of the polymers in solar cells to films of neat polymer (Figure 4.19b and 4.17). Indeed, contrarily to the stability of the relative neat films, solar cells based on P(1) and P(3) resulted the most light stable by preserving ≈ 85% of their initial performance with reduction only ascribed to the FF. While, P(2) and P(4) based cells exhibited the greatest degradation showing a decrease in PCE up to ≈ 55% and 42% of their initial photovoltaic efficiency, respectively. To note, part of the degradation for P(2)-based devices arises from thermally induced effects, as previously described. The divergence of stability trend between neat polymer films and the corresponding BHJ solar cells highlights that the photo-chemical degradation involves several processes, which cannot merely ascribed to the polymer structure.

An additional analysis revealed that the absorption spectra of P(1)-P(4):$PC_{61}BM$ blends, before and after light stress, were almost unchanged (data not shown), which suggest the negligible differences in the BHJ morphology. This confirms the complexity of the scenario about the causes of light-induced degradation and demonstrates that the presence of PCBM in the BHJ partially preserves the photo-bleaching of the active layer and mitigates the rates of photo-degradation. Despite the investigation of neat polymer films provides precious information on the stability of the chemical structures, this results rather inconclusive in terms of stability assessment of the corresponding OPV devices. Indeed, the presence of internal interfaces, PCBM molecules or the differences in terms of processing, fundamental for the optimization of the initial device performance, induce different morphological distribution of the polymer chains and hence of the resulting BHJ photo-stability where the intrinsic polymer light-resistance is one of the fundamental requirements but not enough to predict the behavior of a complete device.

To conclude, in this work, the polymer structure was demonstrated to play an important role on the photodegradation of the corresponding neat films. In detail, the use of alkoxy side chains on the BDT unit in P(1) showed a relatively faster degradation while the use of an unsubstituted TT comonomer in P(4) resulted the most light-stable neat film. Despite that, a different trend was found for the corresponding BHJ solar cells. Interestingly, the best candidates resulted P(1) and P(3), which showed great initial device

efficiency as well as remarkable light stability as evidenced by retention of about 85% of the initial performance after ageing. If compared to the poor stability of P(2)-based cells, this demonstrates the beneficial role, in terms of light resistance of the corresponding polymer, of using relatively short side chains. This suggests that the use of relatively compact substituents on the BDT unit improves the light stability as a consequence of enhanced inter-chains interactions and reduced void fractions in the BHJ films. The relatively high performance of blade-coated solar cells based on P(1) and P(3) in conjunction with the great light stability represents a guideline to further explore the potential of this class of polymers, which seem promising candidates for the development of efficient, light and thermally-stable polymers for OPV applications.

4.3.3 Light stability of interlayers: impact of the Al-doping on the ZnO properties

Part of this paragraph is adapted with permission from:

M. Prosa, M. Tessarolo, M. Bolognesi, O. Margeat, D. Gedefaw, M. Gaceur, C. Videlot-ackermann, M. R. Andersson, M. Muccini, M. Seri, J. Ackermann, *ACS Appl. Mater. Interfaces* **2015**, *8*, 1635. Copyright 2016 American Chemical Society.

In order to optimize the charge collection of organic solar cells, interlayers are typically inserted at the BHJ/electrode interface to reduce bimolecular recombinations and improve the ohmic contact. Over the years, the development of new materials and their optimization clearly contributed to push the efficiencies of PSCs. Typically, high work function materials such as PEDOT:PSS or MoO_3 are used as hole transporting interlayers (HTLs) at the anode while low work function materials like (PFN),[41] polyethylenimine ethoxylated (PEIE),[42] TiO_x[40] or ZnO[39] are used as electron transporting layers (ETLs) at the cathode.

Among ETLs, ZnO is one of the most attractive because of its electron conductivity, low work function, good optical transmittance, non toxicity and low cost.[143] In addition, the possibility to be synthesized in the form of nanoparticles (ZnO NPs) results in solution processable ZnO inks which generate films with high conductivity and without the need of additional post-treatments.[144]

Despite the attracting properties of ZnO for photovoltaic applications, one limitation concerns its oxygen susceptibility. Indeed, the conductivity of ZnO is negatively influenced by chemisorbed oxygen which captures electrons from the conduction band thus creating a depletion region with high resistivity.[145][146] This process is physically

reversible and, if ZnO is irradiated with ultraviolet light, chemisorbed oxygen molecules are released from the ZnO layer thus restoring the conductivity of the material.[147][148] Although light irradiation could restore the conductivity of ZnO, prolonged illumination could induce irreversible degradation. Indeed, UV light soaking in the presence of oxygen triggers the formation of "chemical defects" which reduce the reduce the n-type behavior of the ZnO. These are likely p-type defect of the lattice structure that induce an increase of the ZnO e work function.[149][150][151][152]

As a consequence, the presence of oxygen during ZnO film processing could represent an issue for the photostability of solar cells. In addition, since the adsorption of oxygen is a surface-related phenomenon, structures with a high surface-to-volume ratio, as in the case of films of ZnO NPs, might be particularly sensitive to light exposure if processed in air. In this context, a deeper investigation on the role of light soaking on solar cells containing a layer of air-processed ZnO NPs is of particular interest.

Despite the above-mentioned suitability of ZnO for photovoltaic applications, the use of undoped ZnO for large scale production of optoelectronic devices could be challenging in term of processing. Indeed, in industrial fabrication, relatively thick layers in the order of 100 nm are preferred to ensure a complete substrate coverage avoiding the risk of defects. Since the conductance of such thick layer of ZnO would not be sufficient to ensure efficient performance of the relative device,[153] ZnO is usually doped with small amounts of metal ions such as Al, Ga, etc. Among them Aluminum-doped ZnO (AZO) is one of the most studied for photovoltaic applications.[154] Indeed, similarly to ZnO, AZO can be processed in the form of solution-processable NPs inks and, besides showing the same advantages of ZnO in terms of work function, transparency and processability, it is characterized by a conductivity which is three order of magnitude higher.[155] Therefore, AZO is introduced to facilitate the use of ZnO-based materials in industrial processes like roll-to-roll.

Roll-to-roll industrial coating processes mostly take place in ambient conditions and the effect of air as well as light soaking of undoped ZnO is known to be detrimental. Therefore, it is crucial to understand the effects of prolonged illumination on solar cells based on air-processed AZO films.

To this end, during the PhD program a series of solution-processable ZnO-based NPs were investigated: *i)* pristine, *ii)* 0.03 at.% (AZO$_{0.03}$), *iii)* 0.37 at.% (AZO$_{0.37}$) and *iv)* 0.8 at.% (AZO$_{0.8}$) Aluminum-doped.[112] Figure 4.20 shows their optical and morphological properties and the relative energy levels. In detail, the morphology of the corresponding

thin films deposited over ITO resulted homogeneous with surfaces relatively smooth as revealed by a roughness of 8, 6, 4 and 4 nm (RMS) for ZnO, $AZO_{0.03}$, $AZO_{0.37}$ and $AZO_{0.8}$ film, respectively. All the ZnO-based layers showed similar UV-vis spectra (Figure 4.20e) characterized by an optimal transmittance higher than 80% over the entire visible range with an absorption peak at 345 nm. The energy levels of the valence and conduction bands resulted similar for all ZnO (-7.7 eV and -3.6 eV, respectively) and AZO_x (-7.8 eV and -3.7 eV, respectively) films which would favor a good energy matching with the adjacent materials (Figure 4.20f). The great optical, morphological and energetic properties make the reported ZnO/AZO_x suitable for their incorporation as ETL in PSCs. To note, the Aluminum concentration in the NPs did not influence the properties of the AZO_x with respect to ZnO as confirmed by the similar properties of all the inks.
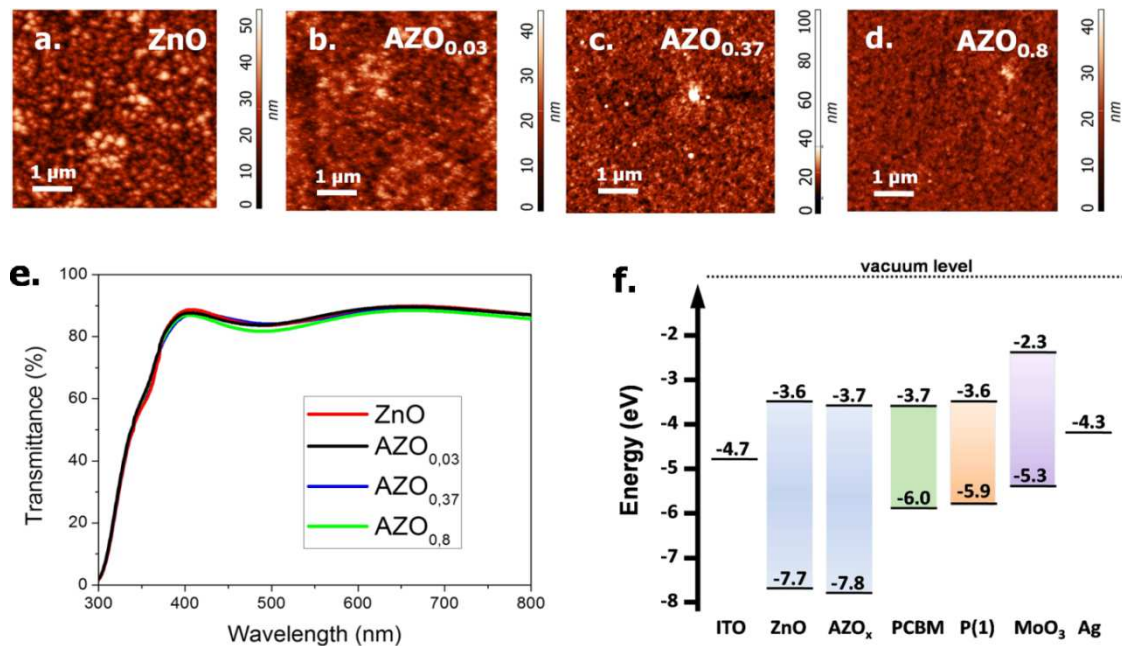
Figure 4.20. AFM images (5 µm x 5 µm) recorded in tapping mode of ZnO (a), $AZO_{0.03}$ (b), $AZO_{0.37}$ (c) and $AZO_{0.8}$ (d) deposited on glass/ITO substrates. The surface roughness of the corresponding layers (RMS) is 8, 6, 4 and 4 nm, respectively. e) Transmittance spectra of the reported films and f) energy level diagram of the materials used in PSCs.

A set of solution-processed PSCs was fabricated using a newly synthesized polymer PFQ2T-BDT (named P(1)) as electron donor material (Figure 4.21a) of the BHJ in conjunction with $PC_{61}BM$ as electron acceptor. Details on the synthesis, optical and electrochemical properties of P(1) are reported in the reference [112].

In view of stability tests under prolonged light-stress, the inverted device geometry was preferred (Figure 4.21b) in order to minimize eventual contributions to degradation arising from sensitive electrodes/interfaces.[113]

The thickness of all the different ZnO/AZO_x films was intentionally fixed around 40 nm in order to avoid electrical differences arising between doped and undoped NPs. The reported formulations were processed by spin coating either in air or in inert atmosphere (N_2 environment) and successively annealed at 140°C for 15 minutes to remove eventual water content adsorbed on the solid structure and, in the case of air-processing, immediately transferred inside a glove box to minimize moisture contact.
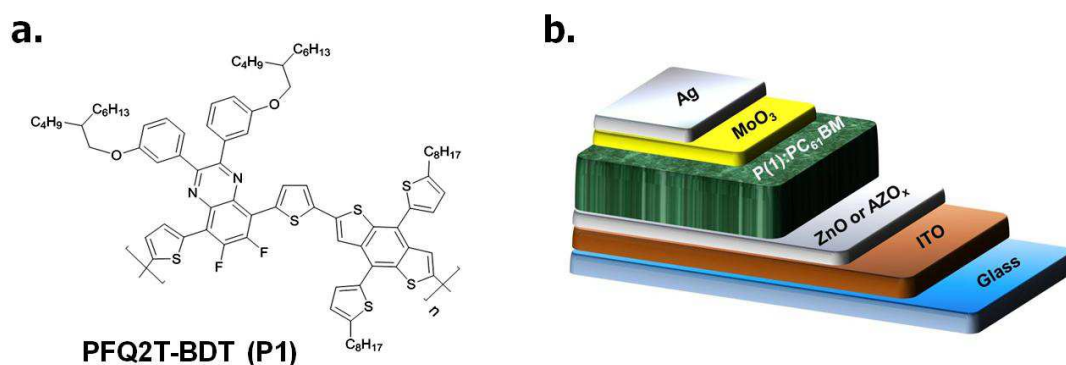
Figure 4.21. a) Chemical structure of PFQ2T-BDT (named P(1)) electron donor polymer; b) representation of the inverted device configuration of the single junction PSCs fabricated using the different ZnO/AZO_x NPs as ETL and P(1):$PC_{61}BM$ as BHJ.

Freshly prepared PSCs based on ZnO (Device A), $AZO_{0.03}$ (Device B), $AZO_{0.37}$ (Device C) and $AZO_{0.8}$ (Device D) showed nearly identical photovoltaic performance (Table 4.6 and Figure 4.22) with PCEs over 4%, Jsc of $\approx$ 8.7 mA/cm^2, Voc of $\approx$ 0.87 V, FF of $\approx$ 55%, and series (R_s) and shunt (R_{sh}) resistance of $\approx$ 11 Ω cm^2 and $\approx$ 680 Ω cm^2, respectively. Hence, the OPV parameters of fresh PSCs were not influenced by the Al doping level in ZnO as expected from their similar properties. Furthermore, the processing environment of the ETLs did not reveal any effect on the photovoltaic response of the corresponding devices.

Table 4.6. OPV response of freshly prepared PSCs. All the OPV parameters are averaged over 10 samples and mean values are reported with their standard deviation.

PSCs	ETL	ETL processing environ.	J_{SC} [mA/cm^2]	V_{OC} [V]	FF [%]	PCE [%]	R_s [Ω cm^2][a]	R_{sh} [Ω cm^2][b]
Dev. A	ZnO	N_2	8.6 ± 0.3	0.87 ± 0.003	55 ± 2	4.1 ± 0.1	11.5 ± 0.1	670 ± 10
		Air	8.8 ± 0.3	0.87 ± 0.005	55 ± 1	4.2 ± 0.1	10.8 ± 0.1	670 ± 10
Dev. B	AZO$_{0.03}$	N_2	8.7 ± 0.1	0.87 ± 0.003	55 ± 1	4.2 ± 0.1	10.8 ± 0.1	680 ± 10
		Air	8.8 ± 0.3	0.87 ± 0.006	54 ± 2	4.1 ± 0.1	11.3 ± 0.1	660 ± 10
Dev. C	AZO$_{0.37}$	N_2	8.7 ± 0.3	0.87 ± 0.004	55 ± 2	4.2 ± 0.1	11.0 ± 0.1	690 ± 10
		Air	8.7 ± 0.3	0.87 ± 0.005	55 ± 2	4.2 ± 0.1	11.5 ± 0.1	650 ± 10
Dev. D	AZO$_{0.8}$	N_2	8.6 ± 0.2	0.86 ± 0.005	56 ± 1	4.1 ± 0.1	10.5 ± 0.1	690 ± 10
		Air	8.8 ± 0.2	0.86 ± 0.009	54 ± 1	4.1 ± 0.1	10.2 ± 0.1	690 ± 10

[a] R_s was calculated as the slope of the tangent line of the J-V curve at V > Voc; [b] R_{sh} was calculated as the slope of the tangent line of the J-V curve at V = 0.
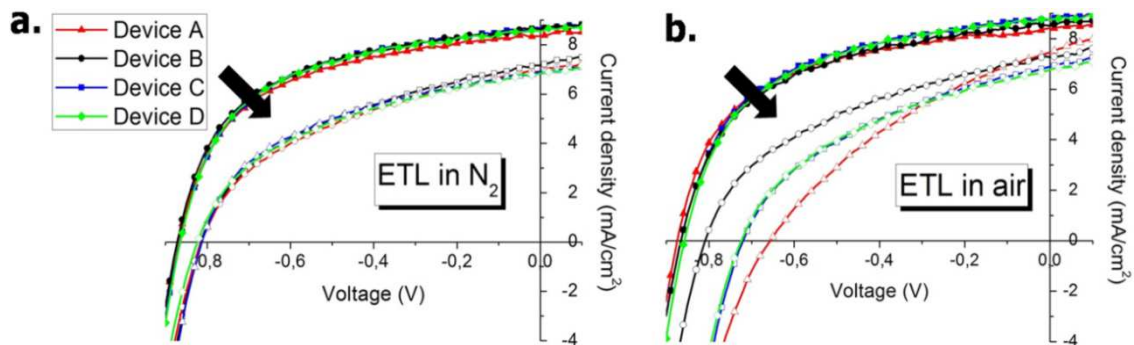
Figure 4.22. J–V plots of fresh (filled symbols) and illuminated for 40 h under AM1.5G simulated sunlight (empty symbols) solar cells based on: ZnO (red), AZO$_{0.03}$ (black), AZO$_{0.37}$ (blue) and AZO$_{0.8}$ (green) ETL. The plots refer to devices in which the ZnO-based ETLs are processed in inert atmosphere (a) or in air (b). The black arrows highlight the transition of the J–V curves when passing from fresh to degraded devices.

To investigate the effect of prolonged irradiation on the stability of the reported solar cells, all devices were kept for 40 hours under standard AM1.5G illumination in inert environment and their J-V plots were measured at defined time intervals. According to their initial OPV responses, all the aged solar cells with ETLs processed in N_2 showed similar J-V plots (Table 4.7 and Figure 4.22). Despite the devices resulted less efficient,

they degraded in similar way and independently on the type of ETL. In detail, Jsc dropped to $\approx$ 7 mA/cm^2, Voc to $\approx$ 0.81 V, FF to $\approx$ 45% and PCE from about 4% to 2.5%. A partial degradation was expected since prolonged illumination is known to reduce the performance of the BHJ active layer. Indeed, as previously discussed, light catalyzes processes such as photobleaching, morphological changes, etc. which are complex and eventually interlinked. However, since the reported solar cells differ only for the ETL and, moreover, the OPV parameters of fresh and aged devices resulted similar, it is reasonable to assume that light-induced processes occurring in device A, B, C and D were not influenced by the nature of the ZnO-based NPs when processed in inert environment. On the contrary, the degradation trend of cells based on air-processed ETLs resulted considerably different as reveled by the correspondent J-V plots and OPV parameters (Figure 4.22 and Table 4.7). In particular, device A where the ETL is based on undoped ZnO exhibited the lowest performance after prolonged illumination; device B using AZO$_{0.03}$ as ETL resulted the most stable and interestingly exhibited the same photovoltaic response irrespectively on the processing environment; devices C and D, respectively using AZO$_{0.37}$ and AZO$_{0.8}$ as ETLs, were less stable compared to device B but still showed an enhanced photostability with respect to device A. Despite the processing environment did not revealed any effect on the degradation trend of device B, devices A, C and D were found to be less stable when the corresponding ETL were processed in air rather than in inert atmosphere. This indicates that ZnO, AZO$_{0.37}$ and AZO$_{0.8}$ layers were affected by light stress depending on their processing environment. To identify the possible causes of the difference in stability of air-processed ZnO and AZO$_x$ ETLs, the trend of decay of the OPV parameters during light exposure was analyzed (Figure 4.23).

Table 4.7. Photovoltaic response of aged PSCs (40 hours under AM1.5G illumination in inert environment) using ETLs based on ZnO, $AZO_{0.03}$, $AZO_{0.37}$ or $AZO_{0.8}$ and processed in inert environment (N_2) or in air. All the OPV parameters are averaged over 10 samples and mean values are reported with their standard deviation.

PSCs	ETL	ETL processing environ.	J_{SC} [mA/cm^2]	V_{OC} [V]	FF [%]	PCE [%]	R_s [Ω cm^2][a]	R_{sh} [Ω cm^2][b]
Dev. A	ZnO	N_2	7.2 ± 0.3	0.81 ± 0.005	43 ± 1	2.5 ± 0.1	18.6 ± 0.1	310 ± 10
		Air	7.5 ± 0.1	0.66 ± 0.002	35 ± 1	1.7 ± 0.1	37.7 ± 0.1	190 ± 10
Dev. B	$AZO_{0.03}$	N_2	6.9 ± 0.5	0.81 ± 0.004	46 ± 1	2.6 ± 0.2	16.5 ± 0.1	390 ± 10
		Air	7.3 ± 0.3	0.81 ± 0.005	43 ± 0.1	2.5 ± 0.1	17.1 ± 0.1	320 ± 10
Dev. C	$AZO_{0.37}$	N_2	7.0 ± 0.2	0.81 ± 0.007	43 ± 1	2.4 ± 0.1	19.6 ± 0.1	330 ± 10
		Air	6.9 ± 0.2	0.72 ± 0.005	40 ± 1	2.0 ± 0.1	20.5 ± 0.1	270 ± 10
Dev. D	$AZO_{0.8}$	N_2	6.9 ± 0.3	0.82 ± 0.005	45 ± 1	2.5 ± 0.1	19.5 ± 0.1	380 ± 10
		Air	6.8 ± 0.1	0.72 ± 0.005	41 ± 1	2.0 ± 0.1	22.4 ± 0.1	280 ± 10

[a] R_s was calculated as the slope of the tangent line of the J-V curve at V > Voc; [b] R_{sh} was calculated as the slope of the tangent line of the J-V curve at V = 0.
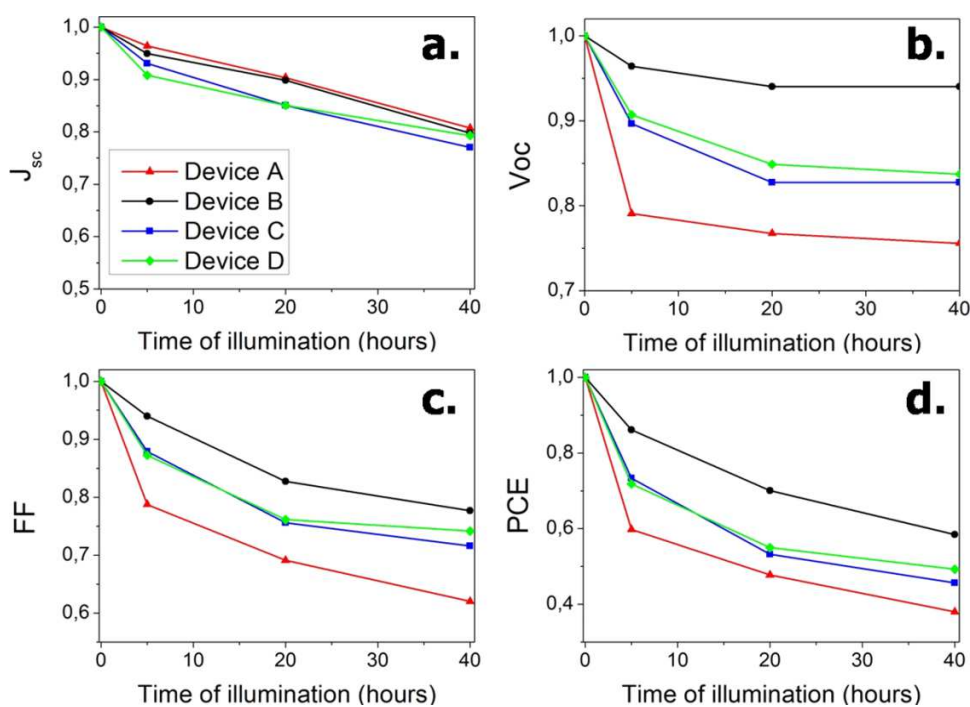
Figure 4.23. Normalized evolution over illumination time of Jsc (a), Voc (b), FF (c) and PCE (d) for device A (red triangles), B (black circles), C (blue squares) and D (green rhomboids).

As shown in Figure 4.23, which exclusively refers to air-processed ETLs, the Jsc decreased with a similar linear trend for all devices (Figure 4.23a). This reduction is ascribed to degradation mechanisms common to all the solar cells and that likely affected in similar way the active layer or the BHJ/interlayer interfaces. Diversely, the decrease of Voc (Figure 4.23b), FF (Figure 4.23c) and PCE (Figure 4.23d) was considerably different within the four types of device and consistently smaller for device B. The degradation trend of Voc and FF for device A, C and D was characterized by an initial drop after 5 hours of illumination which was followed by a smoother decrease up to 40 hours. Interestingly, the differences among the degradation trends of the devices were observed only in the first few hours; then, both the Voc and FF decreased in a similar and gradual way for all the solar cells. Since devices A, B, C and D with air-processed ZnO/AZO$_x$ differed only for the nature of their ETLs, the differences in the overall light-stability is likely ascribed to a light-induced and air-dependent degradation process occurring in the first few hours. Furthermore, as Voc and FF decreased with a similar trend for all devices, it is reasonable to suppose that their decay is related to the same degradation process.

To validate the major role of the air-processed ZnO/AZO$_x$ ETLs on the light-stability of corresponding solar cells, similar devices were fabricated using a different BHJ active layer based on polythieno[3,4-b]-thiophene-*co*-benzodithiophene (PTB7):PCBM. The resulting devices were characterized and then kept under AM1.5G illumination for 24

hours in inert atmosphere. As shown in Figure 4.24, the degradation behavior resulted similar to that of P(1):PCBM-based cells (Figure 4.23b) with $AZO_{0.03}$-based cells more stable than the other devices while the cells using ZnO resulted the most degraded. Moreover, the trend of the normalized Voc over illumination proceeded in a similar way compared to that of P(1):PCBM BHJ cells thus highlighting the susceptibility of the cells in the first few hours of illumination. This confirms the role of ZnO and AZO_x on the light-stability of solar cells when the ETLs are processed in air. To note, as active layers based on PTB7:PCBM are typically affected by a consistent light-induced degradation, P(1):PCBM was selected for a systematic and detailed investigation.
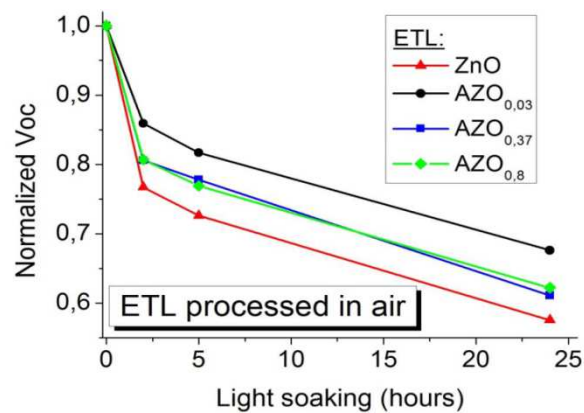
Figure 4.24. Evolution of normalized Voc over illumination time (24 hours in inert atmosphere) for PTB7:PCBM BHJ solar cells using ZnO (red triangles), $AZO_{0.03}$ (black circles), $AZO_{0.37}$ (blue squares) and $AZO_{0.8}$ (green rhomboids) as ETLs. All the ETLs were processed in air while the BHJ active layer was processed in inert environment.

Typically, the degradation processes occurring in the ETL of organic solar cells may have influences on the bulk conductivity and on the charge selectivity of the selective layer. In the first case, an increase of the series resistance of the relative device would be expected while, in the latter process, the charge selectivity would be compromised and hence the overall shunt resistance of the solar cell would reduce. In both cases, the FF would be affected. However, in the case of a reduction of charge selectivity, bimolecular recombinations would result in a negative impact also on the device Voc. From these considerations, the series (Rs) and shunt (Rsh) resistance of fresh and aged devices A, B, C and D using air-processed ETLs were compared (Table 4.6 and 4.7). In detail, a slight increase in Rs was observed after prolonged light-exposure for all the solar cells, with only degraded device A showing a relatively higher value (37.7 Ω cm^2) if compared to the others ($\approx$ 20 Ω cm^2). On the contrary, Rsh was considerably different within degraded

devices A, B, C and D (Table 4.7). In particular, Rsh of device B which included $AZO_{0.03}$ was the less affected, while for device A, C and D, Rsh was considerably affected thus indicating a limitation of the charge selectivity of the ETL with subsequent Voc reduction. To further analyze the electrical properties and behavior of the different solar cells, dark J-V curves of fresh and aged devices based on air-processed ETLs are reported in Figure 4.25.
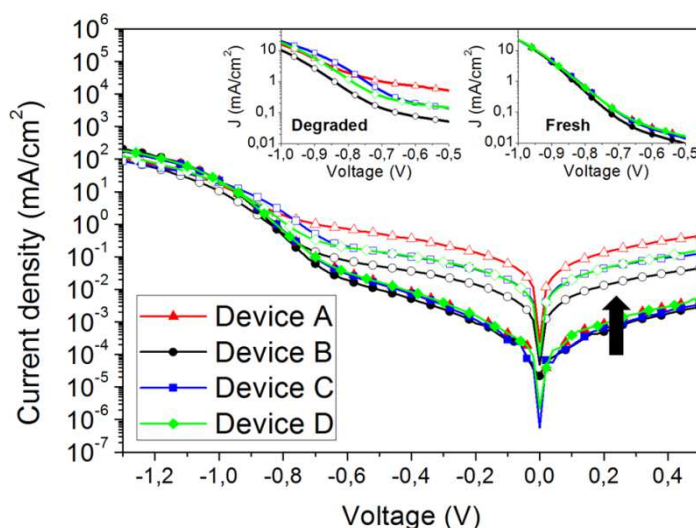
Figure 4.25. Dark J-V plots (semilogarithmic) of fresh (filled symbols) and aged under prolonged light stress (empty symbols) devices A (red triangles), B (black circles), C (blue squares) and D (green rhomboids). The black arrow indicates the transition of the J-V curves from fresh to degraded devices. In the inset, a zoom-in of the range between -1 and -0.5 V is shown for fresh (right) and aged (left) devices.

Aged solar cells, in the voltage range from +0.5 V to -0.4 V of the dark J-V curves (Figure 4.25), showed the characteristics of an ohmic resistor. The highest dark current in reverse bias was measured for device A; intermediate values were reported for device C and D while device B was characterized by the lowest dark current. This means that the diode behavior of the cells based on $AZO_{0.37}$, $AZO_{0.8}$ and especially undoped ZnO was poorer than the cell based on $AZO_{0.03}$. In addition, by observing the forward bias region (ranging from -0.4 V to -1.3 V), the small slope of the curves referring to devices A, C and D between -0.5 V and -1.0 V (Figure 4.25 inset) reflected a diode ideality number greater than 1.[156] This behavior in forward bias is indicative of a non-ideal recombination of injected charges due to the presence of shunts in the ETLs, in agreement with the lower R_{sh} values reported in Table 4.7.

It was demonstrated that organic solar cells containing ZnO as ETL, which has been previously UV-soaked in dry air, suffer of shunt losses.[157] Indeed, the UV treatment of

the oxygen present in the dry air causes the introduction of interstitial oxygen atoms in the ZnO lattice which act as p-type defects with the subsequent decrease of the ZnO Fermi level.[158][159] This promotes the extraction of holes from the HOMO level of the BHJ donor material and hence a raising of the dark currents in reverse bias.[157] In addition, a reduction of the Voc is expected as observed for the case of device A, C and D (Table 4.7). It is reasonable to assume the air-processing of ZnO/AZO$_x$ interlayers favors the chemisorptions of oxygen on the NPs surface, which results detrimental for the device Voc and FF during the prolonged illumination as a consequence of the formation of the aforementioned shunts. Since the amount of adsorbed oxygen on the ETLs is limited, the related degradation process was evident only in a fixed time interval (few hours of irradiation). This likely explains the fast reduction of Voc and FF of devices A, C and D in the first hours. Moreover, the formation of shunt points also elucidates the simultaneous degradation trend of FF and Voc.

To validate this hypothesis on the UV/oxygen dependent degradation of ZnO/AZO$_x$-based solar cells, all the devices employing air-processed ETLs were subjected to a light test using UV-filtered AM1.5G illumination. Indeed, since oxygen can degrade the ZnO/AZOx films only in the presence of UV light, the use of a filter should hinder the described shunting formation. For this reason, the J - V plot of all devices with air-processed ETLs was measured before and after UV-filtered prolonged illumination (Figure 4.26).
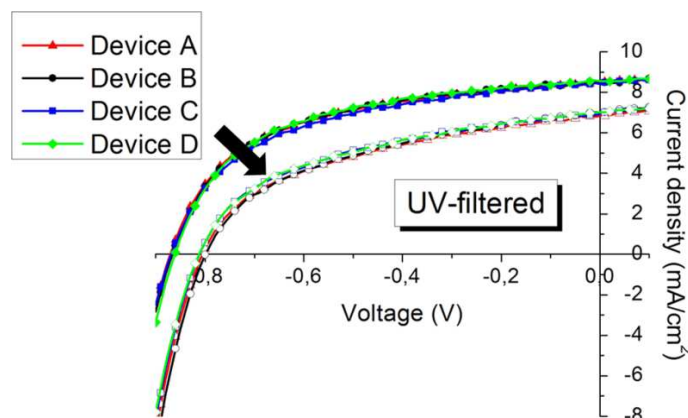
Figure 4.26. J-V plot of devices A (red triangles), B (black circle), C (blue squares) and D (green rhomboids) using air processed ETLs. Filled symbols refer to fresh devices while empty symbols to cells after UV-filtered AM1.5G illumination in inert atmosphere for 40h. the black arrow highlights the transition of the J-V curves from fresh to aged devices.

Interestingly, the J - V curves of all aged devices resulted identical. Device A, which was affected by a substantial degradation during AM1.5G prolonged illumination, matched the response of aged device B thus showing the same stability under UV-filtered prolonged irradiation. This suggests that, as the oxygen cannot interact with the ZnO/AZO$_x$ NPs, all the devices were equally degraded by the same processes, which are not related to the nature of the ETLs and are reasonably ascribed to light-induced degradation of the active layer. Accordingly, it was previously demonstrated that BHJ devices based on a series of similar donor polymers were characterized, under prolonged illumination, by photo-bleaching of the active films with subsequent reduction of the device performance (Figure 4.19).

It can be concluded that the different behavior of ZnO, AZO$_{0.03}$, AZO$_{0.37}$ and AZO$_{0.8}$ under prolonged irradiation, was due to the adsorption of molecular oxygen on the NPs during processing which resulted in the formation of harmful species under UV-illumination. The clear effect of the Al doping on ZnO properties revealed the possibility to fully recover the loss in photovoltaic performance of air-processed ZnO-based devices after prolonged light soaking by doping the ZnO NPs with a small amount of Aluminum (0.03 at. %). Higher concentrations of Al doping restored the oxygen-related light soaking instability of undoped ZnO. To note, even though photodegradation still occurred for higher Al doping concentrations, the stability of AZO$_{0.37}$ and AZO$_{0.8}$ based devices was improved in comparison to the analogous device based on undoped ZnO.

The origin of the improved light stability for AZO$_x$ ETLs is ascribed to several reasons. It is kwon that the presence of a thin Al layer on ZnO prevents the Voc losses of the solar cells under prolonged illumination.[156] This is attributed to the Al induced shift of the Fermi level towards the ZnO conducting band which increases the photo-stability of the resulting devices. Similarly, the here reported Al-doping of ZnO NPs leads to an improvement in the ETL conductivity and a passivation of defect states.

Furthermore, oxygen typically chemisorbs on ZnO structural point defects, in particular Zn vacancies.[160] As Aluminum can fill in Zn vacancies because Al^{3+} ions have larger nuclear charge and smaller atomic radius than Zn^{2+}, it is reasonable to suppose that the number of Zn vacancies decreases by doping ZnO with Aluminum thus limiting the oxygen adsorption.[161][162][163] This means that Al dopants modify the surface chemistry of ZnO leading to a reduced amount of adsorbed oxygen molecules on the ETL during air-processing and hence a greater stability of the solar cells.

Both the effects may contribute to the improved photo-stability of the corresponding air-processed BHJ devices. It is still unclear why devices based on ETLs with higher Al-doping levels ($AZO_{0.37}$ and $AZO_{0.8}$) were less photostable than those based on $AZO_{0.03}$. One possibility could be that at higher doping levels aluminum species able to interact with the oxygen are generated at the AZO surface, likely inducing new defect states under prolonged UV exposure. This may lead to transport barriers probably responsible for increased charge recombinations processes in the $AZO_{0.37}$- and $AZO_{0.8}$-based devices.

This confirms that AZO_x NPs represent an excellent class of charge-selective materials for roll-to-roll processing because, aside from the good electrical conductivity, they lead to clear improvements in the UV stability of air-processed organic solar cells. Interestingly, despite $AZO_{0.03}$ NPs contain only a small amount of Al, the photo-stability is not influenced by the contact with oxygen during processing. This, in conjunction with the electrical conductivity of the resulting films, which is three orders of magnitude higher than the analogous undoped ZnO layers, makes it attractive and suitable for thick film processing on large-scale in view of real world application of PSCs.

In conclusion, in this Chapter, the solvent used to process the BHJ active layer was demonstrated to be relevant for the stability of the corresponding PSCs under heating stress. Interestingly, the use of processing solvents with slightly different chemical-physical properties than the common ones represents an alternative approach to obtain thermally stable solar cells without sacrificing their photovoltaic performance.

To note, the development of a non-invasive advanced characterization technique, operating on complete solar cells, allowed to correlate the photovoltaic response to the photo-physical properties of the device components. This represents an interesting breakthrough for the selective analysis of the BHJ morphology evolution and the degradation of the interlayers/electrodes over the testing period.

The investigation of the light stability on films of pristine polymers and on the corresponding BHJ solar cells provided guidelines towards the development of efficient and light-stable PSCs. In particular, a comparative study on polymers characterized by similar chemical structures revealed the benefit to use short and relatively compact side chains substituents on the polymer backbone to improve the resistance of BHJ active layers to prolonged illumination. Moreover, the investigation of the light resistance of solar cells using different ZnO NPs as ETLs revealed the great advantage to use the class of Aluminum-doped ZnO NPs for an enhanced light stability of air-processed PSCs.

127

Chapter 5

Organic tandem solar cells

5.1   General overview

Over the last years, organic solar cells progressively raised their performance resulting more than ever promising.[164] Despite some fundamental thermodynamic losses limit the energy conversion of the photovoltaic devices (Figure 5.1a), solution-processed single-junction OSCs have reached power conversion efficiencies over 11%.[165][166][167] Nevertheless, there is still significant room to further enhance the device performance, which is one of the key requirements for the commercialization of this technology.

Hereafter, a brief overview of the main thermodynamic limitations introduces the possible approaches to further improve the solar cell efficiency.
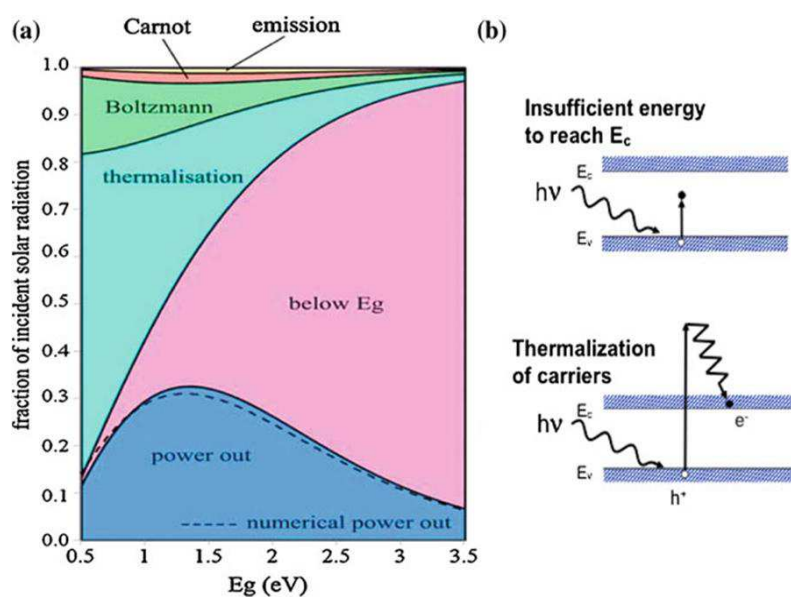
Figure 5.1. a) Losses and energy conversion fractions in photovoltaic devices as a function of the absorber band-gap; b) main losses mechanisms in solar cells, sub-band gap irradiation (top panel) and thermalization (bottom panel).[90]

As demonstrated by Shockley and Queisser,[168] a single layer of semiconducting absorber is typically subjected to different intrinsic energy losses due to: *i*) photon energy

mismatch, *ii*) Carnot mechanism, *iii*) Boltzmann processes and *iv*) emissive/radiative recombination pathways.

The first type of losses is related to an energy mismatch between the solar photons and the band-gap of the absorbing material. Photons with energies smaller than the semiconductor energy-gap cannot be absorbed and are transmitted through the active layer (Figure 5.1b, top panel). This means that part of the solar energy cannot contribute to the energy conversion of the solar cell. On the contrary, photons with energies equal or higher than the semiconductor band-gap are typically absorbed. However, an excess of energy above the band-gap would be dissipated as thermal energy (thermalization) and would not be useful for the energy conversion (Figure 5.1b, bottom panel). Similarly to the transmission, thermalization losses are related to a mismatch between the energy gap of the absorber and the solar photons. It is noteworthy that, despite the extra-energy of the excitons appears useless in terms of photovoltaic conversion because dissipated via thermalization mechanisms, a possible beneficial contribution to the process of free-charges formation is still debated.[169][170][171]

Other losses concern the Carnot process where a solar cell is considered as an engine which absorbs thermal energy from the sun to work. Since the origin of the energy flow arises from the temperature difference, this process is accompanied by a loss in the device Voc.

Another thermodynamic loss arises from the irreversible generation of entropy (Boltzmann process).

Finally, a minor mechanism, which still limits the sunlight conversion in free charge carriers, is the recombination of excitons via thermal or radiative decay.

Considering these main limitations and also accounting for the relatively low dielectric constant of organic semiconductors, their typically low mobility and the additional recombination pathways that can take place in a BHJ, efficiencies around 15% are predicted for single-junction organic solar cells assuming a donor band-gap of 1.45 eV, an EQE of 80% and a FF of 75%.[48]

In this scenario, as shown in Figure 5.1a, the most significant losses arise from the energy mismatch between the incident photons and the absorber band-gap. Indeed, thermalization and transmission of solar photons account for the major part of solar energy not converted in electricity. A possible approach to minimize this loss consists in the introduction of more photoactive components in the BHJ in order to harvest more sunlight. Indeed, because of the nature of organic materials, semiconducting polymers

with different energy-gaps (and absorption spectra) are available for photovoltaic applications. Hence, two complementary absorbing electron-donors are typically mixed with an electron acceptor exploiting the so called ternary concept to better match the solar spectrum.[172][72][173] Interestingly, the approach of a three components BHJ solar cell led to impressive device efficiencies approaching 12%.[174][165][175][167] Similarly, the effectiveness of the use of four components BHJs was recently demonstrated.[176][177]

As alternative approach to the use of multi-components active layers, the solar cell can be divided into sub-cells where each active layer absorbs photons in a limited interval of energy and transmits the rest to the other sub-cells (Figure 5.2a). In this architecture, called multi-junction, the sub-cells are stacked in a single device and electrically connected through intermediate contacts. By narrowing the absorption range of each sub-cell and increasing the amount of junctions, most of the solar photons can be absorbed by the entire stack (Figure 5.2b) thus drastically reducing the thermalization processes since the light passes photoactive layers with a progressively smaller energy gap (Figure 5.2a).[178]
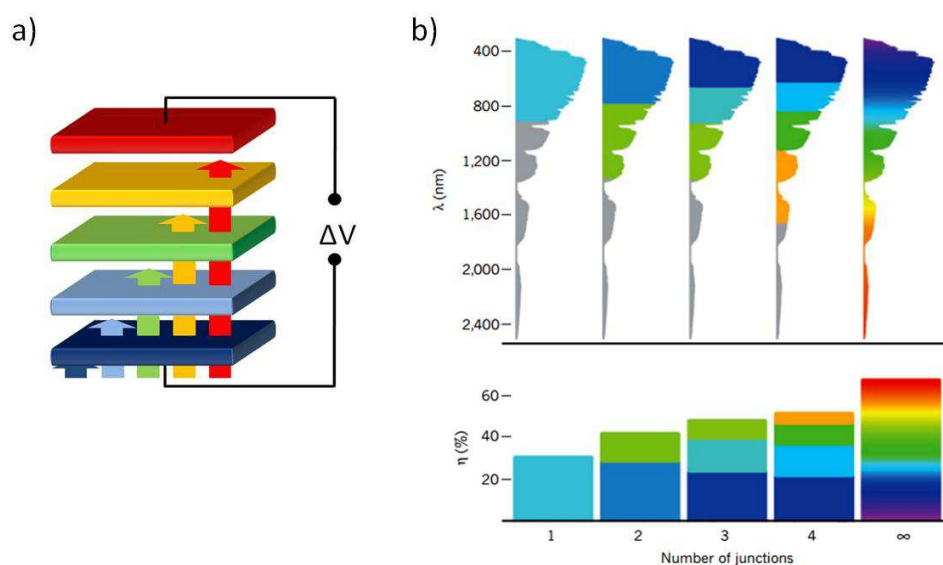
Figure 5.2. a) Representative example of the light-absorption in a 5-junctions solar cell; b) Illustrative part of solar spectrum absorbed by a multi-junction solar cell as a function of the number of sub-cells (top panel) and the relative efficiency from ideal solar cells (bottom panel). Reprinted by permission from Macmillan Publishers Ltd: Nature [179], copyright 2012.

Despite infinite junctions would be theoretically preferred to enhance the device efficiency (Figure 5.2b, bottom panel), the use of a multitude of layers introduces issues in terms of fabrication. An optimal trade-off is represented by the use of double-junction

or *tandem* devices where only two sub-cells with complementary absorbing active layers are monolithically stacked in a single device (Figure 5.3).[180] Following this approach and assuming EQE and FF values of 80% and 75%, respectively, for each sub-cell, Li *et al.*[47] predicted the possibility to reach efficiencies up to 21% for organic tandem solar cells, using active layers based on donors with ≈ 1.6 eV and ≈ 1.2 eV of energy-gap.

In this architecture, the sub-cells of the tandem device can be either connected in series (2-terminal) or in parallel (3-terminal) (Figure 5.3a and 5.3b, respectively).[181] When connected in series, the flowing current in steady-state conditions is constant throughout the tandem device, while the voltage is the sum of those generated by the sub-cells. On the contrary, in the parallel connection, the tandem photo-current is the sum of the currents of the sub-cells while the voltage is constant and limited by the sub-cell with lower Voc.

When both sub-cells show the same electrical properties, both types of connection were demonstrated to potentially lead to the same performance. Besides, when the performance of the sub-cells is different, a series connection is preferred in the case of large differences between the Voc of the sub-cells while parallel connection is favorable for differences in their Jsc. However, concerning the FF, lower values are usually reported for series connection rather than parallel. This would suggest that the use of a parallel connection would generally allow for higher performance of the tandem device.[181] Nevertheless, this connection requires the use of three external terminals for the electrical connection of the entire stack.[182] Since the two sub-cells are monolithically stacked, this would result in a more complicated fabrication, which explains the prevalent investigation of series-connected organic tandem cells over the recent years. In this sight, solution-processed and series-connected organic tandem solar cells are mainly discussed hereafter.
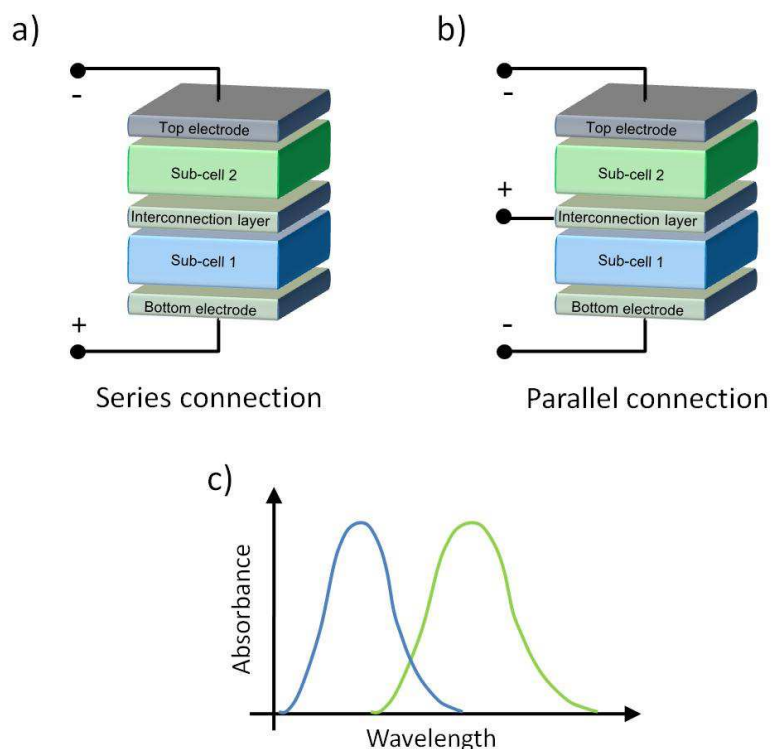
Figure 5.3. Tandem organic solar cells with series- (a) or parallel- (b) connected sub-cells; c) representative complementary absorption spectra of the sub-cells.

Working principle and limitations

According to Kirchhoff's law, the series connection implies that the Voc of the tandem is the sum of the sub-cells' Voc. For an effective series connection, opposite charge carriers coming from the bottom and the top sub-cells should recombine through an interconnecting layer (ICL) which acts as an intermediate contact (also called *recombination layer*). However, if the sub-cells photo-generate different amounts of charges at a fixed voltage, unbalanced recombinations occur. This means that charges accumulate inside a sub-cell with subsequent generation of recombination regions, which detrimentally influence the quality of the overall charge collection processes inside the tandem device. This is indeed of relevant importance for the efficiency of the tandem, highlighting the strong dependence of the tandem performance on the Jsc and FF of the sub-cells.

In a simplified view, considering differently performing sub-cells, two extreme cases can be considered:[183]

- the combination of a bottom sub-cell characterized by low Jsc_1 and high FF_1, and a top sub-cell with low FF_2 and high Jsc_2 (Figure 5.4a);

- the combination of a bottom sub-cell limited by a low FF_1 and low Jsc_1, while a top sub-cell showing both high FF_2 and high Jsc_2 (Figure 5.4b).

As the current flowing in a tandem architecture is the same throughout the device, an horizontal line can be drawn at each point of the J - V plots of the sub-cells in order to obtain the J - V response of the resulting tandem device. As shown in Figure 5.4a, when a sub-cell with low Jsc_1 and high FF_1 is combined with a second cell having high Jsc_2 and low FF_2, the Jsc of the resulting tandem is limited by the Jsc_1 while the FF is similar to that of the first sub-cell (FF_1). On the contrary, in the second case (Figure 5.4b), the use of a sub-cell with low FF_1 and Jsc_1, strongly affects the FF of the tandem which, however, shows a high Jsc arising from the remarkable Jsc_2 and FF_2 of the second sub-cell.

In this sight, the incorporation of two solar cells with complementary absorbing active layers in a double-junction architecture is not a sufficient condition to obtain well performing tandem devices. Indeed, to fully exploit the potential of the double-junction, a fine balance of the sub-cell characteristics is needed.

Moreover, as polymer-based BHJs are typically characterized by broad absorption spectra, a partial overlap of the absorption of the bottom and top sub-cells is expected. This reduces the amount of solar photons reaching the top sub-cell thus limiting the tandem OPV response. In this view, an optimization of the optical properties (*e.g.* the BHJ thickness) of each sub-cells is also required. Computational methods represent a powerful tool to provide precious information on the tandem Jsc as a function of the BHJ thickness (and spectral response) of each sub-cell, avoiding a large systematic experimental work. Nonetheless, it is worthy to note that the modulation of the optical properties on a sub-cell has also an impact on its electrical properties since an eventual reduction or increase of the BHJ thickness to tune its optical absorption, also influences the size and composition of the BHJ nanodomains. Hence, properties such as charge photo-generation and transport across the BHJ are subsequently modified.
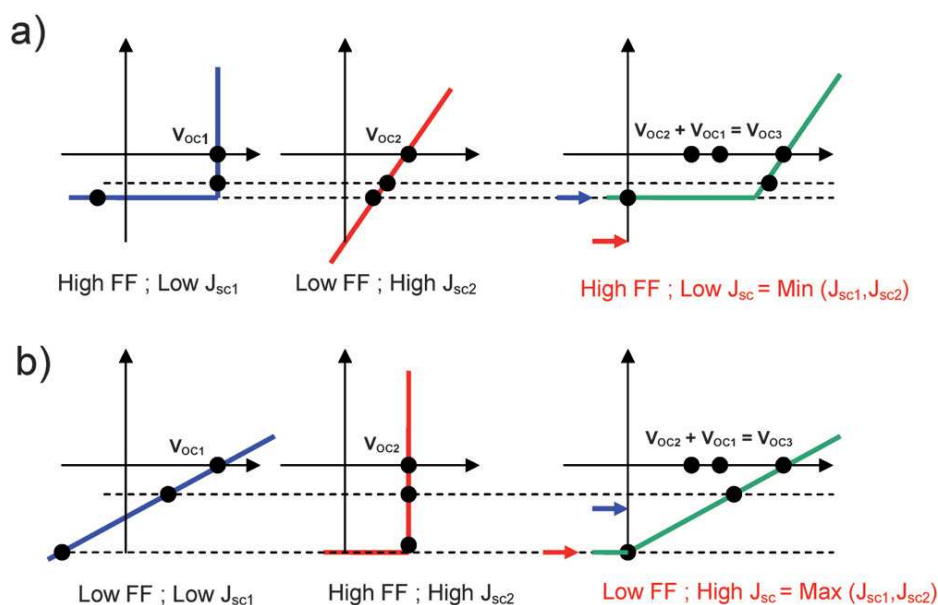
Figure 5.4. Schematic J - V plots of two potential sub-cells and of their incorporation in tandem architecture; two extreme cases are reported. Reproduced from Ref. [183] with permission of The Royal Society of Chemistry.

The interconnecting layer

In an organic tandem device, the two monolithically piled sub-cells are electrically connected through the insertion of an intermediate contact (ICL). This ensures the series connection through the recombination of opposite charge carriers coming from the two sub-cells.

In the first studies on organic tandem devices, a thin layer of an evaporated metal was used as ICL.[184] Since the solar photons transmitted from the bottom sub-cell should pass through the ICL and reach the top sub-cell, the thickness of the metal was limited to few nanometers to ensure a moderate transmittance. The metallic behavior of the ICL offered a good electrical connection between the sub-cells.

However, an important issue was related to the lack of charge selectivity of the metal determining the recombination of most of the charges generated in the proximity of the ICL, with subsequent reduction of the photovoltaic efficiency.

In sight of this, charge selective ICLs were introduced. A typical ICL is composed by, at least, two layers which selectively extract one type of carriers from each sub-cell thus favoring an effective recombination of opposite charges (Figure 5.5).[185][186] In this approach, an electron (n- type) and a hole (p-type) transporting layer are typically sandwiched in order to form a narrow and bent depletion region which favors the transport and recombination of charges at the p/n interface. Following this approach, the

effective operation of the ICL allowed the fabrication of tandem solar cells with a PCE up to 12.7%,[14] the highest value reported for the OPV technology.
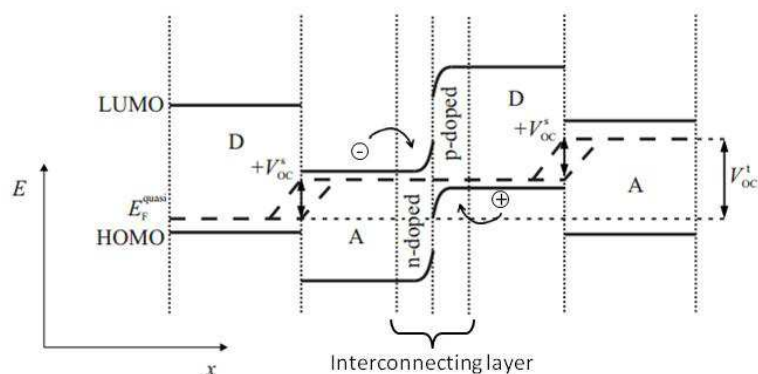
Figure 5.5. Schematic energy level diagram of a tandem solar cell at open circuit conditions using a double-layer as interconnecting layer (ICL).[187]

Despite the necessity of a good charge selectivity and transparency, the ICL should fulfill additional requirements for its incorporation in a tandem architecture.

A summary of the main requirements for the ICL integration in series-connected tandem solar cells is given hereafter:

- the quasi-Fermi levels of the HTL and ETL should be aligned in order that their contact acts as a charge recombination zone;
- the ICL should be characterized by low electrical resistance to minimize potential losses;
- the transport and thus the recombination of opposite charges should be balanced to avoid charge accumulation;
- the ICL should be highly transparent to not hamper the light harvesting in the top sub-cell;
- the optical spacer effect of the ICL should be considered to further enhance the light distribution inside the tandem architecture;
- the HTL and ETL should be chemically/physically inert and robust to protect the underlying layers against the damage from further layers deposition;
- the ICL processing should be compatible with the mass production (*e.g.* roll-to-roll, R2R) requirements, such as solution-deposition, low-temperature processing, environmental resistance, layer thickness ≥ 100 nm, etc.;
- the ICL should be stable under prolonged light/thermal stress to ensure good reliability and lifetime of the corresponding tandem device.

Despite the aforementioned requirements are generally valid for series-connected tandem solar cells, the nature and the processing conditions of the ICL need to be carefully considered and evaluated for each individual system. Indeed, depending on the device configuration, further limitations may be imposed to the ICL. For instance, in a standard configuration, the use of PEDOT:PSS as HTL needs to be carefully considered as the typical acidity of PEDOT:PSS solution can be detrimental for the underlying layer (*e.g.* ZnO).[188]

Considering the device stability, the inverted device configuration is usually preferred. Despite the following works focus on inverted configuration, for the sake of completeness, both the standard and inverted configurations of tandem organic solar cell architecture are reported in Figure 5.6.
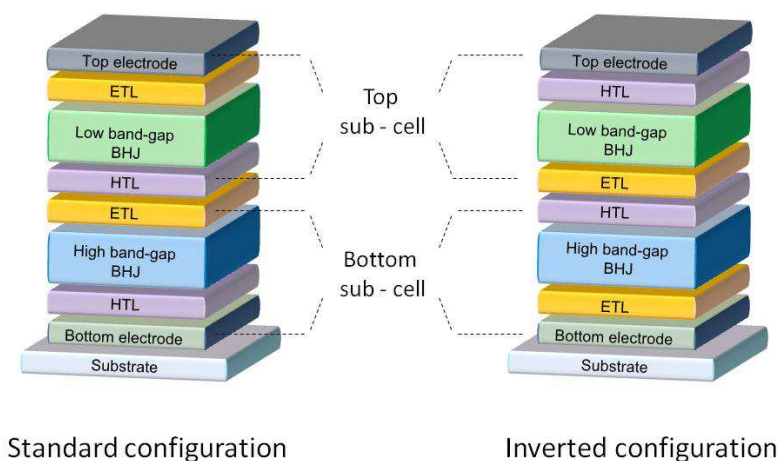
Figure 5.6. Standard (left) and inverted (right) configurations for organic tandem solar cells.

Because of the multitude of requirements for an effective interconnection of the tandem sub-cells, the ICL is one of the most critical parts of multi-junction devices, which still requires deeper investigations.

In this context, during the PhD project two comprehensive studies on this topic were carried out and hereafter discussed. In particular, one work concerns the issues related to the nature and processing of the ICL, while a second study focuses on the ICL physics by facing the electrical problems affecting its operation.

5.2   Optimization of the interconnection layer by solvent treatment of PEDOT:PSS

Aiming to the mass production of organic tandem solar cells, an ICL compatible with R2R processing is necessarily required. As above mentioned, the use of the inverted device configuration is preferred even though the materials selection as ICLs is strongly limited to few options. Among them, the best candidates are PEDOT:PSS and ZnO, respectively as HTL and ETL.[189][190][191] Indeed, both materials can be processed from solution at relatively low temperature, showing good electrical and optical properties in agreement with the aforementioned requirements for an effective ICL.[192]

Despite the promising properties of the selected materials, the use of an inverted tandem configuration requires the deposition of the HTL over the bottom BHJ layer. In this kind of configuration, one of the main challenges is to establish a reproducible procedure for the deposition of a smooth and homogeneous film of PEDOT:PSS on the top of a hydrophobic organic layer. PEDOT:PSS is indeed a water dispersion characterized by high surface tension that typically exhibits a poor wettability over organic surfaces. To overcome this issue, one possibility is to modify the surface properties of the BHJ layer. However, post-processing methods applied to the active layers (*e.g.* solvent washing, plasma treatments, etc.) can compromise their operation and, in addition, are often poorly compatible with processing techniques for large scale production.[189][193] Furthermore, these methods are typically developed for a specific BHJ blend and hence not generally optimized for all the active layers.[194] On the contrary, a more general approach is the surface tension modification of the PEDOT:PSS ink. The addition of alcoholic co-solvents such as isopropanol to the pristine PEDOT:PSS dispersion was demonstrated to lower its surface tension from ≈ 70 mN m^{-1} to ≈ 20 mN m^{-1}.[195] However, large dilutions (typically over 60% v/v of co-solvent in PEDOT:PSS) are required and, to achieve the correct film thickness, several consecutive depositions could be necessary. Moreover, the use of high concentrations of co-solvents can cause aggregation in some PEDOT:PSS formulations and, in addition, the surface tension of the modified ink can still result not suitable to properly wet the organic layer.[195][196] As a result of these limitations, this method cannot be considered generally applicable onto any BHJ.

As alternative approach, the introduction of a surfactant into the initial PEDOT:PSS ink (hereafter named m-PEDOT:PSS for simplicity) is widely demonstrated in literature as an effective method to deposit the PEDOT:PSS over the active layer for single-junction (SJ) architectures.[197] The benefit to use surfactants over co-solvents is that small amounts of surfactant (even less than 1% in weight) are typically sufficient to tune the PEDOT:PSS surface tension with a negligible dilution of the ink. In this approach, the PEDOT:PSS covering the active layer typically acts as top electrode and hence highly conductive inks are preferred. Similarly, for the fabrication of ICLs for tandem devices, low sheet resistive (or high in-plane conductive) formulations have been widely adopted.[198] However, the high in-plane conductivity is not required for the formation of a quasi-ohmic contact between PEDOT:PSS and ZnO therefore the use of highly conductive inks are unnecessary for the ICL of a tandem solar cell.[190] Moreover, low-conductive PEDOT:PSS (*i.e.* Heraeus Clevios P VP AI 4083) when compared to other highly conductive PEDOT:PSS formulations (*i.e.* PH500 or PH1000), besides a slightly lower leakage current, has lower viscosity which facilitates the processability into smooth and homogeneous films.[199][200] However, the use of m-PEDOT:PSS has been successfully reported exclusively with an additional layer of pristine PEDOT:PSS inserted between m-PEDOT:PSS and ZnO.[191] The absence of the additional layer typically led to tandem solar cells with limited photovoltaic performance.[201][202] Due to the presence of the surfactant, a morphological rearrangement of the PEDOT and PSS chains inside the film is known to occur during drying.[203] In detail, the phase separation between PEDOT and PSS increases and a PSS-rich layer forms on the top of the film, even for PEDOT:PSS formulations with low PSS content. This morphological rearrangement, acting similarly to a Schottky barrier, while enhancing the electron blocking properties of the m-PEDOT:PSS by limiting the leakage current and interface recombination in single-junction architectures with standard geometry,[204] could be detrimental for the functionality of the ICL of inverted tandem solar cells.

In this sight, the origin of the resulting electrical losses were analyzed on solution-processed inverted polymer tandem solar cells incorporating an ICL based on ZnO and low-conductive m-PEDOT:PSS, where 1% v/v of nonionic fluorosurfactant (Zonyl FS-300, Chapter 2) was added to the pristine PEDOT:PSS ink.[205] As alternative method, following the literature procedure, the pristine PEDOT:PSS formulation was diluted with various amount of IPA. However, the IPA-modified PEDOT:PSS solution led to films

with poor quality, after the deposition on the active layer, and not working devices were obtained, thus this method was not further considered.

For the fabrication of the tandem solar cells, a high band-gap polymer, HBG-1 (provided by Merck),[121][206] was used as electron donor material for the bottom sub-cell while a low band-gap polymer, PMDPP3T,[207] was chosen for the top sub-cell. The absorption spectra of the resulting polymer:PCBM blends are reported in Figure 5.7a while the device structure is showed in Figure 5.7b.
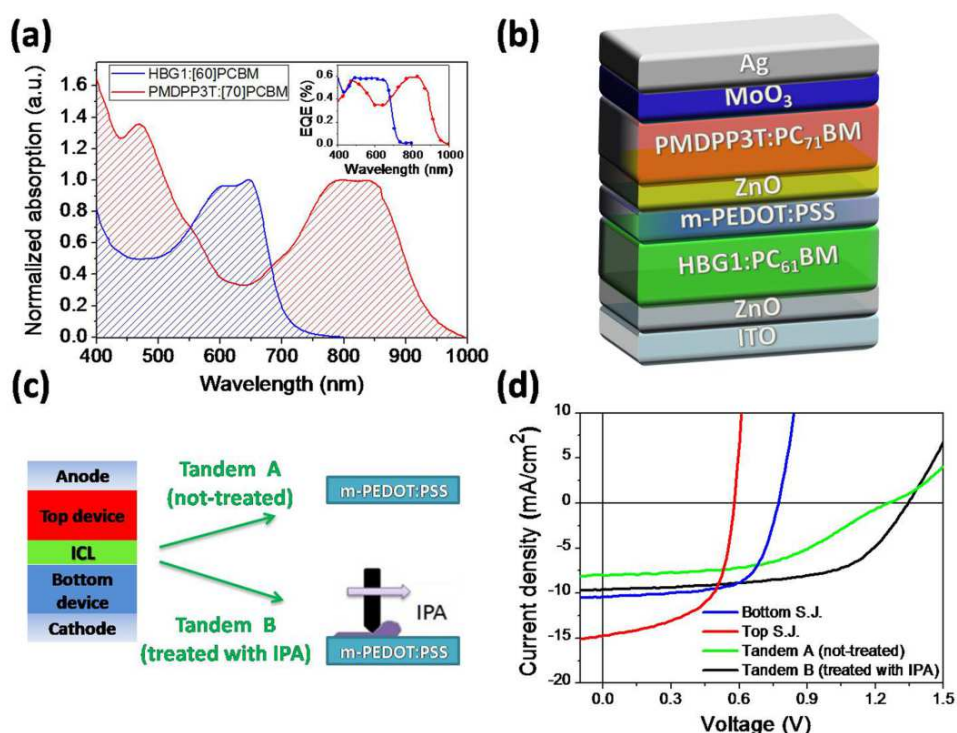
Figure 5.7. a) Absorption spectra of HBG-1:$PC_{61}BM$ (blue) and PMDPP3T:$PC_{71}BM$ (red) films used as active blends respectively of the bottom and top sub-cell of tandem devices; in the inset, their EQE spectra in single-junction architecture is reported; b) representation of the inverted tandem PSCs; c) simplified schematization of the m-PEDOT:PSS used in the ICLs of the reported tandem cells, not-treated (tandem A) or surface washed with IPA (tandem B); J-V plots of the bottom (blue) and top (red) sub-cells in single-junction architecture and the response of the tandem cells using treated (black) or not-treated (green) m-PEDOT:PSS in the ICL.

The relatively low overlap between the absorption regions of the two active layers, in conjunction to the large red-shifted spectrum of the PMDPP3T:$PC_{71}BM$ blend, resulted in a wide spectral absorption of the tandem structure allowing an optimal exploitation of the incident sunlight. This was also confirmed by the EQE profiles of the reference sub-cells in single-junction architecture reported in the inset of Figure 5.7a.

All the devices were fabricated, except the top electrode, by blade coating under ambient conditions. The ICL was optimized in the range of thickness compatible to mass production ($\geq$ 100nm) and using moderate processing temperatures ($\leq$ 80°C). The optimal thickness in terms of photovoltaic performance for the bottom and top active layers was found to be 240 nm and 120 nm, respectively. The same thicknesses were used to fabricate reference solar cells in single-junction architecture (SJ). In detail, for the bottom and top sub-cells, the device structures ITO/ZnO/HBG-1:$PC_{61}BM$/m-PEDOT:PSS/Ag and ITO/ZnO/PMDPP3T:$PC_{71}BM$/MoO_3/Ag were, respectively, used. Figure 5.7d and Table 5.1 show their photovoltaic response.

Table 5.1. Photovoltaic parameters of reference SJ and tandem PSCs averaged over 18 devices.

Device	ICL	J_{SC} [mA/cm^2]	V_{OC} [V]	FF [%]	$PCE_{AV.}$ [%]	PCE_{MAX} [%]
Bottom SJ	-	10.4 ± 0.6	0.77 ± 0.02	62 ± 2	4.9 ± 0.2	5.1
Top SJ	-	14.9 ± 0.5	0.58 ± 0.01	62 ± 2	5.3 ± 0.3	5.6
Tandem A	m-PEDOT:PSS/ZnO	8.2 ± 0.2	1.25 ± 0.03	45 ± 5	4.5 ± 0.4	4.9
Tandem B	IPA-treated m-PEDOT:PSS/ZnO	9.5 ± 0.1	1.34 ± 0.01	60 ± 2	7.6 ± 0.2	7.8

The reference SJ devices showed good photovoltaic performance with an average PCE of 4.9% and 5.3% for the bottom and top sub-cell, respectively. Despite that, the corresponding tandem device showed relatively low performance with a PCE of 4.5% (Tandem A, Figure 5.7c and Table 5.1). In particular, the resulting Voc of 1.25 V, lower than the sum of the Voc of the two sub-cells (0.77 V + 0.58 V = 1.35 V), and the poor FF (45%) indicate that the efficiency is limited by the m-PEDOT:PSS/ZnO ICL, as similarly reported in literature.[201][202] Indeed, the corresponding J - V curve (Figure 5.7d) showed a S-shape, characteristic of charges which accumulate in the ICL and only partially recombine at the m-PEDOT:PSS/ZnO interface. This is likely ascribed to the typical vertical phase segregation induced by the surfactant occurring inside the m-PEDOT:PSS film upon drying, which leads to the formation of a PSS-enriched capping layer where ZnO is then deposited.[203][204] Because of the poor conducting properties of the PSS, this layer acts similarly to a Schottky barrier thus creating a capacitive (rather than ohmic) interface between m-PEDOT:PSS and ZnO in the ICL, which also explains the poor FF of the tandem cells.

In this context, several studies demonstrated the possibility to modify the surface morphology and composition of polymeric films through post-processing methods.[208][209] In particular, by treating PEDOT:PSS films with polar solvents, a modification of the surface distribution of PEDOT and PSS chains was observed.[210][211] In sight of this, different solvents were here used to wash, by blade-coating, the m-PEDOT:PSS surface. We found that the use of highly polar alcoholic solvents such as methanol and ethanol led to macroscopic crack formation in the PEDOT:PSS layer, while the less polar IPA did not macroscopically alter the film surface. However, multiple washing steps with IPA led again to macroscopic damages of the m-PEDOT:PSS film. As a result, IPA was selected as potential good candidate for the washing procedure, representing also a non-toxic, environmentally friendly and inexpensive solvent.[212]

Remarkably, the tandem solar cells where the m-PEDOT:PSS was treated with a single IPA treatment (Tandem B, Figure 5.7d), exhibited a strongly improved efficiency (over 50% compared to the tandem device with untreated m-PEDOT:PSS (Tandem A, Figure 5.7d)), reaching a PCE up to 7.8%. In detail, the Voc (1.34 V) approached the theoretical value while the high FF of 60% and Jsc of 9.5 mA/cm^2 resulted comparable to the values reported by the limiting sub-cells (single-junction architecture).

Considering that all the layers of the tandem devices A and B were processed under the same conditions, the strong efficiency improvement can be ascribed to the enhanced performance of the ICL obtained through the IPA treatment.

For a deeper investigation on the properties of the ICLs based on untreated and IPA-treated m-PEDOT:PSS, the ICL was inserted in devices with specific structures:

- Structure 1 (ITO/ICL/Ag): to investigate the electrical properties, the ICL is comprised between two electrodes;

- Structure 2 (ITO/ZnO/Active layer/ICL/Ag): the ICL acts as a buffer layer of single-junction devices. This architecture is an effective sub-structure of the tandem stack, which is useful to provide detailed information on the overall ICL operation.

As shown in Figure 5.8, the electrical response (I - V plot) of the devices with Structure 1, containing untreated m-PEDOT:PSS, revealed an S-shaped curve typical of a diode-like behavior. On the contrary, when the m-PEDOT:PSS surface was treated with IPA, the devices showed an ohmic behavior where the S-kink in the I-V plot was completely eliminated.
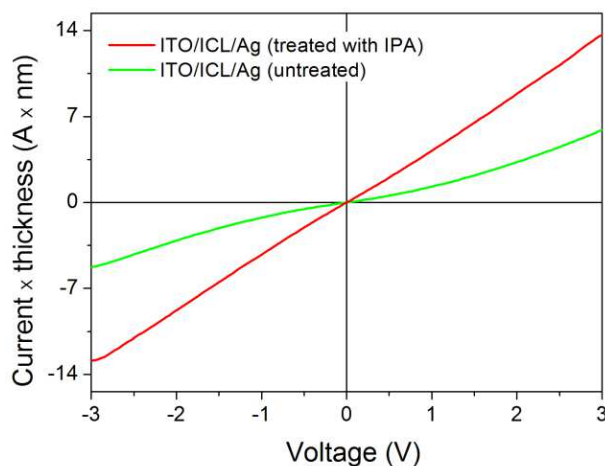
Figure 5.8. I - V response of devices with structure 1, considering the thickness of the layers, where the m-PEDOT:PSS of the ICL is untreated (green line) or surface-treated using IPA (red).

Considering the Structure 2, the HBG-1:PC$_{61}$BM active layer was investigated using the ICL either with or without the IPA post-treatment on the m-PEDOT:PSS (Table 5.2). The resulting response was compared to the single-junction reference bottom cell (Bottom SJ, Table 5.1) from which differed for the presence of an additional selective layer of ZnO between the m-PEDOT:PSS and the silver electrode. The device performance from Structure 2 are expected to be similar to those of the reference cells only if the ICL acts as a selective and ohmic contact. This means that holes and electrons should efficiently recombine at the m-PEDOT:PSS/ZnO interface of the ICL thus avoiding charge accumulation.

In detail, devices using the ICL without any post-treatment (device *a*, structure 2) showed a S-shaped J-V plot with Jsc of 9.4 mA/cm^2, a low Voc of 0.65 V and a FF of 48%, resulting in a poor PCE of 2.9% (Figure 5.9 and Table 5.2), in agreement with the OPV response of the corresponding Tandem A (Table 5.1).

On the contrary, the analogous device containing IPA-treated m-PEDOT:PSS in the ICL (device *b*, Figure 5.9 and Table 5.2) resulted in a higher performance compared to device *a*, with a PCE passing from 2.9% to 4.1%. The greatly improved FF (from 48% to 60%) and Voc (from 0.65V to 0.77V) values clearly demonstrate the positive effect of the IPA treatment on the ICL behavior. To note the resulting photovoltaic response of device *b*, even if slightly lower, was comparable to the reference single-junction solar cells (Bottom SJ, Table 5.1). The main difference was indeed represented by the partial reduction of the Jsc, likely ascribed to the different optical properties and light distribution within the two stacks, due to the presence of an additional layer in device *b*.

The benefits arising from the IPA treatment on the m-PEDOT:PSS were generally validated by using a different active layer in the Structure 2. To this end, the benchmark blend P3HT:PC$_{61}$BM was selected (Figure 5.9 and Table 5.2). Again, while device *c* with untreated m-PEDOT:PSS gave a low PCE of 2%, device *d* which contained IPA-treated m-PEDOT:PSS showed a PCE improvement by ≈ 30%, reaching a PCE of 2.5% (Figure 5.9), in agreement with the OPV response of air-processed P3HT:PCBM solar cells reported in literature.[213]
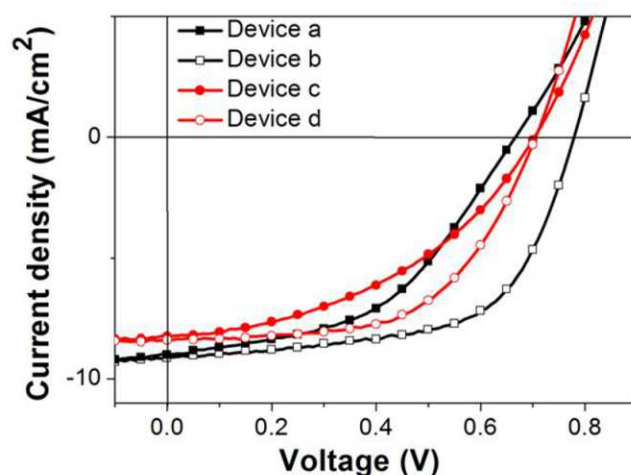
Figure 5.9. J-V plots of devices with structure 2 using HBG-1:PCBM (black, devices *a* and *b*) or P3HT:PCBM (red, devices *c* and *d*) as active layer. The devices present untreated (device *a* and device *c*) or IPA-washed (device *b* and *d*) m-PEDOT:PSS in the ICL.

Table 5.2. Photovoltaic parameters, averaged over 18 devices, of cells using structure 2.

Active layer		SJ devices using structure 2: ITO/ZnO/active layer/ICL/Ag					
	Dev.	ICL	J_{SC} [mA/cm^2]	V_{OC} [V]	FF [%]	PCE$_{AV.}$ [%]	PCE$_{MAX}$ [%]
HBG-1: PC$_{61}$BM	*a*	m-PEDOT:PSS/ZnO	9.4 ± 0.3	0.65 ± 0.2	48 ± 1	2.9 ± 0.1	3.0
	b	IPA-treated m-PEDOT:PSS/ZnO	8.7 ± 0.3	0.77 ± 0.1	60 ± 2	4.1 ± 0.2	4.3
P3HT: PC$_{61}$BM	*c*	m-PEDOT:PSS/ZnO	7.9 ± 0.3	0.54 ± 0.01	46 ± 3	2.0 ± 0.1	2.1
	d	IPA-treated m-PEDOT:PSS/ZnO	8.3 ± 0.2	0.55 ± 0.01	55 ± 2	2.5 ± 0.2	2.6

To shed light on the morphological modifications involved in the PEDOT:PSS layer by the surfactant and IPA-treatment, the surface morphology of the different films was investigated through AFM measurements. As PEDOT:PSS consists of an intermix of hard

PEDOT-rich grains and soft PSS-rich chains, their domains can be distinguished in the AFM phase images. In particular, while PEDOT regions appear as bright areas, the PSS segments result in darker areas.

By comparing the surface morphology of pristine and m-PEDOT:PSS films deposited on ITO, it was evident the different PEDOT and PSS distribution (Figure 5.10). Indeed the surfactant, by screening the Coulombic interactions between the SO_3 groups of PSS and the PEDOT backbone, favors their phase segregation, which causes a stretching of the PSS macromolecules and the formation of elongated aggregates of PEDOT chains randomly dispersed in the layer. Moreover, because of its nature, PSS remains solvated longer than PEDOT during drying and hence the more freely-moving PSS chains emerge on the film surface thus forming a PSS-enriched capping layer.[204] To note, while this process led to a slightly decrease in the sheet resistance of the m-PEDOT:PSS film as reported in literature, it was almost ineffective in terms of bulk vertical conductivity as measured in hole-only devices using the structure ITO/PEDOT:PSS/Au or ITO/m-PEDOT:PSS/Au which respectively resulted 1.6 ($\pm$ 0.2) x 10^{-6} S cm^{-1} and 1.8 ($\pm$ 0.2) x 10^{-6} S cm^{-1}.[214]
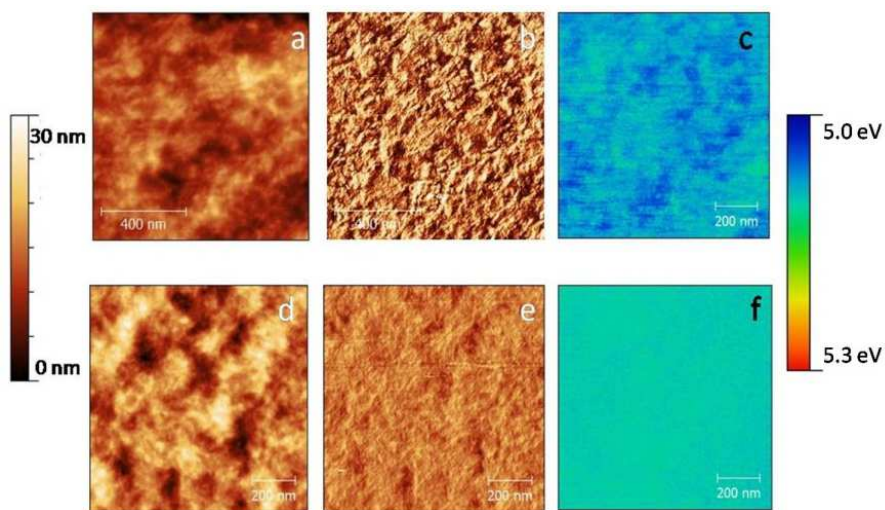
Figure 5.10. AFM topography, phase and KPFM images of m-PEDOT:PSS (a, b and c, respectively) and pristine PEDOT:PSS (d, e and f, respectively) deposited over a glass/ITO substrate.

The IPA treatment on the m-PEDOT:PSS layer determined an increase of the surface roughness from 3.5 nm to 5.7 nm (Figure 5.11a and 5.11b) and a concomitant reduction by $\approx$ 10% of the film thickness (from 100 $\pm$ 4 nm to 90 $\pm$ 4 nm). As already demonstrated in previous works on PEDOT:PSS, post-processing methods using alcoholic solvents

over PEDOT:PSS partially remove the excess of insulating PSS phase at the top of the film while favoring a morphology reorganization of the remaining PEDOT-enriched layer.[210] Here, this process was confirmed by the AFM phase images of untreated and IPA-treated m-PEDOT:PSS films, where a different distribution of the PEDOT and PSS phases was observed (Figure 5.11c and 5.11d).

It is noteworthy that despite the clear effects of the IPA washing on the m-PEDOT:PSS phase distribution, no relevant modifications in terms of thickness (40 ± 2) and morphology (RMS ≈ 7 nm) occurred on the over-deposited ZnO film. This suggests that the aforementioned morphological rearrangement of the m-PEDOT:PSS layer was the main responsible for the improved m-PEDOT:PSS/ZnO interface *via* the reduction of the electrical resistance induced by the insulating PSS capping layer. This is reflected in an improved operation of the ICL which led to great device performance not only for the device structures 1 and 2 but also for the corresponding tandem device B (Table 5.1).
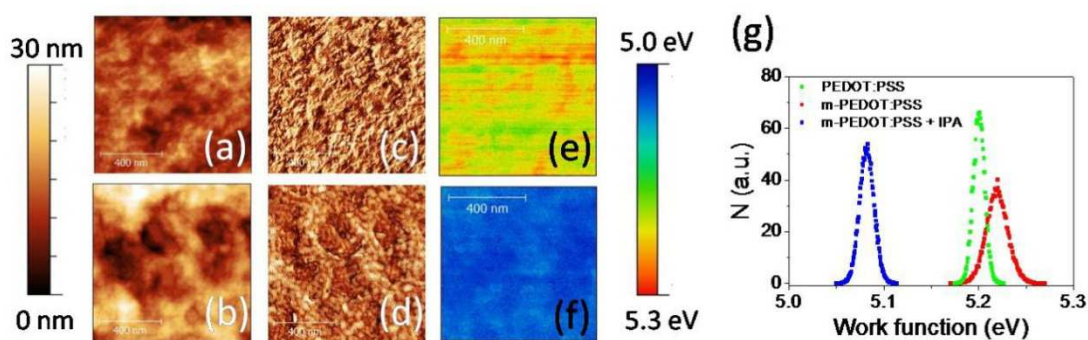
Figure 5.11. AFM topography (a) phase (c) and KPFM (e) images of m-PEDOT:PSS. AFM topography (b) phase (d) and KPFM (f) images of IPA-treated m-PEDOT:PSS; g) histogramof workfunctions measured on pristine PEDOT:PSS (green), untreated m-PEDOT-PSS(red), IPA treated m-PEDOT:PSS (blue).

To further deepen the understanding on the films composition, ATR-FTIR spectra of untreated and IPA-washed m-PEDOT:PSS films were measured and compared to those of the pristine PEDOT:PSS and pure fluorosurfactant (Figure 5.12). The most intense absorption peak of the fluorosurfactant was centered at 1150 cm^{-1} and was attributed to the C-F stretching vibrations. This peak was detected as a shoulder in the spectrum of the m-PEDOT:PSS while it almost disappeared in that of IPA-treated m-PEDOT:PSS film (inset in Figure 5.12). This result clearly indicates that the superficial IPA treatment removes a consistent amount of fluorosurfactant. Indeed, upon drying, the concentration of fluorosurfactant likely increases on the top of the layer to mediate between the film

bulk, enriched with the hydrophobic PEDOT phase, and the film surface, enriched with solvated PSS molecules.

In parallel, the peaks at 1133, 1038 and 1009 cm^{-1} attributed to SO$_3^-$ stretching vibrations and the peak around 1240 cm^{-1} which gets contributions from both PSS and fluorosurfactant, reduced their intensity when passing from untreated to the IPA-treated m-PEDOT:PSS films. These observations confirm the removal of the fluorosurfactant and the depletion of PSS, occurring with the washing treatment, from a superficial layer of the m-PEDOT:PSS film, both processes contributing to lower the electrical resistance of the HTL at the interface with ZnO in the ICL, improving its functionality and enhancing the performance of the corresponding tandem device.

A further confirmation of the partial removal of PSS chains with the IPA surface washing arose from the absorption spectra (see ref. [205]). The intensity of the absorption peaks at 195 and 220 nm, attributed to PSS,[215] decreased when passing from the untreated to the IPA-washed m-PEDOT:PSS films. On the contrary, the spectrum in the infrared region, characteristic of the PEDOT phase absorption,[216] remained constant in intensity for both films. It is worth mentioning that the enhanced functionality of the ICL and the relative improved photovoltaic performance of the tandem cells obtained after the IPA treatment were not related to optical effects induced by the thickness variation (optical spacer effect) of the m-PEDOT:PSS and of the relative ICL. Indeed, additional devices similar to Tandem A were fabricated using different thicknesses for the ICL (in particular for m-PEDOT:PSS). However, in all the cases the device PCE resulted lower than that of Tandem B.

All these findings confirmed that the removal of the fluorosurfactant and the depletion of PSS occurring with the IPA treatment were the responsible for the lower electrical resistance of the m-PEDOT:PSS layer and for the improved interface with ZnO, enhancing the ICL functionality and thus the overall performance of the corresponding tandem solar cells.
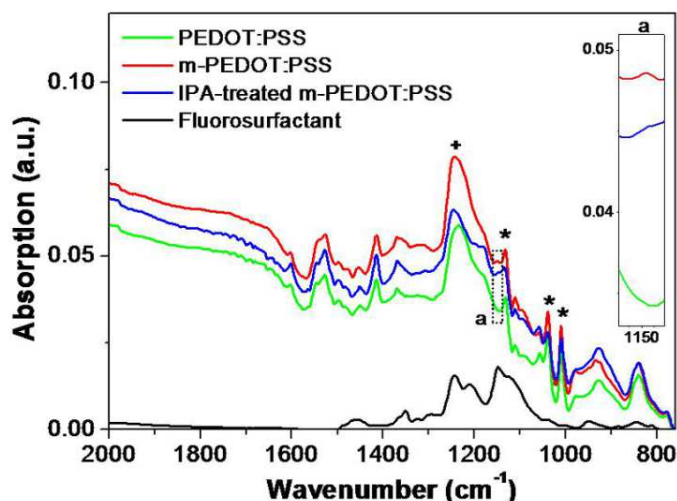
Figure 5.12. ATR-FTIR spectra of films of pristine PEDOT:PSS (green), m-PEDOT:PSS (red), IPA-treated m-PEDOT:PSS (blue) and pure fluorosurfactant (black). The most relevant absorption peaks are indicated as follows: 1240 cm^{-1} (+), 1133, 1038, 1009 cm^{-1} (*). Inset (a): zoom on the absorption at 1150 cm^{-1} of all the films except that with fluorosurfactant.

The change of the morphology and composition of the m-PEDOT:PSS surface with IPA treatment is expected to affect also the work function (WF), which is crucial for the functionality of the PEDOT:PSS/ZnO interface in an efficient ICL. KPFM provides information about local changes in WF at the m-PEDOT:PSS surface. Figures 5.11e and 5.11f show the KPFM images of m-PEDOT:PSS and IPA-treated m-PEDOT:PSS films, respectively, acquired in parallel to the corresponding topography and phase images, while the distribution of the relative WF values is shown in Figure 5.11g. For comparison, the WF distribution obtained from KPFM measurements in pristine PEDOT:PSS deposited on a glass/ITO substrate was also plotted. The latter served as reference (WF of PEDOT:PSS = 5.20 eV, as calculated from the peak value) to determine the offset in the conversion from KPFM contact potential difference to WF. From the analysis on these data, it was observed that *i)* the treatment with the fluorosurfactant led to a broadening of the WF values distribution combined with a slight shift of the peak WF (WF of the m-PEDOT:PSS = 5.23 eV as calculated from the peak) (Figure 5.10f , 5.10c and 5.11g) and *ii)* the washing with IPA shifted the peak WF to lower values (WF of IPA-treated m-PEDOT:PSS = 5.08 eV, as calculated from the peak) and narrowed again the WF distribution, which became similar to that of pristine PEDOT:PSS.

We believe that the inhomogeneous distribution of the surfactant within the m-PEDOT:PSS layer cannot significantly contribute to the shift of the WF. Rather, the concentration gradient of PSS from the bulk to the surface of the m-PEDOT:PSS film

induced by the surfactant, acting similarly to a weak surface dipole,[199][204] can be responsible for the observed slight shift (by 0.03 eV) of the peak WF. In addition, the redistribution of PSS and PEDOT phases when passing from pristine PEDOT:PSS to m-PEDOT:PSS caused the observed broadening of the electronic levels with energy around the WF, leading to the observed weak performance of the corresponding ICL. On the contrary, the IPA treatment restored a narrower WF distribution with a shift of the peak towards lower values by 0.15 eV. The shift was attributed to three main effects: *i)* the partial removal of the excess of PSS phase on the top of the m-PEDOT:PSS film, *ii)* the morphological reorganization of the PEDOT and PSS chains and, *iii)* the removal of the superficial fluorosurfactant.[211][217][218]

Interestingly, the WF shift induced by the washing with IPA brought closer the WF of treated m-PEDOT:PSS (5.08 eV) and ZnO (3.9 eV), favoring the charge recombination at the HTL/ETL interface through the formation of a quasi-ohmic contact, in agreement with the electrical characterization (both substructures and tandem cells) previously described.

The improved ICL operation was also favored by the enhanced electrical behavior of the m-PEDOT:PSS after IPA treatment as revealed by the doubled vertical conductivity, which passed from 1.8 ($\pm$ 0.2) x 10^{-6} S cm^{-1} for the untreated m-PEDOT:PSS to 3.6 ($\pm$ 0.2) x 10^{-6} S cm^{-1} for the IPA-treated m-PEDOT:PSS. This arose from the partial PSS removal and the subsequent reorganization of the PEDOT chains into a more ordered and conductive conformation, which contributed to increase the vertical conductivity of the corresponding film.

The presented results confirm that by simply washing the surface of the m-PEDOT:PSS layer with IPA, morphological and compositional changes in the m-PEDOT:PSS film occurred. In particular, the partial dissolution of the PSS superficial insulating chains, the removal of fluorosurfactant and the conformational reorganization of the PEDOT and PSS chains led to a strong improvement of the functionality of the resulting m-PEDOT:PSS/ZnO ICL by a combination of factors: the optimization of the WF match between the HTL and the ETL, the

formation of an ohmic contact at the HTL/ETL interface and the improvement of the HTL vertical conductivity. The ICL with enhanced functionality led to the improved efficiency (approaching 8%) of the HBG-1:PC$_{61}$BM/PMDPP3T:PC$_{71}$BM-based tandem devices, completely deposited (except the top electrode) by doctor blade in air, whose m-PEDOT:PSS layer of the ICL was post-processed with IPA.

In conclusion, we successfully demonstrated a facile and scalable method based on a simple surface washing procedure with IPA to improve the performance of a solution-processed ICL. The resulting robust ICL based on m-PEDOT:PSS and ZnO nanoparticles had a total thickness of 140 nm, was environmentally stable and needed a low annealing temperature for optimized performance, thus meeting the requirements for large scale production.

5.3 Investigation of the electrical losses in ICLs by photocurrent and electroluminescence analyses

In tandem solar cells, a fine balance between the optical and electrical properties of all the layers is the core of a proper device operation. However, the complexity of the device structure makes this process complicated. While preliminary information on the BHJs properties, for their integration in a tandem structure, are usually obtained on the basis of optical simulations and from the OPV response in single-junction architecture, the optimization of the ICL operation is usually a trial and error process developed in the complete tandem device. In sight of this, the realization of well performing tandem cells is usually an elaborated procedure consisting in the systematic fabrication of different and numerous devices.

Despite a consistent amount of studies focused on the ICLs of multi-junction solar cells, a clear illustration of the processes involved in the intermediate contact is still lacking.[185][219][190][186] This demonstrates the need of a deeper understanding of the physics of the system, which would be beneficial both in terms of device processing and photovoltaic efficiency. The main limitations arise from the position and role of the ICL within the tandem architecture, which make difficult an individual analysis of the ICL by neglecting the contributions from the rest of the device.

A possible approach to selectively study the ICL is through an electrical contact with an external output, *i.e.* using a three terminal connection for the tandem device.[220] Despite this method offers the great advantage to selectively investigate the ICL during real operation, it requires the introduction of an additional conductive layer placed between the HTL and ETL able to furnish the external electrical connection. Since the device structure is adapted to provide an additional external connection, the optical and electrical

processes inside the device may differ from those occurring in the "original" tandem cell (series-connected).

As alternative approach, the incorporation of the whole ICL in single-junction architecture acting as charge selective unit was proposed as a simplified method to investigate the ICL operation (Figure 5.13).[221] Indeed, through the OPV response of this device, information on the ICL operation can be obtained by avoiding the fabrication of a complete tandem stack. This type of solar cell can be considered as a tandem sub-structure. Indeed, while in a complete tandem, the ICL should ensure a selective electrical connection of the two sub-cells, in this sub-structure, the device functioning is ensured only if the ICL allows the flow of one type of charge carriers to the electrode, substantially miming the real operating conditions.
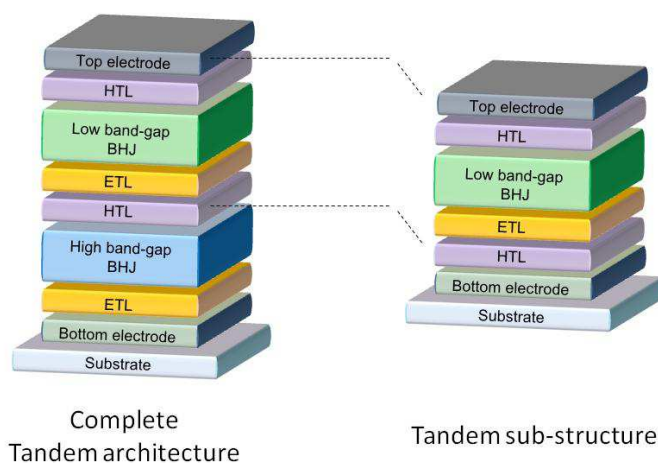
Figure 5.13. Representation of the complete tandem architecture (left) and sub-structure (right).

The use of tandem sub-structures results very useful for a preliminary optimization of the ICL operation. However, several interlinked processes typically occur in a complete tandem device during operation. For instance, the use sub-cells with different photovoltaic responses might determine a different distribution of the electric field within the structure during operation. In this sight, the analysis of the J-V response of tandem sub-structures could be not sufficient to study the complex mechanisms occurring in the ICL of a complete tandem cell.

To this end, hereafter is presented a method developed during the PhD project to investigate the electrical losses of the ICL, which are responsible for the reduction of tandem performance without affecting the photovoltaic response of the corresponding sub-structures.

The approach consists in the analysis of the photo-generated current of tandem substructures in the region of bias over the device Voc (1st quadrant, Figure 5.14), where the solar cell acts as a light emitting diode.

Theoretical background

The photovoltaic performance of organic solar cells are usually analyzed through the response of the device, in terms of photo-generated current density, to different applied biases (J - V plot). The analysis of the current density as a function of the voltage, $J_{illum}(V)$, includes all the processes of charge generation, extraction and injection occurring in the device, thus accounting for both the response to the illumination and the diode characteristics. Hence, the different contributions can be divided in a photo-generated current density (J_{ph}) due to the flux of incident photons and a current density arising from the applied bias, which corresponds to the response of the device in the dark (J_{dark}) (Equation 5.1 and Figure 5.14).[222][223]

$$J_{illum}(V) = J_{ph}(V) + J_{dark}(V)$$ 5.1

In reverse bias, injection of charges in the solar cell is largely inhibited and the total current under illumination is mainly determined by the extraction of photo-generated carriers ($J_{illum} \approx J_{ph}$) (3rd quadrant, Figure 5.14). On the contrary, under forward bias, charges start to be partially injected into the device until a certain threshold voltage at which the diode allows the full injection of charges from the electrodes (1st quadrant, Figure 5.14). As a consequence, the processes occurring inside the device drastically change. Indeed, if illuminating the solar cell at this voltage regime, injected and photo-generated charges are simultaneously present in the device. While the photo-generated charges dominate over the injected ones before reaching the device Voc ($J_{illum} \approx J_{ph}$), by exceeding the Voc the extraction of photo-generated charges is drastically inhibited since they are forced to recombine each other (OLED regime), thus canceling their contribution to the total current density under illumination ($J_{illum} \approx J_{dark}$, for V >> Voc). It means that, in this region, the presence of light does not play any role on the device operation and hence $J_{ph} = (J_{illum} - J_{dark}) \approx 0$. The specific point at which $J_{ph} = 0$ is named compensation

voltage (V_0), where the number of photo-generated charges balances the amount of charges injected from the electrodes (Figure 5.14).
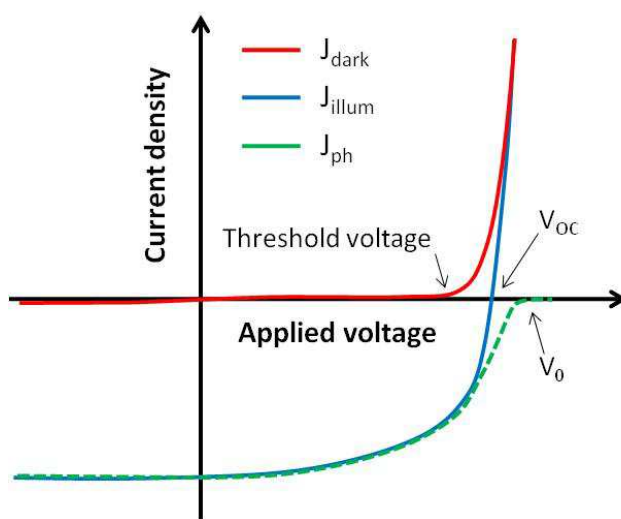
Figure 5.14. Simplified representation of J_{illum} (blue), J_{dark} (red) and J_{ph} (green) as a function of the applied bias. The arrows indicate the voltage threshold, the device Voc and the compensation voltage V_0.

Despite a solar cell biased at voltages higher than the Voc is not under its working regime, the investigation of the device operation in these conditions can provide useful information on possible electrical losses.[224] The electric field (V > Voc) typically drives the photo-generated charges towards the electrodes where they are minorities (holes towards the cathode and electrons towards the anode) and their collection is typically suppressed by the presence of (buffer) selective layers (see paragraph 1.2.1). However, an eventual sub-optimal operation of the buffer layers at this voltage regime would permit the extraction of photo-generated charges at the "wrong" electrodes and, by focusing on the J_{ph}, a positive current is detected. As a result, the analysis of the $J_{ph}(V)$ at $V > V_0$ gives the possibility to visualize eventual electrical losses in the charge selective interlayers which would be typically not detected under the standard operation regime since the internal electric field favors the correct charge extraction in the solar cell.

To validate the reported concept, inverted single-junction solar cells based on PCDTBT:PC$_{61}$BM as BHJ layer were fabricated using different ETLs: *i)* no ETL, *ii)* ZnO, *iii)* PEI or *iv)* ZnO/PEI (Figure 5.15a). The OPV responses of the resulting devices were first investigated in view to analyze their corresponding J_{ph} (V) behavior.
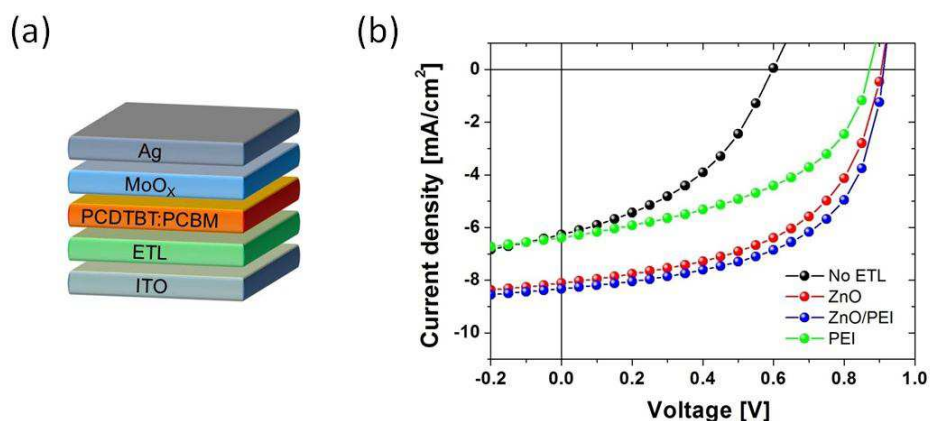
Figure 5.15. Device structure (a) and relative J-V plots (b) of PCDTBT:PC$_{61}$BM-based solar cells using different ETLs: *i)* no ETL (black), *ii)* ZnO (red), *iii)* ZnO/PEI (blue) or *iv)* PEI (green).

Table 5.3. OPV parameters of inverted single-junction cells based on PCDTBT:PC$_{61}$BM and using different ETLs.

Active layer	ETL	J$_{SC}$ [mA/cm^2]	V$_{OC}$ [V]	FF [%]	PCE [%]
PCDTBT:PC$_{61}$BM	-	6.2	0.59	41	1.5
	ZnO	8.4	0.90	56	4.2
	PEI	6.4	0.88	48	2.7
	ZnO/PEI	8.3	0.91	57	4.3

As discussed in Chapter 1, the total absence of an ETL allows the collection of photo-generated holes at the interface with the cathode, thus determining the recombination of opposite carriers with a subsequent reduction of the solar cell performance. According to that, PCDTBT:PCBM-based solar cells without any ETL over the ITO electrode indeed exhibited a poor PCE of 1.5%, as a result of limited Jsc, Voc and FF (Table 5.3).

On the contrary, the use of a ZnO layer as ETL led to solar cells with performance comparable to those reported in literature.[119][59] In detail, a device efficiency over 4% with a Jsc of 8.4 mA/cm^2, Voc of 0.90 V and FF of 56% was obtained. By replacing ZnO with PEI, an expected reduction of the photovoltaic efficiency (2.7%) was observed. This may be ascribed to the slightly different properties of the PEI (compared to ZnO), which should be suitably optimized on the basis of the corresponding device characteristics. Indeed, the layer thickness, surface roughness, polarity and homogeneity of the PEI film are key parameters that largely influence the device operation.[225][226] However, the achievement of the best device performance is beyond the aim of this work, while materials showing different electron transport properties are here preferred.

Finally, optimal OPV responses were recorded by using an additional layer of ZnO between the PEI and the ITO electrode. The ZnO/PEI bi-layer resulted the most effective charge selective unit, among the investigated ETLs, leading to solar cells with PCEs up to 4.3%.

Since the reported PCDTBT:PC_{61}BM-based cells differ exclusively for the type of ETL, the observed differences in terms of OPV response are clearly ascribed to the related mechanisms of charge extraction within the devices.

While the ZnO or the bi-layer ZnO/PEI appeared to ensure an effective solar cell operation, the use of an individual layer of PEI or the total absence of ETL drastically limited the charge collection process of the corresponding solar cells. In this sight, the J_{ph} (V) of the reported solar cells was measured with particular attention on its trend in the region over V_0.

Despite J_{ph} – V curves can in principle be obtained from the difference between the J – V plots measured under illumination and in dark conditions (Equation 5.1), this method is typically not accurate. Indeed, a mismatch in the temperatures under which J_{illum} (V) and J_{dark} (V) are measured, results in an erroneous estimation of J_{ph} (V).[222] For this reason, J_{ph} was calculated by measuring EQE spectra at different applied biases. Indeed, when the device is biased at a defined voltage, the integration of the relative EQE spectrum corresponds to the J_{ph} of the solar cell at that voltage. This arises from the use of a pulsed light, which induces the device to operate under light conditions only at a certain frequency over time. Through the lock-in amplification of the proper electrical phase, the device current density at that frequency is measured while the dark current is suppressed. This corresponds to the difference J_{illum} – J_{dark} which represents the J_{ph} at a defined voltage. By integrating the EQE spectra of the solar cell taken at different applied biases, the J_{ph} – V plot can be created point-by-point.[227] To note, a time-step of 175 Hz from a square wave modulated LED illumination was selected since demonstrated accurate J_{ph} measurements due to negligible thermal contributions during the EQE acquisition (Chapter 2).[222]

To compare the J_{ph} (V) characteristics of the different solar cells, their J_{ph} (V) was normalized to the maximum photocurrent at -1 V in order to eliminate eventual differences related to optical processes in the devices.[223] At this reverse bias, almost all the photo-generated carriers are collected and $J_{ph} \approx qGL$, where q is the elementary charge, G is the generation rate of free carriers and L is the active layer thickness.
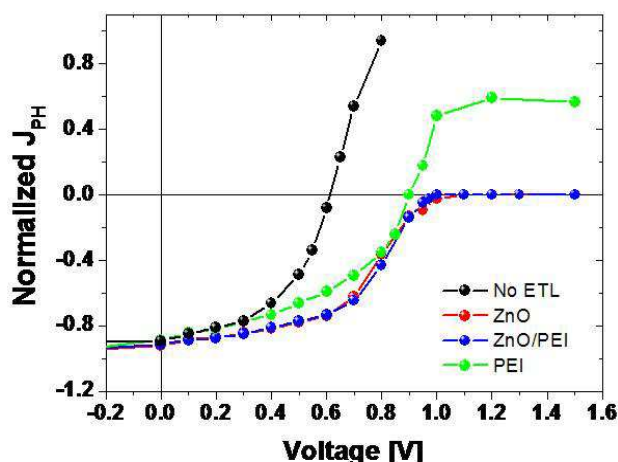
Figure 5.16. J_{ph} – V plots for solar cells using different ETLs: i) no ETL (black), ii) ZnO (red), iii) ZnO/PEI (blue), iv) PEI (green); the curves are obtained from the integration of EQE spectra by biasing the device at defined voltages. All the curves are normalized to the maximum photocurrent at -1 V.

As shown in Figure 5.16, the J_{ph} – V plots of the solar cells at $V < V_0$ were consistent with the corresponding J – V plots measured under standard illumination (Figure 5.15b). On the contrary, the behavior of J_{ph} at $V > V_0$ resulted rather different. While J_{ph} canceled over V_0 for solar cells using ZnO or ZnO/PEI as ETL, a positive J_{ph} was observed for devices without any ETL or containing a PEI layer. In detail, solar cells using PEI as ETL exhibited a J_{ph} reaching a positive *plateau* at 0.5 (relative unit) while a J_{ph} over 0.8 was reported from cells lacking of an ETL. It was difficult to measure further values since the devices degraded due to switching effects.[223]

The presence of a positive J_{ph} at $V > V_0$ means that charge carriers, which exclusively originate from light irradiation, are collected at the electrodes where they are minorities. This can originate from several causes. Simulated studies showed that injection barriers, surface recombination velocity, trap states and series resistance of both the BHJ and electrodes are parameters that strongly influence the shape of the J_{ph} – V plots.[224][223][228] However, in this work, solar cells differ only for the ETL whereas the rest of the device is maintained constant. This allowed to ascribe the differences in the J_{ph} (V) exclusively to the blocking capacity of the selected ETLs. For solar cells without any ETL, the lack of charge selectivity was expected thus explaining the positive J_{ph} at $V > V_0$. In the case of PEI, the positive J_{ph} at $V > V_0$ confirmed the presence of losses in the mechanisms of the ETL operation. These results were in perfect agreement with the limited OPV response of the corresponding solar cells (Table 5.3) thus highlighting the effectiveness of the J_{ph} analysis at $V > V_0$ as method to detect issues related to the operation of ETLs.

In this context, the process of extraction of photo-generated charges from the electrodes was described by Petersen *et al.*[224] as a buildup of minority carriers at the electrode, which causes an alternation of the electric field and triggers the injection of additional majority carriers from the contact. However, the mechanisms, which cause this process of charge extraction, are manifold and can arise from the presence of injection barriers, trap states, reduced selectivity, nature of the ETL, etc..[223] However, the aim of this preliminary work is not the comparison of the different materials or the evaluation of their properties as ETLs, but rather the validation of the J_{ph} (V) analysis as method to detect the electrical losses eventually present in a charge selective layer.

To note, in the case of single-junction solar cells, the analysis of the J_{ph} (V) is not necessary since eventual losses can be simply detected from the standard J – V characterization of the cells. However, the multitude of parameters governing the J – V response of tandem solar cells does not allow a facile analysis of the operation mechanisms. This, in conjunction with the lack of a selective technique for the ICL investigation, highlights the necessity of characterization methods alternative to the J – V characteristic. In this sight, the analysis of the J_{ph} (V) behavior on tandem sub-structures would represent an innovative approach to individuate eventual losses in the ICL operation.

Investigation of the ICL operation in tandem sub-structures

To further enhance the performance of tandem solar cells towards the theoretical maximum, limitations arising from electrical losses in the ICL need to be addressed. In this sight, a contribution to understand the physics of operation of the ICL is here provided through studies on tandem sub-structures based on PCDTBT:PC_{61}BM as active layer. In detail, four different ICLs were analyzed by combining the following materials: ZnO and PEI as ETLs while two different PEDOT:PSS formulations, Clevios P VP AI 4083 and HIL3.3N, were chosen as HTLs (Figure 5.17a). For the sake of simplicity the PEDOT:PSS formulations are respectively named as *4083* and *HIL3.3N*.

The incorporation of the different ICLs in tandem sub-structures led to similar OPV responses among the resulting devices (data not shown), with PCEs comparable to single-junction reference cells (between 3% and 4%). This indicated negligible differences between the ICLs suggesting their similar and apparently satisfying operation.
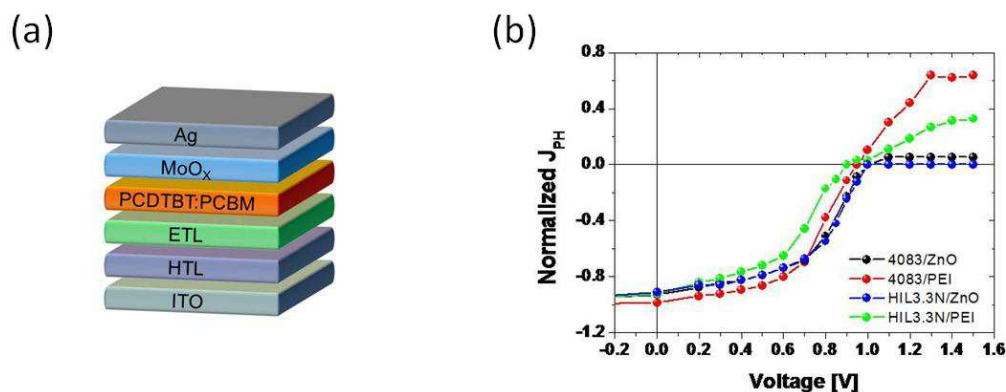
Figure 5.17. Device structure of tandem sub-cells (a) and the relative J_{ph} – V plots (b) using the following HTL/ETL bi-layers as ICL: 4083/ZnO (black), 4083/PEI (red), HIL3.3N/ZnO (blue) and HIL3.3N/PEI (green). The curves are obtained from the integration of EQE spectra by biasing the device at defined voltages. All the curves are normalized to the maximum photocurrent at -1 V.

Interestingly, the analysis of the J_{ph} – V responses showed relevant differences among the reported sub-structures (Figure 5.17b). While devices using the bi-layer 4083/ZnO or HIL3.3N/ZnO as ICL exhibited almost zero J_{ph} at $V > V_0$, the use of PEI instead of ZnO led to positive values of J_{ph} in the same voltage region. The presence of PEI seemed to affect the ICL behavior independently from the formulation of PEDOT:PSS employed in the tandem sub-structures. This was in accordance with the limited OPV response of single-junction solar cells containing PEI as ETL (Figure 5.15 and 5.16).

Diversely from the case of single-junction cells, little electrical issues in the ICL of tandem sub-structures are typically difficult to visualize in the corresponding standard J - V response albeit they identified through J_{ph} – V measurements. On the contrary, in a complete tandem architecture, because of the complex and subtle operation, the full recombination of opposite charges coming from the two sub-cells is indeed fundamental and hence eventual electrical losses, despite negligible in sub-structures even at low electric field (V ≈ Voc), become relevant in the standard J – V response.

The electrical losses in the ICL with negligible effect on the OPV responses (standard J – V analysis) of tandem sub-structures can be possibly caused by: *i)* a behavior as barrier for the injection of charges without limiting the extraction process, or *ii)* the presence of trap states in the ICL.

To distinguish between the two processes, the electroluminescent properties of the reported devices were investigated. This method is a complementary approach to the investigation of the J_{ph} (V).[57][229] Indeed, while in the J_{ph} calculated from EQE measurements, photo-generated charge carriers are <u>extracted</u> from the device, the

electroluminescence arises from the recombination of electrically generated CT excitons via <u>injection</u> of charges into the device.[230] In the latter case, the device is kept under dark conditions and a voltage higher than the Voc (OLED regime) is applied in order to inject charges (J_{dark}) into the diode.

Compared to a barrier-free system, the presence of an eventual injection barrier at the electrode/BHJ interface would result in the need of a higher bias to electrically induce the formation of CT excitons in the device. On the contrary, the presence of a trap state in the ICL does not present any effect on the injection of charges from the electrodes.[231][232][233] To note, as the electroluminescence concerns a light emission from the BHJ, a comparison between the sub-structures was possible as the BHJ nature and processing conditions were the same for all the devices.
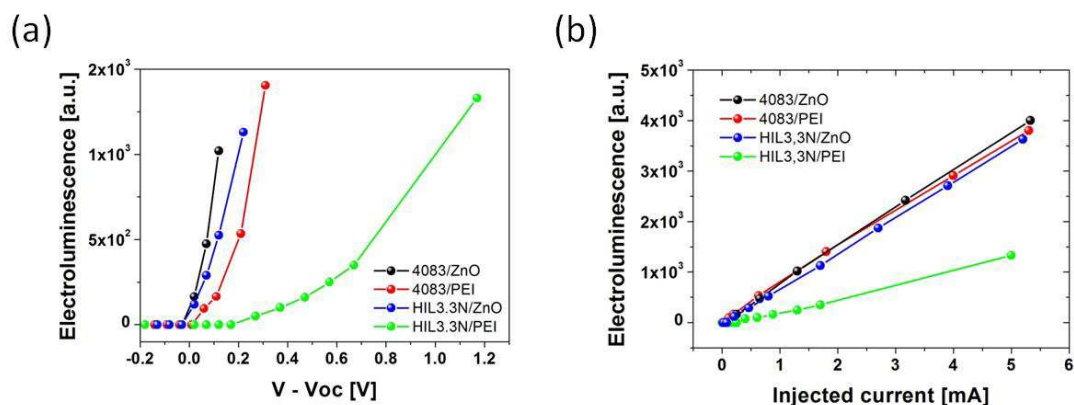
Figure 5.18. Electroluminescence as a function of the bias subtracted of thedevice Voc (a) or as a function of the injected current (b) for the reported tandem sub-structures. The number of counts was measured at 1000 nm, the maximum electroluminescence for all the devices.

As shown in Figure 5.18a, the sub-structures using 4083/ZnO or HIL3.3N/ZnO as ICL exhibited electroluminescence (EL) by applying a bias immediately higher than the device Voc. Similarly, the use of 4083/PEI as ICL reported negligible influence on the electroluminescence response of the relative cells. On the contrary, devices based on HIL3.3N/PEI required additional 0.2 V over the Voc to exhibit electroluminescence. In conjunction with this shift of threshold towards higher voltages, the EL intensity as a function of the applied bias, EL (V - Voc), showed a different trend if compared to that of the other devices (Figure 5.18a). Moreover, as shown in Figure 5.18b, the other devices exhibited a similar linearity of the EL intensity as a function of the injected current, EL (inj. current), while the device containing HIL3.3N/PEI showed a slightly different linear dependence characterized by a higher resistance. The EL (inj. current) linearity

demonstrated a good behavior of the sub-structures diode whereas its lower slope together with the higher bias threshold and the sub-optimal trend of the EL (V-Voc) analysis suggested the presence of an energetic barrier for the charge injection due to the HIL3.3N/PEI ICL.[231][232][233]

Concerning the ICL based on the bi-layer 4083/PEI, the results of electroluminescence demonstrated the absence of issues related to the injection of charges.

As discussed above, an alternative cause of electrical losses in the ICL may be related to the extraction of minority charge carriers via trap states. To evaluate this effect, the Voc of the sub-structure was measured at different light intensities. Indeed, the Voc of well performing devices should theoretically scale as kT/q with the intensity of the standard illumination, where k is the Boltzmann constant and T is the temperature (Chapter 2).[49] The presence of traps increases this dependence which would result in a slope higher than kT/q.[51] From this investigation, a slope of 1.8 kT/q was observed for tandem sub-structures using 4083/PEI as ICL while all the other devices reported a slope of 1.2 kT/q (Figure 5.19). This analysis confirmed the presence of trap states in the ICL (4083/PEI) which explained the extraction of minority charges from the device at $V > V_0$ (Figure 5.17b).
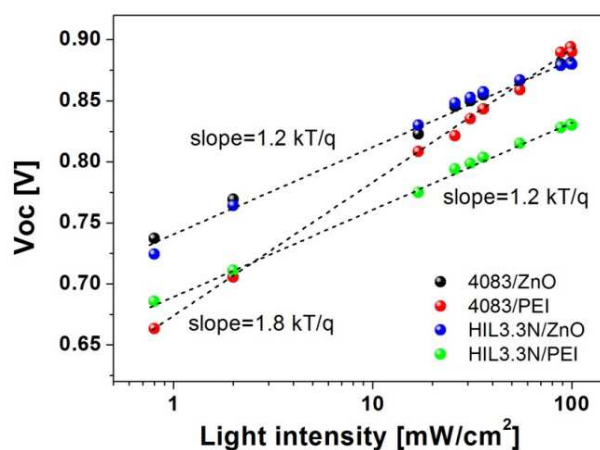
Figure 5.19. Voc of the reported tandem sub-structures as a function of the incident light intensity. The dotted lines represent the fits of the measured data points.

Through the combination of extraction and injection methods performed on tandem sub-structures, the presence and nature of electrical losses in the different ICLs were here demonstrated. However, to prove the effectiveness of this approach, the reported ICLs were introduced in complete tandem cells and their device performances were analyzed. In this sight, a BHJ based on PCDTBT:PC_{61}BM was used for the bottom sub-cell while a

mixture of the low band-gap polymer pDPP5T-2 and the electron acceptor $PC_{71}BM$ was used as BHJ blend for the top sub-cell (Figure 5.21a).

It is noteworthy that in the abovementioned analysis on tandem sub-structures, the ICL was inserted between the bottom electrode (ITO) and the BHJ based on $PCDTBT:PC_{61}BM$. However, in the complete tandem device, a BHJ based on pDPP5T-2:$PC_{71}BM$ was used over the ICL. For this reason, the reported investigations concerning the J_{ph} (V) behavior of the ICLs in tandem sub-structures were repeated by using pDPP5T-2:$PC_{71}BM$ as BHJ. These investigations exhibited results in agreement with those previously reported for $PCDTBT:PC_{61}BM$-based sub-structures (Figure 5.20), confirming again the effectiveness of the proposed method to analyze the ICL quality.
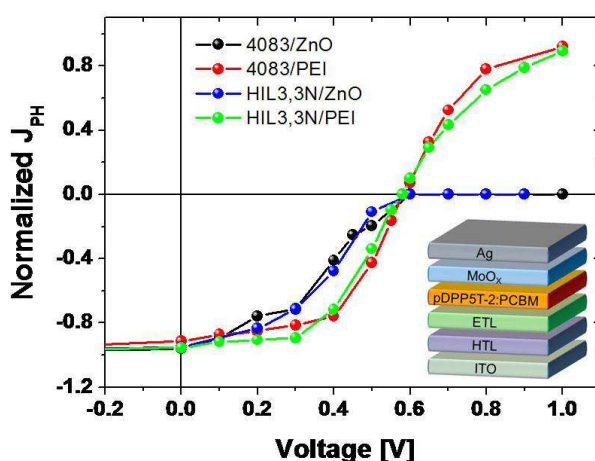
Figure 5.20. J_{ph} – V plots of tandem sub-structures based on pDPP5T-2:$PC_{71}BM$ blends using the following HTL/ETL bi-layers as ICL: 4083/ZnO (black), 4083/PEI (red), HIL3.3N/ZnO (blue) and HIL3.3N/PEI (green). The curves are obtained from the integration of EQE spectra by biasing the device at defined voltages. All the curves are normalized to the maximum photocurrent at -1 V. In the inset, the device structure is reported.

In the complete tandem structure, to avoid eventual limitations due to the deposition of the water-based PEDOT:PSS ink over the hydrophobic BHJ, a thin layer (5 nm) of evaporated MoO_x was deposited over the bottom BHJ in order to optimize the contact at the BHJ/ICL interface. The use of MoO_x indeed provided an optimal connection with the underlying $PCDTBT:PC_{61}BM$ BHJ as confirmed by the above reported results on both single-junction devices and tandem sub-structures where the use of MoO_x as anode interlayer did not exhibit any electrical limitation (Figure 5.16 and 5.17b).

The fabrication of complete tandem solar cells using as ICL the four different combinations of materials led to comparable OPV responses (Figure 5.21b). The similar J

– V curves reflected the modest differences in terms of device efficiency (PCEs between 3.2% and 3.5%).
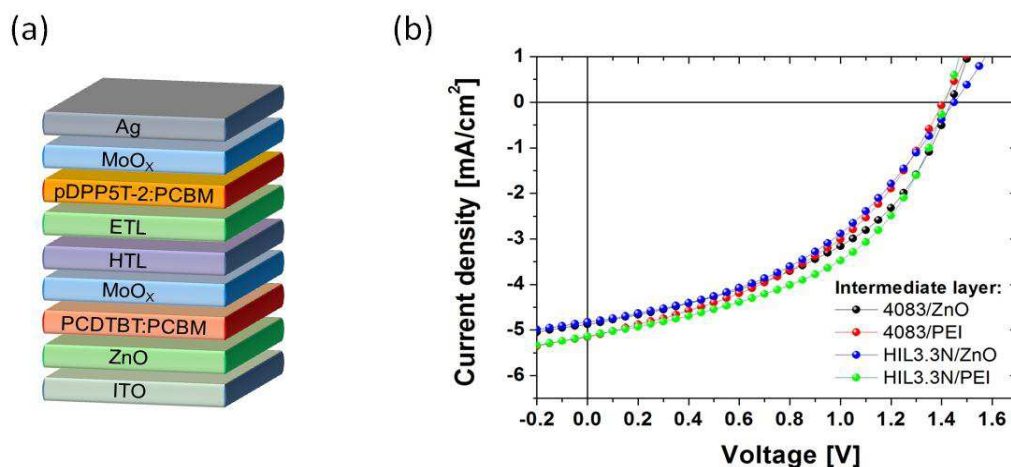
Figure 5.21. a) Representation of the tandem structure and b) J-V plots measured under standard illumination of the relative cells using 4083/ZnO (black), 4083/PEI (red), HIL3.3N/ZnO (blue) or HIL3.3N/PEI (green) as ICL.

However, the presence of minor electrical losses, which affect the ICL operation, are expected to be relevant mainly when the diffusion of charges dominates over drift processes. As a result, the OPV response would be influenced only when the device operates in the regime close to its Voc. According to that, the tandem cells using a layer of PEI in the ICL reported a Voc lower than the other devices based on ZnO in the ICL.

Moreover, the analysis of the tandem Voc as a function of the light intensity reported a slope as high as 2 kT/q for tandem solar cells using PEI in the ICL while 1.6 kT/q for the other devices (Figure 5.22), in agreement with the typical shunt recombination caused by the limited ICL operation. This confirmed the trap-like recombination behavior of the corresponding tandem cells, where the ICL was affected by minor electrical losses, which confirms the effectiveness of the reported approach to reveal the issues of operation of a ICL.

The discussed method represents an elegant and powerful approach operating on tandem sub-structures allowing to visualize and recognize eventual electrical losses, which are of relevant importance to design and develop advanced materials in view of tandem solar cells approaching the theoretical efficiency.
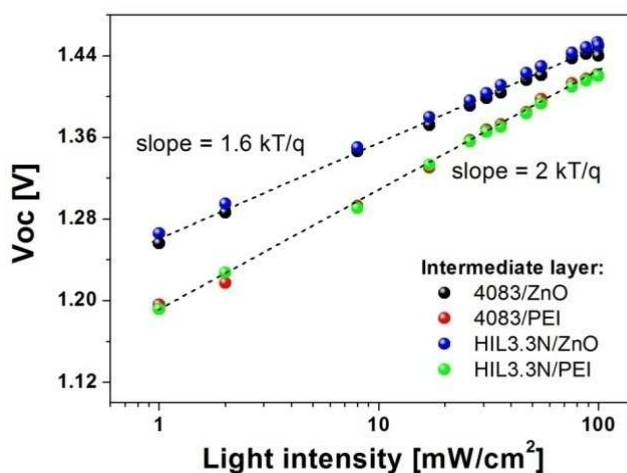
Figure 5.22. Voc as a function of the incident light intensity for tandem solar cells based on different ICLs: 4083/ZnO (black), 4083/PEI (red), HIL3.3N/ZnO (blue) or HIL3.3N/PEI (green). The dotted lines represent the fits of the measured data points.

In this Chapter, the state-of-the-art tandem architecture of PSCs was investigated in view of pushing the solar cell performance towards the theoretical efficiency and obtaining devices compatible with large-scale production processes. Particular attention was devoted to the study of the ICL which currently represents the main limitation of solution-processed tandem polymer solar cells. In detail, a facile and versatile approach for the ICL deposition, fulfilling the R2R requirements, was efficiently demonstrated. Then, an elegant and innovative method to selectively investigate the operation of the ICL revealed the great potential to visualize and recognize the presence of minor electrical losses in the ICL, which were proved to limit the performance of the corresponding tandem solar cells. The combination of an industrial-compatible deposition technique and a fine characterization method for tandem architectures represents a step forward towards the massive production of highly efficient PSCs.

Chapter 6

Environmental impact of organic solar cells

6.1   General overview

The great progress of organic photovoltaics in the past few years heralded this technology as one of the most promising in the emerging scenario. From one side, the advantages of using organic compounds allow for an economic large-scale manufacture of light-weight devices. This reflects into the potential cost-effectiveness of this technology, from the production to the installation of the solar modules. On the other hand, the advantage of avoiding highly toxic substances such as cadmium (Cd), selenium (Se), lead (Pb), etc., present in the other technologies, represents one of the major benefits of organic photovoltaics in terms of sustainability.

However, OPV is still an evolving technology and despite the potential cost of solar modules is predictable from market surveys, their real impact on the environment over the entire life-cycle is more difficult to estimate.[234] Hence the major question to be answered is how "green" organic photovoltaics can be. "Green" is a general term which comprises different meanings besides the environmental impact. In a simplified overview, it includes:

- Sustainability
- Ecological impact
- Bio-toxicology

Sustainability means that the environment, the natural resources and the biological systems should be preserved and last for years in the way that the actual opportunities are provided to the societies of future generations. Therefore, a sustainable technology should avoid the use of fossil sources, since their formation is an extremely long process, or the use of elements with scarce abundance in the Earth's crust. In this context, new technologies not only should exploit renewable energy sources but, more importantly, should use largely diffused and, preferably, recyclable materials. However, to safeguard the integrity of the nature, the influence of the technology deployment on the environment should be considered accordingly. Indeed, during operation, elements with ecological

<u>impact</u> can be produced and released in the environment. Moreover, the production, installation and disposal are phases of a technology directly correlated with the environmental safety since each of them consists of a multitude of sub-processes.

For instance, the fabrication of organic solar modules includes the synthesis of materials, the use of solvents, instruments, etc.. Then, the final module should be transported for the intended application thus including the processes of transport and installation. During operation, the module can suffer of material losses because of the detrimental external conditions. Finally, the disposal/recycling and replacement of the module is required. All these processes include, to some extent, production of CO_2, pollution formation and energy. It is indeed important a deep analysis of all the individual sub-processes to accurate evaluate the ecological impact of a technology. Moreover, despite that, additional parameters such as the <u>biological toxicity</u> should be considered in the evaluation of a technology. This is of relevant importance since the prolonged use of a product can cause unintentional effects as, for instance, the release of elements which can be harmful for the environment and the mankind.

In this complex scenario, considering that organic solar cells exploit the solar energy, which is one of the most promising among renewables, they can be certainly deemed as ecologically sustainable. And, because of the great and easy availability of the solar energy source all over the world, this technology has the additional advantage to be also social sustainable. Moreover, the use organic compounds offer several advantages in terms of processing and properties of the final module, which contribute to a further form of sustainability, *i.e.* the economical one, of relevant importance to ensure an economic growth of the society.

Concerning the environmental impact, one of the main advantages of organic solar cells over the other photovoltaic technologies is the absence of highly toxic elements. In addition, the equivalent CO_2 per functional unit of organic modules produced, rated per kWh of energy generated, amounts to 57.55 g, which is in the same range of the other PV technologies (between 59 and 17 g of equivalent CO_2).[235] However, the environmental impact may arise also from some release of material during operation in outdoor installations. Indeed, some cell components can be released with possible consequences on the environment. This phenomenon is difficult to estimate and systematic investigations are still required. However, it should be considered that organic modules are typically packaged to preserve the operation of the cells, and the thin plastic barriers

used as encapsulation system are properly designed to avoid ingress of water during operation. Only if the physical integrity of the module is affected because of impervious conditions some release may take place. In this case, experimental results indicate that the leach out of silver and zinc are the major implications.[236] Studies on their release into water or soil showed that the Zn concentrations do not even exceed the limit for drinking water thus cannot be considered an issue. On the contrary, more complex is the situation in the case of Ag since critical values were found both in water and soil. Parallel studies estimated the replacement of silver electrodes with carbon-based ones to eliminate any environmental impact. However, the consistently poorer performance of the carbon-based electrodes would represent an important limitation for modules operation. Hence, since silver constitutes a material easily recyclable, its re-use is likely the more advantageous path to pursue.[237]

In this context, the release of compounds in the environment includes also risks associated to the biological activity in the air, water, soil or biota (Figure 6.1). In sight of this, an evaluation of the potential risks were assessed by the consortium of the european project SUNFLOWER that provided preliminary results on the environmental toxicity of nanoparticulate ZnO and PCBM.[20] While PCBM was not evaluated as potentially harmful because of its limited water solubility, the analysis of ZnO nanoparticles in fish cells (in vitro) and in zebrafish (in vivo) demonstrated the induction of the oxidative stress marker gene catalase despite did not evidenced the presence of any apoptotic marker gene.
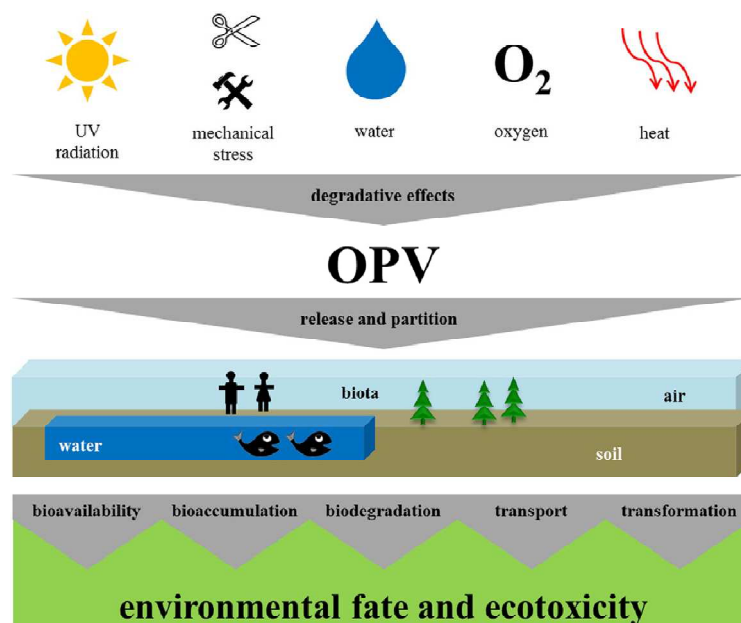
Figure 6.1. Representative factors which can cause degradation in organic photovoltaic devices and the subsequent impact on the environment. Reprinted from Ref. [234], with permission from Elsevier.

Because of the multitude of parameters to consider in order to evaluate how "green" a technology is, a tool which properly incorporates all the factors at all levels was introduced. It is called Life-Cycle-Assessment (LCA) and includes the evaluations of all the processes behind the deployment of a technology, from the raw materials to the end-products, comprising a potential recycling of the materials.[235] The great reliability of the LCA analysis has led to a currently use of this parameter at even the strategic levels, as a tool to assess the sustainability of a technology and support the policies decisions.

However, despite LCA accounts for a multitude of risks associated to the life-cycle of a product, the eco-toxicity of some compounds, especially those at the early phase of research, is unknown to the standard databases and cannot be properly considered. In this context, the synthetic polymers used in organic solar cells are among the materials whose impact is not yet quantified. Moreover, accurate analyses are impossible to provide for all the myriads of organic compounds. Despite that, the highly degradability of these materials under ambient conditions drastically limits the probability of environmental risks. On the contrary, the solvents used to process these materials are typically very harmful, yet a detailed estimation of their ecological impact is mostly unassessable because of the large variety of solvents, additives and mixtures of them, which are employed during the testing phase of new materials.[238] Indeed, regarding the active layer deposition, the viscosity, boiling point (bp) and polarity of the solvent are properties that strongly influence the BHJ morphology and the device performance as a result. In this

context, the most commonly employed solvents are based on halogenated molecules such as chlorobenzene (CB) and 1,2-dichlorobenzene (o-DCB) since they provide an optimal solubility for both the donor and acceptor material present in a BHJ, and show boiling points that allow to modulate the morphology of the active blend during processing. However, the use of halogenated solvents have a dramatic impact on the environment and, furthermore, on human health. They do not exist in nature and hence are more expensive to produce. Moreover, their dangerousness significantly increases the costs for safety equipment and waste disposal in large-scale manufacture.[239] The strong need for greener alternatives led to the search for halogen-free solvents with reduced ecological and human toxicology whereas ensuring an effective solar cell operation. In this context, one of the main issues concerning the use of non-halogenated solvents is their typically low solubility for π-conjugated polymers and fullerene derivatives. Recent studies however showed that methyl substituted benzenes (MBs) represent a class of solvents with good solubility for most polymers.[240] In addition, it has been demonstrated that, by properly adding small amount of solvent additives, the solubility for fullerene derivatives can be also improved. This resulted in environmental friendly PSCs showing performance similar to those of analogous cells processed from halogenated solvents and, in some cases, the use of MBs allowed the achievement of even higher PCEs.[81][241][242] A deep investigation of the effects of non-halogenated solvents on the BHJ can be relevant in view of large-scale application for environmentally friendlier solar cells. In this sight, the role of an eco-friendly solvent on the performance of BHJ solar cells is hereafter discussed through experimental results. Moreover, a parallel analysis on the device stability is also reported since, as demonstrated in Chapter 4, different processing conditions can influence the thermal stability of the resulting organic solar cells. Nevertheless, such additional effects induced by an environmentally friendly solvent are poorly explored in the literature. For this reason a specific study related to this topic is presented and discussed in the following paragraph.

6.2 Effect of environmentally friendly processing on the performance and thermal stability of organic solar cells

Part of this paragraph is adapted with permission from:

M. Seri, D. Gedefaw, M. Prosa, M. Tessarolo, M. Bolognesi, M. Muccini, M. R. Andersson, *J. Polym. Sci. Part A Polym. Chem.* **2016**, *55*, 234.

In view to investigate the properties of BHJs processed from a eco-friendly solvent, a new semiconducting polymer was suitably synthesized and used as electron donor component in BHJ solar cells.[243] The new material is characterized by two different electron deficient units respectively based on a fluorinated quinoxaline (Qx) and an isoindigo (ii) moiety, and an electron rich benzodithiophene (BDT) unit. Thiophene rings were introduced in the structure as π-spacers between the electron rich and deficient building blocks to reduce their steric hindrance and extend the spatial conjugation. The introduction of several alkyl side chains linked to the different structural units ensured to the polymer a sufficient solubility both in common chlorinated and non-chlorinated solvents (> 10 mg/mL in o-DCB or o-xylene), as required for device fabrication.

The molecular structure of the polymer, named PBDTQx-ii, and the synthetic procedure are reported in Figure 6.2 while the number (M_N) and mass (M_W) average molar masses are summarized in Table 6.1. Further details for the material preparation and characterization are reported in ref. [243].
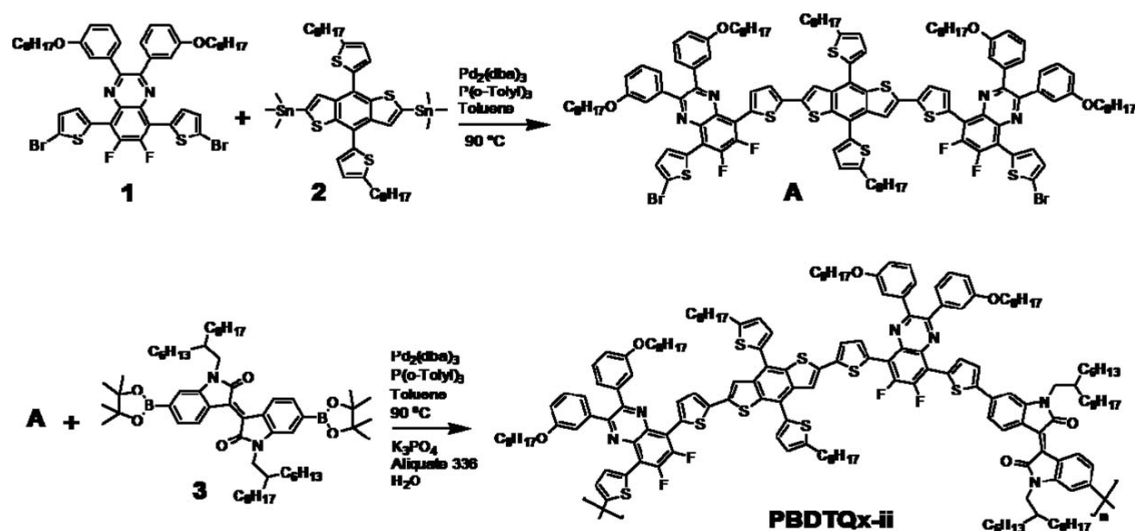
Figure 6.2. Synthetic procedure of the polymer PBDTQx-ii.

Table 6.1. Molecular weight, optical and electrochemical propertie of the pristine polymer PBDTQx-ii.

Polymer	M_N [kDa] [a]	M_N [kDa] [a]	Solution			Thin-film			E_{HOMO} [eV]	E_{LUMO} [eV]
			λ_{max} [nm]	λ_{onset} [nm]	E_{gap}^{opt} [b] [eV]	λ_{max} [nm]	λ_{onset} [nm]	E_{gap}^{opt} [b] [eV]		
PBDTQx-ii	21.4	82.9	633	740	1.67	640	760	1.63	- 5.87	- 3.97

a) Determined by GPC relative to polystyrene standards using 1,2,4-trichlorobenzene as eluent. b) E_{gap}^{opt} = $1240/\lambda_{onset}$.

The HOMO and LUMO energy levels of PBDTQx-ii, investigated through cyclic voltammetry, resulted to be -5.87 eV and -3.97 eV, respectively (Table 6.1). If compared to the similar polymer PFQBDT-TR$_1$ previously reported in literature,[83] PBDTQx-ii exhibited a lower LUMO energy of $\approx$ 0.36 eV (-3.61 eV for PFQBDT-TR$_1$) arising from the strong electron deficient nature of the isoindigo unit where the LUMO orbitals are localized. On the contrary, the HOMO levels resulted similar (-5.89 eV for PFQBDT-TR$_1$) as a consequence of the distribution of the relative orbital over the entire polymer backbone. The presence of a similarly low-lying HOMO suggests a high device Voc when PBDTQx-ii is mixed with PCBM in BHJ solar cells, according to the difference LUMO$_A$ - HOMO$_D$. Moreover, the HOMO energy is in the optimal range to ensure a good air stability of the polymer.[244]

Concerning the optical properties, the polymer PBDTQx-ii showed a relatively broad absorption spectrum both in dilute chloroform solution and as thin film (Table 6.1 and Figure 6.3). This indicates that a consistent part of the solar photons are absorbed and hence can possibly contribute to the photocurrent generation of the corresponding solar cell.

Note that, in agreement with the electrochemical data, the polymer PBDTQx-ii showed a broader absorption with a reduced optical band gap ($\Delta E_{gap}^{opt} \approx$ 0.1 eV) in comparison with the above mentioned reference system PFQBDT-TR$_1$, confirming the benefits arising from the introduction of the isoindigo moiety in the polymer backbone.

The UV-vis absorption profile was based on two main features: a high energy absorption region with two bands between 380 nm and 480 nm, which can be assigned to localized π-π* transitions, and a more intense band at lower energies, between 500 nm and 700 nm, ascribed to the intra- and inter-molecular interactions. This intense band arises from inter-molecular charge-transfer like interactions between the electron-rich and electron-poor moieties and from the inter-molecular interactions between the polymeric chains. Interestingly, the absorption spectrum of the polymer at the solid state was slightly red-

shifted than the relative spectrum measured in solution. The shift of both the absorption onset ($\approx$ 20nm) and the maximum ($\approx$ 7) nm suggests a partial ordering at the solid state which is favorable for the resulting charge transport properties.
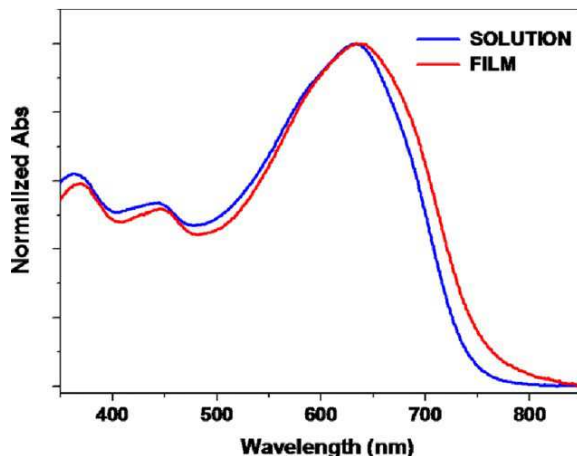
Figure 6.3. UV-vis absorption spectra of polymer PBDTQx-ii, normalized to the relative maxima, in dilute chloroform solution (blue) and as thin film (thickness $\approx$ 60 nm) deposited from chloroform on glass (red).

In order to investigate the effects of a greener solvent, compared to common chlorinated ones, on the device operation and stability, a set of BHJ solar cells were fabricated using a mixture of PBDTQx-ii and PC$_{61}$BM as active layer. While o-DCB was used as reference processing solvent, o-xylene was chosen as a greener alternative (Table 6.2). The lower environmental impact arises from the faster evaporation rate of o-xylene which, if accidentally gets into soil or waters, is fast released into air where sunlight converts it into less harmful chemicals within a couple of days. Otherwise, if trapped, o-xylene can be broken down by small organisms. Despite the potential effect of o-xylene on human health are still not comprehensive, preliminary results indicate negligible effects under short-term exposure and both the International Agency for Research on Cancer (IARC) and EPA did not classified o-xylene as a carcinogenic solvent.[241]

Besides the great advantages of o-xylene over o-DCB in terms of ecological impact, further advantages are provided in terms of economical sustainment. Indeed, the production costs of halogenated compounds are typically higher than those of methyl-benzenes, which can be obtained by simple distillation or solvent extraction from crude oil. In addition, the toxic chlorination processes create additional environmental concerns typically not present in the production of methyl-benzenes.

Besides the interesting advantages, methyl-benzene derivatives exhibit small drawbacks for BHJ application. Indeed, because of their poor solubility towards fullerenes (Table

6.2), the corresponding BHJ films are typically characterized by a severe phase segregation, which is detrimental for the solar cell operation. In this context, the rational analysis of the chemical-physical properties of methyl-benzene derivatives led to the obtainment of PSCs with promising performance[245] arising from the use of small amount of additive co-solvents.[246][238][247]

Table 6.2. Physical-chemical properties of o-DCB and o-xylene solvents.

	o-DCB [$C_6H_4Cl_2$]	o-xylene [C_8H_{10}]
Molecular formula		
Molar mass	147.00 g mol^{-1}	106.17 g mol^{-1}
Boiling point	180°C	144°C
Melting point	-17°C	-25°C
Viscosity	1.324 mPa s	0.760 mPa s
Dielectric constant	10.12	2.56
Solubility of fullerene (C_{60})	27.0 mg ml^{-1}	8.7 mg ml^{-1}
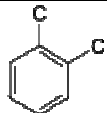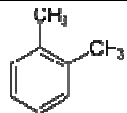
To evaluate the effect of the replacement of o-DCB with o-xylene on the device properties, BHJ solar cells with structure glass/ITO/ZnO/active layer/MoO$_3$/Ag were fabricated in order to ensure the best performance and stability. All the devices were fabricated, except the top electrode, by blade-coating in air.

The optimal PBDTQx-ii:PC$_{61}$BM blend ratio was found to be 1:2 (wt/wt) both in o-DCB and o-xylene as processing solvent (Table 6.3 and Figure 6.4). This was the result of a meticulous process of optimization of the active layer thickness, processing conditions and post-processing treatments of the BHJ. Both active blends showed the best results if processed in presence of DIO (3% v/v) as solvent additive. However, since DIO is an halogenated co-solvent, we also proved that halogen-free additives guarantee comparable benefits in terms of performance.[243]

Interestingly, the devices where the active layer is deposited from o-xylene showed a PCE of 4.5% in comparison to the 4% for the reference o-DCB processed cells. This is clearly ascribable to the processing solvent since the devices are similar in all the parts and processing methods. As shown in Table 6.3 and Figure 6.4, while a slight enhancement was exhibited in the device Voc from 0.78 V to 0.79 V, major differences came from the device Jsc which improved from 8.1 mA/cm^2 to 8.9 mA/cm^2, respectively for o-DCB and

o-xylene based-cells. Negligible differences were reported for the FF which resulted maintained at 64% thus indicating an optimal nanoscale morphology and charge transport properties of both PBDTQx-ii:PC$_{61}$BM based cells.
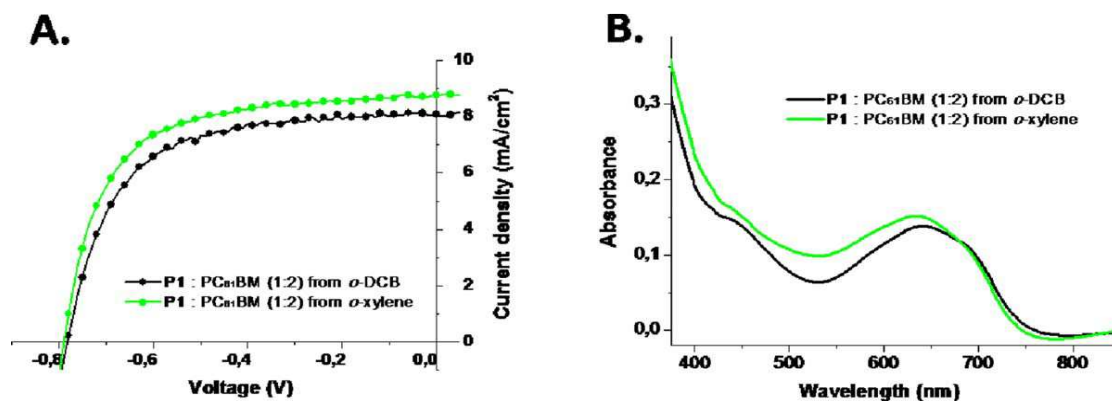
Figure 6.4. J-V plots (a) and absorption spectra (b) of optimized PBDTQx-ii:PC$_{61}$BM solar cells processed from o-DCB (black) or o-xylene (green).

Table 6.3. OPV parameters of optimized inverted PBDTQx-ii:PCBM solar cells processed from o-DCB or o-xylene. The reported data are averaged over six different devices.

Active layer[a]	D:A ratio [wt/wt]	Process. Solvent	Thickn. [nm]	V_{OC} [V]	J_{SC} [mA/cm^2]	FF [%]	PCE [%]
PBDTQx-ii: PC$_{61}$BM	1:2	o-DCB + 3% (v/v) DIO	75	0.780 ± 0.003	8.1 ± 0.3	64 ± 1	4.0 ± 0.1 (4.2)[b]
	1:2	o-xylene + 3% (v/v) DIO	90	0.790 ± 0.004	8.9 ± 0.2	64 ± 1	4.5 ± 0.1 (4.7)[b]

[a] No annealing; [b] Maximum PCE.

The improvement of the performance by using o-xylene instead of o-DCB as processing solvent is a remarkable result since highlights that the use of an environmentally friendly solvent, if properly chosen, might slightly enhance the corresponding OPV response. This mainly results from the enhanced Jsc (≈ 10%), which is a consequence of the more intense absorption profile with respect to that of the o-DCB based BHJ (Figure 6.4b). Indeed, the possibility of forming a thicker active layer (≈ 75 and ≈ 90 nm for o-DCB and o-xylene processed films, respectively) without affecting the excitons formation and charge transport properties of the active layer further contributes to the light harvesting of the solar cell (Table 6.3). To note, the use of thicker active blends showed a reduction of the OPV response for both types of devices as a result of a reduction of Jsc and FF. On

the contrary, thinner BHJ layers contributed to an increase of the charge transport properties (higher FF) while considerably reduced the Jsc because of limited light harvesting capability.

The possibility to have a slightly thicker and more efficient BHJ using o-xylene as processing solvent is the result of a fine entanglement and orientation of the polymeric chains during the drying process accordingly to the organization of the fullerene acceptor molecules. This improved nanoscale morphology is likely the responsible for a more suitable charge transport properties with reduced recombination even for thicker films.

To further clarify the effect of the different solvents on the self-organization of the PBDTQx-ii:PC$_{61}$BM BHJs, their surface morphology was analyzed through tapping-mode AFM (Figure 6.5). Accordingly to the similar OPV responses and FF, the surface morphology of the films differently processed from o-DCB or o-xylene reported quite similar features and a proper BHJ morphology. In detail, the defined domains suggest the formation of relatively organized donor:acceptor nanostructures, which reflect the optimal photovoltaic response of the corresponding solar cells. However, despite the absence of evident morphological differences, by carefully looking at the details, additional considerations can be drawn. Indeed, the topography of the film processed from o-DCB was characterized by a more regular and homogeneous surface with relatively less defined domains (Figure 6.5b). This suggests a modest aggregation and ordering of the polymer chains, which is in accordance with the need of a slightly thinner film to guarantee an optimal charge transport within the blend. On the contrary, the active film processed from o-xylene showed a relatively rougher surface (Figure 6.5b) characterized by fine and structured domains, which likely indicate a slightly higher degree of aggregation of the components at the solid state. This indeed allowed for a thicker film, which enhanced the light harvesting properties of the corresponding solar cell resulting in a greater PCE. This slightly different structuring of the nanodomains well correlates with the relative increase of the device Voc (10 mV) as a result of possible changes in the D:A interfaces, molecular distances, aggregation, orientation of the molecules, etc..
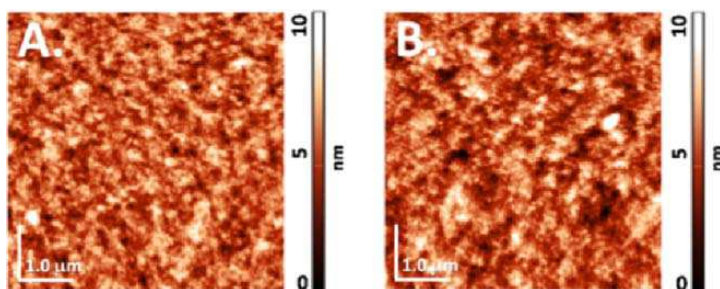
Figure 6.5. AFM images (size: 5 µm x 5 µm) of PBDTQx-ii:PCBM films processed from o-DCB (a) or o-xylene (b). The root mean square (RMS) are respectively 1.2 nm and 1.7 nm.

In sight of these results, o-xylene can be considered an effective alternative to process the BHJ blend of organic solar cells since it allows for thicker active films with proper morphology which are beneficial for photovoltaic performance in comparison to similar systems processed from the environmental harmful o-DCB.

Besides the evaluation of the initial OPV response of PBDTQx-ii:PCBM solar cells, we further investigated the impact of the processing solvent on the thermal stability by monitoring the evolution of the photovoltaic performance during thermal ageing. This is an innovative study since the stability of the devices is often poorly considered in the investigation of the effect of the environmentally friendly solvents on BHJ solar cells. Nevertheless, it is of relevant importance in view of the technology scale-up. In this sight, the reported device were left in dark and inert atmosphere at 85°C for 100 hours, in accordance with the ISOS-D-2 standard testing protocol.[115] Because of the identical structure of the solar cells, eventual differences after the thermal stress can be exclusively ascribed to the different processing solvent of the BHJs.

Simultaneously, the shelf-life was also evaluated by monitoring the performance of identical devices stored in dark and inert atmosphere at room temperature for 100 hours.[243] A limited drop in PCE ($< 3\%$) evidenced negligible effects of the processing solvent on the shelf-life of both the types of solar cells. This allows to consider eventual reductions of the device responses to degradation processes induced by the thermal stress. As shown in Figure 6.6 and Table 6.4, a nearly identical drop in the PCE is reported for both the type of differently processed solar cells. In detail, an initial thermal burn-in is reflected by a drop of the device performance which stabilize over time (Figure 6.6a). After the thermal stress, devices processed from o-DCB and o-xylene respectively exhibited a drop in their PCEs of $\approx 20\%$ and $\approx 24\%$. This drop arises from a reduction of Jsc (6-10 %) and FF (14-16%), which is due to an increase of the internal resistances (increase of the series resistance and reduction of the parallel resistance) of the solar cells

as clearly evidenced by their J-V plots.[243] This is likely ascribed to slight morphological changes of the active blend, which partially re-organizes with consequent influences in terms of charge transport and recombination dynamics (FF) with subsequent limitation of the extracted charges (Jsc).
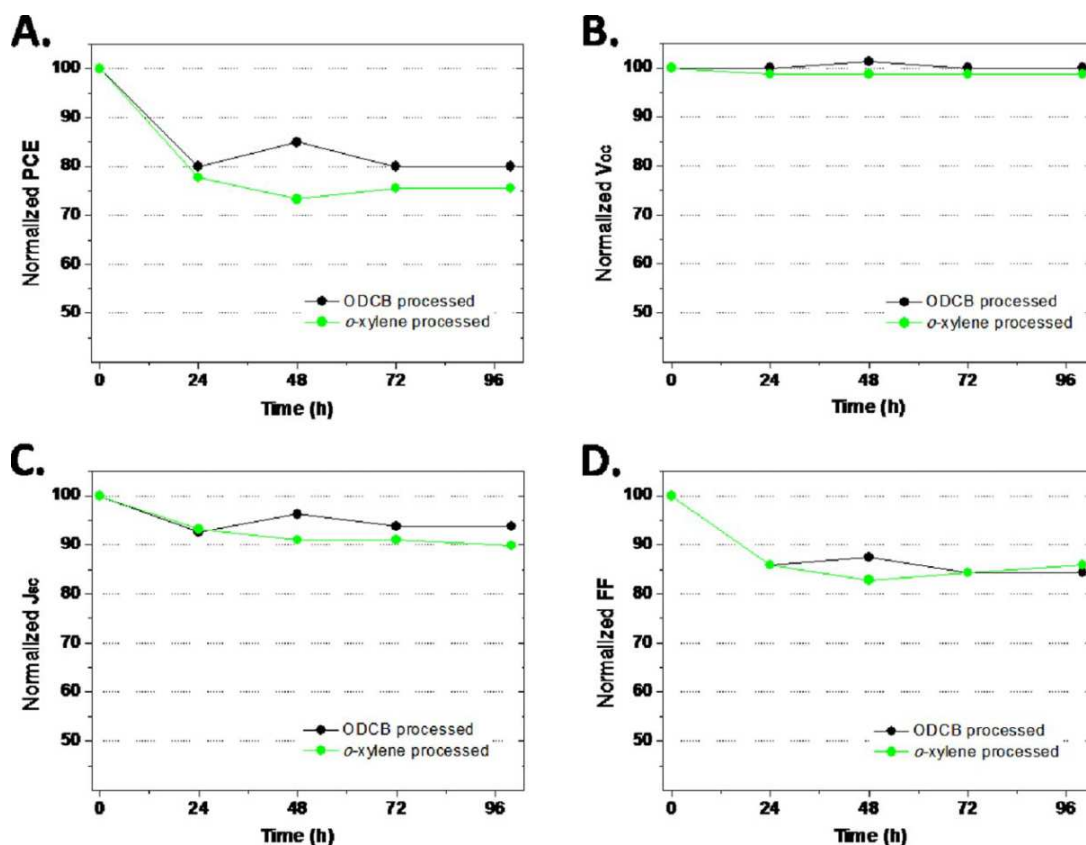
Figure 6.6. Evolution of the normalized OPV parameters for PBDTQx-ii:PCBM solar cells processed from o-DCB (black) or o-xylene (green) during thermal stress at 85°C in inert and dark conditions.

Table 6.4. OPV parameters of PBDTQx-ii:PCBM based solar cells processed from o-DCB or o-xylene, freshly prepared and after 100 hours of thermal stress at 85°C in inert and dark conditions. The reported data are averaged over five different devices.

Process. solvent	Device	V_{OC} [V]	J_{SC} [mA/cm^2]	FF [%]	PCE [%]
o-DCB[a]	Fresh	0.780 ± 0.003	8.1 ± 0.3	64 ± 1	4.0 ± 0.1
	Aged	0.78 ± 0.01	7.6 ± 0.5 (-6%)[b]	54 ± 1 (-16%)[b]	3.2 ± 0.2 (-20%)[b]
o-xylene[a]	Fresh	0.790 ± 0.004	8.9 ± 0.2	64 ± 1	4.5 ± 0.1 (4.7)[b]
	Aged	0.78 ± 0.01 (-1%)[b]	8.0 ± 0.2 (-10%)[b]	55 ± 1 (-14%)[b]	3.4 ± 0.1 (-24%)[b]

[a] +3% (v/v) of DIO;   [b] Loss percentage relative to the corresponding parameter at time a (fresh device).

To give a deeper insight of the impact of the different processing solvents on the thermal stability of the BHJ cells, the relative surface morphologies were investigated through AFM topography (Figure 6.7). Interestingly, features similar to the relative fresh devices were exhibited for both types of devices. In detail, after the thermal stress, the cells processed from o-DCB reported quite regular and homogeneous surface with apparently less connected domains (Figure 6.7a - aged), while the same blend prepared from o-xylene showed a finer and more textured nanostructures (Figure 6.7b - aged), which are indication of a slightly increased internal resistance in the BHJ. However, such discrete variations and the absence of evident morphological changes are consistent with the observed trend of OPV performance, thus confirming the good stability of PBDTQx-ii:PCBM solar cells which are able to retain ≈ 80% of their initial performance after 4 days at 85°C.
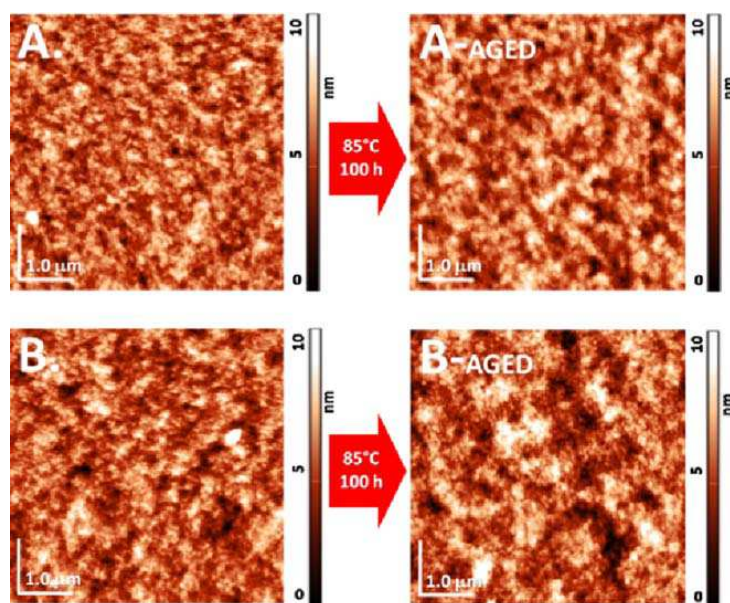
Figure 6.7. AFM images (size: 5 µm x 5 µm) of PBDTQz-ii:PCBM solar cells processed from o-DCB (a) or o-xylene (b). A and B images are the same reported in Figure 6.5 while on the right side the same films after 100 hours at 85°C of thermal stress are named as A-aged and B-aged. The RMS for both aged films is ≈ 1.6 nm.

In this work, the effect of an eco-friendly solvent on the performance and thermal stability of BHJ solar cells is presented by using a properly synthesized electron donor polymer. However, a further confirmation of the effectiveness of the o-xylene as processing solvent is also provided in the paragraph 4.2.2. Indeed, despite not discussed, the use of o-xylene instead of o-DCB reported a improved initial performance and a

dramatically increased thermal stability of the corresponding solar cells for a period as long as 150 hours.

In sight if this, the eco-friendly o-xylene as replacement of the common hazardous chlorinated solvents is here demonstrated to be an effective alternative which confers a further potential to the entire organic photovoltaic technology to succeed. The improvement in the initial OPV response of o-xylene processed BHJ cells, in conjunction with a thermal resistance comparable or greater than o-DCB processed devices, clearly indicates the benefit of this alternative solvent as a way to further improve the device sustainability without affecting the photovoltaic response of organic solar cells.

Chapter 7
Summary and outlook

This thesis aimed at developing the organic photovoltaic technology through the analysis of core aspects of BHJ solar cells such as their performance, stability and environmental impact.

Indeed, despite the *exploit* shown by organic photovoltaics in the last few years, fundamental limitations arising from the poor reliability of the devices still slow the deployment of the organic photovoltaic technology. In this context, a part of this thesis was devoted to the investigation of the solar cells resistance to thermal or light stress. International testing protocols were followed in order to provide useful information to the overall scientific community. In particular, the solvent used to dissolve and process the BHJ active layer was demonstrated to play a role in the thermal resistance of the solar cell. The replacement of the common hazardous solvent o-DCB with the environmentally friendlier alternative o-xylene showed a remarkable improvement of the thermal resistance of solar cells after 150 hours at 85°C. In this context, an advanced characterization technique was properly developed in order to selectively discern between the degradation processes affecting either the active layer or the electrode materials. This technique, based on the use of a confocal microscope, resulted very attractive for its non-invasiveness, the higher resolution if compared to the standard methods present in the literature, the possibility to operate on complete solar cells and to correlate the photovoltaic response to the photo-physical properties of the device components.

A comparative study where films of pristine donor polymers and the corresponding BHJ solar cells were subjected to prolonged sunlight illumination showed that different degradation processes occur in the two different systems. In this work, the comparative investigation of polymers characterized by similar chemical structures provided guidelines for the synthesis of efficient and stable organic semiconductors. In this sight, a particularly interesting resistance to prolonged illumination was revealed by the use of short and relatively compact side chains substituents on the BDT unit of push-push polymers.

Further analysis on the light stability of organic solar cells focused on the investigation of the ZnO operation as ETL, upon prolonged illumination. The adsorption of ambient oxygen on the surface of air-processed ZnO nanoparticles revealed a detrimental effect on the corresponding solar cell under UV exposure. The alternative use of aluminum-doped (0.03 at. %) ZnO nanoparticles was demonstrated to avoid the oxygen induced degradation of the solar cell under prolonged illumination and evidenced the potential of AZO nanoparticles as candidate material for ETLs showing long light resistance and high compatibility to industrial processing in ambient conditions.

The important breakthroughs reached in terms of device stability, allowed to focus on other aspects of BHJ solar cells. Preliminary studies on the chemical structure – properties relationship of newly synthesized semiconducting polymers and fullerene derivatives provided guidelines towards the obtainment of highly performing PSCs. In this context, aiming to even more push the device efficiency, a core section of the thesis was devoted to the investigation of the critical aspects related to state-of-the-art tandem devices. In particular, despite the enormous potential of multi-junction cells arising from the minimization of unexploited solar photons, the solution-processing of an efficient ICL over the bottom active layer represents an important limitation. In a thorough analysis on PEDOT:PSS/ZnO based ICLs, the modification of the PEDOT:PSS dispersion, to facilitate the ICL formation, was demonstrated to be the cause of a poor ICL operation. In this sight, a facile and versatile approach, fully compatible with the large-scale processing methods, was effectively developed. This revealed the total restoring of the ICL operation and an optimal tandem operation. In this context, in view of pushing the solar cell performance towards the theoretical efficiency, an elegant approach to selectively investigate the ICL operation was effectively developed. In detail, by analyzing the photo-generated current of devices under light-emitting-diode regime, minor electrical losses of the ICL, which affect the operation of double-junction architectures, were visualized and recognized. The innovative approach, which operates on sub-structures, avoids the elaborated fabrication of complete multi-junction solar cells and hence provide a powerful investigation of ICL operation losses aiming at the design and development of advanced materials for high performing multi-junction organic solar cells.

The great progress in terms of device efficiency and stability through the here proposed routes led to the analysis of another important aspect for organic solar cells, *i.e.* the environmental impact. Indeed, despite the eco-friendliness is reported as one of the great advantages of organic photovoltaics over the other renewable technologies, toxic and

expensive halogenated solvents are typically used for the BHJ processing to ensure a great device operation. This indeed reduces the potential of organic photovoltaics as a green energy technology. In this view, the replacement of common halogenated solvents with the cheaper and environmentally friendlier o-xylene was effectively demonstrated to preserve the solar cell efficiency. Interestingly, further investigation of the device stability under thermal stress revealed a comparable or even increased resistance of the solar cells by using o-xylene as processing solvent of the BHJ. This represents an example of an effective path to further improve the device sustainability of organic photovoltaics, an additional advantage for this technology to succeed.

It is noteworthy that, in the reported works, all the devices were fabricated by solution and, heading to the industrialization of this technology, the requirements of the large-scale manufacture were considered in the experimental procedures. The use of processing techniques such as the doctor blading represents a connection point between the investigation of laboratory-confined devices and the development of methods suitable for large-scale manufacturing.

The combined analysis of basic research on standard cells and the development of innovative methods on state-of-the-art devices presented in this thesis, framed in the context of a sustainable up-scale of the technology, represents an effective route towards high efficient, reliable and sustainable organic solar cells.

Finally, the combination of the learnings arising from the here presented specific investigations and the fabrication of larger sized modules are necessary in view of the industrialization of this technology. In this sight, stability investigations on the state-of-the-art architectures (i.e. multi-junctions) are needed since the complexity of the structure could introduce additional degradation mechanisms. Moreover, flexible substrates covered by bendable electrodes need to be introduced and analyzed in order to fully exploit properties of organic solar cells such as foldability and wearability, not investigated in this thesis. The replacement of the stiff ITO as bottom electrode would result in a reduction of the costs. Nonetheless, alternative electrodes likewise efficient need to be investigated. In this context, detailed analysis on the production of large-scale solar modules should be carried out both in terms of costs, eco- and bio-impact of the final products for real world application.

BIBLIOGRAPHY

[1]   http://climate.nasa.gov/effects/.

[2]   M. Leduc, H. D. Matthews, R. de Elía, *Nat. Clim. Chang.* **2016**, *6*, 474.

[3]   P. Friedlingstein, R. M. Andrew, J. Rogelj, G. P. Peters, J. G. Canadell, R. Knutti, G. Luderer, M. R. Raupach, M. Schaeffer, D. P. van Vuuren, C. Le Quéré, *Nat. Geosci.* **2014**, *7*, 709.

[4]   K. A. Mazzio, C. K. Luscombe, *Chem. Soc. Rev.* **2014**, *44*, 78.

[5]   D. B. Needleman, J. R. Poindexter, R. C. Kurchin, I. M. Peters, G. Wilson, T. Buonassisi, *Energy Environ. Sci.* **2016**, *9*, 2122.

[6]   S. B. Darling, F. You, *RSC Adv.* **2013**, *3*, 17633.

[7]   http://www.ez2c.de/ml/solar_land_area/.

[8]   https://en.wikipedia.org/wiki/Solar_power_in_Morocco.

[9]   N. Armaroli, V. Balzani, *Chem. - A Eur. J.* **2016**, *22*, 32.

[10]   M. A. Green, *Nat. Energy* **2016**, *1*, 15015.

[11]   A. J. Sangster, *Green Energy Technol.* **2014**, *194*, 145.

[12]   D. Bi, C. Yi, J. Luo, J.-D. Décoppet, F. Zhang, S. M. Zakeeruddin, X. Li, A. Hagfeldt, M. Grätzel, *Nat. Energy* **2016**, *1*, 16142.

[13]   S. D. Stranks, H. J. Snaith, *Nat. Nanotechnol.* **2015**, *10*, 391.

[14]   M. Li, K. Gao, X. Wan, Q. Zhang, B. Kan, R. Xia, F. Liu, X. Yang, H. Feng, W. Ni, Y. Wang, J. Peng, H. Zhang, Z. Liang, H. Yip, X. Peng, Y. Cao, Y. Chen, *Nat. Photonics* **2016**, 4.

[15]   M. A. Green, K. Emery, Y. Hishikawa, W. Wilhelm, E. D. Dunlop, *Prog. Photovolt Res. Appl.* **2015**, *23*, 1.

[16]   https://www.nrel.gov/pv/.

[17]   N. Espinosa, M. Hösel, D. Angmo, F. C. Krebs, *Energy Environ. Sci.* **2012**, *5*, 5117.

[18]   https://energy.gov/.

[19]   C. L. Cutting, M. Bag, D. Venkataraman, *J. Mater. Chem. C* **2016**.

[20]   http://www.sunflower-fp7.eu/site/.

[21]   https://www.infinitypv.com/.

[22]   http://www.opvius.com/.

[23] O. V Mikhnenko, P. W. M. Blom, T.-Q. Nguyen, *Energy Environ. Sci. Energy Environ. Sci* **2015**, *8*, 1867.

[24] H. Kallmann, M. Pope, *J. Chem. Phys.* **1959**, *30*, 585.

[25] C. W. Tang, *Appl. Phys. Lett.* **1986**, *48*, 183.

[26] Y.-J. Cheng, Y.-J. Cheng, S.-H. Yang, S.-H. Yang, C.-S. Hsu, C.-S. Hsu, *Chem. Rev.* **2009**, 5868.

[27] M. Bolognesi, *Dr. Thesis* **2013**.

[28] G. Yu, J. Gao, J. C. Hummelen, F. Wudl, a. J. Heeger, *Science (80-.).* **1995**, *270*, 1789.

[29] J. J. M. Halls, C. A. Walsh, N. C. Greenham, E. A. Marseglia, R. H. Friend, S. C. Moratti, A. B. Holmes, *Lett. to Nat.* **1995**, *376*, 498.

[30] S. Morita, A. A. Zakhidov, K. Yoshino, *Solid State Commun.* **1992**, *82*, 249.

[31] N. S. Sariciftci, L. Smilowitz, A. J. Heeger, F. Wudl, *Science (80-.).* **1992**, *258*, 1474.

[32] L. Dou, J. You, Z. Hong, Z. Xu, G. Li, R. a. Street, Y. Yang, *Adv. Mater.* **2013**, *25*, 6642.

[33] D. Moses, *Nat. Mater.* **2014**, *13*, 4.

[34] K. Wang, C. Yi, C. Liu, X. Hu, S. Chuang, X. Gong, *Sci. Rep.* **2015**, *5*, 9265.

[35] N. Camaioni, R. Po, *J. Phys. Chem. Lett.* **2013**, *4*, 1821.

[36] K. Vandewal, S. Albrecht, E. T. Hoke, K. R. Graham, J. Widmer, J. D. Douglas, M. Schubert, W. R. Mateker, J. T. Bloking, G. F. Burkhard, A. Sellinger, J. M. J. Fréchet, A. Amassian, M. K. Riede, M. D. McGehee, D. Neher, A. Salleo, *Nat. Mater.* **2014**, *13*, 63.

[37] A. Rao, P. C. Y. Chow, S. Gélinas, C. W. Schlenker, C.-Z. Li, H.-L. Yip, A. K.-Y. Jen, D. S. Ginger, R. H. Friend, *Nature* **2013**, *500*, 435.

[38] Y. J. Lee, J. Yi, G. F. Gao, H. Koerner, K. Park, J. Wang, K. Luo, R. A. Vaia, J. W. P. Hsu, *Adv. Energy Mater.* **2012**, *2*, 1193.

[39] X. Yu, T. J. Marks, A. Facchetti, *Nat. Mater.* **2016**, *15*, 383.

[40] R. Po, C. Carbonera, A. Bernardi, N. Camaioni, *Energy Environ. Sci.* **2011**, *4*, 285.

[41] Z. He, C. Zhong, X. Huang, W. Y. Wong, H. Wu, L. Chen, S. Su, Y. Cao, *Adv. Mater.* **2011**, *23*, 4636.

[42] Y. Zhou, C. Fuentes-Hernandez, J. Shim, J. Meyer, A. J. Giordano, H. Li, P. Winget, T. Papadopoulos, H. Cheun, J. Kim, M. Fenoll, A. Dindar, W. Haske, E. Najafabadi, T. M. Khan, H. Sojoudi, S. Barlow, S. Graham, J.-L. Bredas, S. R. Marder, A. Kahn, B. Kippelen, *Science (80-.).* **2012**, *336*, 327.

[43] B. Azzopardi, C. J. M. Emmott, A. Urbina, F. C. Krebs, J. Mutale, J. Nelson, *Energy Environ. Sci.* **2011**, *4*, 3741.

[44] H. Kang, G. Kim, J. Kim, S. Kwon, H. Kim, K. Lee, *Adv. Mater.* **2016**, 7821.

[45] F. C. Krebs, *Sol. Energy Mater. Sol. Cells* **2009**, *93*, 394.

[46] https://www.spincoating.com/en/affordable-spin-coaters/1/.

[47] N. Li, D. Baran, G. D. Spyropoulos, H. Zhang, S. Berny, M. Turbiez, T. Ameri, F. C. Krebs, C. J. Brabec, *Adv. Energy Mater.* **2014**, *4*, 1.

[48] V. D. C. Deibel, *Reports Prog. Phys.* **2010**, *73*, 96401.

[49] L. J. A. Koster, V. D. Mihailetchi, R. Ramaker, P. W. M. Blom, *Appl. Phys. Lett.* **2005**, *86*, 123509.

[50] L. J. A. Koster, E. C. P. Smits, V. D. Mihailetchi, P. W. M. Blom, *Phys. Rev. B - Condens. Matter Mater. Phys.* **2005**, *72*, 1.

[51] M. M. Mandoc, F. B. Kooistra, J. C. Hummelen, B. De Boer, P. W. M. Blom, *Appl. Phys. Lett.* **2007**, *91*, 263505.

[52] J. G. F. Hide, H. Wang, *Synth. Met.* **1997**, *84*, 979.

[53] P. Schilinsky, C. Waldauf, C. Brabec, *Appl. Phys. Lett.* **2002**, *81*, 3885.

[54] N. Gasparini, M. Salvador, S. Fladischer, A. Katsouras, A. Avgeropoulos, E. Spiecker, C. L. Chochos, C. J. Brabec, T. Ameri, *Adv. Energy Mater.* **2015**, *5*, 1501527.

[55] K. Vandewal, K. Tvingstedt, A. Gadisa, O. Inganäs, J. V Manca, *Nat. Mater.* **2009**, *8*, 904.

[56] M. A. Faist, T. Kirchartz, W. Gong, R. S. Ashraf, I. Mcculloch, J. C. De Mello, N. J. Ekins-daukes, D. D. C. Bradley, J. Nelson, *J. Am. Chem. Soc.,* **2011**, *134*, 685.

[57] U. Rau, *Phys. Rev. B - Condens. Matter Mater. Phys.* **2007**, *76*, 1.

[58] T. Kirchartz, J. Nelson, U. Rau, *Phys. Rev. Appl.* **2016**, *5*, 1.

[59] D. Baran, N. Li, A. C. Breton, A. Osvet, T. Ameri, M. Leclerc, C. J. Brabec, *J. Am. Chem. Soc.* **2014**, *136*, 10949.

[60] M. Hallermann, I. Kriegel, E. Da Como, J. M. Berger, E. Von Hauff, J. Feldmann, *Adv. Funct. Mater.* **2009**, *19*, 3662.

[61] L. J. A. Koster, S. E. Shaheen, J. C. Hummelen, *Adv. Energy Mater.* **2012**, *2*, 1246.

[62]   U. Würfel, D. Neher, A. Spies, S. Albrecht, *Nat. Commun.* **2015**, *6*, 6951.

[63]   M. C. Scharber, D. Mühlbacher, M. Koppe, P. Denk, C. Waldauf, A. J. Heeger, C. J. Brabec, *Adv. Mater.* **2006**, *18*, 789.

[64]   R. Po, M. Maggini, N. Camaioni, *J. Phys. Chem. C* **2010**, *114*, 695.

[65]   S. X. and E. H. K. and A. W. and E. Negishi, *Sci. Technol. Adv. Mater.* **2014**, *15*, 44201.

[66]   L.-C. Campeau, K. Fagnou, *Chem. Soc. Rev.* **2007**, *36*, 1058.

[67]   H. J. Son, F. He, B. Carsten, L. Yu, *J. Mater. Chem.* **2011**, *21*, 18934.

[68]   L. Lu, T. Zheng, Q. Wu, A. M. Schneider, D. Zhao, L. Yu, *Chem. Rev.* **2015**, *115*, 12666.

[69]   L. Dou, Y. Liu, Z. Hong, G. Li, Y. Yang, *Chem. Rev.* **2015**, *115*, 12633.

[70]   M. S. Vezie, S. Few, I. Meager, G. Pieridou, B. Dörling, R. Shahid, A. R. Goñi, H. Bronstein, I. Mcculloch, S. Hayes, J. Nelson, *Nat. Mater.* **2016**, *15*, 1.

[71]   A. Katsouras, N. Gasparini, C. Koulogiannis, M. Spanos, T. Ameri, C. J. Brabec, C. L. Chochos, A. Avgeropoulos, *Macromol. Rapid Commun.* **2015**, *36*, 1778.

[72]   D. Baran, R. S. Ashraf, D. A. Hanifi, M. Abdelsamie, N. Gasparini, J. A. Röhr, S. Holliday, A. Wadsworth, S. Lockett, M. Neophytou, C. J. M. Emmott, J. Nelson, C. J. Brabec, A. Amassian, T. Kirchartz, J. R. Durrant, I. Mcculloch, D. Baran, R. A. Ashraf, S. Holliday, A. Wadsworth, S. Lockett, P. J. R. Durrant, *Nat. Mater.* **2016**, *1*, 1.

[73]   M. T. Dang, L. Hirsch, G. Wantz, *Adv. Mater.* **2011**, *23*, 3597.

[74]   H. Yao, L. Ye, H. Zhang, S. Li, S. Zhang, J. Hou, *Chem. Rev.* **2016**, *116*, 7397.

[75]   R. C. Coffin, J. Peet, J. Rogers, G. C. Bazan, *Nat. Chem.* **2009**, *1*, 657.

[76]   L. Dou, C. Chen, K. Yoshimura, K. Ohya, W. Chang, J. Gao, Y. Liu, E. Richard, Y. Yang, **2013**, 2.

[77]   Y. Zou, J. Yuan, lixia qiu, Z.-G. Zhang, Y. Li, Y. He, L. jiang, *Chem. Commun.* **2016**, *52*, 8.

[78]   S. Nho, G. Baek, S. Park, B. R. Lee, M. J. Cha, D. C. Lim, J. H. Seo, S.-H. Oh, M. H. Song, S. Cho, *Energy Environ. Sci.* **2015**, *9*, 240.

[79]   H. Kang, S. Jung, S. Jeong, G. Kim, K. Lee, *Nat. Commun.* **2015**, *6*, 6503.

[80]   S.-W. Baek, J. H. Kim, J. Kang, H. Lee, J. Y. Park, J.-Y. Lee, *Adv. Energy Mater.* **2015**, 1501393.

[81]   J. Zhao, Y. Li, G. Yang, K. Jiang, H. Lin, H. Ade, W. Ma, H. Yan, *Nat. Energy* **2016**, *1*, 15027.

[82] D. Gedefaw, M. Tessarolo, W. Zhuang, R. Kroon, E. Wang, M. Bolognesi, M. Seri, M. Muccini, M. R. Andersson, *Polym. Chem.* **2014**, *5*, 2083.

[83] M. Tessarolo, D. Gedefaw, M. Bolognesi, F. Liscio, P. Henriksson, W. Zhuang, S. Milita, M. Muccini, E. Wang, M. Seri, M. R. Andersson, *J. Mater. Chem. A* **2014**, *2*, 11162.

[84] M. Bolognesi, D. Gedefaw, D. Dang, P. Henriksson, W. Zhuang, M. Tessarolo, E. Wang, M. Muccini, M. Seri, M. R. Andersson, *RSC Adv.* **2013**, *3*, 24543.

[85] S. C. Price, A. C. Stuart, L. Yang, H. Zhou, W. You, *J. Am. Chem. Soc.* **2011**, *133*, 4625.

[86] W. W. H. Wong, J. Subbiah, S. R. Puniredd, W. Pisula, D. J. Jones, A. B. Holmes, *Polym. Chem.* **2014**, *5*, 1258.

[87] J.-H. Kim, C. Eun Song, N. Shin, H. Kang, S. Wood, I.-N. Kang, B. J. Kim, B. Kim, J.-S. Kim, W. Suk Shin, D.-H. Hwang, *ACS Appl. Mater. Interfaces* **2013**, *5*, 12820.

[88] M. S. and M. R. A. Desta Gedefaw, Marta Tessarolo, Margherita Bolognesi, Mario Prosa, Renee Kroon, Wenliu Zhuang, Patrik Henriksson, Kim Bini, Ergang Wang, Michele Muccini, *Beilstein J. Org. Chem.* **2016**, *12*, 1629.

[89] J.-L. Bredas, *Mater. Horizons* **2014**, *1*, 17.

[90] Y. Yang, G. Li, *Progress in High-Efficient Solution Process Organic Photovoltaic Devices: Fundamentals, Materials, Devices and Fabrication*; 2015.

[91] G. J. Zhao, Y. J. He, Y. Li, *Adv. Mater.* **2010**, *22*, 4355.

[92] C. Zhan, X. Zhang, J. Yao, *RSC Adv.* **2015**, *5*, 93002.

[93] S. Holliday, R. S. Ashraf, A. Wadsworth, D. Baran, S. A. Yousaf, C. B. Nielsen, C.-H. Tan, S. D. Dimitrov, Z. Shang, N. Gasparini, M. Alamoudi, F. Laquai, C. J. Brabec, A. Salleo, J. R. Durrant, I. McCulloch, *Nat. Commun.* **2016**, *7*, 11585.

[94] S. Shi, J. Yuan, G. Ding, M. Ford, K. Lu, G. Shi, J. Sun, X. Ling, Y. Li, W. Ma, *Adv. Funct. Mater.* **2016**, *26*, 5669.

[95] C. B. Nielsen, S. Holliday, H.-Y. Chen, S. J. Cryer, I. McCulloch, *Acc. Chem. Res.* **2015**, *48*, 2803.

[96] D. Baran, T. Kirchartz, S. Wheeler, S. Dimitrov, M. Abdelsamie, J. Gorman, R. Ashraf, S. Holliday, A. Wadsworth, N. Gasparini, P. Kaienburg, H. Yan, A. Amassian, C. J. Brabec, J. Durrant, I. McCulloch, *Energy Environ. Sci.* **2016**.

[97] D. Sun, D. Meng, Y. Cai, B. Fan, Y. Li, W. Jiang, L. Huo, Y. Sun, Z. Wang, *J. Am. Chem. Soc.* **2015**, *137*, 11156.

[98] A. Varotto, N. D. Treat, J. Jo, C. G. Shuttle, N. A. Batara, F. G. Brunetti, J. H. Seo, M. L. Chabinyc, C. J. Hawker, A. J. Heeger, F. Wudl, *Angew. Chemie - Int. Ed.* **2011**, *50*, 5166.

[99] F. Matsumoto, T. Iwai, K. Moriwaki, Y. Takao, T. Ito, T. Mizuno, T. Ohno, *J. Org. Chem.* **2012**, *77*, 9038.

[100] M. Cristofani, E. Menna, M. Seri, M. Muccini, M. Prosa, S. Antonello, M. Mba, L. Franco, M. Maggini, *Asian J. Org. Chem.* **2016**, *5*, 676.

[101] P. A. Troshin, H. Hoppe, J. Renz, M. Egginger, J. Y. Mayorova, A. E. Goryachev, A. S. Peregudov, R. N. Lyubovskaya, G. Gobsch, N. S. Sariciftci, V. F. Razumov, *Adv. Funct. Mater.* **2009**, *19*, 779.

[102] S. V. Kesava, Z. Fei, A. D. Rimshaw, C. Wang, A. Hexemer, J. B. Asbury, M. Heeney, E. D. Gomez, *Adv. Energy Mater.* **2014**, *4*, 1.

[103] K. Vakhshouri, D. R. Kozub, C. Wang, A. Salleo, E. D. Gomez, *Phys. Rev. Lett.* **2012**, *108*, 1.

[104] H. C. Liao, C. C. Ho, C. Y. Chang, M. H. Jao, S. B. Darling, W. F. Su, *Mater. Today* **2013**, *16*, 326.

[105] J. K. Lee, W. L. Ma, C. J. Brabec, J. Yuen, J. S. Moon, J. Y. Kim, K. Lee, G. C. Bazan, A. J. Heeger, *J. Am. Chem. Soc.* **2008**, *130*, 3619.

[106] S. J. Lou, J. M. Szarko, T. Xu, L. Yu, T. J. Marks, L. X. Chen, *J. Am. Chem. Soc.* **2011**, *133*, 20661.

[107] W. A. Hammed, R. Yahya, A. L. Bola, H. N. M. E. Mahmud, *Energies* **2013**, *6*, 5847.

[108] P. Cheng, C. Yan, Y. Li, W. Ma, X. Zhan, *Energy Environ. Sci.* **2015**, *8*, 2357.

[109] M. T. Dang, L. Hirsch, G. Wantz, J. D. Wuest, *Chem. Rev.* **2013**, *113*, 3734.

[110] M. Jørgensen, K. Norrman, S. A. Gevorgyan, T. Tromholt, B. Andreasen, F. C. Krebs, *Adv. Mater.* **2012**, *24*, 580.

[111] M. Jørgensen, K. Norrman, F. C. Krebs, *Sol. Energy Mater. Sol. Cells* **2008**, *92*, 686.

[112] M. Prosa, M. Tessarolo, M. Bolognesi, O. Margeat, D. Gedefaw, M. Gaceur, C. Videlot-Ackermann, M. R. Andersson, M. Muccini, M. Seri, J. Ackermann, *ACS Appl. Mater. Interfaces* **2015**, *8*, 1635.

[113] I. T. Sachs-Quintana, T. Heumüller, W. R. Mateker, D. E. Orozco, R. Cheacharoen, S. Sweetnam, C. J. Brabec, M. D. McGehee, *Adv. Funct. Mater.* **2014**, *24*, 3978.

[114] P. Cheng, X. Zhan, *Chem. Soc. Rev.* **2016**.

[115] M. O. Reese, S. a. Gevorgyan, M. Jørgensen, E. Bundgaard, S. R. Kurtz, D. S. Ginley, D. C. Olson, M. T. Lloyd, P. Morvillo, E. a. Katz, A. Elschner, O. Haillant, T. R. Currier, V. Shrotriya, M. Hermenau, M. Riede, K. R. Kirov, G. Trimmel, T. Rath, O. Inganäs, F. Zhang, M. Andersson, K. Tvingstedt, M. Lira-Cantu, D. Laird, C. McGuiness, S. Gowrisanker, M. Pannone, M. Xiao, J. Hauch, R. Steim, D. M. Delongchamp, R. Rösch, H. Hoppe, N. Espinosa, A. Urbina, G. Yaman-Uzunoglu, J. B. Bonekamp, A. J. J. M. Van Breemen, C. Girotto, E. Voroshazi, F. C. Krebs, *Sol. Energy Mater. Sol. Cells* **2011**, *95*, 1253.

[116] S. Schuller, P. Schilinsky, J. Hauch, C. J. Brabec, *Appl. Phys. A Mater. Sci. Process.* **2004**, *79*, 37.

[117] B. Conings, S. Bertho, K. Vandewal, A. Senes, J. D'Haen, J. Manca, R. A. J. Janssen, *Appl. Phys. Lett.* **2010**, *96*, 0.

[118] M. Tessarolo, A. Guerrero, D. Gedefaw, M. Bolognesi, M. Prosa, X. Xu, M. Mansour, E. Wang, M. Seri, M. R. Andersson, M. Muccini, G. Garcia-Belmonte, *Sol. Energy Mater. Sol. Cells* **2015**, *141*, 240.

[119] Z. Li, K. Ho Chiu, R. Shahid Ashraf, S. Fearn, R. Dattani, H. Cheng Wong, C.-H. Tan, J. Wu, J. T. Cabral, J. R. Durrant, *Sci. Rep.* **2015**, *5*, 15149.

[120] M. T. Dang, G. Wantz, H. Bejbouji, M. Urien, O. J. Dautel, L. Vignau, L. Hirsch, *Sol. Energy Mater. Sol. Cells* **2011**, *95*, 3408.

[121] M. Bolognesi, M. Prosa, M. Tessarolo, G. Donati, S. Toffanin, M. Muccini, M. Seri, *Sol. Energy Mater. Sol. Cells* **2016**, *155*, 436.

[122] F. C. Krebs, M. Jørgensen, *Adv. Opt. Mater.* **2014**, *2*, 465.

[123] A. Rivaton, S. Chambon, M. Manceau, J. Gardette, N. Lemaître, S. Guillerez, *Polym. Degrad. Stab.* **2010**, *95*, 278.

[124] A. Rivaton, B. Mailhot, G. Derderian, P. O. Bussiere, J. Gardette, *Macromolecules* **2003**, *36*, 5815.

[125] M. Manceau, S. Chambon, A. Rivaton, J. Gardette, S. Guillerez, N. Lamaitre, *Sol. Energy Mater. Sol. Cells* **2010**, *94*, 1572.

[126] I. Fraga Domínguez, A. Distler, L. Lüer, *Adv. Energy Mater.* **2016**, 1601320.

[127] A. Rivaton, A. Tournebize, J. Gaume, P.-O. Bussière, J.-L. Gardette, S. Therias, *Polym. Int.* **2014**, *63*, 1335.

[128] M. Manceau, A. Rivaton, J.-L. Gardette, S. Guillerez, N. Lemaître, *Polym. Degrad. Stab.* **2009**, *94*, 898.

[129] Y. W. Soon, H. Cho, J. Low, H. Bronstein, I. Mcculloch, J. R. Durrant, *Chem. Commun.* **2013**, *49*, 1291.

[130] T. Heumueller, W. R. Mateker, A. Distler, U. F. Fritze, R. Cheacharoen, W. H. Nguyen, M. Biele, M. Salvador, M. von Delius, H.-J. Egelhaaf, M. D. McGehee, C. J. Brabec, *Energy Environ. Sci.* **2015**, *9*, 247.

[131] M. A. Miranda, J. Pérez-Prieto, E. Font-Sanchis, J. C. Scaiano, *Prog. React. Kinet. Mech.* **2001**, *26*, 139.

[132] C. P. Yau, S. Wang, N. D. Treat, Z. Fei, B. J. Tremolet De Villers, M. L. Chabinyc, M. Heeney, *Adv. Energy Mater.* **2015**, *5*, 1.

[133] A. Tournebize, A. Rivaton, H. Peisert, T. Chassé, *J. Phys. Chem. C* **2015**, *119*, 9142.

[134] B. J. Tremolet de Villers, K. A. O'Hara, D. P. Ostrowski, P. H. Biddle, S. E. Shaheen, M. L. Chabinyc, D. C. Olson, N. Kopidakis, *Chem. Mater.* **2016**, *28*, 876.

[135] M. Manceau, E. Bundgaard, J. E. Carlé, O. Hagemann, M. Helgesen, R. Søndergaard, M. Jørgensen, F. C. Krebs, *J. Mater. Chem.* **2011**, *21*, 4132.

[136] G. Williams, Q. Wang, H. Aziz, *Adv. Funct. Mater.* **2013**, *23*, 2239.

[137] D. Gedefaw, M. Tessarolo, M. Prosa, M. Bolognesi, P. Henriksson, W. Zhuang, M. Seri, M. Muccini, M. R. Andersson, *Sol. Energy Mater. Sol. Cells* **2016**, *144*, 150.

[138] X. C. Wang, Y. P. Sun, S. Chen, X. Guo, M. J. Zhang, X. Y. Li, Y. F. Li, H. Q. Wang, *Macromolecules* **2012**, *45*, 1208.

[139] R. Singh, G. Pagona, V. G. Gregoriou, N. Tagmatarchis, D. Toliopoulos, Y. Han, Z. Fei, A. Katsouras, A. Avgeropoulos, T. D. Anthopoulos, M. Heeney, P. E. Keivanidis, C. L. Chochos, *Polym. Chem.* **2015**, *6*, 3098.

[140] D. M. de Leeuw, M. M. J. Simenon, a. R. Brown, R. E. F. Einerhand, *Synth. Met.* **1997**, *87*, 53.

[141] X. Xu, Y. Wu, J. Fang, Z. Li, Z. Wang, Y. Li, Q. Peng, *Chem. - A Eur. J.* **2014**, *20*, 13259.

[142] T. Heumueller, T. M. Burke, W. R. Mateker, I. T. Sachs-Quintana, K. Vandewal, C. J. Brabec, M. D. McGehee, *Adv. Energy Mater.* **2015**, *5*, 1.

[143] S. Ben Dkhil, D. Duché, M. Gaceur, A. K. Thakur, F. B. Aboura, L. Escoubas, J. J. Simon, A. Guerrero, J. Bisquert, G. Garcia-Belmonte, Q. Bao, M. Fahlman, C. Videlot-Ackermann, O. Margeat, J. Ackermann, *Adv. Energy Mater.* **2014**, 1.

[144] I. Jeon, J. W. Ryan, T. Nakazaki, K. S. Yeo, Y. Negishi, Y. Matsuo, *J. Mater. Chem. A* **2014**, *2*, 18754.

[145] A. J. Morfa, B. I. Macdonald, J. Subbiah, J. J. Jasieniak, *Sol. Energy Mater. Sol. Cells* **2014**, *124*, 211.

[146] Y. Jin, J. Wang, B. Sun, J. C. Blakesley, N. C. Greenham, *Nano Lett.* **2008**, *8*, 1649.

[147] A. Manor, E. a. Katz, T. Tromholt, F. C. Krebs, *Adv. Energy Mater.* **2011**, *1*, 836.

[148] S. Trost, K. Zilberberg, A. Behrendt, A. Polywka, P. Görrn, P. Reckers, J. Maibach, T. Mayer, T. Riedl, *Adv. Energy Mater.* **2013**, *3*, 1437.

[149] S. Bai, Y. Jin, X. Liang, Z. Ye, Z. Wu, B. Sun, Z. Ma, Z. Tang, J. Wang, U. Würfel, F. Gao, F. Zhang, *Adv. Energy Mater.* **2014**, 1401606.

[150] B. A. MacLeod, B. J. Tremolet de Villers, P. Schulz, P. F. Ndione, H. Kim, A. J. Giordano, K. Zhu, S. R. Marder, S. Graham, J. J. Berry, A. Kahn, D. C. Olson, *Energy Environ. Sci.* **2015**, *8*, 592.

[151] P. Romero-Gomez, R. Betancur, A. Martinez-Otero, X. Elias, M. Mariano, B. Romero, B. Arredondo, R. Vergaz, J. Martorell, *Sol. Energy Mater. Sol. Cells* **2015**, *137*, 44.

[152] H. Liu, Z. Wu, J. Hu, Q. Song, B. Wu, H. Lam Tam, Q. Yang, W. H. Choi, F. Zhu, *Appl. Phys. Lett.* **2013**, *103*.

[153] T. Stubhan, H. Oh, L. Pinna, J. Krantz, I. Litzov, C. J. Brabec, *Org. Electron.* **2011**, *12*, 1539.

[154] T. Stubhan, I. Litzov, N. Li, M. Salinas, M. Steidl, G. Sauer, K. Forberich, G. J. Matt, M. Halik, C. J. Brabec, *J. Mater. Chem. A* **2013**, *1*, 6004.

[155] H. Oh, J. Krantz, I. Litzov, T. Stubhan, L. Pinna, C. J. Brabec, *Sol. Energy Mater. Sol. Cells* **2011**, *95*, 2194.

[156] Z. Kam, X. Wang, J. Zhang, J. Wu, *ACS Appl. Mater. Interfaces* **2015**, *7*, 1608.

[157] Q. Bao, X. Liu, Y. Xia, F. Gao, L.-D. Kauffmann, O. Margeat, J. Ackermann, M. Fahlman, *J. Mater. Chem. A* **2014**, *2*, 17676.

[158] P. Adhikary, S. Venkatesan, N. Adhikari, P. P. Maharjan, O. Adebanjo, J. Chen, Q. Qiao, *Nanoscale* **2013**, *5*, 10007.

[159] J. M. Cho, S. W. Kwak, H. Aqoma, J. W. Kim, W. S. Shin, S. J. Moon, S. Y. Jang, J. Jo, *Org. Electron. physics, Mater. Appl.* **2014**, *15*, 1942.

[160] S. Wilken, J. Parisi, H. Borchert, *J. Phys. Chem. C* **2014**, *118*, 19672.

[161] A. Aprilia, P. Wulandari, V. Suendo, Herman, R. Hidayat, A. Fujii, M. Ozaki, *Sol. Energy Mater. Sol. Cells* **2013**, *111*, 181.

[162] S.-Y. Kuo, W.-C. Chen, F.-I. Lai, C.-P. Cheng, H.-C. Kuo, S.-C. Wang, W.-F. Hsieh, *J. Cryst. Growth* **2006**, *287*, 78.

[163] O. Pachoumi, C. Li, Y. Vaynzof, K. K. Banger, H. Sirringhaus, *Adv. Energy Mater.* **2013**, *3*, 1428.

[164] A. Polman, M. Knoght, E. C. Garnett, B. Ehrler, W. Sinke, *Science (80-.).* **2016**, *352*, 307.

[165] G. Zhang, K. Zhang, Q. Yin, X. Jiang, G. Zhang, K. Zhang, Q. Yin, X. Jiang, Z. Wang, J. Xin, W. Ma, *J. Am. Chem. Soc.* **2017**.

[166] K. H. Park, Y. An, S. Jung, H. Park, C. Yang, *Energy Environ. Sci.* **2016**, *9*, 3464.

[167] N. Gasparini, L. Lucera, M. Salvador, M. Prosa, G. D. Spyropoulos, P. Kubis, H.-J. Egelhaaf, C. J. Brabec, T. Ameri, *Energy Environ. Sci.* **2017**, DOI: 10.1039/c6ee03599j.

[168] W. Shockley, H. J. Queisser, *J. Appl. Phys.* **1961**, *32*, 510.

[169] A. A. Bakulin, A. Rao, V. G. Pavelyev, P. H. M. van Loosdrecht, M. S. Pshenichnikov, D. Niedzialek, J. Cornil, D. Beljonne, R. H. Friend, *Science (80-.).* **2012**, *335*, 1340.

[170] G. Grancini, M. Maiuri, D. Fazzi, A. Petrozza, H. Egelhaaf, D. Brida, G. Cerullo, G. Lanzani, *Nat. Mater.* **2012**, *12*, 29.

[171] J. Lee, K. Vandewal, S. R. Yost, M. E. Bahlke, L. Goris, M. A. Baldo, J. V Manca, T. Van Voorhis, *J. Am. Chem. Soc.* **2010**, *132*, 11878.

[172] N. Gasparini, X. Jiao, T. Heumüller, D. Baran, G. J. Matt, S. Fladischer, E. Spiecker, H. Ade, C. J. Brabec, T. Ameri, *Nat. Energy* **2016**, 1.

[173] N. Gasparini, A. García-Rodríguez, M. Prosa, Ş. Bayseç, A. Katsouras, A. Avgeropoulos, G. Pagona, V. G. Gregoriou, C. L. Chochos, S. Allard, U. Scherf, J. Brabec, T. Ameri, *Front. Energy Res.* **2017**, *4*, doi: 10.3389/fenrg.2016.00040.

[174] T. Kumari, S. M. Lee, S. Kang, S. Chen, C. Yang, *Energy Environ. Sci.* **2017**, *10*, 10.1039/C6EE02851A.

[175] L. Nian, K. Gao, F. Liu, Y. Kan, X. Jiang, L. Liu, Z. Xie, X. Peng, T. P. Russell, Y. Ma, *Adv. Mater.* **2016**, *28*, 8184.

[176] M. Nam, M. Cha, H. H. Lee, K. Hur, K. Lee, J. Yoo, I. K. Han, S. J. Kwon, D. Ko, *Nat. Commun.* **2017**, *8*, 1.

[177] T. Goh, J. S. Huang, K. G. Yager, M. Y. Sfeir, C. Y. Nam, X. Tong, L. M. Guard, P. R. Melvin, F. Antonio, B. G. Bartolome, M. L. Lee, N. Hazari, A. D. Taylor, *Adv. Energy Mater.* **2016**, *6*.

[178] L. C. Hirst, N. J. Ekins-Daukes, *Prog. Photovolt Res. Appl.* **2011**, *19*, 286.

[179] M. Graetzel, R. A. J. Janssen, D. B. Mitzi, E. H. Sargent, *Nature* **2012**, *488*, 304.

[180] J. You, L. Dou, Z. Hong, G. Li, Y. Yang, *Prog. Polym. Sci.* **2013**, *38*, 1909.

[181] a. Hadipour, B. de Boer, P. W. M. Blom, *Org. Electron. physics, Mater. Appl.* **2008**, *9*, 617.

[182] S. Sista, Z. Hong, M. H. Park, Z. Xu, Y. Yang, *Adv. Mater.* **2010**, *22*, 77.

[183] T. Ameri, G. Dennler, C. Lungenschmied, C. J. Brabec, *Energy Environ. Sci.* **2009**, *2*, 347.

[184] M. Hiramoto, M. Suezaki, M. Yokoyama, *Chem. Lett.* **1990**, 327.

[185] L. Zuo, C.-Y. Chang, C.-C. Chueh, S. Zhang, H. Li, A. K.-Y. Jen, H. Chen, *Energy Environ. Sci.* **2015**, *8*, 1712.

[186] X. Du, O. Lytken, M. S. Killian, J. Cao, T. Stubhan, M. Turbiez, P. Schmuki, H. Steinrück, L. Ding, R. H. Fink, N. Li, C. J. Brabec, *Adv. Energy Mater.* **2016**, 1601959.

[187] R. Timmreck, S. Olthof, K. Leo, M. K. Riede, *J. Appl. Phys.* **2010**, *108*.

[188] D. J. D. Moet, P. De Bruyn, P. W. M. Blom, *Appl. Phys. Lett.* **2010**, *96*.

[189] S. Kouijzer, S. Esiner, C. H. Frijters, M. Turbiez, M. M. Wienk, R. A. J. Janssen, *Adv. Energy Mater.* **2012**, *2*, 945.

[190] N. Li, D. Baran, K. Forberich, M. Turbiez, T. Ameri, F. C. Krebs, C. J. Brabec, *Adv. Energy Mater.* **2013**, *3*, 1597.

[191] H. F. Dam, T. R. Andersen, E. B. L. Pedersen, K. T. S. Thydén, M. Helgesen, J. E. Carlé, P. S. Jørgensen, J. Reinhardt, R. R. Søndergaard, M. Jørgensen, E. Bundgaard, F. C. Krebs, J. W. Andreasen, *Adv. Energy Mater.* **2015**, *5*, 1.

[192] G. D. Spyropoulos, P. Kubis, N. Li, D. Baran, L. Lucera, M. Salvador, T. Ameri, M. Voigt, F. C. Krebs, C. J. Brabec, *Energy Environ. Sci.* **2014**, *7*, 3284.

[193] Y. Zhou, C. Fuentes-Hernandez, J. W. Shim, T. M. Khan, B. Kippelen, *Energy Environ. Sci.* **2012**, *5*, 9827.

[194] P. N. Yeh, S. H. Liao, Y. L. Li, H. R. Syue, S. A. Chen, *Sol. Energy Mater. Sol. Cells* **2014**, *128*, 240.

[195] A. Savva, M. Neophytou, C. Koutsides, K. Kalli, S. A. Choulis, *Org. Electron. physics, Mater. Appl.* **2013**, *14*, 3123.

[196] H. J. Snaith, H. Kenrick, M. Chiesa, R. H. Friend, *Polymer (Guildf).* **2005**, *46*, 2573.

[197] M. Yi, S. Hong, J. R. Kim, H. Kang, J. Lee, K. Yu, S. Kee, W. Lee, K. Lee, *Sol. Energy Mater. Sol. Cells* **2016**, *153*, 117.

[198] J. Tong, S. Xiong, Y. Zhou, L. Mao, X. Min, Z. Li, F. Jiang, W. Meng, F. Qin, T. Liu, R. Ge, C. Fuentes-Hernandez, B. Kippelen, Y. Zhou, *Mater. Horizons* **2016**, *3*, 452.

[199] W. Kim, N. Kim, J. K. Kim, I. Park, Y. S. Choi, D. H. Wang, H. Chae, J. H. Park, *ChemSusChem* **2013**, *6*, 1070.

[200] R. Po, C. Carbonera, A. Bernardi, F. Tinti, N. Camaioni, *Sol. Energy Mater. Sol. Cells* **2012**, *100*, 97.

[201] C. Y. Chang, L. Zuo, H. L. Yip, Y. Li, C. Z. Li, C. S. Hsu, Y. J. Cheng, H. Chen, A. K. Y. Jen, *Adv. Funct. Mater.* **2013**, *23*, 5084.

[202] D. Gupta, M. M. Wienk, R. A. J. Janssen, *ACS Appl. Mater. Interfaces* **2014**, *6*, 13937.

[203] M. Vosgueritchian, D. J. Lipomi, Z. Bao, *Adv. Funct. Mater.* **2012**, *22*, 421.

[204] C. M. Palumbiny, J. Schlipf, A. Hexemer, C. Wang, P. Müller-Buschbaum, *Adv. Electron. Mater.* **2016**, *2*, 1500377.

[205] M. Prosa, M. Tessarolo, M. Bolognesi, T. Cramer, Z. Chen, A. Facchetti, B. Fraboni, M. Seri, G. Ruani, M. Muccini, *Adv. Mater. Interfaces* **2016**, *3*, 1600770.

[206] M. Pfannmöller, H. Heidari, L. Nanson, O. R. Lozman, M. Chrapa, T. Offermans, G. Nisato, S. Bals, *Nano Lett.* **2015**, *15*, 6634.

[207] S. Roland, S. Neubert, S. Albrecht, B. Stannowski, M. Seger, A. Facchetti, R. Schlatmann, B. Rech, D. Neher, *Adv. Mater.* **2015**, *27*, 1262.

[208] N. Li, C. J. Brabec, *Energy Environ. Sci.* **2015**, *8*, 2902.

[209] Z. Xiao, Y. Yuan, B. Yang, J. Vanderslice, J. Chen, O. Dyck, G. Duscher, J. Huang, *Adv. Mater.* **2014**, *26*, 3068.

[210] D. Alemu, H.-Y. Wei, K.-C. Ho, C.-W. Chu, *Energy Environ. Sci.* **2012**, *5*, 9662.

[211] S.-I. Na, G. Wang, S.-S. Kim, T.-W. Kim, S.-H. Oh, B.-K. Yu, T. Lee, D.-Y. Kim, *J. Mater. Chem.* **2009**, *19*, 9045.

[212] C. Capello, U. Fischer, K. Hungerbühler, *Green Chem.* **2007**, *9*, 927.

[213] M. Bolognesi, M. Tessarolo, T. Posati, M. Nocchetti, V. Benfenati, M. Seri, G. Ruani, M. Muccini, *Org. Photonics Photovoltaics* **2013**, *1*, 1.

[214] A. M. Nardes, M. Kemerink, R. A. J. Janssen, J. A. M. Bastiaansen, N. M. M. Kiggen, B. M. W. Langeveld, A. J. J. M. Van Breemen, M. M. De Kok, *Adv. Mater.* **2007**, *19*, 1196.

[215] A. Fallahzadeh, J. Saghaei, M. H. Yousefi, *Appl. Surf. Sci.* **2014**, *320*, 895.

[216] Y. H. Kim, C. Sachse, M. L. MacHala, C. May, L. Müller-Meskamp, K. Leo, *Adv. Funct. Mater.* **2011**, *21*, 1076.

[217] T. W. Lee, Y. Chung, *Adv. Funct. Mater.* **2008**, *18*, 2246.

[218] J. Hwang, F. Amy, A. Kahn, *Org. Electron. physics, Mater. Appl.* **2006**, *7*, 387.

[219] S. Lu, X. Guan, X. Li, W. E. I. Sha, F. Xie, H. Liu, J. Wang, F. Huang, W. C. H. Choy, *Adv. Energy Mater.* **2015**, *5*, 1.

[220] D. Bahro, M. Koppitz, A. Mertens, K. Glaser, J. Mescher, A. Colsmann, *Adv. Energy Mater.* **2015**, *5*, 1.

[221] B. Lechêne, G. Perrier, K. Emmanouil, S. Kennou, B. Bouthinon, R. De Bettignies, *Sol. Energy Mater. Sol. Cells* **2014**, *120*, 709.

[222] Z.-E. Ooi, R. Jin, J. Huang, Y. F. Loo, A. Sellinger, J. C. DeMello, *J. Mater. Chem.* **2008**, *18*, 1644.

[223] D. J. Wehenkel, L. J. A. Koster, M. M. Wienk, R. A. J. Janssen, *Phys. Rev. B - Condens. Matter Mater. Phys.* **2012**, *85*, 125203.

[224] A. Petersen, T. Kirchartz, T. Wagner, *Phys. Rev. B* **2012**, *85*, 1.

[225] D. Yang, P. Fu, F. Zhang, N. Wang, J. Zhang, C. Li, *J. Mater. Chem. A* **2014**, *2*, 17281.

[226] S. Woo, W. Hyun Kim, H. Kim, Y. Yi, H. K. Lyu, Y. Kim, *Adv. Energy Mater.* **2014**, *4*, 1.

[227] T. J. K. Brenner, Z. Li, C. R. McNeill, *J. Phys. Chem. C* **2011**, *115*, 22075.

[228] R. a Street, K. W. Song, S. Cowan, *Org. Electron.* **2011**, *12*, 244.

[229] U. Hoyer, L. Pinna, T. Swonke, R. Auer, C. J. Brabec, T. Stubhan, N. Li, *Adv. Energy Mater.* **2011**, *1*, 1097.

[230] K. Tvingstedt, K. Vandewal, A. Gadisa, F. Zhang, *J. Am. Chem. Soc.* **2009**, *131*, 11819.

[231] P. J. Jesuraj, K. Jeganathan, *RSC Adv.* **2014**, *5*, 684.

[232] J. Reinhardt, M. Grein, C. Bühler, M. Schubert, U. Würfel, *Adv. Energy Mater.* **2014**, *4*, 1.

[233] G. J. A. H. Wetzelaer, M. Kuik, P. W. M. Blom, *Adv. Energy Mater.* **2012**, *2*, 1232.

[234] Y. Zimmermann, A. Schäffer, C. Hugi, K. Fent, P. F. Corvini, M. Lenz, *Environ. Int.* **2012**, *49*, 128.

[235] N. Espinosa, M. Hosel, M. Jorgensen, F. C. Krebs, *Energy Environ. Sci.* **2014**, *7*, 855.

[236] N. Espinosa, Y.-S. Zimmermann, G. A. dos Reis Benatto, M. Lenz, F. C. Krebs, *Energy Environ. Sci.* **2016**, *9*, 1674.

[237] F. C. Krebs, N. Espinosa, M. Hösel, R. R. Søndergaard, M. Jørgensen, *Adv. Mater.* **2014**, *26*, 29.

[238] C. Sprau, F. Buss, M. Wagner, D. Landerer, M. Koppitz, A. Schulz, D. Bahro, W. Schabel, P. Scharfer, A. Colsmann, *Energy Environ. Sci.* **2015**, *8*, 2744.

[239] P. G. Jessop, *Green Chem.* **2011**, *13*, 1391.

[240] S. Zhang, L. Ye, H. Zhang, J. Hou, *Mater. Today* **2016**, http://dx.doi.org/10.1016/j.mattod.2016.02.019.

[241] C.-C. Chueh, K. Yao, H.-L. Yip, C.-Y. Chang, Y.-X. Xu, K.-S. Chen, C.-Z. Li, P. Liu, F. Huang, Y. Chen, W.-C. Chen, A. K.-Y. Jen, *Energy Environ. Sci.* **2013**, *6*, 3241.

[242] Y. Deng, W. Li, L. Liu, H. Tian, Z. Xie, Y. Geng, F. Wang, *Energy Environ. Sci.* **2015**, *8*, 585.

[243] M. Seri, D. Gedefaw, M. Prosa, M. Tessarolo, M. Bolognesi, M. Muccini, M. R. Andersson, *J. Polym. Sci. Part A Polym. Chem.* **2016**, *55*, 234.

[244] L. Huo, J. Hou, S. Zhang, H. Y. Chen, Y. Yang, *Angew. Chemie - Int. Ed.* **2010**, *49*, 1500.

[245] S.-L. Lim, K.-H. Ong, J. Li, L. Yang, Y.-F. Chang, H.-F. Meng, X. Wang, Z.-K. Chen, *Org. Electron.* **2017**, *43*, 55.

[246] M. E. Farahat, C.-S. Tsao, Y.-C. Huang, S.-H. Chang, W. Budiawan, C.-G. Wu, C. W. Chu, *J. Mater. Chem. A* **2016**, DOI: 10.1039/c6ta01368f.

[247] K. Chen, H. Yip, C. W. Schlenker, D. S. Ginger, A. K. Jen, *Org. Electron.* **2012**, *13*, 2870.